

# **A Decade of ERS Satellite Orbits and Altimetry**



# **A Decade of ERS Satellite Orbits and Altimetry**

Proefschrift

ter verkrijging van de graad van doctor  
aan de Technische Universiteit Delft,  
op gezag van de Rector Magnificus prof. dr. ir. J. T. Fokkema,  
voorzitter van het College voor Promoties,  
in het openbaar te verdedigen

op vrijdag 20 december 2002 te 13.30 uur

door

Remko SCHARROO

ingenieur luchtvaart- en ruimtevaarttechniek  
geboren te 's-Gravenhage

*Dit proefschrift is goedgekeurd door de promotor:*

Prof. ir. K. F. Wakker

*Samenstelling promotiecommissie:*

Rector Magnificus,	voorzitter
Prof. ir. K. F. Wakker,	Technische Universiteit Delft, promotor
Prof. ir. B. A. C. Ambrosius,	Technische Universiteit Delft
Prof. dr. ir. A. W. Heemink,	Technische Universiteit Delft
Prof. C. C. Tscherning,	Københavns Universitet, Denemarken
Prof. dr. D. J. Wingham,	University College London, Verenigd Koninkrijk
Dr. P. Vincent,	Centre National d'Études Spatiales, Frankrijk
Dr. J. Benveniste,	European Space Agency, Italië

*Published and distributed by:* DUP Science

DUP Science is an imprint of

Delft University Press

P. O. Box 98

2600 MG Delft

The Netherlands

Telephone: +31 15 27 85 678

Telefax: +31 15 27 85 706

E-mail: [Info@Library.TUdelft.NL](mailto:Info@Library.TUdelft.NL)

ISBN 90-407-2369-9

Keywords: orbit determination, satellite altimetry, gravity field models

Copyright © 2002 by R. Scharroo

All rights reserved. No part of the material protected by this copyright notice may be reproduced or utilized in any form or by any means, electronic or mechanical, including photocopying, recording or by any information storage and retrieval system, without written permission from the publisher: Delft University Press.

Printed in The Netherlands

# Contents

<b>Preface</b>	<b>ix</b>
<b>Summary</b>	<b>xv</b>
<b>Samenvatting</b>	<b>xvii</b>
<b>Abbreviations, Acronyms, and Symbols</b>	<b>xix</b>
<b>1 The ERS Satellites and Altimetry</b>	<b>1</b>
1.1 ERS satellites and their missions . . . . .	2
1.1.1 Instrumentation . . . . .	3
1.1.2 Orbit . . . . .	5
1.1.3 Attitude . . . . .	6
1.2 Satellite radar altimetry . . . . .	7
1.2.1 Altimeter range and biases . . . . .	7
1.2.2 Altimeter range corrections . . . . .	9
1.2.3 Sea surface height corrections . . . . .	10
1.2.4 Altimeter height residuals . . . . .	12
1.2.5 Crossover height differences . . . . .	13
1.2.6 Dual-satellite crossovers . . . . .	16
1.2.7 Collinear tracks . . . . .	16
1.3 Applications of satellite altimetry . . . . .	17
<b>2 Enhancement and Validation of ERS Altimeter Data</b>	<b>21</b>
2.1 Introduction . . . . .	21
2.2 ERS OPR Version 3, Version 5, and Version 6 . . . . .	22
2.3 Altimeter measurements . . . . .	23
2.3.1 Significant wave height . . . . .	23
2.3.2 Backscatter and wind speed . . . . .	26
2.3.3 Range and sea state bias . . . . .	27
2.3.4 Altimeter biases and drifts . . . . .	28
2.3.5 Time tagging . . . . .	29

2.4	Propagation corrections . . . . .	30
2.4.1	Dry tropospheric and inverted barometer corrections . . . . .	30
2.4.2	Radiometric wet troposphere corrections . . . . .	31
2.4.3	Model wet tropospheric correction . . . . .	32
2.4.4	Ionospheric correction . . . . .	32
2.5	Orbits and other geophysical corrections . . . . .	35
2.6	Data flagging and editing . . . . .	36
2.7	Error budget of ERS altimeter data . . . . .	38
2.8	Examples . . . . .	39
2.8.1	Changes in global mean sea level . . . . .	40
2.8.2	Global distribution of sea level variations . . . . .	42
<b>3</b>	<b>Precise Orbit Determination for the ERS Satellites</b>	<b>47</b>
3.1	Introduction . . . . .	47
3.2	History . . . . .	49
3.2.1	First-generation precise orbits . . . . .	49
3.2.2	Second-generation precise orbits . . . . .	49
3.2.3	Third-generation precise orbits . . . . .	50
3.3	Orbit determination . . . . .	50
3.4	Tracking data . . . . .	52
3.4.1	Satellite Laser Ranging (SLR) . . . . .	53
3.4.2	Precise Range and Range-Rate Equipment (PRARE) . . . . .	57
3.4.3	Doppler Orbitography Integrated by Satellite (DORIS) . . . . .	57
3.4.4	Altimeter ranges and crossovers . . . . .	58
3.5	Models and constants . . . . .	59
3.5.1	Gravity field models . . . . .	60
3.5.2	Non-conservative forces . . . . .	60
3.5.3	Arc length . . . . .	62
3.6	Orbit quality assessment . . . . .	64
3.7	Pros and cons of using altimeter tracking data . . . . .	64
<b>4</b>	<b>ERS-1 Radar Altimeter Range Calibration</b>	<b>67</b>
4.1	Introduction . . . . .	67
4.1.1	Overall description and scenario . . . . .	68
4.1.2	Details of the calibration procedure . . . . .	70
4.2	GPS campaigns and local surveys . . . . .	73
4.2.1	The October 1990 GPS campaign . . . . .	74
4.2.2	The September 1991 GPS campaign . . . . .	75
4.2.3	GPS results . . . . .	76
4.2.4	<i>Acqua Alta</i> tower survey . . . . .	77
4.3	Orbit determination . . . . .	79
4.4	Altimeter measurements . . . . .	87
4.4.1	Altimeter data processing per pass . . . . .	89
4.4.2	Doppler correction . . . . .	92

---

4.5	Tide gauge measurements . . . . .	93
4.6	The results . . . . .	93
4.6.1	Error budgets . . . . .	93
4.6.2	The final result . . . . .	94
<b>5</b>	<b>The Time Tag Bias of ERS Altimeter Data</b>	<b>99</b>
5.1	Introduction . . . . .	99
5.2	The variation of the timing error with time . . . . .	101
5.3	ERS altimeter datation mechanism . . . . .	103
5.4	Constant time errors induced by the time-stamping quantisation . . . . .	105
5.5	Temperature and clock frequency variations . . . . .	106
5.6	Daily and annual variation of the timing error . . . . .	112
5.7	Possible geophysical effects and other explanations . . . . .	114
5.7.1	Diurnal variation of the timing bias . . . . .	114
5.7.2	Annual variation of the timing bias . . . . .	116
5.7.3	Mean timing bias . . . . .	117
5.8	Conclusions . . . . .	118
<b>6</b>	<b>Gravity Field Model Tailoring for the ERS Satellites</b>	<b>121</b>
6.1	Linear perturbation theory . . . . .	121
6.2	Isolating the gravity-induced orbit errors . . . . .	124
6.3	Tailoring the gravity field model . . . . .	126
6.4	Independent assessment of DGM-E04 . . . . .	128
6.5	Gravity-induced orbit errors . . . . .	130
6.5.1	Precise orbit determination results . . . . .	131
6.5.2	High-elevation SLR passes . . . . .	132
6.5.3	Geographically anti-correlated orbit error . . . . .	133
6.5.4	Geographically fully-correlated orbit error . . . . .	135
6.5.5	Orbit differences . . . . .	137
6.6	Non-gravitational orbit errors . . . . .	139
6.6.1	Collinear tracks . . . . .	139
6.6.2	Orbital overlaps . . . . .	141
6.7	Error budget . . . . .	142
6.8	Conclusions and outreach . . . . .	144
6.8.1	Room for improvement . . . . .	144
6.8.2	Remaining considerations . . . . .	145
<b>7</b>	<b>Conclusions and Recommendations</b>	<b>147</b>
<b>A</b>	<b>Least-Squares Collocation</b>	<b>151</b>
A.1	Theory of least-squares collocation . . . . .	152
A.2	Covariance functions . . . . .	153
A.3	Implementation . . . . .	155

<b>B</b>	<b>The Gravity Induced Radial Orbit Error</b>	<b>159</b>
B.1	Introduction . . . . .	159
B.2	The problem . . . . .	160
B.3	The geopotential . . . . .	162
B.4	The Lagrange planetary equations . . . . .	165
B.5	Secular perturbations . . . . .	166
B.5.1	Ground track repetition . . . . .	168
B.5.2	Frozen orbit . . . . .	168
B.5.3	Sun-synchronous orbit . . . . .	169
B.6	Linear orbit perturbations . . . . .	169
B.7	Radial orbit perturbations on a nearly circular orbit . . . . .	171
B.8	Frequency spectrum of the radial orbit error . . . . .	173
B.8.1	Lumped coefficients . . . . .	173
B.8.2	Zonal coefficients . . . . .	176
B.8.3	Resonance . . . . .	176
B.8.4	Limitations due to arc length . . . . .	177
B.9	Spatial distribution of the radial orbit error . . . . .	178
B.9.1	From orbital elements to geographic location . . . . .	178
B.9.2	Radial orbit error at a geographical location . . . . .	180
<b>C</b>	<b>An Efficient Way to Compute the Gravity-induced Radial Orbit Error</b>	<b>183</b>
C.1	An example of the computation of geographically correlated radial orbit errors . . . . .	183
C.2	Software performance . . . . .	185
	<b>Bibliography</b>	<b>187</b>
	<b>Curriculum Vitae</b>	<b>197</b>



# Preface

When I started to work on the topics of satellite altimetry and precise orbit determination it was 1989. Our group at the Department of Aerospace Engineering of Delft University of Technology (DUT) was called Section Orbital Mechanics and we had three workstations with 200 Megabytes of disk space and some resources at a mainframe computer to our disposal. All the altimeter data we possessed was three months from Seasat and just over two years from Geosat. Given the disk capacity it was just possible to process data covering bits of ocean areas of about  $30^\circ \times 20^\circ$  at a time. Several tapes had to be mounted to select the relevant data and transfer them on hard disk. Once the processing was finally completed and orbit errors of a metre or more were removed, it took about 10 minutes just to plot your result: a mean ocean surface or a map of the ocean variability. The best way to transfer this information and store the pictures was by making a photograph of the image on screen, develop it and send it to colleagues by mail. Needless to say, in between all of this, we had some time left to give each  $30^\circ \times 20^\circ$  box an appropriate name.

Now, in 2002, the group has grown to become the Delft Institute for Earth-Oriented Space Research (DEOS). A single powerful personal computer with a disk capacity of 200 *Gigabytes* can hold the nearly 20 satellite-years of data from ERS-1, ERS-2, TOPEX/Poseidon, GFO and Jason-1 *on-line*. Orbit errors have dropped by almost two orders of magnitude and removal of the remainder has become optional. In a few seconds global maps of sea level variability or mean sea level change can be plotted on a computer screen or stored in electronic image formats, turned into animations, and shared by e-mail or web pages with colleagues or other interested persons world wide.

However, the success story of satellite altimetry is not only about increasing disk space and the capabilities of current workstations and the Internet. The success lies in the dedication of many of my colleagues in making the altimeter missions work: to get the project off the ground, to select the best mission scenario to fulfil the science objectives, to launch and operate the satellite, to calibrate and validate the data products, and *most of all* to enhance these products with new information, new models, new insights, new orbits. This way many new applications of satellite altimetry have seen the light that had previously been inconceivable.

My involvement with the ERS-1 mission started in 1990, about half a year before its launch, with the 'Venice arc calibration'. The goal of this ESA-lead project was to compute the range bias of the ERS-1 altimeter. This is the offset between the actual distance from the satellite to the sea surface and the one measured by the radar altimeter. DUT's contribution to this project consisted of additional laser tracking by its Modular Transportable Laser Ranging System (MTLRs-2), the precise positioning of the satellite over the calibration site near Venice, Italy, the construction of the altimetric sea level at the site and the calculation of the altimeter bias. At the time, with orbit errors in the tens of centimetres, the precise positioning could only be provided by so-called *short arc techniques*. It is remarkable that the value for the altimeter bias computed then [Francis *et al.*, 1993] is still undisputed. Later results still support this value well within the error margins. Chapter 4 of this thesis discusses the project and shows the results.

We all looked anxiously forward to the launch of ERS-1. At the time we had only a few years of altimeter data. We knew that we could map meso-scale ocean phenomena from this data; we knew we could make a reasonable mean sea surface and create a new look on the ruggedness of the ocean floor. ERS-1 was going to give us more: higher latitudes and maybe data precise enough to resolve the static dynamic topography and to map the ocean currents.

At the time, the Section of Orbital Mechanics was well established in the use of laser tracking data for the computation of geodetic satellites, like LAGEOS and Starlette [*e.g.*, Noomen *et al.*, 1988; Scharroo *et al.*, 1991]. Our next aim would be ERS-1: studies had indicated a promising future for its orbits [Wakker *et al.*, 1983, 1987].

I remember well discussing with Bob Cheney (National Oceanic and Atmospheric Administration, NOAA) before ERS-1's launch, how jointly we could create an ocean product within a week or two. It would be an Interim Geophysical Data Records (or IGDR), a product completely missing from the ESA data stream. This could be distributed to the science community far before the official ESA ocean product (OPR) was available. DUT would provide the orbits, NOAA would enhance and distribute the altimeter data. We expected to start off with orbit accuracies of around 1.5 metres and to improve that figure to about 50 cm using gravity field model tailoring [Zandbergen *et al.*, 1986; Zandbergen, 1991].

When the first ERS-1 Symposium was held in Cannes in October 1992, it became embarrassingly clear how important the IGDRs had been. Fifteen months into the mission the OPR data were still *in statu nascendi*. Luckily, the IGDRs had found their way throughout the altimeter community, otherwise Cannes would have seen very little reporting on the contribution of the ERS-1 radar altimeter to ocean science and geodesy. The production of OPR products improved rapidly thereafter.

Meanwhile, the quality of ERS-1 orbits improved rapidly. When the main tracking device on board the satellite, PRARE, failed soon after launch, we thought we were doomed. But the laser community rapidly spun up the data rate and we figured out how to inject the altimeter data themselves into the orbit determin-

ation. Together with our colleagues at the GeoForschungsZentrum and the University of Texas at Austin we have been driving the error margin down, always challenging each other to do better. New gravity field models were generated, tailor-made for the ERS satellites. We finally crushed the expected orbit errors by as much as an order of magnitude [Scharroo and Visser, 1998]. Chapters 3 and 6 and Appendix B describe the steps that have led to this remarkable achievement.

By 1993 the orbit errors were already down to 30 cm, accurate enough to construct global dynamic ocean topography maps from ERS-1 data [Naeije *et al.*, 1994]. At the same time the first detailed global mean sea surface from ERS-1 altimetry were produced [Anzenhofer *et al.*, 1994; Wisse *et al.*, 1994].

Another unexpected surprise was the newly developed technique of Interferometric SAR: an application of ERS-1 that was not foreseen. Now, SAR interferometry is considered *the* tool for the detection of land displacements in large areas around a seismic event [*e.g.*, Hanssen *et al.*, 2000]. Equally unexpected too me was the strong demand for Delft orbits from this user community. The orbit products that had originally only been intended for altimetry are now being used by numerous SAR processing softwares, like DORIS (DUT), ROI PAC (JPL/CalTech), and DIAPASON (CNES).

When ERS-1 appeared to be in tip-top shape at the end of the design lifetime of 3 years, it was time to look at the ocean in vaster detail than ever before. The still classified data of Geosat had opened up a wealth of spreading ridges and fracture zones and hotspots to the US Navy. Now scientists too should be allowed that view. The ERS-1 Geodetic Mission started and prompted the US Navy to release the Geosat data, since these had lost their tactical value. Now the challenge was to create a mean sea surface from non-repeating altimeter tracks [Scharroo, 1996]. Soon we all wanted to have the Sandwell and Smith [1997] marine gravity poster on our walls. Suddenly, gravity was known better over the global oceans than over large chunks of the land surfaces, which culminated in vastly improved knowledge of the ocean bathymetry.

We had the good fortune that ERS-1 was still running at full speed when ERS-2 was launched on 21 April 1995. Meanwhile the NOAA IGDR production had become a near-realtime operation. Using DUT orbit predictions NOAA cranked out a product, now called *RGDR* (R for Realtime), 12 hours after the end of each day. In this way, only two weeks into the ERS-2 mission DUT and NOAA created the first report on the intercalibration of ERS-1 and -2 [Scharroo *et al.*, 1995].

A year of tandem operation would follow until finally in June 1996 the curtain on ERS-1 fell because of financial reasons. This was a very important year for the advancement of satellite altimetry. We created the best gravity model for ERS orbit computation at the time and for years to come, slashing the orbit errors down to a mere 4-5 cm (Chapter 6). New tide models of astonishing precision came out. We learnt about timing errors and bias jumps in the ERS altimeter measurements (Chapter 5). Better models for the electromagnetic bias became available. All these achievements assisted the cross-calibration of the ERS altimeters.

By then we had already collected very valuable information on the rise and

fall of several El Niño cycles. Soon ERS-2 would observe the largest El Niño phenomenon of the last century (1997/1998), both with measurements of sea surface temperature and sea surface height.

The production of the RGDRs including near-realtime orbit computations for ERS-2 is now fully automated. Except for the few occasions when serious manoeuvres or payload shutdowns break up the process, it has been running for months at a time without any human intervention. Even these orbits have reached an accuracy generally better than 10 cm. As far as altimetry is concerned, ERS-2 has truly become an operational satellite.

From time to time ERS-1 was regularly revived to run experiments and in the end the SAR became almost fully operational again. Unfortunately, ERS-1 started to become an old lady: her solar panel had degraded significantly. On 10 March 2000 a failure in the attitude control system ended her long mission and excellent service record, which by then had grown to almost 9 years, 3 times as much as planned. There are few Earth-Observation satellites that made it that long.

It looked for a while like ERS-2 would see the same demise as ERS-1, limping along with a degraded sense of attitude. All but one gyroscope failed or performs badly. A new attitude control algorithm seems to have saved the mission recently, regaining her good attitude and aiming for a cross-calibration with Envisat with renewed spirit. Nonetheless, the altimeter data from 2000 and 2001 is not really up to standard. More work will have to be done to counteract the effects of off-nadir pointing and degradation of the altimeter receiver.

This, however, is but one of the problems faced with the processing of ERS altimeter data. Unfortunately, the production process of OPR data was not set up to accommodate any alterations since the beginning of the mission of ERS-1 and ERS-2. Thus, the ERS-2 OPRs still include geophysical and instrument corrections out of 1995, not to speak of ERS-1, in which case we are facing at least 3 more years of outdatedness. It has become a major undertaking to upgrade all the altimeter data, measurements *and* corrections, and stay up-to-date with the current insights into the matter, as shown in Chapter 2. The Radar Altimeter Database System (RADS) under construction at DEOS aims at providing freshly reprocessed data to a wider user community.

This thesis covers five main research topics, all with a single common goal: improving the quality of the ERS altimeter data, either by directly improving the basic range measurements, or the most important correction, the satellite orbit. The five topics are:

**Upgrading of ERS altimeter data**, as described in Chapter 2, includes the homogenisation of the measurements and their corrections to facilitate the comparison between the two satellites as well as with other satellite altimeters like TOPEX/Poseidon.

**Precise orbit determination** has made huge advancements after it seemed doomed by the loss of the PRARE tracking system. Chapter 3 describes the methods and models that have been developed over the years to improve the orbit precision of ERS-1 and ERS-2.

**Absolute calibration** of the ERS-1 altimeter range measurements was performed in-flight during an extensive local calibration campaign in the Northern Adriatic. Key elements, like the precise short-arc orbit determination and the combination of many measurements into a single calibration result, are presented Chapter 4.

**Accurate time tagging** of the altimeter measurements is of key importance to the quality of the measurements of sea level. Chapter 5 attempts to model the currently unexplained variations of the timing errors.

**Development of a gravity field model** tailored to the ERS satellites, as described in Chapter 6, was pivotal to the improvement of the precision of the ERS orbit determination.

Personally, the launch of ERS-1 marked the beginning of my academic career, which afterwards has been focused mainly on ERS-1 and ERS-2. The complexity of the missions and their wide multi-disciplinary use have brought together many great minds. It is their common effort that made the altimeter missions of both satellites such a success. This thesis touches upon a number of issues that troubled the ERS altimeter missions and to whose solution I hope I have contributed something over the last ten years.

I would like to thank my promotor, Professor Karel Wakker, for his enduring confidence that my long stay at DEOS would ultimately culminate in the writing of this thesis. I am also indebted to him and his insight that ERS-1 would be much more than just 'another satellite' and its orbit determination alone would already pose a serious bane to the young PhD student's mind. Neither of us would have thought, however, that it could occupy me still, 13 years later. I am also very grateful to my supervisor, Professor Boudewijn Ambrosius, for his continuing support and interest in all facets of my work as well as my personal life. All my colleagues at DEOS throughout the years deserve to be mentioned as they contributed to a very pleasant atmosphere to work in, but I like to name particularly Marc Naeije, Ejo Schrama, and Pieter Visser, whose critical reading of the first draft of this thesis have significantly enhanced the quality in the end. Additionally, I would like to commend and thank my paranympths, Andrea Walpersdorf and Edwin Wisse, for their long-lasting moral support. I am also grateful for the many helpful discussions with my colleagues at NOAA, who let me work quietly in my cubical or in New Hampshire, as long as I supplied them with a daily dose of Dutch liquorice.

Special thanks are for my parents, for all reasons combined. Finally, my deepest gratitude goes to Annabelle, Rosalie and Clara, who have tied me to my desk, served me lunches, teas and dinners on the few occasions that they actually saw me, and always remind me, with their love and humour, that there is a life after the thesis.

Remko Scharroo, Cornish, New Hampshire, November 2002.



# Summary

The First European Remote Sensing Satellite, ERS-1, was launched in July 1991, followed by ERS-2 in April 1995. Both satellites carry a radar altimeter to serve operational applications and scientific research in the fields of geodesy, oceanography, glaciology and meteorology. Together, the satellites have now been operating for over twelve years. This thesis embarks on the a voyage along several milestones in the lifetime of these satellites, and particularly of its altimeters.

Both altimeter missions were hampered by a number of misfortunes, ranging from hardware failures, via design mishaps, to a sub-optimally designed ground segment. Yet, the altimeter data, when properly processed and supplied with a precise orbit, can compete favourably with data supplied by specialised altimeter satellites like TOPEX/Poseidon and Jason-1. The upgrading of all altimeter corrections and the tweaking of the basic altimeter measurements of range, significant wave height and backscatter coefficient, are essential steps in this process, outlined in this thesis. Having accomplished that, the ERS altimeters allow the monitoring of annual, semi-annual and secular changes in sea level, which are important factors in study of climate change.

A key role in the processing of altimeter data plays the position of the satellite, and its progress in time, the satellite orbit. The quality of the recovered sea surface height is limited by the precision at which the orbit can be determined. A long journey along several stepwise improvements of the orbit determination process, both in the technique as well as in the modelling, have resulted in the reduction of the orbit error by a factor of 30! A major player in this process was the establishment of a gravity field model tailored to the ERS satellites that, when applied to ERS orbit determination, outperformed any of the previous and contemporary general-purpose models. Yet, it is shown that this model, DGM-E04, is not just a fabrication for the benefit of ERS only, but is equally suitable for the orbit determination of TOPEX/Poseidon and as a long-wavelength geoid model.

The calibration of the ERS-1 altimeter in 1991 required, at a time when the orbit errors were still counted in decimetres, if not metres, a short-arc orbit determination technique centred over the calibration site off the coast of Venice. Again, through elaborate surveying, gathering of altimeter corrections and tide gauge measurements, problem solving and elimination of errors, a final absolute range

bias of  $-41.5$  cm was established, a value that is still within the error margins of more recent estimates.

A timing error in the ERS altimeter data was discovered in 1995 and its cause remained a mystery ever since, especially when the timing error appeared to exhibit daily, annual and inter-annual variations as well. Although the exact cause may never be found, the issue is examined in fine detail and a model is constructed to eliminate the timing error for the benefit of the quality of the altimeter data.



# Samenvatting

De eerste Europese Remote Sensing Satelliet, ERS-1, werd in juli 1991 gelanceerd, gevolgd door ERS-2 in april 1995. Beide satellieten zijn voorzien van een radar hoogtemeter ten bate van operationele toepassingen en wetenschappelijk onderzoek op het terrein van geodesie, oceanografie, glaciologie en meteorologie. Samen functioneren de satellieten al meer dan 12 jaar. Dit proefschrift voert langs verschillende mijlpalen gedurende het leven van deze satellieten, en in het bijzonder van hun radar hoogtemeters.

Beide altimeter missies hebben te lijden gehad van een aantal tegenslagen, van het falen van apparatuur, via ontwerpfoutjes, tot een sub-optimaal ontwerp van het grond-segment. De altimeter gegevens kunnen echter, wanneer ze juist worden verwerkt en voorzien van een nauwkeurige satellietbaan, prima concurreren met gegevens die door gespecialiseerde altimeter satellieten als TOPEX/Poseidon en Jason-1 worden verstrekt. Het verbeteren van alle altimeter correcties en het aanpassen van de primaire altimeter metingen van afstand, significante golfhoogte en *backscatter* coëfficiënt, zijn essentiële stappen in dit proces, zoals beschreven in dit proefschrift. Als dit eenmaal bewerkstelligd is, kunnen de ERS hoogtemeters gebruikt worden voor het bepalen van jaarlijkse, half-jaarlijkse en lange-termijn veranderingen in de zeespiegel, belangrijke factoren in de studie van klimaatverandering.

Een vooraanstaande rol in de verwerking van hoogtemeter gegevens is weggelegd voor de positie van de satelliet en diens verloop in de tijd, de satelliet baan. De kwaliteit waarmee de hoogte van de zeespiegel kan worden bepaald wordt beperkt door de nauwkeurigheid waarmee de satellietbaan kan worden berekend. Een lange weg langs vele stapsgewijze verbeteringen in de baanberekening, zowel in de techniek als in de modellering, hebben geleid tot een 30-voudige reductie van de baan fouten! Een belangrijke speler in dit proces was de ontwikkeling van een gravitatie model dat toegesneden is op de ERS satellieten. Wanneer het wordt toegepast voor de baanberekening van de ERS satellieten, voldoet het beter dan ieder algemeen gravitatie model dat tot dan toe beschikbaar was. Dit model, DGM-E04, is niet slechts een fabricatie ten gunste van alleen ERS, maar is ook even geschikt voor de baanberekening van TOPEX/Poseidon en als langgolvig geïde model.

In 1991, toen baanfouten nog in decimeters of zelfs in meters werden gerekend,

was een *short-arc* baanberekening nodig voor de kalibratie van de ERS-1 hoogtemeter over het kalibratie platform voor de kust van Venetië. Uiteindelijk werd de absolute afstandsmeetfout, door uitgebreide landmeting, verzameling van hoogtemeter correcties en getijde metingen, oplossing van problemen en het elimineren van fouten, op  $-41.5$  cm vastgelegd. Deze waarde valt nog altijd, binnen de fouten marges, samen met meer recente schattingen.

Een tijdfout in de ERS hoogtemeter gegevens was al in 1995 ontdekt, maar naar de oorzaak ervan is het nog altijd gissen, vooral sinds het ook nog dagelijkse, jaarlijkse en inter-jaarlijkse veranderingen schijnt te vertonen. Hoewel de werkelijke oorzaak waarschijnlijk nooit gevonden zal worden, wordt dit onderwerp in detail behandeld en is een model geconstrueerd dat de tijdfout moet elimineren ten gunste van de kwaliteit van de altimeter gegevens.

# Abbreviations, Acronyms, and Symbols

## List of abbreviations and acronyms

Abbreviations and acronyms that occur only once in the text, with explanation, are not included in this list.

AIUB	Astronomical Institute of the University of Berne
ATSR	Along-track Scanning Radiometer
AVISO	Archiving, Validation and Interpretation of Satellite Oceanographic data
BM3	Sea-state Bias Model with 3 coefficients
CERSAT	Centre ERS d'Archivage et de Traitement
CNES	Centre National d'Études Spatiales
CODE	Centre for Orbit Determination in Europe
cpd	Cycle per day
cpr	Cycle per revolution
CSR	Center for Space Research
DEOS	Delft Institute for Earth-Oriented Space Research
DGM	Delft Gravity Field Model
DORIS	Doppler Orbitography Integrated by Satellite
DUT	Delft University of Technology
ECMWF	European Centre for Medium-range Weather Forecasts
ECN	European Calibration Network
EGM	Earth Gravity Model
ERS-1, ERS-2	First and Second European Remote-sensing Satellite
ESA	European Space Agency
ESOC	European Space Operations Centre
ESRIN	European Space Research and Information Centre
ESTEC	European Space Research and Technology Centre
ETRF	European Terrestrial Reference Frame
FES	Finite Element Solution

FFT	Fast-Fourier Transform
GDR	Geophysical Data Records
GFO	Geosat Follow-On
GFZ	GeoForschungsZentrum
GIM	GPS Ionosphere Map
GOME	Global Ozone Monitoring Experiment
GOT	Goddard Ocean Tide Model
GPS	Global Positioning System
GRGS	Groupe de Recherches de Géodésie Spatiale
GSFC	Goddard Space Flight Center
IGDR, MGDR, RGDR	Interim/Merged/Real-time Geophysical Data Records
IRI	International Reference Ionosphere
ISDGM	Istituto per lo Studio della Dinamica delle Grandi Masse
JGM	Joint Gravity Model
JPL	Jet Propulsion Laboratory
LAGEOS	Laser Geodetic Satellite
LPT	Linear Perturbation Theory
LRR	Laser Retroreflector
LST	Local Solar Time
MSIS	Mass Spectrometer Incoherent Scatter
MSS	Mean Sea Surface
MSSL	Mullard Space Science Laboratory
MTLRS	Modular Transportable Laser Ranging System
MWR	Microwave Radiometer
NASA	National Aeronautics and Space Administration
NIMA	National Imagery and Mapping Agency
NOAA	National Oceanic and Atmospheric Administration
OBC	On-Board Clock
OPR	Ocean Product
OSU	Ohio State University
PATN	Precise Time-Correlation Tables
PCA, TCA	Point/Time of Closest Approach
PGM, PGS	Preliminary Gravity Model/Solution
POD	Precise Orbit Determination
PRARE	Precise Range and Range-rate Equipment
RADS	Radar Altimeter Database System
RMS	Root-mean-square
SAR	Synthetic Aperture Radar
SBT	Satellite Binary Time
SLR	Satellite Laser Ranging
SPTR	Scanning Point Target Response
SSB	Sea-state Bias
SSH	Sea Surface Height
SWH	Significant Wave Height

TEC	Total Electron Content
TEG	Texas Earth Gravity
TOPEX	Topography Experiment
USO	Ultra-Stable Oscillator
UT	University of Texas at Austin
UTC	Coordinated Universal Time
V3, V5, V6	OPR Versions 3, 5, and 6
WAM	Wave Model

## List of symbols

$A$	Matrix of partials
$A$	Satellite cross-sectional area
$A, B, a, b, c$	Coefficients in least-squares fit
$a$	Acceleration due to non-potential forces
$a$	Semi-major axis of the satellite orbit
$a_e$	Scaling factor close to the mean equatorial radius of the Earth
$b$	Altimeter bias
$C$	Covariance matrix
$C$	Computed quantity
$C_D, C_R$	Drag and solar radiation coefficient
$\bar{C}_{lm}, \Delta\bar{C}_{lm}$	Gravity field coefficient and its error
$c$	Vector of unknowns
$c$	Speed of light
$D_{imp}$	Amplitude function
$d$	Distance
$E$	Eccentric anomaly
$e$	Eccentricity of the satellite orbit
$\bar{F}_{imp}$	Normalised inclination functions
$F_D, F_R$	Drag and solar radiation force
$f$	Frequency
$G_{lpq}$	Eccentricity functions
$H$	Height (above reference ellipsoid)
$h$	Altimeter range or range correction
$i$	Orbital inclination
$j, k, l, m, n, p, q$	Counters
$M$	Mean anomaly
$N$	Normal matrix
$N_D, N_R$	Number of revolutions per day and per repeat cycle
$n$	Noise vector
$n$	Orbit angular motion
$O$	Observed quantity

---

$P$	Step length of on-board clock
$\overline{P}_{lm}$	Normalised associated Legendre functions
$P_{lmjk}$	Covariances of the geopotential coefficient errors
$\overline{Q}_{lm}$	Latitude function in gravitational orbit error
$\mathbf{R}$	Geocentric position vector of tracking station
$R$	Disturbing potential
$\mathbf{r}$	Geocentric position vector of satellite
$r$	Orbit radius (distance between geocentre and satellite)
$\Delta r$	Radial orbit error
$\overline{S}_{lm}, \Delta \overline{S}_{lm}$	Gravity field coefficient and its error
$S_{lmpq}$	Phase functions
$\mathbf{s}$	Vector of signals
$\mathbf{t}$	Signal part of measurement vector
$t$	Time
$U$	Gravity potential
$V$	Velocity of satellite with respect to atmosphere
$\mathbf{W}$	Matrix of weights
$\mathbf{x}$	Measurement vector
$x, y, z$	Station coordinates
$\mathbf{y}$	Orbit state vector
$\epsilon$	Error variance/covariance matrix
$\theta$	Greenwich sidereal time
$\lambda$	Longitude
$\mu$	Earth's gravitational parameter
$\rho$	Range between tracking station and satellite
$\sigma$	Error standard deviation
$\tau$	Travel time
$\phi$	Phase angle
$\phi$	Geocentric latitude
$\psi_{lmpq}$	Orbit error phase angle
$\Omega$	Right ascension of the ascending node
$\omega$	Argument of the perigee

# The ERS Satellites and Altimetry

The European Remote Sensing Satellites ERS-1 and ERS-2 are now flying for a full decade. Launched in 1991, ERS-1 was the most complex satellite ever launched by the European Space Agency (ESA). Although designed for an operational life time of 3 years, ERS-1 remained fully operational till 1996. Its twin, ERS-2, was launched in 1995 and is still faithfully providing a wealth of information. The satellites embarked on a challenging mission: the monitoring of various facets of the ocean-atmosphere system as well as land use. The suite of microwave and infrared remote sensing instruments were designed to measure wind speeds, wave heights, ocean temperature and elevation, ice elevations, scattering properties of land and ocean, and ozone concentration.

A key instrument on both satellites is the radar altimeter, measuring the height of the satellite above the ocean surface. From this range measurement, the absolute sea level or the variations in sea level can be inferred. In order to do so, the range measurements must be subtracted from the altitude of the satellite, defined in a well-defined reference frame. The accuracy of the absolute sea level measurements by a radar altimeter is therefore always limited by the accuracy of the computed satellite altitude. It is the object of the precise orbit determination (POD) to provide the satellite position at any time during the mission with centimetric precision. Since the altitude of the satellite is of primary importance to altimetry, the focus in this thesis will be on the computation of the satellite altitude rather than the other two orbit components (cross-track and along-track position).

This Chapter will briefly introduce the ERS satellites, their missions, orbit design and instrumentation, followed by an equally brief description of the basic principles and applications of satellite radar altimetry. For a comprehensive overview of the operation of radar altimeters and their contribution to geodesy, oceanography and glaciology the reader is referred to the books edited and authored by *Rummel and Sansò* [1993], *Klokočník et al.* [1994] and *Fu and Cazenave* [2001].

## 1.1 ERS satellites and their missions

ERS-1 was the first European Earth observation satellite which made use of microwave sensors. It had been in development for over a decade when it was launched on an Ariane 4 rocket from Kourou, French Guyana, on 17 July 1991 at 1:46:31 UTC. After being placed into an orbit with an altitude of about 790 km and an inclination of  $98.5^\circ$  it successfully deployed its instruments and entered the *Commissioning Phase* or *Phase A*. During this period all instruments were tested and their measurements were carefully calibrated and validated against models and *in-situ* measurements made on Earth and from aeroplanes [Attema and Francis, 1991]. Because of its 3-day repeat orbit, such activities could be repeated on a single location every 3 days. The story of the precise absolute calibration of the radar altimeter range measurements is captured in Chapter 4.

Then its actual planned mission of two to three years commenced: to provide measurements of the atmosphere, ocean, land, and ice. The data would be used to support Earth science research and to allow monitoring of the evolution of environmental and climatic changes and land use [Duchossois, 1991; Bruzzi, 1991].

After the 3-month Commissioning Phase the orbit was slightly shifted, yet maintaining a 3-day repeat cycle. This *First Ice Phase* or *Phase B* was later repeated as the *Second Ice Phase* or *Phase D*. During these periods the orbits were optimal for the polar research with the SAR instrument.

The *Multi-disciplinary Phase* or *Phase C* started in April 1992 and would be the main part of the mission. The 35-day repeat cycle would benefit all instruments and science disciplines, hence the name. But when the planned mission ended little under two years later, the satellite was still in perfect shape. A secondary objective of the mission, to map the mean sea surface at high spatial resolution, could now be fulfilled. The two *Geodetic Phases*, *Phases E and F*, were completed before the launch ERS-2, each filling a single repeat cycle of 168 days, providing a mapping with a spatial resolution of around 5 km. ERS-1 was kept operational for one more year, flying a 35-day repeat orbit in tandem with ERS-2, after which ERS-1 was put into hibernation in June 1996. Only occasional measurements were made after this period, until a failure in the on-board attitude control system ended the mission on 10 March 2000.

The follow-up mission ERS-2, a satellite nearly identical to ERS-1, had been launched on 21 April 1995, in order to provide continuity of measurements. It came equipped with some new or improved instruments, in order to enhance the mission objectives. The two spacecraft have operated in tandem for over a year during the *Tandem Phase* or *Phase G* for ERS-1, *Phase A* of ERS-2. Until its failure, ERS-1 was flying 32 minutes ahead of ERS-2 in the same orbital plane, which caused ERS-1 to precede ERS-2 by 24 hours along the same ground track. During this Tandem Mission, the instruments of both satellites could be inter-compared or *cross-calibrated*. Results from this period can be found in Chapter 6.

A complete list of the mission phases, their specifics and their purpose is given



Name of phase	start date	mean altitude (km)	period (rev/day)	AN (°)	Purpose
<b>ERS-1</b>					
A. Commissioning Ph.	25 Jul 91	789.78	43/ 3	7.62	Calibration and validation of instruments and data.
B. First Ice Ph.	28 Dec 91	789.78	43/ 3	5.75	Optimal observation of polar ice sheets with SAR.
C. Multi-disciplinary Ph.	14 Apr 91	796.13	501/ 35	0.13	Optimal global sampling for most instruments.
D. Second Ice Ph.	23 Dec 93	789.78	43/ 3	5.75	Repeat of measurements of polar ice sheets with SAR.
E. First Geodetic Ph.	10 Apr 94	783.85	2523/176	0.02	High spatial resolution sampling with radar altimeter.
F. Second Geodetic Ph.	28 Sep 94	783.85	2523/176	0.09	Densify spatial coverage even more.
G. Tandem Ph.	21 Mar 95	796.13	501/ 35	0.13	Cross-calibration with ERS-2 instruments.
<b>ERS-2</b>					
A. Multi-disciplinary Ph.	21 Apr 95	796.13	501/ 35	0.13	Optimal global sampling for most instruments.

Table 1.1 Phases of the ERS missions. The table lists for each phase: the letter and name of the phase, the start date, the mean altitude of the satellite above the reference ellipsoid, the length of the repeat period in revolutions and in days, the longitude of the first ascending node (AN) in a repeat cycle and the main purpose of the mission phase.

in Table 1.1. For more information about the ERS satellites, read *ESA Bulletin*, numbers 65 and 83.

### 1.1.1 Instrumentation

The ERS satellites were designed around the bus of the SPOT satellite [Fortescue and Stark, 1995], a series of French satellites observing the Earth in the visible spectrum and flying in *sun-synchronous* orbits, just like the ERS satellites (Section 1.1.2). The Service Module and Payload Electronics Module on ERS-1 and ERS-2 form a box which measures roughly  $2 \times 2 \times 3$  m. Suspended underneath this box by a pantograph is the  $24 \text{ m}^2$  solar array, which rotates to maintain Sun pointing (see Figure 1.1).

For communications and tracking purposes, both satellites are equipped with the following systems [Francis *et al.*, 1991]:

- Two S-band antennas, one on the Earth-pointing side and one on the opposite side for use during loss of attitude control;
- A dish-shaped X-band antenna for high-bandwidth communications;
- The Precise Range and Range-rate Equipment (PRARE) for precise satellite or-

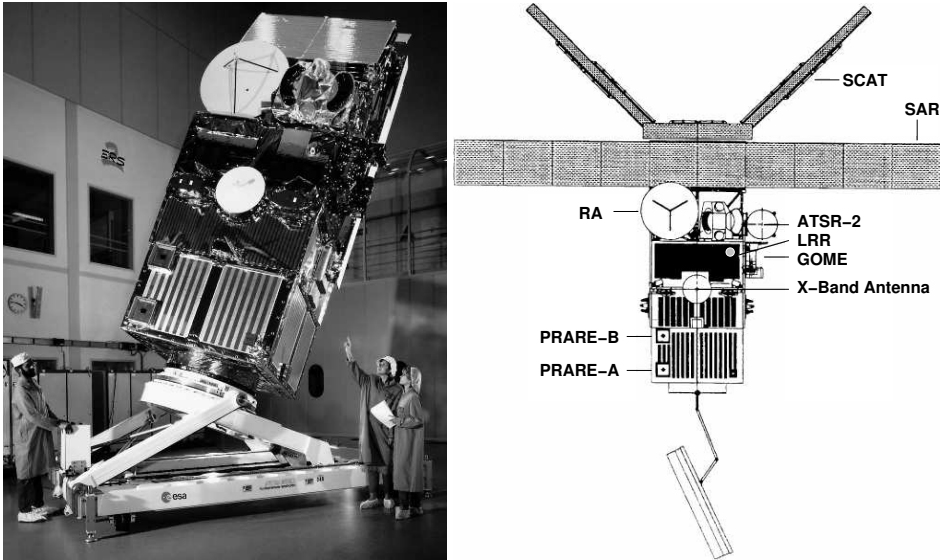


Figure 1.1 *Left:* ERS-1 in launch configuration at ESTEC, Noordwijk, The Netherlands (Courtesy: ESA). *Right:* ERS-2 instruments.

bit determination, which failed shortly after the launch of ERS-1, but operates nominally on ERS-2;

- A passive Laser Retroreflector (LRR), a dome with nine corner cube mirrors, to allow Satellite Laser Ranging (SLR) as a backup for orbit determination.

The intrinsic and the performances of the two tracking systems will be discussed and analysed in Chapters 3 and 6.

On top of the payload module, the Antenna Support Structure is mounted. This structure consists of a set of struts on which the following antennas for the microwave instruments are carried:

- The Synthetic Aperture Radar (SAR) operates in the Image Mode, obtaining high-resolution imagery 100 km in width to the right of the track, or in the Wave Mode, providing  $5 \text{ km} \times 5 \text{ km}$  images which can be interpreted to wave spectra;
- The dish-shaped Radar Altimeter (RA), measuring wave height, surface backscatter, and height above the earth surface (ocean, land, or ice);
- The three panel Wind Scatterometer Antenna (SCAT) can be operated over ocean surfaces, capturing the 2-dimensional wind field across a 500-km swath.

The Along-Track Scanning Radiometer and Microwave Sounder (ATSR-M) is mounted on top of the payload module and consists of two instruments, an Infrared Radiometer and a Microwave Sounder (MWR). The infrared radiometer

provides measurements of sea surface temperature at a resolution of  $1 \text{ km} \times 1 \text{ km}$  across a swath of 500 km right of the ground track. The MWR assists the altimeter with its measurements of total water vapour content in the atmosphere below the satellite.

The ERS-2 spacecraft is almost identical to ERS-1, but adds the Global Ozone Monitoring Experiment (GOME), designed to monitor the ozone hole in the upper atmosphere. The PRARE instrument on ERS-2 was upgraded and made fully redundant for improved reliability and performed without major problems [Massmann *et al.*, 2000].

### 1.1.2 Orbit

ERS-1 and -2 orbit the Earth in approximately 100.5 minutes in the same orbital plane. This means that the satellites follow each other along roughly the same imaginary elliptical trace in space with ERS-2 trailing its companion by about 32 minutes. When the orbits are projected onto the Earth surface, these *ground tracks* also overlap. But since the Earth rotates by almost  $8^\circ$  in 32 minutes, ERS-2 will not be on the same track that ERS-1 has just covered, but on a track ERS-1 covered exactly one day before. This 1-day ground track spacing was maintained until the final demise of ERS-1 in 2000.

The orbits are *sun-synchronous*, which means that the inclination ( $98.5^\circ$ ) and altitude (nearly 800 km) have been selected such that the Earth's gravitational flattening causes the orbital plane to precess at exactly the same rate as the apparent mean motion of the Sun around the Earth. Therefore, the *ascending node* is always passed at approximately the same local solar time (LST), in the case of ERS at 22:30. *Descending nodes* are passed at 10:30 LST (see Figure 1.2). This makes it possible to make repeated observations at the same local solar time, providing similar viewing conditions. For example, in this way one avoids the strong daily variations that overpower the monitoring of sea surface temperature by the ATSR. Other implications of the sun-synchronous orbit are discussed in Section B.5.3 of Appendix B.

Another characteristic of the ERS orbit is common to all satellites that carry a radar altimeter: the perigee of the elliptical orbit is fixed near the North Pole. This makes the altitude variation symmetric between ascending and descending passes so that at their crossing points the satellite is at more or less the same altitude, again promoting similar conditions. Read more about these so-called *frozen orbits* in Section B.5.2.

Although the satellites fly high above what we observe as 'the atmosphere', there is still a significant amount of particles at 800 km to make the satellite sense a drag force. Eventually, this will lower the satellite altitude and will cause it to drift away from its designated orbit and ground track. During periods of high solar activity the atmosphere expands appreciably, increasing the density at the ERS altitude, and hence the drag, by an order of magnitude or more. Hydrazine thrusters are used for occasional orbit maintenance manoeuvres boosting the satellite back to just above its nominal altitude. The goal of these manoeuvres is to ensure that the

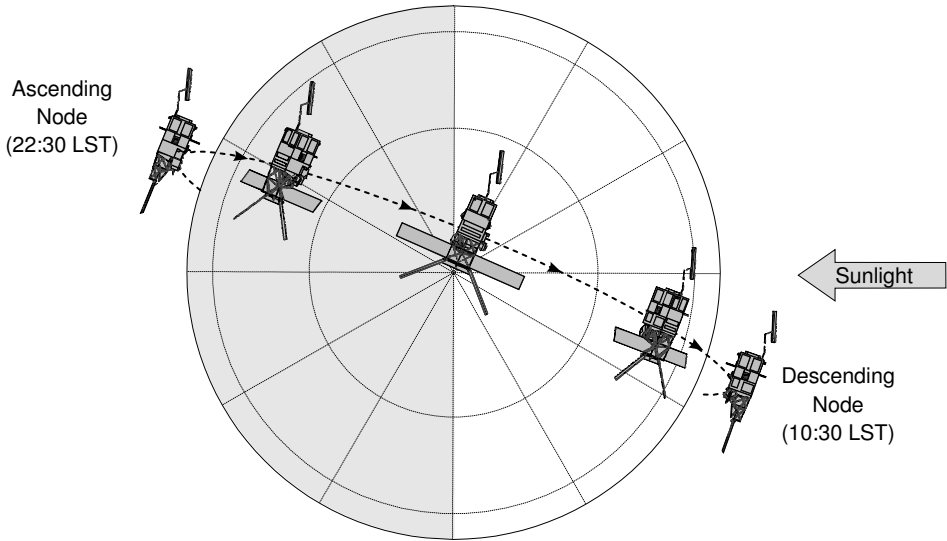


Figure 1.2 Illustration of the sun-synchronous orbit, the attitude of the satellite, and the pointing of the solar array, as seen from above the North Pole.

actual ground track is kept within 1 km of the nominal ground track and the mean local solar time is maintained within 1 minute. Such manoeuvres occur as rarely as once every two months during the mid-1990's up to as frequently as 3 times a month during high solar activity in 1991-1992.

### 1.1.3 Attitude

Both ERS satellites are three-axis-stabilised using a set of six reaction wheels. The satellites appear to fly 'sideways' as illustrated in Figure 1.2. The radar altimeter points in the nadir direction and the SAR looks to the right of the track. The rotation axis of the solar arrays is therefore in the cross-track direction. Note that although the angle between the orbital plane and the Sun direction varies slightly with the seasons, the plane of the solar array makes a fixed angle with its rotation axis. However, the periodic rotation of the solar array is stepwise adjusted for the seasonal motion of the Sun with respect to the equator, so that the power supply is maximised. During every orbit, the satellites spend about 34 minutes in eclipse.

The nominal mode of the attitude control system is called the *Yaw-Steering Mode*. In this mode, the yaw axis keeps pointing toward the local vertical, defined by an ellipsoid that approximates the Earth's shape. The pitch axis, which is in the direction of the solar array rotation axis, is kept normal to the true ground velocity vector (taking Earth rotation into account) to provide Doppler compensation. Since early 2000 the attitude control of ERS-2 has been seriously degraded due to the dropout of five of the six gyroscopes that monitor the attitude. After a short

period of operating on one gyro, ERS-2 functioned without gyros until December 2001 when a new one-gyro attitude control algorithm was uploaded to the satellite. Although it was attempted to sustain a proper nadir pointing of the altimeter, this could not always be guaranteed, hence degrading the altimeter performance. Altimeter results beyond 1999 should therefore be considered with care.

## 1.2 Satellite radar altimetry

After Skylab, GEOS 3, Seasat, and Geosat, ERS-1 was the fifth satellite in the world to carry a radar altimeter. Apart from studying in detail the sea surface and all kinds of medium- and large-scale ocean current systems with a higher precision than the previous missions had allowed, one of the goals was to obtain a better understanding of the long-term global sea level rise. The simultaneous measurements of ERS-1, ERS-2 and the dedicated altimeter satellites TOPEX/Poseidon (a US/French mission launched on 10 August 1992), GFO (the US Navy Geosat Follow-On, operational since 29 November 2000), and Jason-1 (the TOPEX follow-on launched in on 17 December 2001), are instrumental to the assessment of these phenomena.

This Section describes, in short, the operation of a radar altimeter and the corrections to be applied to the altimeter range in order to compute an accurate estimate of the sea surface height. For details of the corrections applied to the ERS data used in this thesis, the reader is referred to Chapter 2.

### 1.2.1 Altimeter range and biases

The radar altimeter is a nadir pointing instrument, which sends radar pulses with a linearly changing frequency, a so-called *chirp*, to the ocean surface. Figure 1.3 illustrates how the echos from thousands of reflecting elements on the surface are compared with the transmitted chirp and then submitted to a Fast Fourier Transform (FFT). The characteristic increase and flattening out of the returned power as a function of *FFT gate number* (i.e., time) is called the *waveform* [Brown, 1977]. The location of the point of maximum rate of increase (the leading edge), the slope of the increase and the total received power are the three principle properties that are measured by a radar altimeter, shown in Figure 1.4. This process is performed by an algorithm called *tracker* [Chelton et al., 1989]. The on-board tracker is usually optimised to sense the leading edge and keep it centred in the middle of the *tracking window*, i.e., around gate number 32. Any excursion of the leading edge from the mid-point is input to an  $\alpha$ - $\beta$  *tracking loop* which predicts the location of the next leading edge for the timing of the next pulse [Jensen, 1999]. For Geosat and TOPEX, the output of the on-board tracker are used as the actual measurements.

In order to obtain a more accurate measurements, and avoid the correlation between consecutive measurements that is intrinsic to the  $\alpha$ - $\beta$  tracker, the ERS waveforms are *retracked* individually on-ground, without any feed-back loop.

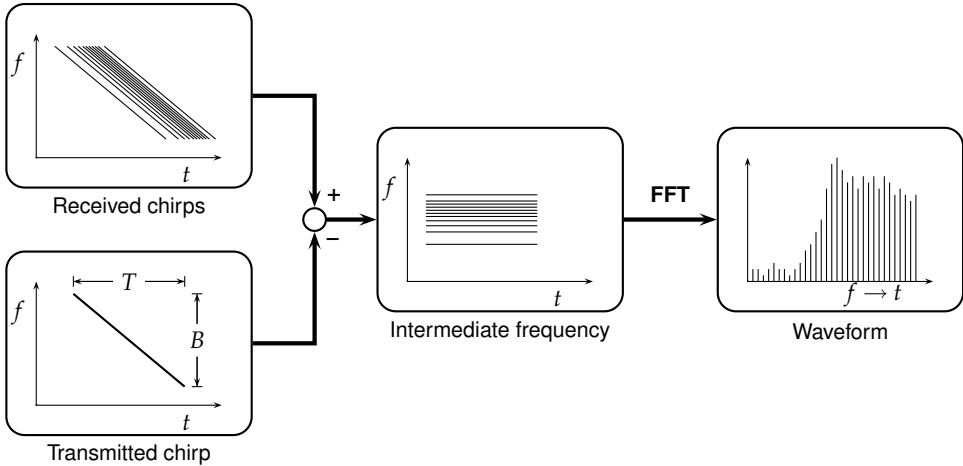


Figure 1.3 Diagram showing the conversion of the received radar echo to a waveform. The chirp transmitted by the ERS altimeters has a duration  $T$  of 20  $\mu$ s and a bandwidth  $B$  of 330 MHz.

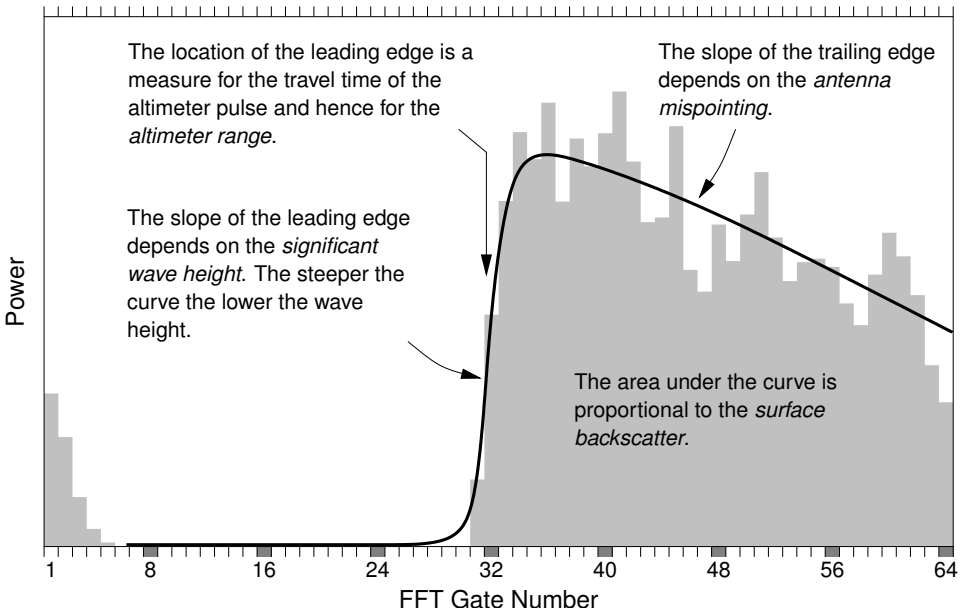


Figure 1.4 Example of an ERS-1 altimeter waveform. The scale along the horizontal axis indicates the gate number, with every eighth being shaded, and is a measure for the travel time of the altimeter pulse. The vertical axis indicates the received power over each interval. The grey bar graph represents an actual waveform. The black curve resembles a fit to the data determined by a waveform retracker.

From the basic properties of the waveform, straightforward conversions determine the important physical measurements of *altimeter range*, *significant wave height (SWH)*, and *surface backscatter* [Chelton *et al.*, 1989, 2001]. Over ocean surfaces, an empirical relationship can be used to convert the backscatter to an estimate of *wind speed* [Witter and Chelton, 1991].

Assuming the radar pulse travels at the speed of light,  $c$ , the (uncorrected) altimeter range can be estimated from the travel time,  $\tau$ ,

$$h_{alt} = \frac{c\tau}{2} \quad . \quad (1.1)$$

This range is quite a bit longer than the actual height of the satellite above the sea surface: after the return pulse arrives at the antenna dish, it is first reflected down to the antenna feed, then follows several metres of wave guide to the receiver and then still a lengthy winding path through the altimeter instrument. A more practical reference point for the altimeter range, than some point in the instrument, is the plane of the antenna aperture. Most of the path length from there to the instrument can be estimated or calibrated in a laboratory environment before launch. The remainder, the internal path in the instrument varies with temperature and age of the instrument and has to be monitored in-flight. This is done every few minutes by means of a so-called *internal open-loop calibration*.

For several reasons the laboratory calibrations of the internal and external path lengths may be biased: part of the path is omitted, the laboratory environment is different for the space environment, or the measurement equipment insufficiently precise. Since the variable part of the path delay is monitored by the internal calibration, the remaining error should be a constant bias. It was the aim of the ERS-1 *in-flight* calibration (Chapter 4) to determine this bias.

The ERS altimeters transmit 1020 pulses per second. Since the return from one pulse does not produce a waveform that is too noisy to accurately pinpoint the leading edge, 50 pulses are averaged into one waveform. Hence, measurements are produced at a rate of roughly 20 Hz. The precision of the measurements is again boosted by averaging 20 elementary measurements into one 1-Hz measurement. During this process, outliers are detected and rejected. The 1-Hz measurement not only contains values for range, wave height and backscatter, but also their respective variations within the 1-second period.

## 1.2.2 Altimeter range corrections

In practise, it is more customary to refer the origin of the measured range back to the satellite centre of mass than to the antenna aperture plane. This means that the vertical offset of the radar antenna to the centre of mass has to be added to the range.

Refraction by neutral and charged particles in the atmosphere delay the radar pulse and lengthen the altimeter range. To counterbalance this pulse delay a range correction is to be applied to the uncorrected range. The range correction is split up

into three parts: the *dry tropospheric* and *wet tropospheric correction* are based on the atmospheric pressure, temperature and partial pressure of water vapour in the troposphere; the *ionospheric correction* accounts for charged particles in the ionosphere and can be modelled or determined directly by dual-frequency altimeters. Since by definition (or rather by common practise) all altimeter corrections are *added* to the altimeter range, all these propagation corrections are *negative*.

At the interaction of the radar pulse with the ocean surface there is a dependency on wave height. Since the radar pulse is more effectively reflected by the wave troughs than the wave crests, the average wave form is biased toward the wave troughs. Hence, the estimated range will refer to a point lower than the instantaneous mean (or spatially averaged) sea level across the footprint. The excess range or *electromagnetic bias* is roughly proportional to the significant wave height. In addition, the tracking algorithm may also introduce a wave height dependent bias called *tracker bias*. Several attempts have been made to separate the electromagnetic bias (which should be independent of the instrument) and the tracker bias (which may differ from instrument to instrument) [e.g., Gaspar and Florens, 1998], but to no avail. In this thesis we will simply use the combined effect known as *sea state bias* or SSB.

Generally, the actual corrected range is of little interest for most applications in the field of oceanography or geodesy. What counts is the height of the sea surface (or *sea surface height*, SSH) above a well-defined reference surface, the *reference ellipsoid*. This height can easily be computed by subtracting the corrected altimeter range from the orbital altitude [e.g., Klokočník et al., 1994] (see Figure 1.5), or

$$H_{alt} = H_{orb} - h_{alt} - h_{corr} \quad , \quad (1.2)$$

where

$H_{orb}$  = satellite altitude above a reference ellipsoid;

$h_{alt}$  = measured altimeter height above the sea surface, corrected for instrumental delays and centre-of-mass offset;

$h_{corr}$  = range corrections for propagation delays and sea surface interaction;

$H_{alt}$  = altimetric sea surface height above the reference ellipsoid.

### 1.2.3 Sea surface height corrections

The sea surface height itself consists of the *geoid height*, *dynamic (sea surface) topography*, *tidal elevation* and *inverse barometer effect*:

$$H_{sea} = H_{geoid} + h_{dyn} + h_{tide} + h_{invbaro} \quad . \quad (1.3)$$

Depending on the application, either of these elements may be recovered from altimetry, assuming that the others are well modelled or can be eliminated. These so-called *geophysical corrections* are also important for the validation of the altimeter measurements.



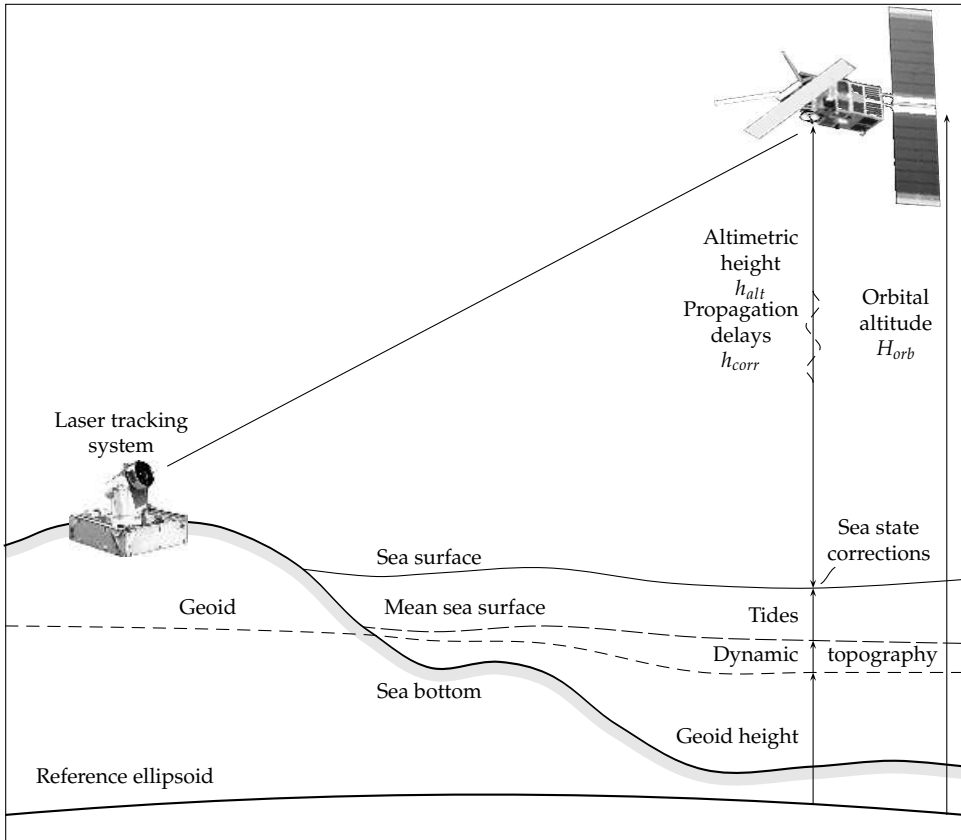


Figure 1.5 The principle of satellite radar altimetry.

The *geoid height* plays an important role in geodesy. It is the level at which the sea surface would be in the absence of wind, circulation and tides. The geoid is solely determined by the gravity field of the Earth. Various models for the geoid exist, based on extensive sets of parameters that model the gravity field at different wavelengths. The simplest model for the geoid is the *reference ellipsoid*, a sphere flattened at the poles and centred on the Earth's centre-of-mass. This ellipsoid functions as the reference (hence the name) for many height definitions. The geoid height is one of those: it varies between about  $-100$  m (near India) and  $+90$  m (near Iceland) with respect to the reference ellipsoid. It is clear that satellite altimetry can contribute to the improvement of our knowledge of the geoid (and hence our knowledge of the gravity field) as well as to the establishment of a precise reference frame [Scharroo *et al.*, 2000a]. A very readable account of the estimation of global gravity field models using satellite altimetry is provided by Rapp [1993].

The *dynamic topography* is that part of the sea surface height that is determined by ocean circulation and varies globally by a few metres [e.g., Zlotnicki, 1993]. The

slope of the dynamic topography is, by approximation and apart from a latitude dependence, proportional to the velocity of the local ocean current. We distinguish between the *stationary dynamic topography*, which mainly describes the large-scale mean circulation in the oceans, and the *time-variant dynamic topography* which is mainly determined by meso-scale features, like ocean eddies and meanders. The combination of the geoid and stationary dynamic topography is called the *mean sea surface*.

The *tidal elevation* is caused by the gravitational pull of the Sun and Moon on the solid Earth and on the oceans (hence called *solid-Earth* and *ocean tides*). Smaller contributions are the suppression of the ocean floor due to the ocean tides (*ocean loading tides*) and motions of the ellipsoid due to polar motion (*pole tides*) [e.g., Le Provost, 2001; Wahr, 1981, 1985].

The atmosphere also exerts a force on the ocean surface. Changes in atmospheric pressure loading result in variations of the sea level. When we assume isostatic response, an increase of 1 millibar of atmospheric pressure results in approximately 1 cm decrease of sea level. Since this motion of sea level resembles that of an upside-down barometer, the effect is called the *inverted barometer effect*. In fact, the response is more complex: a global increase of atmospheric pressure by 1 millibar can not result in a global drop of sea level, because the water has nowhere to go [Ponte *et al.*, 1991]. Also, in semi-enclosed seas there will be only limited outflow. Hence, sea level will not respond in an isostatic manner to pressure changes, but only with some delay. Generally, however, the inverted barometer response is accurate at middle and high latitudes at time-scales longer than a few days [Gaspar and Ponte, 1997, 1998; Dorandeu and Le Traon, 1999], but is more complex in shallow waters [Ponte and Gaspar, 1999].

The ERS altimeter data are retrieved from the ESA altimeter ocean products (OPRs) provided by CERSAT (Centre ERS d'Archivage et de Traitement) [CERSAT, 1994]. The TOPEX/Poseidon altimeter data used for comparisons and validation of the ERS results stem from the Merged Geophysical Data Records (MGDRs) produced by AVISO (Archiving, Validation and Interpretation of Satellite Oceanographic data) [AVISO, 1996]. These products basically contain the altimeter measurements and their corrections plus the geophysical corrections mentioned above. Unfortunately, the products for the various satellites differ in format and content. To harmonise the data and their corrections, and to introduce the most recent geophysical models and off-line data corrections, the Radar Altimeter Database System (RADS) was set up, ensuring up-to-date and consistent altimeter data throughout the different missions (see Chapter 2).

## 1.2.4 Altimeter height residuals

In the above we have seen how the sea surface height can be measured by a radar altimeter and how it can be derived from models for the mean sea surface, tides, *etc.* In the absence of errors, the measured and modelled sea surface heights would be exactly the same and would coincide with the actual sea level. However, the

Measurement or model	Error (cm)	
	ERS	TOPEX
Altimeter range	3.0	2.0
Orbital altitude	5.0	2.0
Dry tropospheric correction	1.0	1.0
Wet tropospheric correction	1.5	1.5
Ionospheric correction	1.0	0.7
Ocean tides	3.0	3.0
Solid Earth tides	0.5	0.5
Inverse barometer correction	2.0	2.0
Sea state bias	1.0	1.0
Sea surface variability	4.0	4.0
Mean sea surface	11.0	11.0
Altimeter height residual (total)	14.0	13.0

Table 1.2 Approximate contribution of errors in measurements, models and orbits, and sea surface variability to altimeter height residuals of ERS and TOPEX.

measurements contain noise, the computed orbit contains errors, and the models are not perfect either. Thus, the measured and modelled sea surface differ and neither of them coincides with the actual sea level.

It is hard to tell where the actual sea level is located at any given place and time, unless this point is close to a tide gauge or buoy instrumented with a Global Positioning System (GPS) receiver. So direct comparison of the altimetric height with ground truth is only possible at a few locations globally [e.g., Mitchum, 1994; Nerem and Mitchum, 2001]. However, a comparison between  $H_{alt}$  (1.2) and  $H_{sea}$  (1.3) is possible at millions of points throughout the global oceans. The differences between observed and computed sea level, the *altimeter height residual*  $\Delta H$ ,

$$\Delta H = H_{alt} - H_{sea} \quad , \quad (1.4)$$

is dominated by errors in the mean sea surface and the orbital altitude. A comprehensive list of contributions to the altimeter height residuals is given in Table 1.2.

The altimeter height residuals can build a good picture of the errors in the measurements and models, assuming they can be separated in space and time. For example, errors in the orbital altitude are mainly long-wavelength phenomena (order 10 000 km and over), while errors in the mean sea surface are dominant at shorter wavelengths (up to order 1000 km).

### 1.2.5 Crossover height differences

At locations where ascending and descending tracks cross over oceans, the satellite is able to sample the sea surface on the same location, but at different epochs. These locations are generally known as *crossovers*. Because measurements are available at the same location, the height of the mean sea surface (and the associated errors)

can be eliminated by computing the difference between the two altimeter height residuals. In contrast to the altimeter height residuals, the crossovers provide no information on the absolute errors, but only on the relative errors.

The generation of crossover height differences follows the iterative process described by Wisse *et al.* [1995]. First, the location of all crossovers and the corresponding epochs are estimated analytically by crossing all ascending and descending tracks during a selected period. Subsequently, crossovers that do not contain sufficient altimeter data around the two epochs (*e.g.*, those over land or near a coast) are rejected. The positions and epochs of the remaining ones are re-estimated at the crossing of two linear fits through four measurement locations along either track around the estimated position. Combinations of passes with extreme shallow angles, passes with a time interval larger than 17.5 days, and crossovers with too few surrounding 1-Hz measurements are rejected. Altimeter height residuals along both passes are filtered and interpolated with a quadratic polynomial at the location of the crossover.

The difference between the respective interpolated height residuals is called the *crossover height difference residual*, or just *crossover difference* and is only partly due to actual sea level change between the two epochs. The remaining part is caused by errors in the applied altimeter range corrections, tide models, or the computed orbit altitude, of which the latter is generally the largest effect. If these errors are different on crossing arcs, they will appear in the crossover differences. Invisible to the crossover differences are errors that are invariant in space and/or time, like a *temporally invariant* altimeter range bias or a *spatially invariant* error in the model for the mean sea surface height.

Figure 1.6 shows the ascending and descending tracks of ERS-2 over the North Sea and the crossovers at their intersections. The Figure also indicates the *shortest* possible time interval between the measurements that make up the crossovers. It is clear from this illustration that that time interval varies considerably with latitude, from as short as a few hours up to 17.5 days, half the repeat cycle of ERS-2. In this lies the reason for ignoring the crossovers built from passes that are separated by more than 17.5 days: beyond that you are just building different linear combinations of essentially the same passes, as illustrated in Figure 1.7.

The root-mean-square (RMS) of the crossover differences becomes a measure of the cumulative height errors. This *crossover RMS* is historically dominated by orbit error, but currently is a grant mixture of all spatio-temporally varying errors, in range measurement as well as corrections. It is important to keep in mind that the time interval between the two crossing passes varies significantly, so that there are *short- and long-interval* crossovers. Short-interval crossover differences will generally be smaller because the time-variant errors have had less time to decorrelate. In other words, over a short time interval part of the error in, for example, the dry tropospheric correction will be the same and will cancel in the crossover difference. This is less likely to happen as the time interval grows.

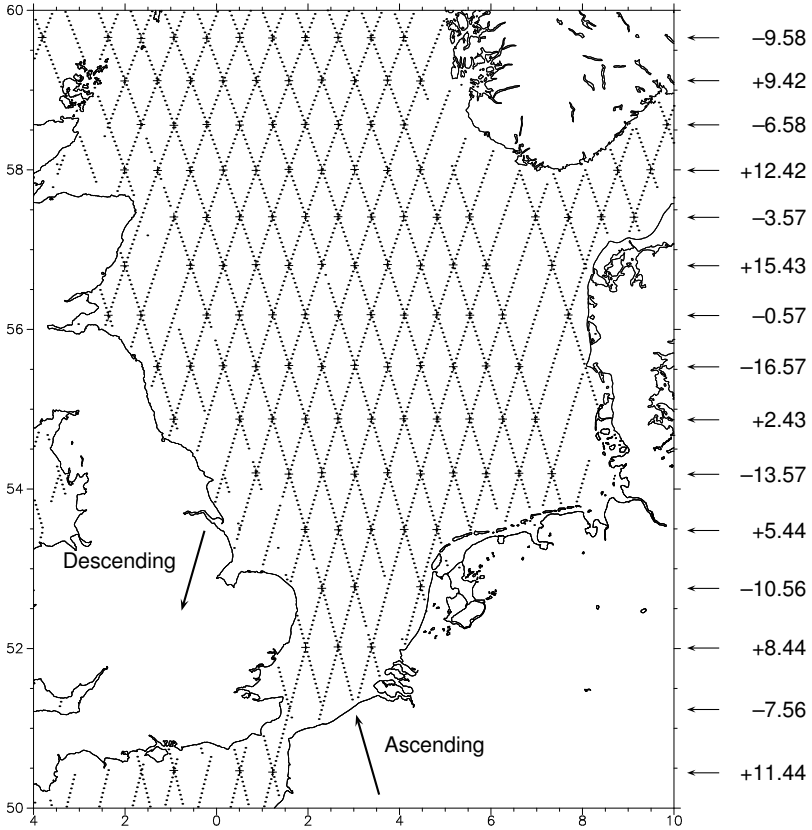


Figure 1.6 Distribution of 1-Hz altimeter measurements (dots) and crossovers (crosses) across the North Sea during a typical ERS-2 repeat cycle. The numbers on the right side of the plot indicate the time lapse (in days) between the ascending and descending pass at the crossovers at the given latitude. Negative numbers indicate that the ascending pass occurred before the descending pass.

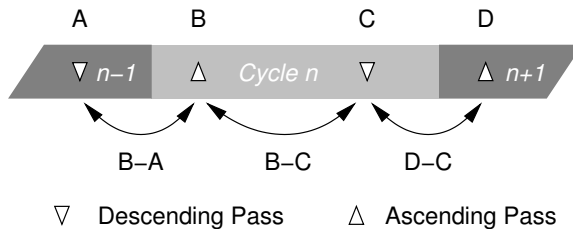


Figure 1.7 Illustration of the combination of ascending passes and descending passes into crossovers. Crossovers 'B-A' and 'D-C' have a time interval of less than half the repeat period; all other combinations of the same passes, like crossover 'B-C' and also 'D-A' span a period larger than half the repeat period.

### 1.2.6 Dual-satellite crossovers

When two satellites fly simultaneously, crossovers height differences between the two satellites are available. In case of ERS and TOPEX/Poseidon this provides the possibility to improve the ERS orbits by minimising the crossover height differences between ERS and TOPEX/Poseidon during the orbit determination process [e.g., *Born et al.*, 1986; *Kozel*, 1995]. It is a valid assumption in this procedure, that the major part of the discrepancy is due to ERS orbit errors, since those of TOPEX/Poseidon, and the ocean variability is of a significantly smaller magnitude [*Moore et al.*, 1998].

A disadvantage of using dual-satellite crossovers in the orbit determination is that, in addition to the usually estimated parameters, also an altimeter height bias and time tag bias between two altimeters are to be estimated. Moreover, a shift between the coordinate frames is not to be ruled out. In addition, it makes strong assumptions on the quality of the orbit and of the altimeter data of one satellite, generally TOPEX/Poseidon. If such assumptions are wrong, it will negatively affect the orbit of ERS. Besides, it makes ERS data no longer independent of TOPEX/Poseidon, which can cause errors in the TOPEX/Poseidon orbits or altimeter data to remain undetected.

In this thesis dual-satellite crossovers between ERS-1 or ERS-2 on one side and TOPEX or Poseidon on the other are not used in the orbit determination but are only used for independent quality analysis. The crossovers between ERS-1 and ERS-2 during the Tandem Mission *are* used in the POD: it provides a unique opportunity to link the two satellites in a common reference frame and allowing the one to benefit from the tracking of the other (see Chapter 6).

### 1.2.7 Collinear tracks

The ground track of ERS-2 repeats itself after 35 days and thus provides repeated measurements at the same location at fixed intervals of 35 days. During the Commissioning Phase and the two Ice Phases of ERS-1 the repeat interval was even as little as 3 days (Section 1.1). Now two sea level profiles along the same ground track (so-called *collinear tracks*) will contain the same mean sea surface profile, which can be eliminated easily by differencing the two sea level profiles. Like with the crossover height differences, this will highlight the variations in measurement, model and orbit errors and actual unmodelled sea surface variations [e.g., *Cheney et al.*, 1983]. The long-wavelength differences are associated with orbit errors, while short-wavelength differences are dominated by sea surface variability associated with eddies and meanders.

One problem in the analysis of collinear tracks might be that the tracks are not truly collinear but may be separated by up to about 2 km. As a result, the cross-track slope of the geoid (or more precisely the mean sea surface) will introduce differences in the sea level profiles [e.g., *Brenner et al.*, 1990]. This can be easily compensated for by using a model for this slope, or even more straightforward by first subtracting the mean sea level (at the measurement location) before making

the comparison. Current mean sea surface models are sufficiently accurate that the error in the modelled sea surface slope adds no more than  $1 \text{ cm}^2$  to the sea level variance.

### 1.3 Applications of satellite altimetry

Applications of satellite altimetry are numerous and can be found particularly in geodesy, oceanography and meteorology. Nowadays, the precision and fast processing of near-realtime data even allows operational use of altimetry. A few applications are listed below.

**Gravity and geophysics.** To this field of research satellite altimetry contributes in two ways. At the short spatial wavelengths the sea surface height variations are dominated by geoid undulations [Cazenave *et al.*, 1996] best expressed in the form of gravity anomalies. Maps of these gravity anomalies [Sandwell and Smith, 1997; Andersen and Knudsen, 1998] reveal bathymetric features as well as short wavelength variations in the density of the Earth's crust. This leads to improved mapping of the ocean floor [Smith and Sandwell, 1994, 1997; Knudsen and Andersen, 1996; Sandwell and Smith, 2001], to many contributions to geophysical to marine geophysics [e.g., Cazenave and Royer, 2001], and to interests from (gas) mining companies. The strategic advantage of better knowledge of the marine gravity field lead to the launch of the initially classified Geosat Geodetic Mission, which lasted from March 1985 to September 1986. In 1990 the U.S. Navy declassified the data south of  $60^\circ$  South, and two years later all data south of  $30^\circ$  South. The Geosat data for the entire global sea surface was declassified in 1995 after ERS-1 had completed the its Geodetic Mission.

At long wavelengths it difficult to separate the geoid and ocean dynamic topography. Here satellite altimetry helps determining the gravity field indirectly as a measurement for gravity induced orbit error (Chapter 6).

**Oceanography.** Altimetry is has become an invaluable source of information for the study of ocean currents. Again we should distinguish the larger and smaller spatial scales. At the global scale altimetry contributes to the mapping of the general ocean circulation pattern. However, the present geoid models that are use as a reference for the ocean dynamic topography are not accurate enough to determine the absolute ocean circulation with sufficient detail. The focus is therefore mainly on annual and inter-annual variations until more precise geoids will become available through the new gravity missions, CHAMP (CHALLENGING Mini-satellite Payload), GRACE (Gravity Recovery And Climate Experiment) and GOCE (Gravity Field and Steady-State Ocean Circulation Mission) [e.g., Fu and Chelton, 2001].

At the short wavelengths, current variations in the form of eddies and meanders dominate the circulation pattern and have historically been the main fo-

cus of the use of altimetry to oceanography [e.g., Lutjeharms, 1981; Wakker et al., 1990; Le Traon and Morrow, 2001]. Mapping of eddies and current meanders with altimetry has even grown to an operational activity (e.g., the MERCATOR project) and benefits ship routing and sailors. At intermediate spatial scales the study of the El Niño phenomenon has also attracted the aid of altimeter data [e.g., Cheney and Miller, 1988; Cardon et al., 1998].

**Ocean tides.** Initially just another correction to altimeter data, the study of ocean tides has become one of the main drivers of the TOPEX/Poseidon mission. Currently, all state-of-the-art global ocean tide models have assimilated altimeter data in some form or another, leading to unprecedented precisions in the order of 2-3 cm [e.g., Smith et al., 2000; Le Provost, 2001].

Contributions of ERS altimetry to ocean tide modelling, however, are insignificant. Although the satellites could, in principle, improve the spatial resolution of tide models in coastal areas, all attempts in this directions have been futile. One of the problems faced in using ERS altimeter data for tide modelling is that most of the diurnal tides are invisible, are aliased to long periods, or are only separable from other tidal constituents after very long periods. However, the value of ERS altimeter data for operational storm surge forecasting has been recognised [e.g., Phillippart et al., 1998]. Such forecastings provide a few hours warning ahead of time and allow measures to be taken to avoid flooding in sensitive coastal areas like the Rhine Delta.

**Sea level change.** Over the last century, estimates of long-term sea level change have been obtained from tide gauge measurements. Results on the extend of sea level change have varied considerably depending on the time span or the particular set of tide gauges used. These discrepancies are the result of some fundamental problems with tide gauge measurements. First, tide gauges measure relative to the land on which they are embedded, which may move at a vertical rate comparable with sea level change. Second, the distribution of tide gauges is far from global: they are generally located near coasts. On top of that its distribution has changed over the years [Douglas, 1991].

Satellite altimetry differs in both respects. The reference, the satellite orbit, is tied to a global well-defined reference frame linked to the Earth's centre of mass. And the spatial distribution is nearly global. Still it is too early to say that satellite altimetry provides the ultimate answer on the rate of sea level change. Small drifts in the measurements of range and even of wave height may be confused for sea level change. The outcome also relies heavily on the accuracy of the measurement corrections and most of all the satellite altitude. A combination of tide gauge and altimeter measurements will have to be used to effectively study recent changes in global sea level [e.g., Mitchum, 1994].

**Ice sheet monitoring.** The Antarctic and Greenland ice sheets comprise 77% of the Earth's fresh water reserves and 99% of the global glaciers [Zwally and Brenner, 2001]. Their suggested demise due to global warming would cause drastic climatic and ecological changes. The Geosat altimeter provided the first



detailed mapping of the topography of Greenland South of 72.2°N and Antarctica North of 72.2°S. The mapping was densified and extended to 81.5° by ERS-1 and ERS-2 [e.g., Bamber, 1994; Ekholm, 1996]. Knowledge of the surface topography of the ice sheets was significantly enhanced by satellite altimetry: errors in non-altimetric elevation maps were found to regularly exceed 100 m. Moreover, analysis of the surface slopes derived from these maps provide details on a multitude of vital parameters for the understanding of the ice sheet dynamics: the direction of ice flows, the locations of ice divides and drainage basins, and the direction and magnitude of the gravitational pull acting on the ice sheet [Remy and Minster, 1997].

Although the absolute accuracy of ice elevation measurements is limited to a few metres (depending on the surface slope) [Bamber *et al.*, 1998], the relative accuracy of repeated ice elevation measurements (on collinear tracks or crossovers) is an order of magnitude better. This makes it possible to detect rather subtle changes in the ice elevation. Wingham *et al.* [1998] demonstrated, based on ERS-1 and ERS-2 crossover measurements, that the elevation of the Antarctic Ice Sheet interior fell by  $9 \pm 5$  mm/yr in 1992-1996, thus demoting ice sheet melting from the major cause of sea level rise to the lower ranks of contributing factors.

**Meteorology.** The wave height measurements provided by satellite altimeters are very valuable for the global modelling of the sea state (wave height and wave age) which in turn is input to meteorological models. The European Centre for Medium-range Weather Forecasts (ECMWF), for example, assimilates the ERS-2 altimeter wave heights in near realtime into its operational wave model (WAM). The addition of altimetry in the WAM model has significantly improved the accuracy of the model output and improved its forecasting capabilities [Janssen, 2000].

It will be evident that most applications of satellite altimetry require not only accurate altimeter measurements but equally accurate altimeter corrections and orbits. This thesis will highlight some contributions to the improvement of ERS altimeter products in view of the challenging demands imposed by a variety of applications that have significantly enhanced our knowledge of the oceans and the processes that govern them.



# Enhancement and Validation of ERS Altimeter Data

The ERS altimeter data presented in this thesis are extracted from the Radar Altimeter Database System (RADS) developed at DEOS. The RADS project has recently gone into the second phase in which the data can be really exploited. The data base is now on-line and features the altimeter data plus their geophysical corrections for Geosat, ERS-1, TOPEX/Poseidon, ERS-2 and GFO in a common, and flexible, format that allows different data contents for the different satellites and can be easily extended with new ancillary corrections.

The merging of ERS-1 and ERS-2 altimeter data from the OPRs [*CERSAT*, 1996] into the RADS data base was quite a troublesome undertaking. A long list of adjustments to the measurements and geophysical corrections finally compiles an accurate and unified ERS data set, that meets the standards required for research in geodesy, oceanography and climate change.

## 2.1 Introduction

Unfortunate misconceptions and bad publicity have degraded ERS-1 and ERS-2 to the ranks of 'low-accuracy altimeter missions', where they do not belong. In fact, the mission goals on performance of the principle altimeter measurements (range, significant wave height and wind speed) and of the radiometer were as tempting as those of TOPEX/Poseidon. Careful analyses show that levels of noise, precision and stability are very competitive.

The reason for the lack of confidence in ERS altimeter data may be found in the insufficient involvement of the user community in the definition of the ERS altimeter data products and ESA's inability to make adequate upgrades to algorithms and ancillary corrections. For example, more precise orbits, generally available to the public at no cost, were never incorporated.

ERS-1 altimeter data have a history of product and algorithm definitions dating back to 1990, and not surprisingly they were soon surpassed by TOPEX-aided knowledge and models. Upgrades were never made. But also the well-determined re-calibrations to the measurements and improvements to the retracking algorithms were never introduced. Only as late as 1995 the altimeter product generation was upgraded, with the drawback that no reprocessing of older ERS-1 data was envisioned, leaving the end user to deal with two completely different data sets for the same satellite.<sup>1</sup>

A user of ERS altimeter data, unfamiliar with the products' heritage, but knowing that the measurements are made by two nearly identical satellites, in two identical orbits, with two identical altimeters, expects to deal with *one* type of altimeter product common to both ERS-1 and ERS-2, in which the data of the two satellites is virtually indistinguishable.

Few expectations could have a more disappointing outcome. In reality the user of ERS altimetry has to deal with *three* different kinds of data sets: one used for ERS-1 prior to the Tandem Mission, one used for ERS-1 during the Tandem Mission, and one used for ERS-2.

The task undertaken by DEOS is the construction of a unified multi-satellite altimeter database containing data from Geosat, ERS-1, TOPEX/Poseidon, ERS-2, Jason-1, and Envisat. This includes the detailed validation and upgrading of the data to common formats and standards. A long list of re-calibration algorithms and updated geophysical corrections finally provides a unified and accurate ERS-1/2 altimeter data set that allows the reconstruction of many ocean parameters with equal efficiency as all other altimeters, but with the denser 35- and 176-day coverages and the rapidly revisiting during the 3-day repeat.

## 2.2 ERS OPR Version 3, Version 5, and Version 6

ESA provides two different versions of the altimeter Ocean Products for ERS-1 and ERS-2. They differ in format, applied retracker, and/or ancillary data. ERS-1 data are released in two versions of OPR data: *Version 3 (V3)* for Phases A through F (July 1991 till March 1995) and *Version 6 (V6)* for Phase G. ERS-2 data were only released in OPR V6. The differences between the versions are:

**Format:** V3 conforms to data standards set by the Committee on Earth Observation Satellites (CEOS) and V6 follows the standards suggested by the Consultative Committee for Space Data Systems (CCSDS).

**Retracker:** V6 is based on a more accurate retracker, which means that all measurements of range, significant wave height (SWH) and wind speed are incompatible with V3.

---

<sup>1</sup> Altimeter data of ERS-1 Phase C was finally reprocessed and made available in 2002.

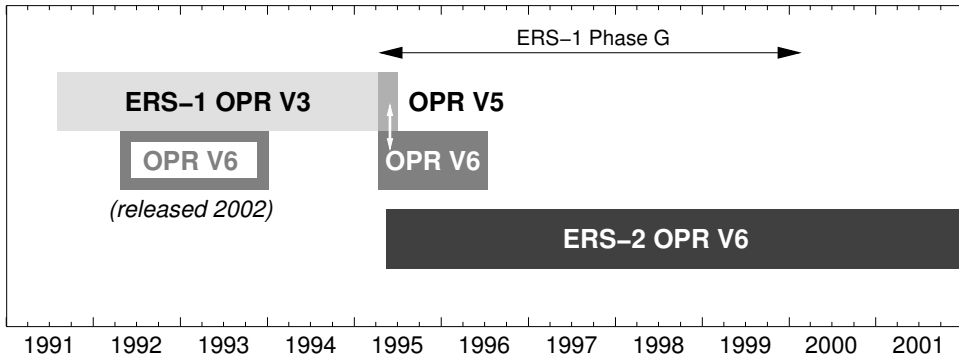


Figure 2.1 Availability of ERS-1 and ERS-2 OPR products versions 3, 5 and 6.

**Propagation corrections:** Data from the MWR on V6 are processed with new calibration values in the algorithms to convert brightness temperatures to wet tropospheric delay. A new sea state bias model was introduced.

**Orbit:** V6 finally has a bit more accurate orbit, at the same time introducing differences in geographically correlated orbit errors.

**Geophysical corrections:** V6 features newer models for ocean tides, load tides and mean sea surface.

Without significant adjustments, V3 and V6 data can not be merged together or with TOPEX/Poseidon data for accurate geodetic or oceanographic studies. Even between the V6 data of ERS-1 and ERS-2 still some differences remain. This Chapter describes the process of harmonisation of V3 with V6 and how to upgrade them both to be more compatible with TOPEX/Poseidon data.

The only way to intercompare V3 and V6 is by analysis of ERS-1 cycles 145–148 from the beginning of Phase G that were processed with both Versions 5 (V5) and 6 (Figure 2.1). In this case V5 is identical to V3, except that the product format corresponds with V6. As a result, in the following V5 can be read as V3.

## 2.3 Altimeter measurements

### 2.3.1 Significant wave height

Since the latest OPR data version (V6) uses a retracker different from the original version for ERS-1 (V3), the registration of wave height will be different. If not compensated, this end will cause inaccurate registration of the sea level through the sea state bias. In fact, this is one of the main causes why two different sea state bias algorithms are proposed for V3 and V6 data [*Gaspar and Ogor, 1996*].

Figure 2.2 shows the scatter plot of SWH from V5 and V6. Clearly in V5 all wave heights are underestimated, particularly at low wave heights. Those wave

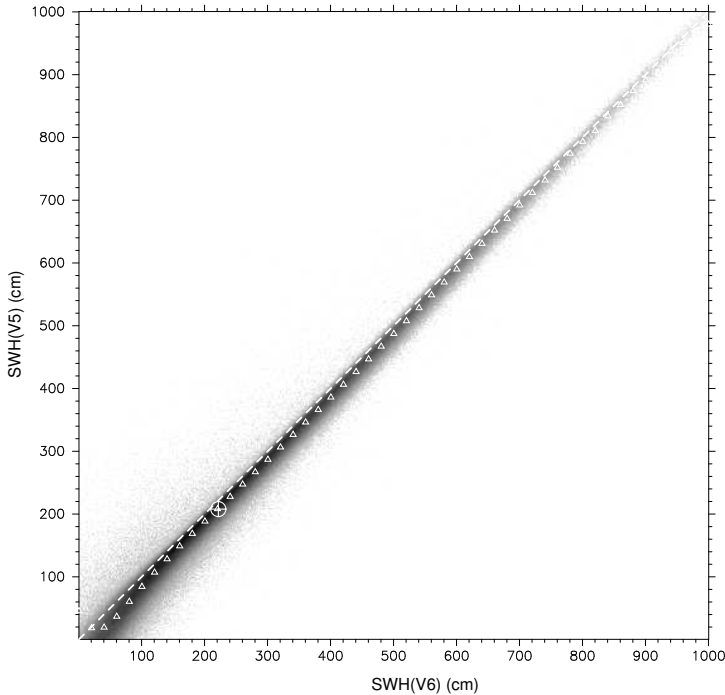


Figure 2.2 Scatter plot comparing the ERS-1 significant wave heights according to software versions V5 and V6.

heights will have dropped below zero (which is physically impossible) and were consequently set to zero. The difference between V5 and V6 wave heights is shown in Figure 2.3. The line fit obtained by DEOS (light grey line in Figure 2.3) is determined through least-squares adjustment of four parameters (two slopes and the location of the breaking point) and better represents the difference at higher wave heights than the (dark grey) line fit by *Stum et al.* [1998]. This fit leads to the correction algorithm (SWH in metres):

$$\begin{aligned} \text{SWH(V5)} < 1.256: & \text{SWH(V6)} = 0.900 \text{ SWH(V5)} + 0.247 \\ \text{else:} & \text{SWH(V6)} = 1.003 \text{ SWH(V5)} + 0.117 \end{aligned}$$

Note that the new correction differs from the one proposed to the user by several tens of centimetres at higher wave heights. Although at low wave heights the two corrections agree very well, it is hard to translate the V5 wave heights to V6 wave heights since they were truncated to zero at low wave heights. This truncation makes it impossible to reset the low wave heights to proper level. Were the negative wave heights kept in the OPR products this would firstly have prompted earlier warning about the underestimation of wave heights and secondly would have allowed the reconstruction to proper values at a later stage. The lesson to be learnt is *not* to build in artificial limits in a data product.

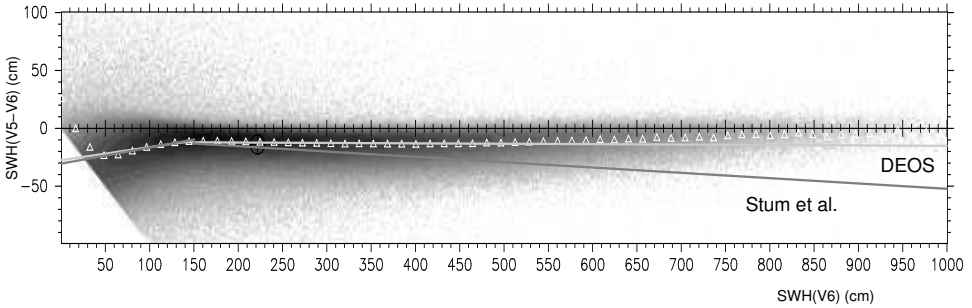


Figure 2.3 Scatter plot showing the difference between ERS-1 wave heights according to software versions V5 and V6, as a function of SWH. The dark grey line represents the correction to be applied to the V5 data according to *Stum et al.* [1998]. The light grey line represents the correction developed at DEOS.

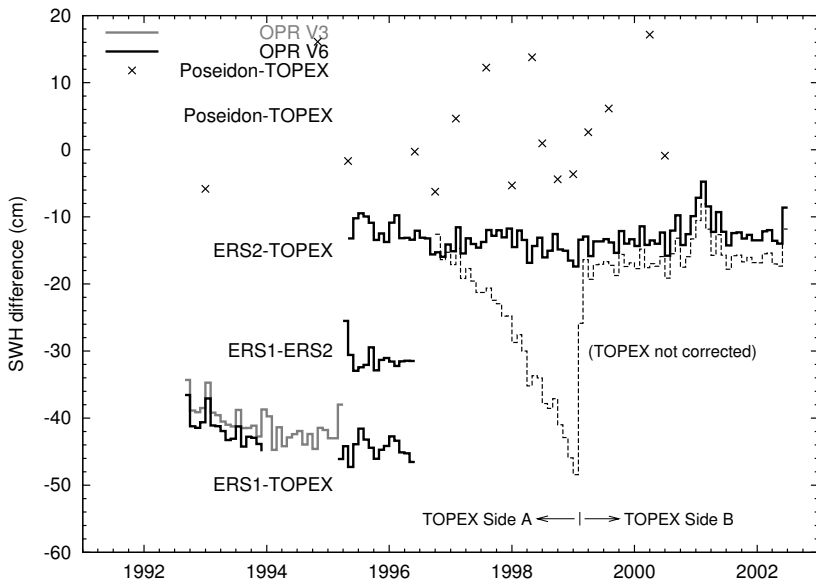


Figure 2.4 Comparison between significant wave heights recorded by ERS-1, ERS-2, TOPEX and Poseidon altimeters at their crossovers points. The monthly mean differences in significant wave height are plotted as a function of time. The black lines are based on ERS OPR V6 data, the grey line on ERS-1 OPR V3 data. The dashed line in the ERS-2/TOPEX SWH differences shows the effect of ageing on the TOPEX Side A altimeter wave heights and the slight bias of the Side B wave heights. The solid line shows differences after correction of the TOPEX wave heights. The crosses indicate TOPEX/Poseidon SWH differences for comparison.

After the new correction has been applied to all V3 ERS-1 data, it is essential to compare ERS and TOPEX wave heights (Figure 2.4). The comparison shows that during the tandem mission ERS-1 and ERS-2 had a seemingly constant bias of about 30 cm between their respective SWH recordings despite our new correction. This is because ERS-1 is measuring systematically low at low wave heights for which no simple correction can be applied<sup>2</sup>.

Early 2002, nearly six years after the end of ERS-1's mission and long after this exercise was performed and their results published [Scharroo *et al.*, 2000c], ESA produced another set of OPRs V6 for ERS-1, this time for the Multi-Disciplinary Phase (Phase C, April 1992 till December 1993). This gives the opportunity to independently assess, in hindsight, the corrections applied to all V3 data. Figure 2.4 shows that the mean SWH from the corrected V3 data and the new V6 data match within 2 cm, which sufficiently accurate for our purposes.

The dashed line in Figure 2.4 shows how the wave heights measured by TOPEX started to increase mid-1996, resulting in a decline of the ERS-2/TOPEX SWH differences. By early 1999 TOPEX wave heights had grown by as much as 40 cm. This was a clear sign of the ageing of TOPEX Side A altimeter and prompted the decision to switch the TOPEX altimeter to the redundant Side B on 10 February 1999. Although the direct effect on the altimeter range is deemed to be small [Hancock *et al.*, 1999], the indirect effect on the measured sea level through the sea state bias (which is approximately 5% of the SWH) is considerable.

In order to compensate for the effect, the SWH anomaly first has to be quantified. Challenor and Cotton [1998] found a near linear drift of the TOPEX wave heights in comparison to a limited number of collocated buoy measurements. A more compelling case for a parabolic trend can be made using the millions of short-interval ERS-2/TOPEX crossovers. Assuming that the ERS-2 wave heights are stable, and there is no indication of the contrary, the correction to the TOPEX SWH (in cm) is:

$$\begin{aligned} 15 \text{ Nov } 96 - 10 \text{ Feb } 99 : \text{SWH}' &= \text{SWH} - 55.15 - 0.07053 D - 0.00001947 D^2 \\ \text{After } 10 \text{ Feb } 99 : \text{SWH}' &= \text{SWH} - 3.20 \end{aligned}$$

where D is the number of days since 1.0 January 2000. After the SWH is corrected, and the sea state bias correction updated, there appears no significant bias between sea surface heights determined by TOPEX Side A and Side B [Dorandeu, 1999; Haines *et al.*, 1999, 2002].

### 2.3.2 Backscatter and wind speed

Since the beginning of 2000 a few events have impacted the behaviour of the ERS-2 backscatter coefficient [Dorandeu *et al.*, 2000].

<sup>2</sup>Because of the underestimation of low wave heights by the ERS-1 altimeter, in the ERS-2 altimeter the amplification level of the return signal was raised. This makes the comparison of wave height, and range between the satellites even more complicated



- A drop in the backscatter coefficient  $\sigma_0$  occurred on 16 January 2000. The reason for it is still a mystery since it was completely uncorrelated to any on-board anomaly. The drop of the backscatter is located in a place that is not controlled by the instrument. Only by analysis of the data it was discovered.
- The second event is related to the implementation of a new attitude rule to pilot ERS-2 with only one gyroscope instead of three and the subsequent payload switch-on on 10 February 2000. First gyroscope 6 was used for a week, than gyroscope 5.
- The backscatter jumped up again on 3 March 2000, marking the end of the period in which the Digital Earth Sensor (a pivotal instrument for the attitude control with one or no gyroscopes) is occasionally blinded by the Sun.

The recommendation made by *Dorandeu et al.* [2000] based on the data is to correct the backscatter (in dB) as follows:

$$16 \text{ Jan} - 10 \text{ Feb } 2000: \quad \text{Sigma}0' = \text{Sigma}0 + 0.15$$

$$10 \text{ Feb} - 3 \text{ Mar } 2000: \quad \text{Sigma}0' = \text{Sigma}0 + 0.35$$

$$3 \text{ Mar } 2000 \text{ and beyond: } \text{Sigma}0' = \text{Sigma}0 + 0.10$$

The change of backscatter coefficient also affects the wind speed which is directly recovered from the backscatter using an empirical relationship known as the *Modified Chelton-Wentz algorithm* [*Witter and Chelton, 1991*].

### 2.3.3 Range and sea state bias

The change of retracker directly influences the measurement of range and significant wave height. Additionally, the influence of wave height on the range measurement, the so-called *tracker bias*, can change. Although the contribution of the retracker algorithm constitutes only part of the sea state bias, it is important to evaluate whether the dependency of the range retrieval to wave height has changed from V5 to V6. Figure 2.5 investigates this dependency, by plotting the difference between V5 and V6 ranges against wave height. There appears none, from which we conclude that SSB is the same for V6 and V5' (after applying our SWH correction). With SWH in metres and wind speed U in m/s [*Gaspar and Ogor, 1996*]:

$$\text{ERS-1 (V5'+V6): } \text{SSB} = \text{SWH} (-0.047 - 0.0035 U + 0.000160 U^2)$$

$$\text{ERS-2: } \text{SSB} = \text{SWH} (-0.048 - 0.0026 U + 0.000126 U^2)$$

Note that we apply the correction to the V6 data *as well as* to the upgraded V5 data. In Figure 2.6 we show that the range difference V5-V6 depends mainly on SWH difference V5'-V6. This is largely undone when the range is corrected for sea state bias by the formulae above. A constant of 24 mm remains due to retracker change and an error in V3 processing.

$$\text{ERS-1 (V5): } \text{RANGE}(V6) = \text{RANGE}(V5) - 0.024 \text{ m}$$

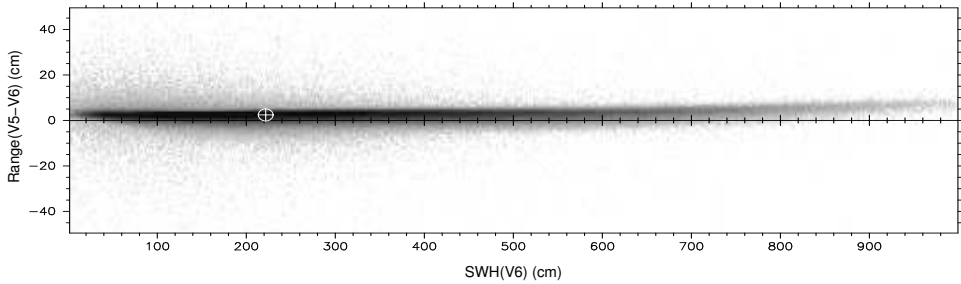


Figure 2.5 Scatter plot showing the difference between ERS-1 ranges according to software versions V5 and V6, as a function of SWH.

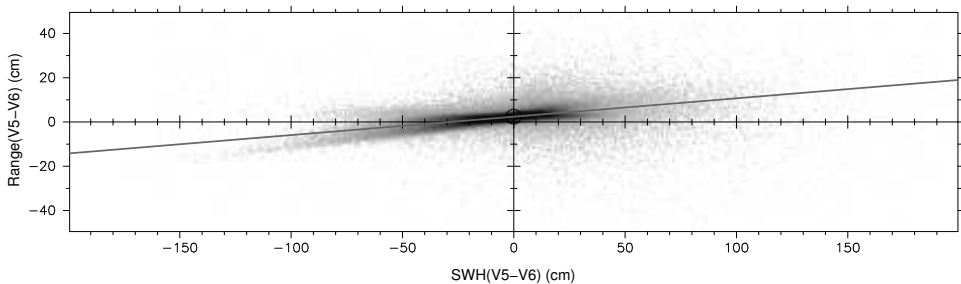


Figure 2.6 Difference between ERS-1 ranges according to software versions V5 and V6, as a function of the difference between V5 and V6 wave heights. The solid line gives the best fit through the data.

### 2.3.4 Altimeter biases and drifts

The range bias of the ERS-1 altimeter was determined *in-flight* (Chapter 4), while the ERS-2 altimeter was calibrated in a laboratory environment, using more advanced techniques than were available before the launch of its predecessor. Since the two altimeters are identical in design and components, the range biases were expected to be nearly, if not completely, the same. The difference between the laboratory calibrations of ERS-1 and ERS-2 was 40.92 cm, which is close to the 41.5 cm resulting from the ERS-1 *in-flight* calibration. The closeness of the two values is remarkable since it is well within the respective error estimates of about 1 and 5 cm.

Because of its tighter error bar, the 40.92 cm value was adopted and applied to both ERS-1 and ERS-2 ranges. For ERS-2 the bias is already incorporated in the OPR processing, for ERS-1 it has to be applied.

Additionally, both ERS-1 and ERS-2 altimeters suffer from rather unfortunate jumps in the range bias when the instruments have been temporarily switched off.

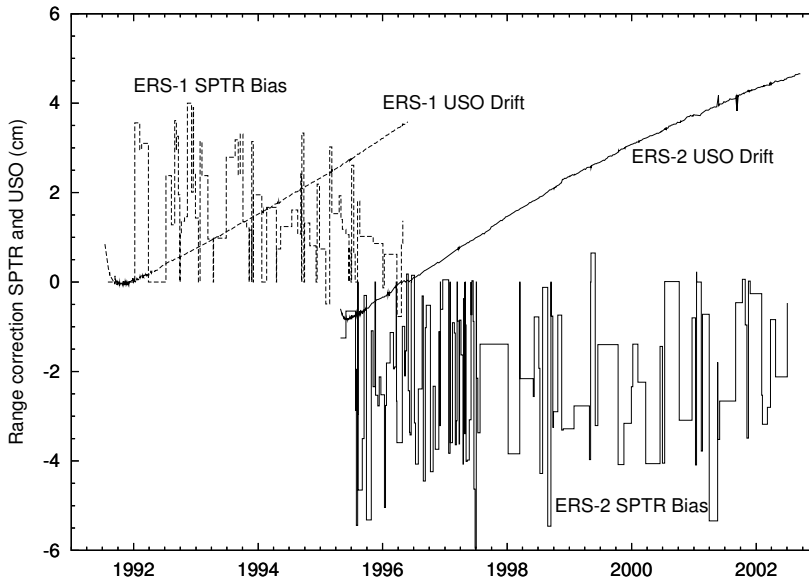


Figure 2.7 Evolutions of the SPTR and USO biases of ERS-1 and ERS-2. Source: ESA/ESRIN.

A correction for this effect (known as *SPTR<sup>3</sup> bias correction*) is determined from on-board calibration data.

Furthermore, the frequency of the ultra-stable oscillators (USO) in the altimeters slowly change with age. Since the range is counted in oscillator cycles, a change in frequency directly affects the range. Luckily, the USO frequency is monitored regularly, and a table is devised that indicates the drift in the USO frequency and the effect on altimeter range. The user has to apply the tabulated SPTR and USO corrections that are made available on-line [Martini and Féménias, 2000] (Figure 2.7).

$$\text{ERS-1: RANGE} = \text{RANGE} + \text{SPTR\_bias} + \text{USO\_drift} + 0.4092 \text{ m}$$

$$\text{ERS-2: RANGE} = \text{RANGE} + \text{SPTR\_bias} + \text{USO\_drift}$$

### 2.3.5 Time tagging

Because the satellite altitude may change as much as 25 metres per second, accurate time tagging (better than 1 ms) is required. The error in the time tagging can be determined from crossover height differences, especially around the mid-latitudes where the effect is the largest. The time tag bias can be determined from crossover analyses (Chapter 5). Although there is a clear annual signal as well, the average

<sup>3</sup>The Scanning Point Target Response (SPTR) procedure reveals differences between path delays of each of the digital bins of the waveform. The SPTR correction is an additive correction to the internal calibration which is based on the path delay of just one bin.

time tag bias values are applied. The difference between ERS-1 and ERS-2 is explained by an error in the OPR processing [Stum *et al.*, 1998]. Before interpolating the DEOS orbits, we correct the time tag:

$$\begin{aligned} \text{ERS-1 (V5 and V6): } & \text{TIME}' = \text{TIME} + 1.5 \text{ ms} \\ \text{ERS-2: } & \text{TIME}' = \text{TIME} + 1.3 \text{ ms} \end{aligned}$$

## 2.4 Propagation corrections

### 2.4.1 Dry tropospheric and inverted barometer corrections

The dry tropospheric correction featuring on the OPR products is based on sea level pressure fields from ECMWF. The sea level pressure for each measurement is interpolated in time and space from these grids. The dry tropospheric delay is then found using the formula by *Saastamoinen* [1972].

In order to determine the inverted barometer correction we have to invert the *Saastamoinen* [1972] formula to reconstruct the sea level pressure and then compute the isostatic response of the ocean:

$$\begin{aligned} \text{Pressure: } & P = \text{DTC} / [-0.002277 (1 + 0.0026 \cos 2\phi)] \\ \text{Inverted barometer: } & \text{IB} = -0.009948 (P - P_0) \end{aligned}$$

where DTC is the dry tropospheric correction in metres,  $\phi$  is the latitude,  $P$  and  $P_0$  are the local and reference sea level pressure in millibar and IB is the inverted barometer effect in metres. It is clear from these equations that, in fact, a variation of pressure has 4.5 times more impact through the inverted barometer effect than through the dry tropospheric correction.

Historically, the consensus was to use a constant reference sea level pressure of 1013.3 mbar, a value that was to represent the global mean sea level pressure. This approach was flawed for three reasons. Firstly, because sea water is an incompressible medium, the mean sea level over the *global oceans* should be the reference, which is not necessarily the same as the global mean sea level pressure over oceans and continents together. Secondly, the mean sea level pressure is closer to 1010.8 mbar and rarely reaches above 1012 mbar<sup>4</sup>. Thirdly, this number is not a constant, but has a roughly annual variation with a 1 mbar amplitude.

The currently adopted approach, suggested by *Dorandeu and Le Traon* [1999], is to use for  $P_0$  the sea level pressure averaged over the global oceans and smoothed with a  $(3 \text{ day})^{-1}$  low-pass filter. Since the mean sea level pressure varies slowly, it has a marginal effect on crossover differences when we consider time intervals up to 17.5 days only. In contrast, for studies of mean sea level variation and rise the consequences are significant. The use of a 1013.3 mbar constant in stead of a varying  $P_0$  introduces an anomalous 25 mm offset and an equally artificial annual

<sup>4</sup>The mythical number of 1013.3 mbar originates from the historical belief that the mean atmospheric pressure at sea level equals 76 cmHg.

variation with a 10 mm amplitude in global mean sea level, obscuring much of the actual annual sea level variation and some of its trend.

### 2.4.2 Radiometric wet troposphere corrections

The 23.8 GHz channel of the ERS-2 radiometer suffered a major loss of power on 26 June 1996 at 16:00. The retrieval of the wet tropospheric delay correction from brightness temperature values had to be re-calibrated. Algorithms are given in the Validation Reports [Calvez, 1996] and were developed by *Eymard and Boukabara* [1996], but we choose a correction published later by *Eymard and Boukabara* [1997] because it provides a slightly lower crossover RMS. First, we have to correct the ERS-2 23.8-GHz brightness temperature TB23 (K) after 26 June 1996, then recompute the radiometer wet tropospheric correction (WTC, negative in metres):

$$\begin{aligned} \text{TB23}' &= 0.93 \text{ TB23} + 19.18 \\ \text{WTC} &= -1.65435 + 0.54668 \log_{10}(280 - \text{TB23}') \\ &\quad - 0.22558 \log_{10}(280 - \text{TB36}) + 0.00137 (U - 7) \end{aligned}$$

The parameters in the above algorithm are different from V3, but here no brightness temperatures are available. Our correction algorithm comes from the comparison of V5 and V6 wet tropospheric delays (Figure 2.8) and differs from the one by *Stum et al.* [1998] particularly at low and high numbers, where our correction performs better:

$$\begin{aligned} \text{WTC}(V5) < -0.402: & \text{WTC}(V6) = 0.869 \text{ WTC}(V5) + 0.027 \\ \text{else:} & \text{WTC}(V6) = 0.770 \text{ WTC}(V5) - 0.012 \end{aligned}$$

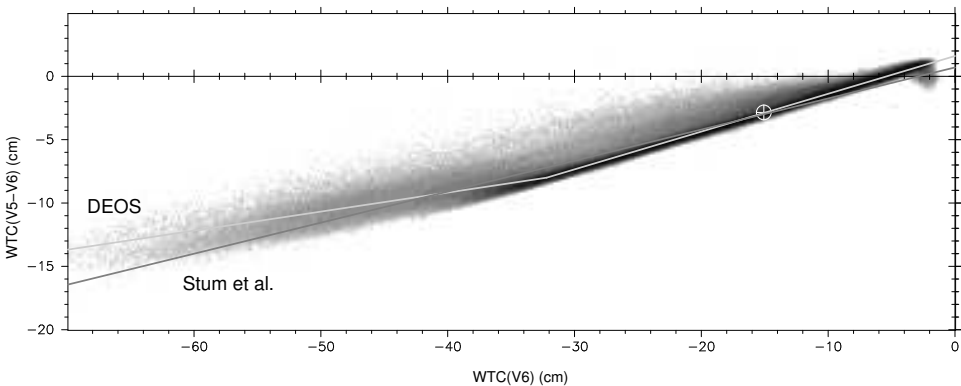


Figure 2.8 Scatter plot of comparing the Wet Tropospheric Correction (WTC) according to software versions V5 and V6, as a function of the delay itself. The dark grey line indicates the correction proposed by *Stum et al.* [1998]. The light grey line represents the correction developed at DEOS.

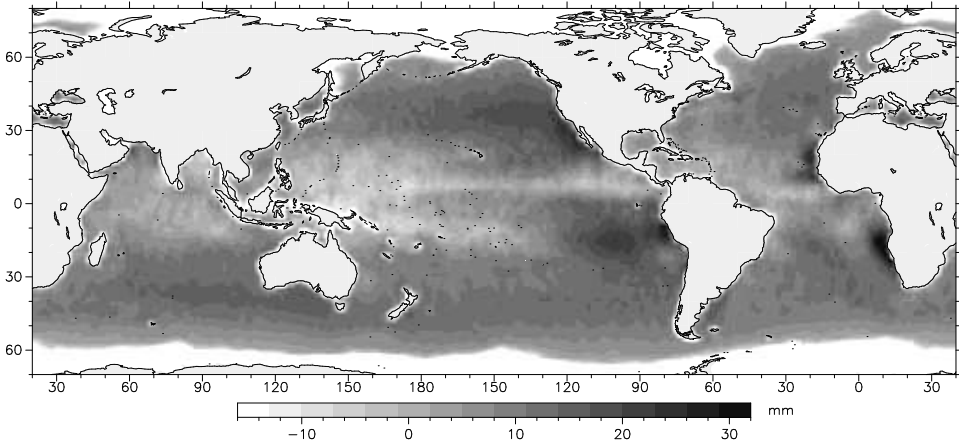


Figure 2.9 Mean difference between wet tropospheric delay corrections determined by the ERS-2 radiometer and the ECMWF model over the period May 1995 to May 2002.

### 2.4.3 Model wet tropospheric correction

An error was discovered in the computation of the model wet tropospheric delay from the temperature and humidity fields provided by ECMWF. This error impacts on all ERS-1 data (V3 and V6) and ERS-2 data until 1 December 1997 [Calvez, 1996]. We have to apply the following adjustment to the model wet tropospheric correction (MWTC negative in metres).

$$\text{All data before 1 Dec 1997: MWTC}' = 0.850 \text{ MWTC} - 0.006$$

Figure 2.9 shows that, despite this adjustment, significant systematic discrepancies between the model and radiometer wet tropospheric corrections remain. The model generally predicts a wetter troposphere (range corrections are more negative), except in the tropics. Other models exhibit a similar behaviour, raising legitimate doubts about the capabilities of the atmospheric models as well as the radiometer in estimating water vapour. Whichever is to blame for the discrepancies between model and measurement, it is clear that it is unwise to mix the two corrections. In this work the radiometer wet tropospheric correction was used throughout.

### 2.4.4 Ionospheric correction

The ionospheric range correction is proportional to the total electron content (TEC, *i.e.*, the density of free electrons along the vertical line between the satellite and the ocean) and inversely proportional to the square of the altimeter frequency,

$$h_{iono} = k \frac{\text{TEC}}{f^2} \quad . \quad (2.1)$$

The unit used for TEC is the TECU, where  $1 \text{ TECU} = 10^{16} \text{ electrons/m}^2$ , and  $k$  is  $-402.50 \times 10^{15} \text{ m Hz}^2/\text{TECU}$ . The disperse nature of the ionospheric delay is used by dual-frequency altimeters, like TOPEX, to estimate the ionospheric correction together with the altimeter range. Single-frequency altimeters, like those of ERS-1 and ERS-2, have to rely on global climatological or empirical ionosphere models to remove the effect of ionospheric delay.

The dual-frequency nature of GPS signals allows estimation of the TEC along the line-of-sight between the GPS satellite and the ground receiver. These slant TEC estimates from a well-distributed global network of receivers can then be converted to global maps of (vertical) TEC. Currently, several institutes produce such GPS-based Ionosphere Maps (GIM) on a timely, daily basis. In this Section only the GIMs from the Centre for Orbit Determination in Europe (CODE) [Shaer, 1999] and the Jet Propulsion Laboratory (JPL) [Iijima *et al.*, 1999; Pi, 2002] are evaluated. Since 1998, both institutes provide 2-hourly maps of TEC, integrated up to GPS altitude. Earlier maps are either not archived or are available only at 24-hour intervals and are not considered.

Climatological models such as the Bent model [Llewellyn and Bent, 1973] (available on both the CERSAT and AVISO data for ERS and TOPEX/Poseidon) and the International Reference Ionosphere 1995 (IRI95) [Bilitza, 1997, 2002] model the density profiles of electrons and ions based on a limited amount of external input (solar radio flux or sun spot number). The TEC is estimated by integrating the electron density along the vertical path between sea surface and satellite. During periods of low solar activity when the sun spot number varies little, the climatological models perform well, but during periods of high solar activity and particularly during ionospheric storms, the TEC estimates have limited accuracy. The advantage over empirical models, however, is that the climatological models can be applied any time, even before the GPS instrument precision and data coverage was sufficient to produce accurate TEC maps.

As mentioned above, the GIM models provide TEC estimates up to GPS altitude (approx. 20,000 km), which is significantly higher than the altitudes of ERS (800 km) and TOPEX/Poseidon (1350 km). However, since 99% of the electrons are below TOPEX altitude, the GIM TEC can be used directly for this satellite. For ERS, the GIM TEC must be reduced by 5-15% depending on location, local time and solar activity. As suggested by Iijima *et al.* [1999], the GIM TEC is multiplied by the ratio between the TECs from IRI95 integrated up to 800 and 1400 km:

$$\text{TEC}_{\text{ERS}}(\phi, \lambda, t) = \text{TEC}_{\text{GIM}}(\phi, \lambda, t) \frac{\text{TEC}_{\text{IRI95}<800\text{km}}(\phi, \lambda, t)}{\text{TEC}_{\text{IRI95}<1400\text{km}}(\phi, \lambda, t)} . \quad (2.2)$$

In order to make a sensible selection for the model to be used with the ERS data a comparison is made between the ionosphere corrections derived from the TOPEX dual-frequency altimeter, the Bent and IRI95 climatological models, the GPS-based CODE and JPL GIMs, and the DORIS ionosphere model (mentioned in Section 3.4.3). Figure 2.10a shows the corrections along two TOPEX passes. Note that both GIM models follow the dual-frequency values closely, but the CODE

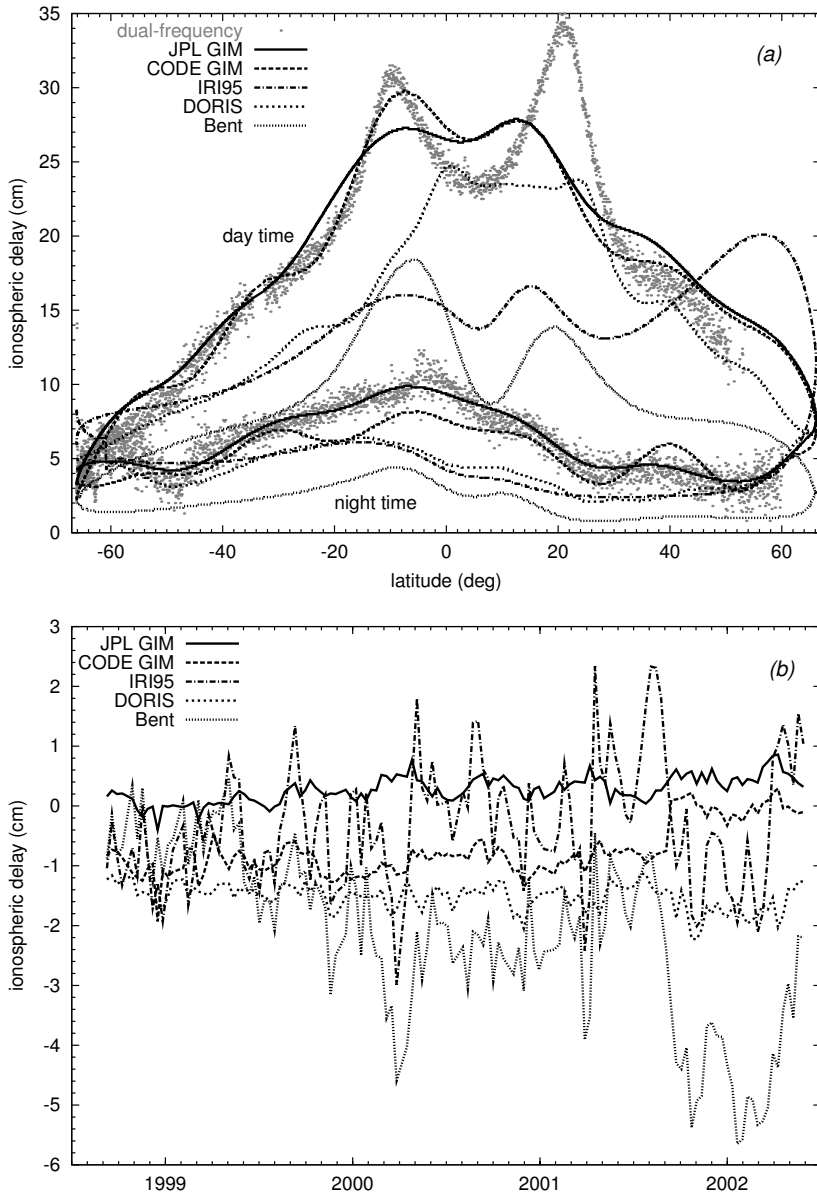


Figure 2.10 Comparison between ionospheric delays determined by the TOPEX dual-frequency altimeter and various models. Note that the delay is the negative of the correction. (a) Delays along Passes 123 and 124 of TOPEX Cycle 348 (28 February 2002). (b) Cycle-by-cycle mean differences between modelled and dual-frequency delay (September 1998 to June 2002).



GIM exhibits an anomalous short-wavelength variation that is not present in the JPL GIM or the dual-frequency values. The difference can be contributed to the way the base functions are chosen to map the global TEC in the inversion process from slant to vertical TEC. CODE uses global spherical harmonics up to degree and order 16, JPL uses local splines. The sharp truncation of the spherical harmonic expansion causes all short-wavelength power to gather in the shortest wavelength (2500 km) and is responsible for the wavy variations in the CODE GIM correction at this wavelength. The choice of local splines avoids this problem, but in return leads occasionally to undefined values in the map. Figure 2.10a further shows how the Bent seriously underestimates the peak TEC values at daytime around the equator and how IRI95 shows discontinuities and other anomalous behaviours near the poles.

The DORIS model is clearly outperformed by both GPS-based models. That earlier comparisons [Imel, 1994] were less compelling is evidently related to the recent disproportional increase of GPS performance and coverage over that of the DORIS network.

Figure 2.10b highlights the long-term behaviour of the ionosphere models by plotting the monthly mean differences with the dual-frequency correction. Both GIM models show little trend with respect to the dual-frequency correction, but the CODE GIM is slightly biased and exhibits a curious jump at Cycle 330. The Bent model shows a serious decline, which indicates that as the solar activity grows the Bent model more and more underestimates the TEC. IRI95 stays closer to the dual-frequency values but has a long-period behaviour as unstable as Bent.

Because of its superior performance the JPL GIM model was chosen as the basis for the ionosphere correction for ERS-2 Cycles 36 onward. Before that no GIM maps are available so we have to rely on either of the climatological models. During low solar activity the difference in their performances is negligible. The ultimate choice for Bent model (before ERS-2 Cycle 36) is solely based on its better around-the-orbit performance. To avoid a discontinuity in the long-term trend, 3 mm are added to the Bent ionospheric delay (3 mm are subtracted from the correction). The consequences of the choice of the ionosphere correction on estimates of sea level change and time tag bias are discussed later.

## 2.5 Orbits and other geophysical corrections

The format and content of the OPR V3 and V6 products is unchanged since 1991 and 1996. Also the AVISO data have not been upgraded since 1996. Meanwhile, many geophysical models have significantly improved and some additional corrections were found to be essential. Below follows the list of the ancillary data that were used in this thesis.

**Orbits:** The orbits featuring on V3 and V6 have a radial accuracy of approximately 14 and 10 cm, while the state of the art is 4-5 cm. The DEOS orbits for ERS-1

and ERS-2, computed with the Delft Gravity Model DGM-E04 (see Chapter 6), and other high-precision orbits are discussed in Chapter 3.

**Reference ellipsoids:** The generally accepted reference ellipsoid in the altimeter community is the so-called *TOPEX ellipsoid* ( $a_e=6378136.3$  m,  $1/f=298.257$ ). The geoid and mean sea surface models mentioned above are already referenced to this ellipsoid and all orbital altitudes are converted to this reference as well.

**Solid Earth tide:** The solid Earth tide is the vertical displacement of the Earth surface in response to the gravitational attraction of Sun and Moon. The tide generating potential is expressed by *Cartwright and Taylor* [1971] and modified by *Cartwright and Edden* [1973]. The constant term, known as the luni-solar flattening of the ellipsoid, is not included.

**Ocean tide models:** The hydrodynamic ocean tide model FES95.2.1 [*Le Provost et al.*, 1998] has long been favoured for its high resolution, accuracy and global coverage, but has been surpassed by a recent update FES99 (also implemented in RADS). Although some altimeter data have been assimilated into these models, they are mostly based on pure hydrodynamic equations.

The counterparts of the hydrodynamic models are those based mainly on the solution of the major harmonic components of the tides from TOPEX/Poseidon altimeter data improving on a previous hydrodynamic model. This procedure was first developed by *Schrama and Ray* [1994], resulting in the model SR95.1. Later successors are GOT99.2 [*Ray*, 1999] and the recent and excellent model GOT00.2 (R. Ray, private communication, 2001). GOT00.2 is also available in RADS and has been the source of ocean and load tides for the processing of ERS and TOPEX/Poseidon data in this thesis.

**Pole tide:** This correction is not included on ERS OPR data. It corrects for the slight change in the orientation of the ellipsoid as a result of polar motion using the expression formulated by *Wahr* [1985].

**Mean sea surface:** OSU MSS95 [*Yi*, 1995] featured on both the OPR V6 and AVISO products. This model was based on ERS-1 Phase E altimeter data fitted to TOPEX tracks. A more recent model is GSFC00.1 (Y. M. Wang, private communication); it includes both ERS-1 and the Geosat Geodetic Mission data, has a higher resolution and is significantly more accurate. The later model is used as reference surface for the altimeter height residuals in this thesis.

**Geoid:** Models have improved since OSU91A and JGM-3 that are provided on ERS OPR versions V3 and V6. EGM96 [*Lemoine et al.*, 1997] is a state-of-the-art alternative.

## 2.6 Data flagging and editing

Although much effort has been put into providing the most accurate ancillary data and into correcting the principle altimeter measurements for offsets, tilts and

Data element [unit]	Factor	ERS		TOPEX	
		Min	Max	Min	Max
Latitude [deg]	0	-90	+90	-90	+90
Longitude [deg]	0	-180	+180	-180	+180
Orbital altitude [km]	1	750	850	1300	1400
Orbital altitude rate [m/s]	0	-30	+30	-30	+30
Altimeter range corrected for instr. effects [km]	-1	750	850	1300	1400
Dry tropospheric correction [m]	-1	-2.4	-2.1	-2.4	-2.1
Radiometer wet tropospheric correction [m]	-1	-0.6	0.0	-0.6	0.0
Bent/JPL GIM ionospheric correction [m]	-1	-0.40	0.00		
Dual-frequency ionospheric correction* [m]	-1			-0.40	+0.04
Inverted barometer correction [m]	-1	-1	+1	-1	+1
Solid Earth tide [m]	-1	-1	+1	-1	+1
GOT00.2 ocean tide [m]	-1	-5	+5	-5	+5
GOT00.2 load tide [m]	-1	-0.5	+0.5	-0.5	+0.5
Pole tide [m]	-1	-0.1	+0.1	-0.1	+0.1
Sea state bias [m]	-1	-1	+1	-1	+1
GSFC00.1 mean sea surface height [m]	-1	-200	+200	-200	+200
Significant wave height [m]	0	0	15	0	15
Backscatter coefficient [dB]	0	6	27	6	27
Wind speed [m/s]	0	0	30	0	30
Sigma range (1-Hz) [m]	0	0	0.09	0	0.05
Number of valid elementary measurements	0	16.5	20.5	8.5	10.5
Sigma SWH (1-Hz) [m]	0	0	0.5	0	0.3
Altimeter height residual [m]		-5	+5	-5	+5

\* Since the dual-frequency ionospheric correction is a measured quantity based on range differences, it can become slightly positive.

Table 2.1 The altimeter height residual is a linear combination of a large number of data elements: measurements, propagation corrections, other geophysical corrections and ancillary information. The value in the column 'factor' indicate the factor by which the data element is multiplied in the linear combination. When any of the data elements (the altimeter height residual included) is outside the limits specified in the columns 'min' and 'max', the measurement is rejected.

drifts, rogue measurements will still exist in the data base. Instead of eliminating those data points, making it impossible to later correct for yet unknown errors, we have flagged data whenever they are conspicuous. These flags include warnings for degraded orbit precision, measurements taken over land, possible contamination of the wet tropospheric delay measurements by land in the microwave radiometer footprint, etc.

Especially the application of a land mask was studied in detail. It was discovered that a significant portion of the ERS data could be originally flagged 'over ocean', where in fact the measurements were taken over in-land lakes or even over dry continents or ice shelves. We devised a land mask that properly distinguishes between ocean, land and lake surfaces.

Even after flagging the data, we are still left with some conspicuous or low-accuracy measurements. These data can be identified by checking the principle measurements (wave height, backscatter coefficient, range, and their RMS-about-mean over a 1-second period) against pre-described limits. On top of that the altimeter height residual, the difference between the altimeter-derived sea level and a static model, may exceed a certain limit, indicating a bad data record, either because the range measurement itself is incorrect, or because the geophysical corrections are inaccurate. Editing limits are listed in Table 2.1. This Table also specifies how the altimeter height residual is computed from the measurements and corrections.

## 2.7 Error budget of ERS altimeter data

During the last decade, the altimeter data corrections and orbits have significantly improved and will remain evolving in the future. An important advantage of the RADS data base is that it can carry a wide variety of ‘competing’ corrections without any changes to the utilities. Comparison of state-of-the-art corrections and those of a few years ago can give us an idea of the precision of the present day models. Obviously, there may be common errors in the models that will not show up in such statistics, making the error estimates too optimistic. On the other hand, the comparison with older models may be too pessimistic in the sense that it demonstrates the precision of the older models rather than the more precise newer ones.

In some cases, there are no alternative models available, in which case we have to rely on estimates of the error as a percentage on the magnitude and variation of the corrections.

The error in each correction contributes directly, in root-sum-square sense, to the total error budget of altimeter-derived sea height residuals. In the case of altimeter crossover height differences, however, we have to consider the errors in the *differences* of the corrections along the two tracks that make up the crossover. To illustrate this, imagine errors in the static reference mean sea surface. They are to be added to the total root-sum-square error in the height residuals, but not to the crossover differences, since these are insensitive to static errors.

Table 2.2 indicates first the total mean and RMS-about-mean contribution of each correction to two years worth of ERS-2 altimeter height residuals and crossover height differences. In the bottom part on this Table, the actual error estimates are listed, based either on educated guesses or on model differences. Note that in most cases the RMS contribution to the crossovers is significantly less than  $\sqrt{2}$  times the RMS contribution to the height residuals. This means that, at a crossover, the corrections, as well as their errors, are highly correlated and *should not* be considered independent.

In the next Chapters we will revisit the error budgets of Table 2.2 regularly and

<b>Corrections</b>					
Correction	Height resid.		Crossover diff.		Comment
	Mean	RMS	Mean	RMS	
SPTR and USO drift	-20	15	0	0	ESRIN tables
Dry troposphere	2302	30	0	26	ECMWF model
Wet troposphere	143	93	1	41	From MWR
Ionosphere	53	34	37	26	JPL GIM model
Inverse barometer	-1	122	1	114	With global mean correction
Solid Earth tide	32	100	-2	140	Cartwright-Taylor-Edden model
Ocean tide	21	329	-7	400	GOT00.2 model
Pole tide	0	3	0	1	Wahr model
Sea state bias	144	77	0	75	BM3 model
Mean sea surface	2765	30533	0	0	GSFC00.1 model

<b>Correction and measurement errors</b>					
Correction	Height resid.		Crossover diff.		Comment
	Mean	RMS	Mean	RMS	
Range bias and noise	50	25	0	35	Assuming uncorrelated noise
SPTR and USO drift	4	3	0	0	Assuming 20% error
Orbit error	12	76	7	93	Based on GFZ - DUT orbit differences
Dry troposphere	2	3	0	3	Estimated: 1% of mean, 10% of RMS
Wet troposphere	12	29	1	21	Difference ECMWF model - MWR
Ionosphere	12	19	1	18	Difference Bent - JPL GIM
Inverse barometer	0	12	0	11	Error is 10% of correction
Solid Earth tide	0	2	0	3	Error is 2% of correction
Ocean tide	1	78	2	26	Based on difference FES95 - GOT00.2
Pole tide	0	0	0	0	Error is 10% of correction
Sea state bias	34	20	0	20	Difference BM3 model and 4.5% SWH
Mean sea surface	0	72	0	0	Difference OSU MSS95 - GSFC00.1

Table 2.2 ERS altimeter range corrections and errors, and their effect on crossover height differences. The top part of the table indicates effect of each correction on sea surface height residuals and crossover height differences expressed as the mean and RMS-about-mean additive contribution. The bottom part lists the same statistics for the estimated error in the altimeter measurements and corrections. Values are in millimetres and were determined over ERS-2 Cycles 36–56 (Sep 1998 – Sep 2000).

show that not only the overall numbers are important, but also the geographical distribution of the errors.

## 2.8 Examples

In the following, two examples are given that illustrate the quality and the lingering problems of the ERS data in the RADS data base.

### 2.8.1 Changes in global mean sea level

Long-term sea level change is of considerable interest to many strands of society: environmentalists, decision makers, and the general public. Since a large part of the world's population lives in coastal areas, and many of them are dependent in some way on the ocean, sea level change may have considerable socio-economic impact. But also the nature preservation of vulnerable wetlands in tidal regions is at stake.

This Chapter may have given the reader an idea of how complicated it is to accurately compute long-term sea level trends from altimeter data. Not only is the signal obscured by large annual variations (Figure 2.13), at the same time all sorts of system anomalies, degradations, processing changes, and correction errors may suggest long-term trends in sea level that are not factual. For example, when the oscillator drift of TOPEX was applied with the wrong sign it was mistaken for a 1 cm/year sea level rise [Nerem, 1995, 1997]. It is therefore imperative that the results of several satellites and tide gauge data are compared [e.g., Mitchum, 1994]. Later studies using TOPEX altimeter data yield varying estimates of sea level rise between 1 and 3 mm/yr [e.g., Nerem et al., 1997; Cazenave et al., 1998].

In the first study of global sea level change using ERS-1 data, Anzenhofer and Gruber [1998] find a sea level rise of 2 mm/yr. Given the short time span of 3 years, this number was hardly significant at the time. They also report the sensitivity to the choice of the ionospheric model and conclude that the issue should be revisited once the data set is extended and corrections are improved.

Since the effect of natural phenomena, like the 1997–1998 El Niño, on global sea level became evident [e.g., Nerem et al., 1999] and the weaknesses in the stability of the altimeters and their corrections attracted more attention [e.g., Mitchum, 1998], altimeter-derived sea level change estimates have been treated with more caution. The current understanding is that about a decade of TOPEX-class altimetry is needed to be able to measure the long-term rate of sea level change, provided the instruments are well monitored by a network of tide gauges [Nerem and Mitchum, 2001].

This Section shows some recent analyses of sea level trends according to ERS-1, ERS-2, TOPEX and Poseidon altimeters using the RADS data processed as described above.

- Figure 2.11 shows the monthly mean differences between the altimeter height residuals at the crossover points of ERS-1, ERS-2, TOPEX and Poseidon. The difference between ERS-2 and TOPEX/Poseidon remains nearly constant until early 2000, when the sea level corrected with the Bent ionosphere model (dashed line) suddenly drops by 1–2 centimetres compared to TOPEX. The use of the JPL GIM model instead of the Bent model (since September 1998, ERS-2 Cycle 36) clearly pays off: it removes any long-term trend between the sea levels measured by the two satellites.

Striking is also the relatively unstable appearance of the ERS-1 data based on OPR V3 (shown in grey in Figure 2.11). Although the data during the Tandem

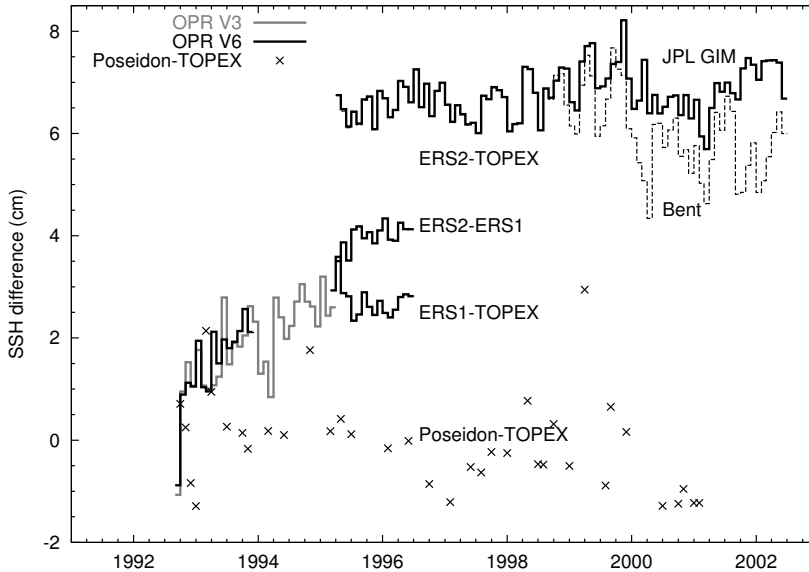


Figure 2.11 Comparison between altimeter height residuals determined by ERS-1, ERS-2, TOPEX and Poseidon at their crossover points. The monthly mean differences of the altimeter height residuals are plotted as a function of time. The black lines are based on ERS OPR V6 data, the grey line on ERS-1 OPR V3 data. The dashed line in the ERS-2/TOPEX height differences shows the effect of using the Bent instead of the JPL GIM ionospheric correction. Before the divergence, the Bent model is used. The crosses indicate TOPEX/Poseidon height differences for comparison.

Phase is well aligned with ERS-2 (except for a bias), the trend in the earlier data is clearly a sign of bad data quality. Unfortunately, it can not be said that the reprocessed OPR V6 data for Phase C (shown in black) show a significant improvement.

- Figure 2.12 shows monthly mean height differences with the GSFC00.1 mean sea surface model. A slight positive trend in global mean sea level (estimated at 3.3 mm/yr) is implied by TOPEX and Poseidon. Note the importance of the ionosphere correction in the estimation of the sea level trend from ERS-2. The dashed line, indicating the use of the Bent model, suggest a drop in sea level as measured by ERS-2, where in fact no significant rise can be found once the JPL GIM model is applied (starting September 1998).

The fact that the three satellites —ERS-1, ERS-2 and TOPEX/Poseidon— lead to different estimates of global sea level rise shows how difficult it is to interpret the long-term behaviour of an altimeter-derived global mean sea level. Even after all external corrections are based on the same models, we still face drifts in the quantities measured by the satellite, range, significant wave height, and ionospheric and wet tropospheric correction. And even when those drifts are carefully avoided or

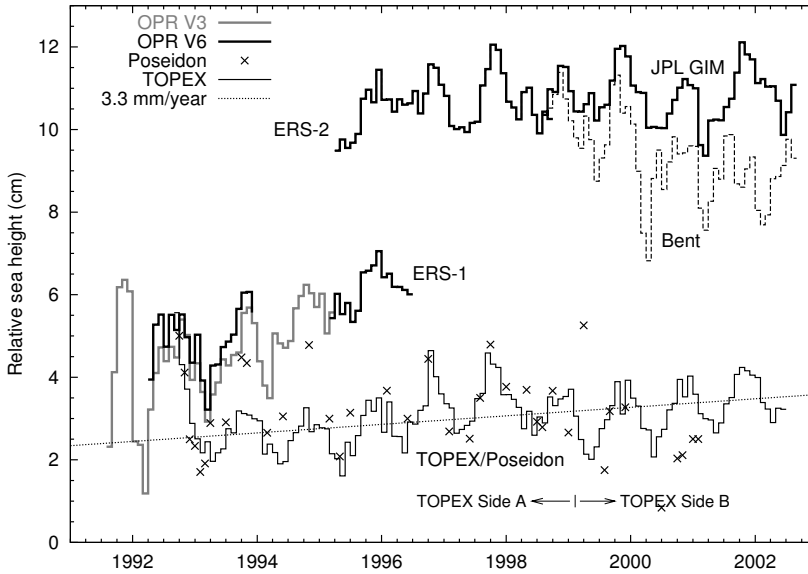


Figure 2.12 Monthly mean sea level height above the GSFC00.1 mean sea surface model. ERS-1 and ERS-2 results are indicated by the thick lines (grey based on OPR V3 data, black on OPR V6 data). The dashed line in the ERS-2/TOPEX height differences shows the effect of using the Bent instead of the JPL GIM ionospheric correction. Before the divergence, the Bent model is used. TOPEX and Poseidon results are represented by the solid thin line and crosses, respectively. The dotted line is a least-squares fit through the TOPEX data and suggests a 3.3 mm/year sea level rise.

corrected for, the different spatio-temporal sampling of global sea level variations may lead to contradicting results.

## 2.8.2 Global distribution of sea level variations

To illustrate the point about spatio-temporal sampling, Figure 2.13 shows the annual amplitude and phase and long-term trend of the variations of the sea surface height as determined from more than 7 years of ERS-2 altimeter data (May 1995 to June 2002). The annual cycle and trend are estimated together with the semi-annual cycle, not shown here. Clearly visible is the yearly oscillation of ‘high water’ between the Northern and Southern Hemisphere associated with heating of the water column and to a lesser extend mass exchange between the hemispheres. The high amplitudes in the areas of the western boundaries currents (Gulf Stream and Kuro Shio) portray strong yearly fluctuations in their meanders. At the same time, the tropical regions seem to live a life of their own. Notice the strong signal associated with the monsoon in the Indian Ocean.

The local trends in sea level vary considerably across the oceans. Sea level rise as much as 3 cm/year can be found within the reach of western boundary



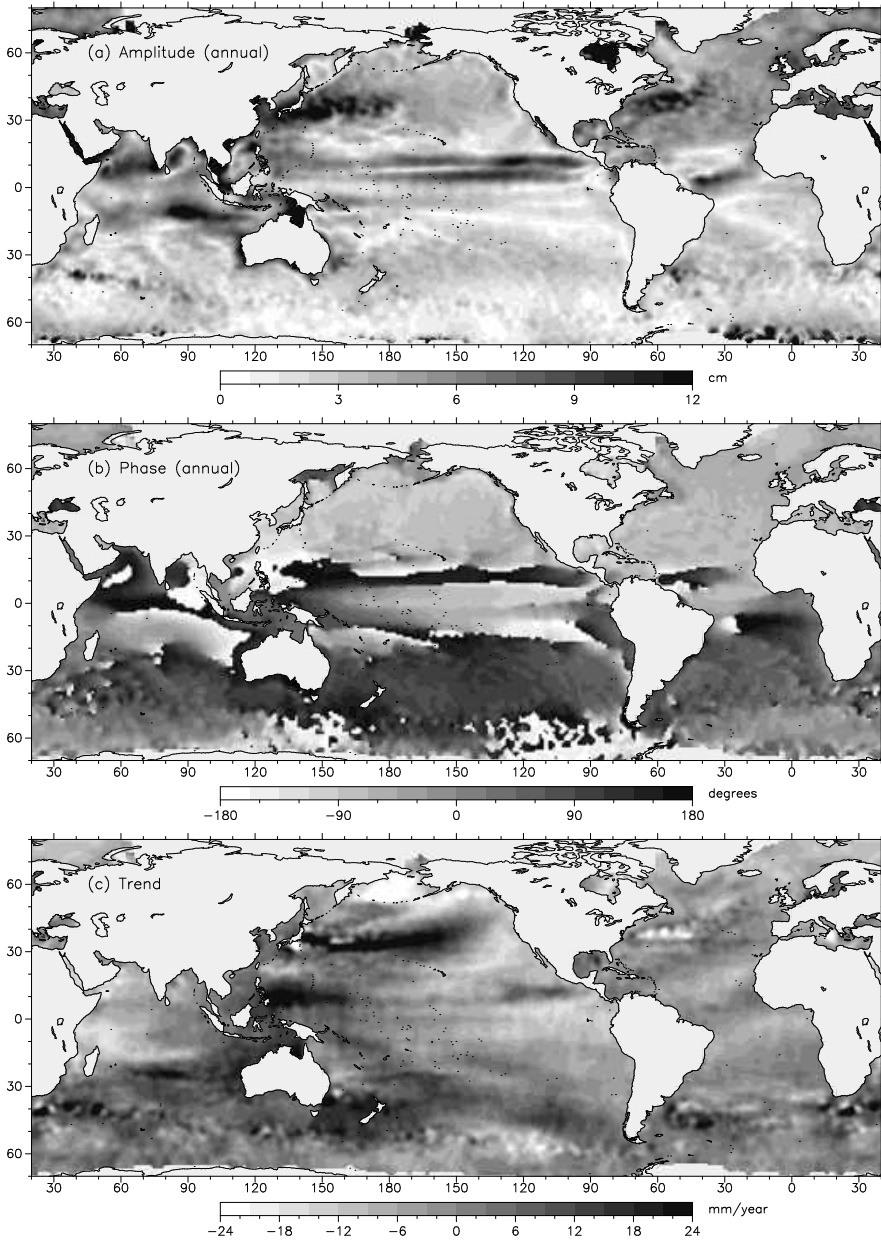


Figure 2.13 The annual cycle and trend in sea level variations observed by ERS-2 during the period May 1995 to June 2002. (a) Amplitude of the annual variation. (b) Phase of the annual variation. A phase of  $0^\circ$  indicates a maximum on 1 January; a phase of  $90^\circ$  indicates a maximum on 1 April. (c) Long-term trend, after removing annual and semi-annual cycles.

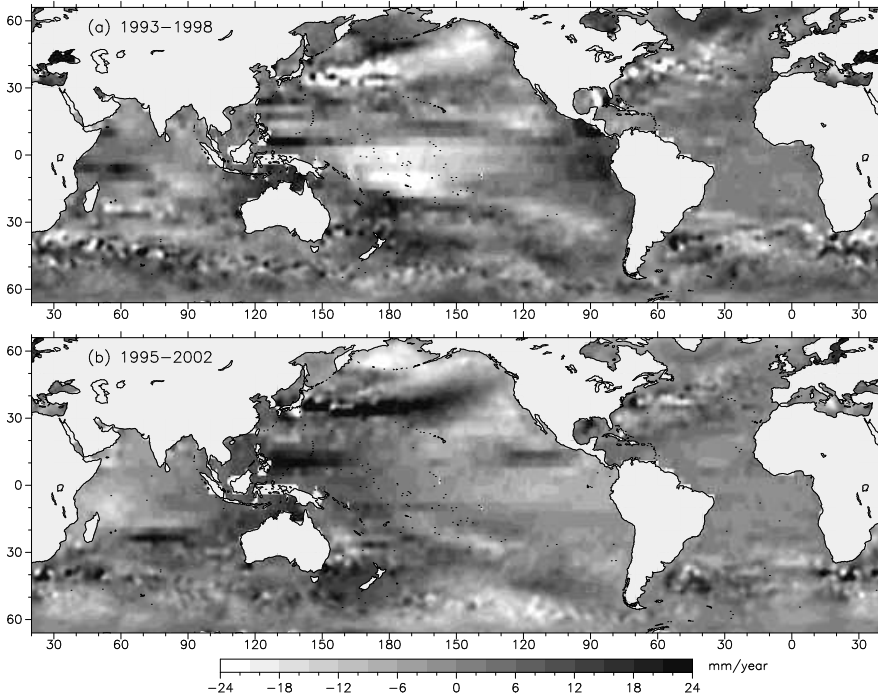


Figure 2.14 Long-term trend in sea level variations observed by TOPEX, after removing annual and semi-annual cycles. (a) January 1993 to December 1998. (b) May 1995 to June 2002.

currents, which is more likely a result of long-term changes in the current's velocity and/or location than it constitutes actual sea level rise. The rise off the coast of the Philippines is probably associated with recent El Niño events. Striking are the large drops of sea level (up to 3 cm/year) in oceanographically quite areas like the Bering Sea and Ionian Sea. The strong negative trend in Ionian sea level is confirmed by tide gauges and coincides cooling of the sea surface [Fenoglio-Marc, 2002]. Rather than blaming climate change, Fenoglio-Marc [2002] contributes the trend to an increase in anti-cyclonic circulation.

These plots make clear that the computation of global mean sea level change will depend on the sampling. A disproportionately large amount of ERS measurements are taken over high latitudes beyond  $66^\circ$ , regions that are not sampled by TOPEX. These regions are also covered by ice during a large part of year, making estimates of sea level change from ERS data more seasonally and regionally biased than those from TOPEX. The alternative to satellite altimeters, tide gauges, also suffer from a sampling problem. They generally are located close to the coast and the majority of long-term records are found in the Northern Hemisphere. Needless to say that estimates of sea level rise, regional as well as global, have to be considered with extreme care.

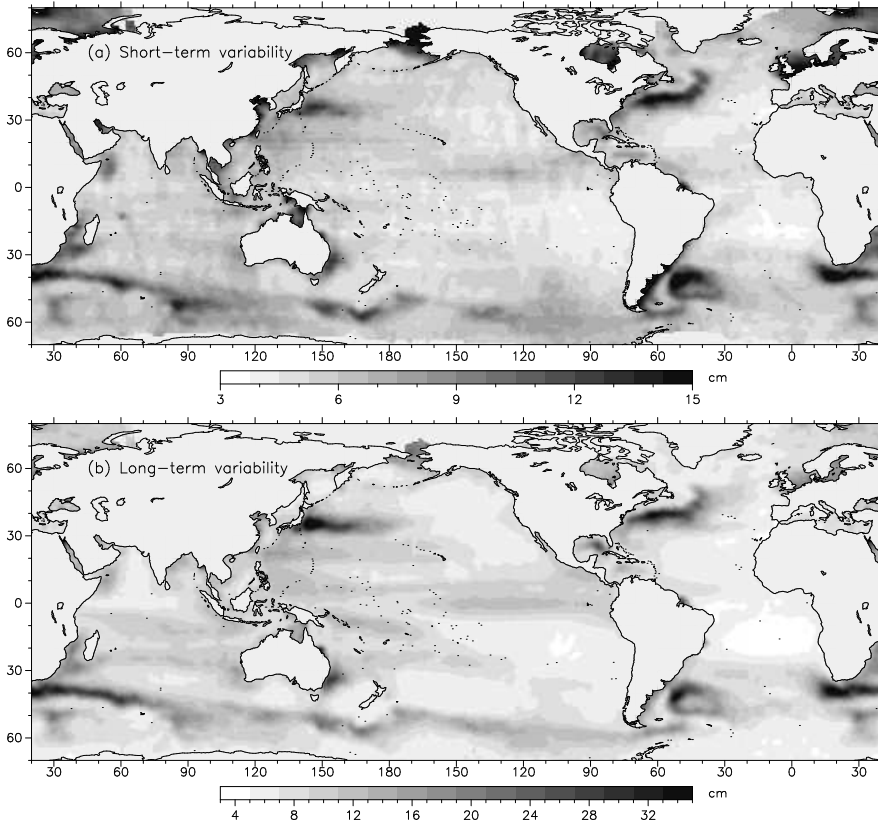


Figure 2.15 Sea level variability based on ERS-2 altimetry during the period May 1995 to June 2002. (a) Short-term (meso-scale) variability computed from crossovers. (b) Long-term variability computed from height residuals after removal of the annual and semi-annual variations displayed in Figure 2.13.

Apart from the geographical sampling, temporal sampling is much more important than one might initially suspect. Figure 2.14b shows sea level trends computed from TOPEX data for the same period as ERS-2 in Figure 2.13c. The two figures are remarkably similar, indicating that, despite its limitations, ERS-2 produces sea level trends comparable with TOPEX. Now move to the period January 1993 though December 1998. Sea level trends for this period, shown in Figure 2.14a, are significantly different from the 1995-2002 period, shown in Figure 2.14b. Some of the largest trends have even changed sign! This makes it evident that even a 6-year period is not sufficient to make statements about local sea level rise.

The model of the annual variation shown in Figure 2.13, along with the mean topography and the semi-annual cycle serves as a *climatological mean sea surface* that is used as a reference of the altimeter tracking data, discussed in Section 3.4.4. At

the same time, the remaining altimeter height residuals are used to map short- and long-term sea level variability, which serve as data weights for altimeter crossovers and height residuals, respectively. These *variability maps*, displayed in Figure 2.15 include contributions due to orbit and corrections errors. The short-term variability is dominant in the areas of energetic currents, whereas on the longer term non-seasonal sea level variations in tropical and subtropical regions become more prominent.

# Precise Orbit Determination for the ERS Satellites

When a satellite radar altimeter overflies an ocean surface, it provides measurements of wind speed and wave height at the satellite's nadir, as well as the range between the sea surface and the satellite. This altimeter range measurement by itself is of little use. It becomes much more valuable when it is differenced with the altitude of the satellite in a well-defined reference frame and above a well-defined reference surface. This can be achieved, for example, by laser tracking systems; when three of such lasers determine their range to the satellite simultaneously, the altitude of the satellite can be determined independently in the reference frame of the laser systems.

Unfortunately, the ERS satellites are not tracked continuously by laser systems, certainly not by three or more simultaneously. PRARE, the Precise Range And Range-rate Equipment that operates on ERS-2, is also not able to ensure continuous tracking of this satellite. Precise orbit determination provides the missing link. Input to this process are whatever tracking data are available —satellite laser ranging data, PRARE data, and, if needed, also altimeter data themselves—, and a large variety of dynamical and geometric models. Output is an orbit model, a table of position and velocity of the satellite at regular intervals, referenced to the global framework of tracking stations. This table can be interpolated to any required time, to give us the orbital altitude of the satellite at that instant.

This Chapter addresses various aspects of the computation of the ERS orbits and the methods used to assess the orbit accuracy.

## 3.1 Introduction

The accuracy at which the absolute sea level, but also land or ice elevation, can be determined from satellite altimetry is always limited by the accuracy of the orbit computation. In fact, the radial orbit error has long been the largest error

source in recovering sea surface height or ice sheet elevation from ERS altimeter measurements. Because of the long-wavelength character of the orbit errors, ERS altimeter data were unsuitable for applications in global ocean circulation studies, ocean tide modelling, and monitoring of seasonal and secular (climate-related) elevation changes. It is this long-wavelength signature that makes orbit errors nearly immune to averaging processes. Whereas data noise and most altimeter correction errors simply average out over a relatively small area, orbit errors, with wavelengths of 10 000 km or larger, simply do not. Initially, the 10-cm overall error budget required by the oceanographic community [Tapley, 1992] just could not be met. Recently, SAR interferometry, with its applications of mapping land surface elevation and elevation changes, is now also demanding ever increasing accuracy of the orbit computation in cross-track direction.

The bulky and low-flying satellites ERS-1 and ERS-2 were never designed for high-accuracy orbit determination, and the loss of the PRARE tracking system left ERS-1 even more poorly equipped for orbit determination. Yet, sub-decimetric orbit accuracy is not of academic interest only. The ERS altimetric system has performed well above expectations and is unique because of its multidisciplinary character, sampling not only ocean but also land and ice surfaces, in combination with the suite of instruments on board, providing, *e.g.*, simultaneous measurements of wet tropospheric content and surface temperature. Undoubtedly, ERS will always lag behind on the 2-cm root-mean-square orbit accuracy of the TOPEX/Poseidon altimeter mission [Marshall *et al.*, 1995]. By stretching the precise orbit determination to its very limits, however, and by years of collaborative research, ERS altimetry can now be regarded a reliable source of information in ocean research and excels in the monitoring of the ice sheet mass balance and (seismic) land movements.

For years, empirical techniques, like crossover height minimisation [*e.g.*, Tai and Fu, 1986; Moore, 1990], have been used to reduce these orbit errors, at the expense of also eliminating part, if not all, of the natural long-wavelength variations of the sea level [Tai, 1991]. The orbit error reduction method using TOPEX/Poseidon data as a reference [*e.g.*, Le Traon *et al.*, 1995b] significantly reduces orbit errors without corrupting the long-wavelength features in sea level [Le Traon and Ogor, 1998]. It removes nonetheless the absolute reference of the ERS data such that it is no longer an independent instrument in the study of sea level change. For those studies, the improvement of the ERS orbit accuracy, through refinement of the orbit determination process, enhancement of the dynamical modelling, and improvement of the tracking data coverage, is imperative.

The next Sections describe the advancement of ERS orbit determination over the years, particularly the contributions by DUT, and the current state of the art.

## 3.2 History

In December 1991 DUT produced the first operationally determined orbit for ERS-1 and has been doing so ever since at the regular pace of two orbital arcs per week. With these orbits and additional geophysical models, the Laboratory for Satellite Altimetry at NOAA has been upgrading the ERS fast-delivery altimeter products provided by ESA to NOAA IGDRs. These were the only reliable altimeter products until about 1.5 years into the ERS-1 mission, when the first OPRs were made available by ESA.

Until today, the DUT orbits for ERS-1 and ERS-2 have found wide application by users and institutes throughout Europe and the United States (*e.g.*, CNES, ESOC, MSSL, NASA, and NOAA).

### 3.2.1 First-generation precise orbits

At the time of the launch of ERS-1 the NASA Goddard Space Flight Center (GSFC) GEM-T2 gravity model [Marsh *et al.*, 1989, 1990] was the most commonly used model. Because this model lacked sufficient high-inclination orbit information in its development, the resulting ERS-1 orbits started at about 140-cm radial accuracy. After GSFC included tracking data of SPOT-2, which runs in an orbit very similar to ERS, in their gravity model PGS-4591, orbit errors reduced drastically to  $\sim 30$  cm [Scharroo *et al.*, 1993a]. ERS-1 tracking data were first included in the first Joint Gravity Models for the TOPEX/Poseidon mission, JGM-1 and JGM-2 (NASA, University of Texas at Austin) [Nerem *et al.*, 1994], and in the GeoForschungsZentrum (GFZ) PGM035 gravity model used to produce the official ESA orbits from the German Processing and Archiving Facility (D-PAF). The introduction of these models in the ERS-1 POD reduced the orbit error to a level of 15–20 cm [Aksnes *et al.*, 1994; Massmann *et al.*, 1994; Scharroo *et al.*, 1993b, 1994], at which the surface force modelling errors (drag and solar radiation) started to dominate [Le Traon *et al.*, 1995b].

A new model for the satellite geometry was developed and successfully implemented in 1993, but incorporating altimeter range measurements as an additional tracking type scored little success in reducing the remaining orbit errors [Scharroo *et al.*, 1993a, 1993b; Visser, 1993; Shum *et al.*, 1994]. Non-dynamic orbit improvement using TOPEX/Poseidon as a reference, with all its associated limitations, seemed the only way to provide sub-decimeteric orbits for ERS-1 [Le Traon *et al.*, 1994, 1995a, 1995b; Le Traon and Ogor, 1998; Smith and Visser, 1995].

### 3.2.2 Second-generation precise orbits

Simultaneous with the launch of ERS-2 and the start of the ERS Tandem Mission (May 1995), DUT introduced JGM-3 [Tapley *et al.*, 1996] in the operational orbit determination. This brought the radial orbit error down to  $\sim 10$  cm, but satellite laser ranging to ERS-1 and ERS-2 simply remained insufficiently abundant and

lacked a regular global distribution required to provide sub-decimeter accuracy everywhere on the globe. With most of the tracking stations located in Europe and North America, orbit accuracy remained poor, especially at southern latitudes. Inclusion of additional tracking data was imperative and found in the form of altimeter crossover height differences, nailing down the orbits everywhere over the oceans and paving the way to introduce additional parameters in the POD to absorb remaining unmodelled or inadequately modelled forces.

In spring 1996, DUT produced a full set of *second-generation* precise ERS-1 and ERS-2 orbits for the period April 1992 until August 1995, on the basis of the JGM-3 gravity model and SLR and altimeter crossover tracking data. Of these, the ERS-1 orbits for mission Phases C, D, E, and F were made available on Internet. The radial orbit accuracy of about 7 cm [Scharroo *et al.*, 1996a, 1996b] was a significant improvement over the 10-cm accuracy of the GFZ/D-PAF orbits featured on the official ESA altimeter products. This was mainly due to the superiority of JGM-3 over the GFZ PGM035 gravity model used in those days to compute these orbits.

### 3.2.3 Third-generation precise orbits

A natural step was to develop a gravity model, tailor-made for ERS orbit determination, starting from JGM-3, and so to reduce the gravity-induced orbit error. The resulting Delft Gravity Model DGM-E04 (whose development is described in Chapter 6 and in Scharroo and Visser [1998]) still forms the basis for the *third-generation* precise ERS-1 and ERS-2 orbits, currently all accessible through Internet [Scharroo, 1997]. In Chapter 6 we will emphasise on the POD for the ERS Tandem Mission, exploiting the unique situation of having the two altimeter missions flying the same orbit. During this period, ERS orbits are computed simultaneously, using ERS-1/2 dual-satellite crossovers to link the orbits tightly in a common reference frame and to have one orbit benefit from the other when SLR tracking is sparse. At the same time, altimeter height differences along collinear tracks and ERS/TOPEX dual-satellite crossovers remain as independent indicators for the radial orbit error. This situation is significantly different from an ERS orbit determination based on ERS/TOPEX dual-satellite crossovers, where TOPEX orbits are merely used as a reference and are not simultaneously adjusted using the constraints of actual satellite dynamics. A discussion of the use of altimeter tracking data in the orbit determination versus the non-dynamic orbit improvement using crossovers is given in Section 3.4.4.

## 3.3 Orbit determination

The ERS orbits are by first approximation elliptical or Keplerian orbits, forming the solution of the equations of motion for the two-body problem based on Newton's



law of gravitation,

$$\frac{d^2 \mathbf{r}}{dt^2} = -\frac{\mu}{r^3} \mathbf{r} \quad . \quad (3.1)$$

Here,  $\mathbf{r}$  is the position vector of the satellite in an inertial reference frame, and  $\mu$  is the Earth's gravitational parameter. This approximation is only valid when the Earth's gravity field is radial-symmetric and there are no other forces acting on the satellite. In reality, the Earth's gravity field is complex and several other forces are at play. A more realistic representation of the equations of motion is

$$\frac{d^2 \mathbf{r}}{dt^2} = \nabla U + \mathbf{a} \quad , \quad (3.2)$$

where  $U$  is the gravity potential, which is usually expanded in a series of spherical harmonics (see Appendix B). The accelerations due to non-potential forces are contained in  $\mathbf{a}$ . This system of second-order differential equations can be integrated from the initial position  $\mathbf{r}(t_0)$  and velocity  $\dot{\mathbf{r}}(t_0)$  at some epoch  $t_0$ , to obtain the position and velocity at any other time  $t$ .

In reality, the initial position and velocity of a satellite in Earth orbit are never known exactly. In addition, certain physical quantities required to define the equations of motion (like the gravity field potential or the atmospheric density) are known only approximately. They are modelled to some degree of detail and to some order of accuracy. Errors in the *force model* will cause the results of the integration to deviate from the actual motion of the satellite. A much better estimate of the trajectory of the satellite can be obtained by making use of *tracking* observations of the satellite's position or motion.

So how does a precise orbit determination program use these observations to compute the orbit? First of all, an  $n$ -dimensional, time-dependent column vector  $\mathbf{y}(t)$ , which describes the satellite's state, is defined. This *state vector* contains as its elements the components of the satellite position  $\mathbf{r}$  and velocity  $\dot{\mathbf{r}}$ , as well as any constant but unknown parameters which appear in the dynamic force model or the measurement model. The time evolution of  $\mathbf{y}$  can be described by an ordinary differential equation

$$\dot{\mathbf{y}} = \mathbf{f}(t, \mathbf{y}) \quad , \quad (3.3)$$

with an initial value

$$\mathbf{y}_0 = \mathbf{y}(t_0) \quad . \quad (3.4)$$

This *initial state vector* is then solved for iteratively, using a least-squares method, to obtain a solution that fits as close as possible with the observation data.

A more detailed description of the orbit determination process can be found in the works by Tapley [1989] and Montenbruck and Gill [2000].

### 3.4 Tracking data

In principle, any observation of the satellite is tracking data. Whether such observation is useful for precise orbit determination is a second issue. Historically, visual observations of azimuth and elevation of a satellite, glowing in the sunlight against a night sky, were used. Currently, laser and radar techniques prevail, providing highly accurate measurements of the satellite's distance,  $\rho$ , or relative velocity,  $\dot{\rho}$ , with respect to a tracking station on Earth or in space. Such observations are known as *range* and *range-rate* measurements, respectively. The link to the satellite position and velocity is specified by

$$\rho = |\mathbf{r} - \mathbf{R}| \quad (3.5)$$

and

$$\dot{\rho} = |\dot{\mathbf{r}} - \dot{\mathbf{R}}| \quad , \quad (3.6)$$

where  $\mathbf{R}$  and  $\dot{\mathbf{R}}$  are the position and velocity of the tracking station in an inertial reference frame.

In the POD process the actual range and range-rate observations are compared to the computed range and range-rate based on the modelled position and velocity of the satellite (the computed orbit) and the modelled position and velocity of the tracking station. The difference between the observed,  $O_i$ , and the computed,  $C_i$ , is called the *measurement residual*. The measurement residuals can be minimised by adjustment of the initial state vector (3.4) as illustrated in Figure 3.1. The most likely orbit solution is the one which provides the smallest sum of the squares of the residuals. Because some of the measurements are expected to be less accurate than others, e.g., as a result of measurements noise, the residuals will be weighted

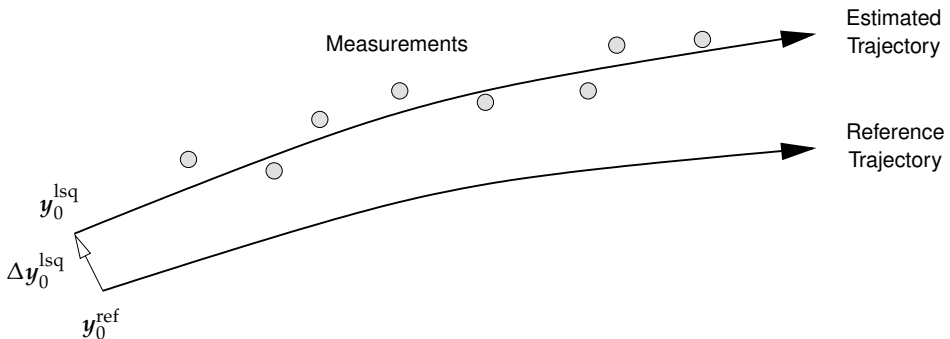


Figure 3.1 The parameters of the initial state vector corresponding to the (a priori) reference trajectory,  $\mathbf{y}_0^{\text{ref}}$ , are adjusted to find the trajectory which best fits to the measurements. This least-squares solution is defined by the initial state vector  $\mathbf{y}_0^{\text{lsq}}$ .

by the inverse of the expected measurement precision. Other a priori information in the form of constraints on the estimated parameters can also be introduced. This procedure is called *Bayesian Least-Squares Estimation* and is well described in *Montenbruck and Gill* [2000, Chap. 8].

The tracking systems that are used for the precise orbit determination of ERS-1 and ERS-2 are described in the following Sections.

### 3.4.1 Satellite Laser Ranging (SLR)

Satellite Laser Ranging (Figure 3.2) is a technique using some 30 ground stations equipped with lasers that fire very short pulses of laser light at the laser retroreflectors mounted on satellites. Some photons will make it back though space and atmosphere to the ground station. Upon detection of the returned photons the travel time  $\tau$  is clocked, which then is a measure for the range  $\rho$  to the satellite, using the simple relation

$$\rho = c\tau/2 \quad . \quad (3.7)$$

Naturally, some corrections for refraction of the laser beam in the atmosphere apply:

- The Marini-Murray tropospheric refraction correction [Marini and Murray, 1973] is computed from meteorological data provided with the tracking data.

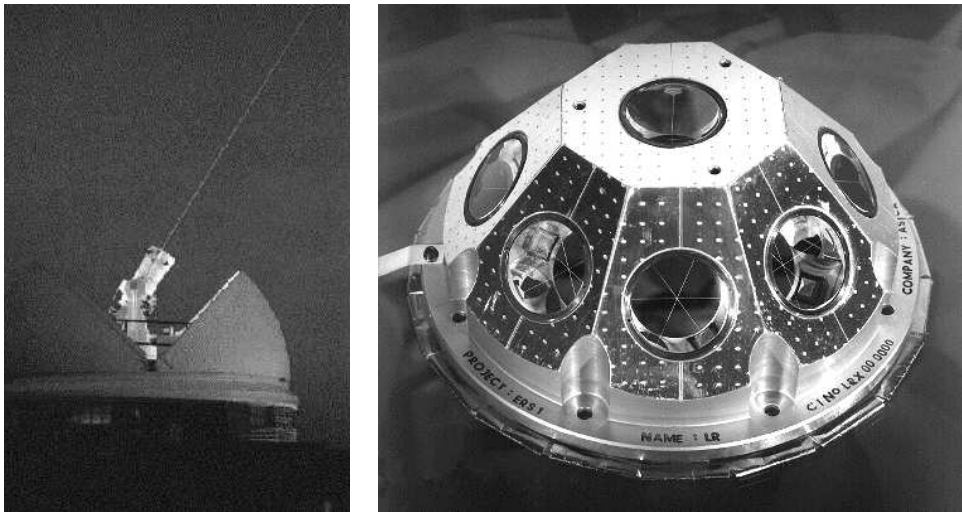


Figure 3.2 *Left:* The laser ranging system at Herstmonceux, England.  
*Right:* The Laser Retro Reflector array of ERS-1 consists of 9 corner-cube retroreflectors. Their axes all point to an imaginary point located 7 mm inside the spacecraft.

Reference point	$X_s$	$Y_s$	$Z_s$
Altimeter	-3786.4	570.0	-840.4
Laser retroreflector	-2850.4	-700.0	-995.0
ERS-1 nominal centre-of-mass	-1827.0	11.8	11.9
ERS-2 nominal centre-of-mass	-1853.0	-9.0	-3.0

Table 3.1 Coordinates of some ERS reference points in a body fixed frame in millimetres [Louet, 1991; Francis, 1991].

- A looking-angle independent range correction to account for the distance between the reflection point of the laser pulse and the centre of the retroreflector cavity lines (4.7 cm) [Louet, 1991]. Fortunately, the geometry of the LRR is much less complicated than the array of reflectors circling the altimeter antenna of TOPEX/Poseidon. Whereas with ERS a looking-angle independent correction suffices, this is definitely not the case for TOPEX/Poseidon.
- The offset of the LRR geometric centre to the satellite's nominal centre of mass listed in Table 3.1.

Since the measurement rate of SLR stations differs considerably from one to the other, all observations are converted to equally-spaced 1-per-15-second pseudo measurements, or *normal points*.

Because some stations are known to deliver SLR data of lower accuracy than others, all SLR normal points are weighted partially by a station-dependent a-priori standard deviation,  $\sigma_s$ , ranging from 1 cm for high-precision lasers to 20 cm for stations with a higher system noise or inaccurate station coordinates. The other part of the weight represents the overall model uncertainty,  $\sigma_0$ , for which a value of 5 cm is chosen. Finally, the total measurement  $\sigma$  is defined as the root-sum-square of  $\sigma_0$  and  $\sigma_s$ . Using these weights, the weighted RMS of fit, defined as

$$\text{wrms} = \sqrt{\frac{1}{n} \sum_{i=1}^n \left( \frac{O_i - C_i}{\sigma_i} \right)^2}, \quad (3.8)$$

will be close to unity for all stations.

During the last decade, the SLR tracking of ERS-1 and ERS-2 has varied considerably, as can be seen in Figure 3.3a. The number of SLR passes acquired per month ranges from about 150 to 500. These variations are mainly due to the weather conditions on the Northern hemisphere and holidays. A typical decrement during the winter is apparent.

In the early days, the majority of stations tracked ERS-1 predominantly on the second half of the pass, because it took a considerable amount of time to 'find' the satellite manually, by adding corrections to the predicted orbit while the satellite was passing by. The orbit predictions were especially hampered by inaccurate drag modelling, which resulted from the high solar activity levels in early 1992. At high levels of  $F_{10.7}$  solar flux, the atmospheric density at satellite altitude can be as

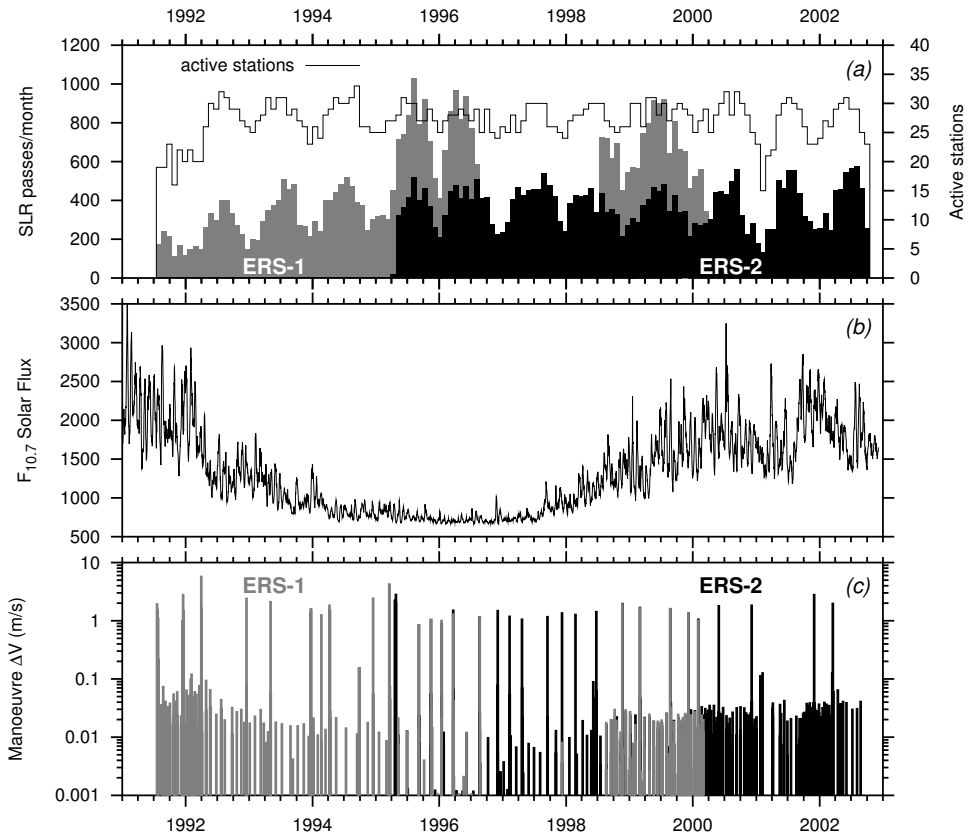


Figure 3.3 (a) The histograms represent the cumulative SLR passes per months for ERS-1 (grey) and ERS-2 (black). The solid line indicates the number of stations actively tracking ERS-1 and/or ERS-2 during monthly periods.  
 (b) Daily  $F_{10.7}$  solar flux values.  
 (c) Magnitude of the velocity change during orbit manoeuvres (in m/s), grey lines for ERS-1, black lines for ERS-2. Note the logarithmic scale.

much as an order of magnitude higher than usual, with a considerable uncertainty. During the mid 1990's, the solar flux reduced to a moderate level, thus facilitating the predictions, the satellite tracking, and the orbit computation.

In Figure 3.3 the correlation between the solar flux and the frequency of the smaller orbit manoeuvres is apparent. Since the atmospheric drag decreases with the solar activity, the orbit manoeuvres to keep the satellite's ground track close to its nominal pattern become less frequent at lower solar activity levels, and have a shorter duration. The large manoeuvres, however, which have a duration of minutes rather than seconds, are exercised to correct the orbital inclination and are not related to drag. The inclination experiences a very small linear drift as a result of solar radiation pressure, pushing the orbital plane closer to the equator.





Figure 3.5    *Left:* PRARE transponder at Matera, Italy.  
*Right:* DORIS beacon at Ny Ålesund, Norway.

### 3.4.2 Precise Range and Range-Rate Equipment (PRARE)

As the name suggests, the Precise Range and Range-Rate Equipment [Schäfer and Schuman, 1995; Bedrich et al., 1997; Massmann et al., 2000] is an instrument for the measurement of range and range-rate between ground station (Figure 3.5) and satellite. The space segment of the system on the satellite transmits a radio-frequency signal at two different frequencies to a ground station. One of the frequencies is transponded back to the satellite. The time lapse between transmission and reception at the space segment is a measure for the range. At the same time the Doppler shift is a measure for the range-rate. The second frequency is used to determine ionospheric propagation delay and correct the travel time of the principle frequency for such delays.

### 3.4.3 Doppler Orbitography Integrated by Satellite (DORIS)

The DORIS tracking system [e.g., Nouël et al., 1988] has been in development for a decade and a half and is now incorporated on many satellites, including the SPOT imaging satellites, TOPEX/Poseidon, Jason-1, and Envisat (but not on ERS-1 or ERS-2). Because of its simplicity, excellent global coverage, perfect track-record, and ever enhanced space-borne receivers, it has become *the* tracking system for the current decade. The range-rate measurements provided by the DORIS sys-

tem are based on the Doppler shift of an omnidirectional signal transmitted by one (or more) terrestrial radio beacons (Figure 3.5) and received by the satellite. Again, the difference between the propagation delays of two signals with distinct frequencies is used to estimate the ionospheric delay. Currently, these ionospheric delay estimates are not only used to correct the DORIS tracking data, but also to provide general-purpose maps of the Total Electron Content (TEC). The maps are very useful, in turn, for the correction for the ionospheric delay in the altimeter ranges, including those of other satellites not equipped with a DORIS receiver or a dual-frequency altimeter.

#### 3.4.4 Altimeter ranges and crossovers

Although the precise orbit determination is mainly conducted to support altimetry, the altimeter data themselves can actually support the precise orbit determination. The altimeter ranges (corrected for atmospheric propagation delays and sea state effects) are a measure for the satellite altitude, be it that the reference is the sea level which varies both in space and time. As a proxy for the sea level, we use a synthetic sea level which is the sum of the mean sea level, seasonal variations in dynamic topography, tides and inverted barometer effect, all based on models (Section 1.2). The sum of the modelled sea surface height and the altimeter range thus become a measure for the orbital altitude over the reference ellipsoid to be compared with the computed orbital altitude. Although the precision of such measurements is limited, the sheer abundance of altimeter data and their near global distribution make them a very suitable tracking device.

In the ERS POD described in this thesis, altimeter height measurements and crossover height differences have been used as tracking data or to monitor the radial orbit accuracy. All altimeter data have been processed, converted to altimeter height residuals, and screened as discussed in Chapters 1 and 2.

Because, as measurements for orbital altitude, the 1-Hz altimeter measurements are noisy and highly correlated from one to the next, it is not efficient to include them directly into the orbit determination process. In addition, they will then overpower the conventional SLR tracking data and do more damage than good. Thus, the number of data points is reduced by making altimeter crossovers and normal points.

Each normal point is created out of 61 *consecutive* 1-Hz measurements by fitting a cubic polynomial through the relative sea heights. If none of the measurements deviate from the fit by more than 3.5 times the RMS-of-fit, and the RMS-of-fit is less than 20 cm, the normal point is accepted. The normal point measurement is the sea height residual indicated by the polynomial at the time of the central measurement. Using 61 measurements per normal point reduces the number of points to roughly the same amount as crossovers and, in good times, the number of SLR normal points, and at the same time removes most of the noise and short wavelength errors in the altimeter data.



Before the altimeter normal points can be used in the orbit determination, the relative sea heights are back-converted to corrected altimeter height measurements, by subtracting the normal point value from the orbital altitude at the middle of the 61 1-Hz measurements. Since these measurements now act as measurements of the height of the satellite above sea level, the reference sea level must be modelled as realistically as possible. This is why besides the mean sea surface also the annual and semi-annual sea level variations (Section 2.8.2) are considered.

Since the applied reference surface has only a limited accuracy, the altimeter tracking data have to be given a weight based on the local long-term sea surface variability determined from previous altimeter data residuals, as described in Section 2.8.2. Values range from 4 cm in the equatorial Atlantic to 40 cm in the areas of energetic currents.

The use of altimeter ranges as tracking data is limited by the uncertainties of the reference level. To bypass this problem, we can use range differences at crossover location as a measure for satellite altitude differences at the corresponding epochs. We can then ignore the mean sea surface, since it is cancelled out in the differencing. Also, variations in the dynamic topography are minute over the time span of one period of orbit determination (normally around a week or less). On top of that, some of the errors in the other models, like tides and propagation corrections, will cancel out. In the end, the only errors in this type of measurement are the altimeter noise and the *differences* in correction errors.

The two relative sea heights in the crossovers are converted back to range measurements by subtracting them from the orbital altitude. The measurement weight varies with the geographical position and is based on a combination of a posteriori orbit error and short-term sea surface variability determined from altimetry, as described in Section 2.8.2. Values range from 3 cm over most of the ocean basins to 18 cm in areas of energetic currents. Because with crossovers we are only concerned with a height difference, the usage and choice of the reference mean sea surface is irrelevant but facilitates the data screening.

The pros and cons of using altimeter heights and crossovers as tracking data for satellite orbit determination is discussed in Section 3.7.

## 3.5 Models and constants

After a period of operational processing system testing, and the selection and tuning of the models applied for the POD, DUT started its operational orbit determination for ERS-1 in December 1991. Since then, many modifications to the operational system setup have been made in order to increase its flexibility and performance. The same modifications have also been adopted in the off-line precise orbit determination. Until today, the precise orbit determination is basically a later rerun of the operational orbit determination thereby taking advantage of the fact that some more SLR tracking data will be available, more precise altimeter data

products can be used, ancillary information will be more accurate, and more time can be spent on problematic orbits.

The procedures and models used for the POD are based on the most up-to-date knowledge of gravity and non-conservative force modelling. In this thesis the orbits obtained with different gravity models are compared, showing the importance of the tailoring of the gravity field to ERS. In addition, some of the other developments in the force modelling are discussed. A concise description of the current-day modelling is provided in Table 3.2.

Besides the satellite state vector, other estimated parameters are the station location for some (mainly mobile) SLR stations and time tag and range biases for stations that are notorious for producing SLR measurements with significant offsets. Since the datation of the altimeter data may not be the same as the SLR standard (UTC), it is important to estimate a time tag bias on the altimeter data. If not, the altimeter ranges appear corrupted by a signal with a frequency of two cycles per revolution (cpr) introduced by shifting the altimeter ranges forward or backward on a flattened Earth; a signal that may well alias into the orbit [Schutz *et al.*, 1982].

### 3.5.1 Gravity field models

In this thesis, three different gravity models, JGM-3 [Tapley *et al.*, 1996] (NASA, University of Texas at Austin), EGM96 [Lemoine *et al.*, 1997] (NASA, NIMA), and DGM-E04 [Scharroo and Visser, 1998] (DUT), have been used to describe the gravitational field of the Earth (including tides). All models are complete to or truncated at degree and order 70. For a satellite at 800 km the higher-order gravitational coefficients have little effect on the orbit. The quality of these gravity field models for the orbit determination of the ERS satellites is evaluated in Chapter 6.

### 3.5.2 Non-conservative forces

The dominant non-conservative forces acting on the satellite are atmospheric drag and solar radiation. Both forces are the sum effect of particles or photons exchanging momentum on the (quite complex) satellite surface, and this requires accurate modelling of the satellite geometry and surface properties.

The atmospheric drag is dependent on the atmospheric density, which varies significantly along the orbit, because of changes in the satellite's altitude, but also from day to day, depending mainly on the solar activity. In the orbit computations both effects are covered by the MSIS86 atmospheric model. To quantify the solar activity, daily  $F_{10.7}$  and 3-hourly  $K_p$  values are input to the model.

Both atmospheric drag and solar radiation pressure act upon a large satellite with a complex shape, of which the attitude varies in time due to the satellite's attitude control strategy and pointing of the solar array.

The satellite geometry of ERS-1 and ERS-2 is modelled by two macro-models consisting of 10 flat panels. Six panels form the satellite bus and payload module,

<b>Measurement Models and Constants</b>	
– SLR observations	Global quick-look SLR normal points (1 per 15 s normal points) retrieved from Eurolas Data Center (EDC) and Crustal Dynamics Data Information System (CDDIS); 10° elevation cutoff and editing of spurious measurements; weight is root-sum-square combination of overall model accuracy (5 cm) and system noise level (1–20 cm).
– SLR correction	Offset of LRR optical centre with respect to LRR reference point (4.3 cm) and to the spacecraft nominal centre of mass (Table 3.1). Marini-Murray topospheric refraction.
– Station coordinates	LSC(DUT)98C01 LAGEOS I/II solution (1988–1998, epoch 1 Jan 1993), advanced to epoch by three-dimensional motions incorporated in the coordinate solution, extended with solutions for new stations based on ERS operational orbit determination.
– Tidal displacement	Wahr model, including frequency dependent and permanent tides ( $h_2 = 0.609, l_2 = 0.0852$ ); pole tide.
– Altimeter residuals	Global enhanced OPR data; converted to 61-second normal points; weights based on local long-term sea level variability (Section 2.8.2).
– Crossover observations	Global enhanced OPR data; converted to crossovers; weights based on local short-term sea level variability (Section 2.8.2).
– Speed of light	$c = 299792.458$ km/s.
<b>Force Model</b>	
– Gravity model	Delft Gravity Model DGM-E04, complete to degree and order 70, including secular $C_{21}$ and $S_{21}$ coefficients and dynamic polar motion; $GM = 398600.4415$ km <sup>3</sup> /s <sup>2</sup> , $a_e = 6378.1363$ km, $1/f = 298.2564$ .
– Tidal gravity	Wahr solid Earth tides; background ocean tides: JGM-3*.
– Third body attraction	JPL DE200 ephemeris for Sun, Moon, Mercury, Venus, Mars, Jupiter, Saturn, Neptune.
– Atmospheric drag	MSIS-86 [Hedin, 1987] with daily $F_{10.7}$ and 3-hourly $K_p$ values.
– Radiation	Solar radiation including umbra, penumbra, and occultation by Moon; Earth albedo.
– Orbit manoeuvres	A priori information from ESOC predictions; adjusted during POD.
<b>Reference Frame</b>	
– Polar motion	Earth orientation and length of day from IERS EOP 90C04 solution.
– Coordinate system	J2000; precession IAU 1976 (Lieske model); nutation IAU 1980 (Wahr model).
<b>Satellite Model</b>	
– Mass	ERS-1, 2377.13 kg; ERS-2, 2502.00 kg (no account for fuel consumption).
– Cross-sections	Satellite-specific macromodels, each consisting of eight fixed and two rotating panels (Section 3.5.2).
<b>Estimated Parameters Per Orbital Arc</b>	
– State vector	Position and velocity at epoch over 5.5-day orbital arcs with 2-day overlap between consecutive arcs.
– Non-conservative forces	6-hourly drag coefficients; 22-hourly 1-cpr along-track and cross-track accelerations; orbit manoeuvres (three-dimensional accelerations).
– Measurement offsets	Coordinates of some (mobile) SLR stations; range and timing bias for some SLR systems; timing bias for both altimeters; relative range bias between ERS altimeters.

\*In fact, this model was not adjusted since JGM-1 [Nerem et al., 1994; Tapley et al., 1996].

Table 3.2 Summary of the dynamical and measurement models used for the ERS third-generation precise orbit determination.

two panels form the front and aft side of the SAR, and a further two rotating panels model the front and aft side of the solar array. At first, each of the panels had been given a size, orientation, and reflective properties, which were representative of their true geometry and the properties of various sub-elements defined in a more detailed micro-model, consisting of 48 panels [Kuijper, 1991]. A major advance was made by adjusting the properties of the panels of the macro-model, such that each of them might not conform to the true geometry or collective reflective properties of that panel but that their overall consistency with the micro-model in describing the actual forces acting on the whole satellite was optimal, judging from Monte Carlo ray-tracing experiments on both the macro-model and micro-model. Because of the attachment of GOME, the ERS-2 macro-model differs slightly from the one of ERS-1.

To compute the drag, the effective cross-sectional area  $A$  is determined, based on the area and orientation of the panels with respect to the satellite's velocity vector. This orientation may vary in time due to the satellite's attitude control strategy and pointing of the solar array. The solar radiation force also takes into account the reflection, absorption, and emission properties of each panel.

Finally, the drag force,  $F_D$ , is determined on the basis of the formula,

$$F_D = C_D \frac{1}{2} \rho V^2 A \quad , \quad (3.9)$$

where  $V$  is velocity of the satellite with respect to the atmosphere,  $\rho$  is the atmospheric density, and  $A$  is the effective cross-sectional area of the satellite. Theoretically, the drag coefficient  $C_D$  is around 2.3. Because of numerous imperfections in the modelling of the surface forces —be it through the modelling of the interaction between atmospheric particles and the satellite surface or the modelling of the atmospheric density—, a drag coefficient is estimated every 6 hours.

Similarly, the solar radiation force,  $F_R$ , is given by

$$F_R = f_R C_R \frac{I}{c} A \quad , \quad (3.10)$$

where  $I$  is the radiation intensity,  $c$  is the velocity of light,  $A$  is the surface area of the satellite and the radiation coefficient  $C_R$  is determined by the reflective properties and the orientations of all panels with respect to the solar rays. In the orbit computations, the scale factor  $f_R$  is fixed to its theoretical value of 1.0.

Additional unmodelled forces are parameterised through so-called *empirical accelerations*: during every 22-hour period the sine and cosine amplitudes of two harmonic 1-cpr accelerations, one in along-track direction and one in cross-track direction, are estimated. Because of the inclusion of SLR, altimeter ranges and crossovers, sufficient data are available to estimate these 24 additional parameters.

### 3.5.3 Arc length

The satellite orbits are generally computed in batches covering about a week worth of tracking data. Such batches are called *orbital arcs*. When consecutive arcs slightly

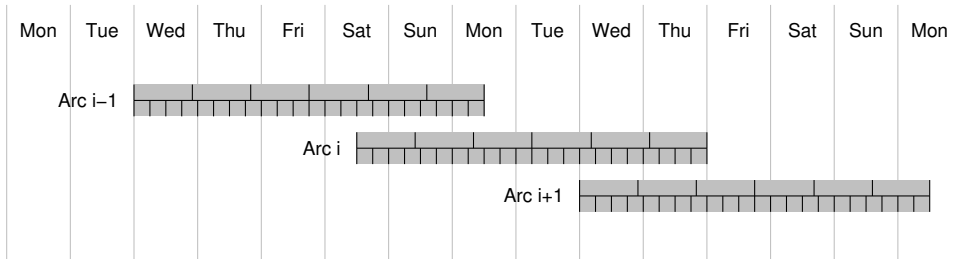


Figure 3.6 The 5.5 day ERS orbit determination arcs at DUT. The tic-marks indicate the 22-hour 1-cpr empirical acceleration and the 6-hour drag coefficient estimation intervals.

overlap a smooth transition between the orbit solutions from one arc to the next can be ensured.

The selected length of the orbital arcs is based on a number of operational considerations:

- Regular distribution of work load led to a weekly repeating schedule, with orbit determinations performed either once or twice a week.
- Seven-day or longer arcs appeared to have a worse precision than half-weekly arcs.
- To monitor the orbit consistency, it was decided to extend the arcs by one day at each end, such that two consecutive orbital arcs overlap by two days.
- The availability of a maximum of recent laser ranging data in the POD fixed the time of the data processing and the interval between the end of a data arc and the start of the data processing.

Based on these considerations for the operational POD data arcs with a length of 5.5 days were selected, while the epochs of successive arcs are separated by 3.5 days (Figure 3.6). The arcs start on Tuesday midnight or Friday noon, and the processing takes place the following Tuesday or Friday, respectively. From the orbit difference for the 2-day overlap period of two consecutive arcs, information about the accuracy of the POD may be obtained.

Only the central 3.5-day period, which is the most precise part of each arc, starting and ending at a crossing of the satellite over the Antarctic, is used to enhance altimeter data products.

Output of the orbit processing are a number of estimated orbital parameters and station coordinates, and an ephemeris file, which describes the position of the satellite's nominal centre of mass in terms geodetic latitude, longitude, and height above the GRS80 reference ellipsoid, as a function of UTC time at 60-second intervals.

### 3.6 Orbit quality assessment

How do we know how accurate the computed orbit actually is? How close is the computed trajectory to the actual one? For this we need observations, preferably some that have not been used in the orbit determination and are representative of the orbit error. Unfortunately, it is hard to find the perfect observation for quality assessment, but there are several ways to get a reasonable measure of the orbit quality. To avoid a biased orbit error estimate several of the following quality checks should be exercised:

**Tracking data residuals.** Generally speaking, the lower the measurement fit, the better the orbit. However, systematic errors in the tracking data can cause systematic errors in the orbit solution without significantly affecting the residuals. It is therefore better to look for independent quality checks.

**Altimeter crossovers.** Some of the altimeter crossovers are part of the orbit determination process, but they are always built from two crossing altimeter passes that both lie within the orbital arc. Hence, crossovers that span different orbital arcs (*i.e.*, with time lapses larger than the extend of the orbital arc) can be considered independent information. The advantage of crossover statistics as a quality assessment tool is also that they give a good estimate of the most important component of the orbit error: the altitude.

**Collinear track differences.** When the sea surface profiles of two altimeter passes along the same track, one or more repeat cycles apart, are compared, the differences are partly due to the orbit error along each pass. We will see later that these differences are virtually free of orbit errors originating from gravity field modelling errors. Collinear track differences are therefore used mainly to study non-gravitational orbit errors.

**Orbit overlap differences.** We can also compare the computed orbits directly at the overlaps of the orbital arcs. This gives some feel of the orbit errors in all three directions, but is prone to the fact that they have a lot of tracking information in common and will thus generally result in an error assessment which is too optimistic.

**High-elevation overflights.** When the satellite flies almost vertically over a laser ranging station, the laser residuals at that point are representative of the radial orbit error. Still care should be taken not to confuse an error in the vertical position of the laser station with radial orbit errors.

### 3.7 Pros and cons of using altimeter tracking data

The use of altimeter data (both the ranges and crossovers) as a tracking data type for precise orbit determination (Section 3.4.4) has long been regarded with suspicion, because of the risk that oceanographic signals may *alias* into the satellite orbit.

This risk comes from the modelled sea surface height that needs to be added to the altimeter range to make it a measure for the orbital altitude (above the reference ellipsoid) and may lack part of the global oceanic variations. If such a signal is absent in the reference surface, the altimetric proxies of orbital altitude will fall short by the same amount. In the orbit determination the orbit will then adjust itself to these erroneous measurements and thus absorb the signal that was absent in the reference model. When this orbit is used later as a reference for altimeter range measurements in the creation of sea surface heights, we will no longer be able to detect the oceanic signal.

This rational assumes that all the oceanic signal can be absorbed by the orbit. It is the question, however, if the parameters of the orbit determination can accommodate such a change in the orbit. This is most certainly not the case unless we consider extremely large scale variations of the sea surface. Most adjustable parameters in the orbit determination (state vector, solar radiation coefficient, drag coefficients and empirical accelerations) control the orbit at scales larger than 10 000 km and are associated with the 1-cpr and, to a lesser extent, 2-cpr frequencies and long-period modulations thereof [e.g., Tapley, 1989]. It is therefore evident that if signals *are* absorbed into the orbit, it can only be at these extremely large scales.

Conversely, this means that the orbit has most degrees of freedom around the 1-cpr frequency. When only few SLR stations track the satellite or when tracking is poorly distributed globally, like around the winter holidays, the 1-cpr frequency will be ill-determined. That is when the altimeter tracking data are most useful to help constrain and decrease the degrees of freedom. To demonstrate the effect of the use of altimeter data in the POD and possible errors in the reference surface, Table 3.3 shows a the results of the POD process for two ERS-2 Cycles, one in winter, one in summer, under several conditions:

1. POD with SLR and altimeter tracking (reference orbit);
2. POD with SLR and altimeter tracking with very low weight;
3. Altimeter heights offset by 10 cm shift along pole axis (Z-axis);
4. Altimeter heights offset by 10 cm shift along X-axis;
5. Altimeter heights offset by 10 cm shift in equatorial plane toward the Sun;
6. Altimeter heights corrupted with 10% of the ocean tides.

The difference between Case 1 and 2 demonstrates the importance of adding the altimeter tracking data, particularly in the winter period when the SLR tracking coverage is poor. Without the altimeter tracking data (*i.e.*, when putting low weight on this data type), the orbit solution has so much freedom that its precision is significantly reduced. Cases 3 and 4 show that the orbit is nearly insensitive to the shift of the reference surface in X direction and slightly sensitive to one in Z direction. Both cases simulate a slowly varying, large scale ocean signal that is invisible to crossovers. Case 5 adds a strong corrupting signal to the crossovers which is almost completely absorbed by the orbit. This case is not representative

	SLR		Altimeter		Orbit difference	Xover RMS
	all	high-prec.	heights	xovers		
<b>Cycle 49 (22 Dec 1999 - 25 Jan 2000)</b>						
Number	4153	3532	26555	9707		
1. SLR, altimetry, crossover tracking	5.73	4.94	11.09	8.98	—	9.52
2. SLR, low weight altim. and xovers	6.58	6.01	16.35	19.07	13.73	18.01
3. Altimeter heights: 10 cm Z shift	6.04	5.31	11.90	9.12	2.61	9.72
4. Altimeter heights: 10 cm X shift	5.73	4.94	11.61	8.96	1.34	9.50
5. Altimeter heights: 10 cm Sun shift	6.27	5.31	11.59	10.42	5.31	13.70
6. Altimeter heights: 10% tide error	5.75	4.96	11.48	9.54	2.23	9.59
<b>Cycle 56 (23 Aug - 26 Sep 2000)</b>						
Number	9405	5009	26763	10844		
1. SLR, altimetry, crossover tracking	6.59	5.25	10.29	9.21	—	10.76
2. SLR, low weight altim. and xovers	6.61	5.33	11.45	11.88	3.93	12.54
3. Altimeter heights: 10 cm Z shift	6.64	5.27	11.80	9.24	0.66	10.80
4. Altimeter heights: 10 cm X shift	6.60	5.24	11.55	9.21	0.22	10.75
5. Altimeter heights: 10 cm Sun shift	6.77	5.34	11.26	12.16	3.21	10.86
6. Altimeter heights: 10% tide error	6.63	5.28	10.72	9.75	0.20	10.76

Table 3.3 Tracking data residuals and overall crossover RMS for several orbit solutions covering two ERS-2 cycles. The different orbit solutions mentioned in the leftmost column are further identified in Section 3.7. The next four columns list the number of tracking data and the RMS of the tracking data residuals (in centimetres) of 10 orbital arcs spanning each cycle. The statistics are (from left to right) for all SLR stations, the high precision SLR stations, and altimeter heights, altimeter crossovers. The sixth column lists the RMS orbit difference with the reference solution and the rightmost column lists the overall crossover RMS for the particular cycle (maximum time interval 17.5 days) based on the *uncorrupted* altimeter data and the orbit solution at hand.

of an ocean signal, but a signal that has a day-night asymmetry, like some tidal components and the ionosphere correction. Case 6 simulates the effect of a true ocean signal to which the orbit appears not very sensitive, that is to say, that errors in the tide model do not propagate through the altimeter data into the orbit. Not considered here are the gravitational tides; errors in their modelling *will* have an effect on the satellite orbit. Note that the sensitivity to errors in the altimeter data is significantly less when the SLR coverage is abundant. In any case, the large and exaggerated errors introduced in the altimeter tracking data have less effect on the orbit precision than not using altimeter data at all.

We can conclude that only global scale ocean signals may be absorbed in the orbit, particularly those that have a North-South asymmetry, like the annual sea height variations. It is therefore important that these variations (see Section 2.8.2) are included in the reference surface. Furthermore, the sensitivity to these signals comes mainly through the altimeter heights, since the crossovers (with a maximum of 5.5-day time interval in the orbit determination) do not observe slow height variations. We can therefore attach more weight to the crossovers than to the altimeter heights.



## Chapter 4

# ERS-1 Radar Altimeter Range Calibration

The ERS-1 altimeter is capable of measuring the height of the satellite above the sea surface, ice or flat land areas with a precision of a few centimetres. However, the measurements may be corrupted by a constant bias, as explained in Section 1.2.1. For the in-flight calibration of the ERS-1 altimeter a procedure has been developed that is based on the selection of a 3-day repeat orbit, in which the satellite overflies an oceanographic platform in the Adriatic Sea every 3 days.

Laser tracking data acquired by a network of European satellite laser ranging systems are used to compute the altitude of the satellite over this platform. Note that, at the time, the global long-arc orbits for ERS-1 had a radial accuracy of around 1 metre, insufficiently accurate to be used for the in-flight calibration. By computing orbits with a very short length (only 15 minutes) the effect of gravity field model errors, by far the largest contributor to the orbit errors, is almost completely removed.

The comparison of this computed altitude with the altimeter height measurements and all kinds of local sea and atmospheric measurements taken at the platform provides an estimate of the altimeter bias. This Chapter addresses the concepts of the calibration, the short-arc orbit determination, and the combination of the available data into a bias estimate, and presents the results obtained at DUT.

## 4.1 Introduction

In order to successfully study long-term ocean phenomena with altimetry, which involves combination of height measurements taken from different satellites and comparison to ground-truth, an absolute reference of all ‘participating’ altimeters is required. Unfortunately, altimeters may be hampered by a height bias, which can not always be determined accurately prior to launch in a laboratory environment. Therefore, a campaign has been set up to calibrate the ERS-1 radar altimeter

in-flight during the ERS-1 Commissioning Phase, the first months of the satellite's mission. Basically, this bias estimation is achieved by comparing the altimeter height measurements over a predefined calibration area with the computed altitude of the satellite (based on SLR tracking data) above sea level recorded by a tide gauge.

This altimeter calibration project was led by the European Space Research and Technology Centre (ESTEC/ESA) and was executed by a team consisting of representatives from various European research institutes. They provided the equipment, skill, and expertise to provide accurate positioning of the satellite, the sea level and various kinds of auxiliary environmental data.

### 4.1.1 Overall description and scenario

The concept of the ERS-1 radar altimeter range calibration evolved during several years before launch of the satellite in July 1991 [Francis and Duesmann, 1988]. My personal involvement in the ERS-1 Radar Altimeter Calibration Team started in November 1990, at a meeting in Venice. Before that, the calibration site was already selected and preparations were well on their way. The main objectives of the calibration concept were to ensure a high level of confidence in the final result, to optimise the redundancy in the overall system, to avoid dependency on external models, and to make maximum use of available European resources and expertise [Francis *et al.*, 1993]:

1. The radar altimeter should preferably be calibrated over open sea, far enough from the coast to avoid contamination of the altimeter measurement by land surfaces in the footprint.
2. The calibration spot should be positioned accurately and be instrumented with a sea-level measuring device (tide gauge). Furthermore, environmental conditions (wind speed, wave height, tropospheric and ionospheric contents) should be monitored in order to derive accurate range corrections for the radar pulse.
3. The calibration area should, however, be sufficiently close to continents to ensure accurate positioning of the site *and* the satellite when it flies over the site.
4. Several SLR systems on the continent, including one close to the satellite track, should provide tracking of the satellite over the calibration site. A network of six SLR sites was expected to provide sufficient tracking even if some of them should fail to track the satellite, because of unfavourable weather (or other) conditions.
5. Apart from political reasons, a site in Europe was preferred, because of its uniquely high occupation by fixed and mobile satellite laser ranging systems.
6. The calibration should be performed on several passes, in order to increase the redundancy of the procedure and help restrain the non-static error budget.
7. The calibration should avoid potential single-point failures, and should be resistant to static errors. Later it would appear that it were those static errors that

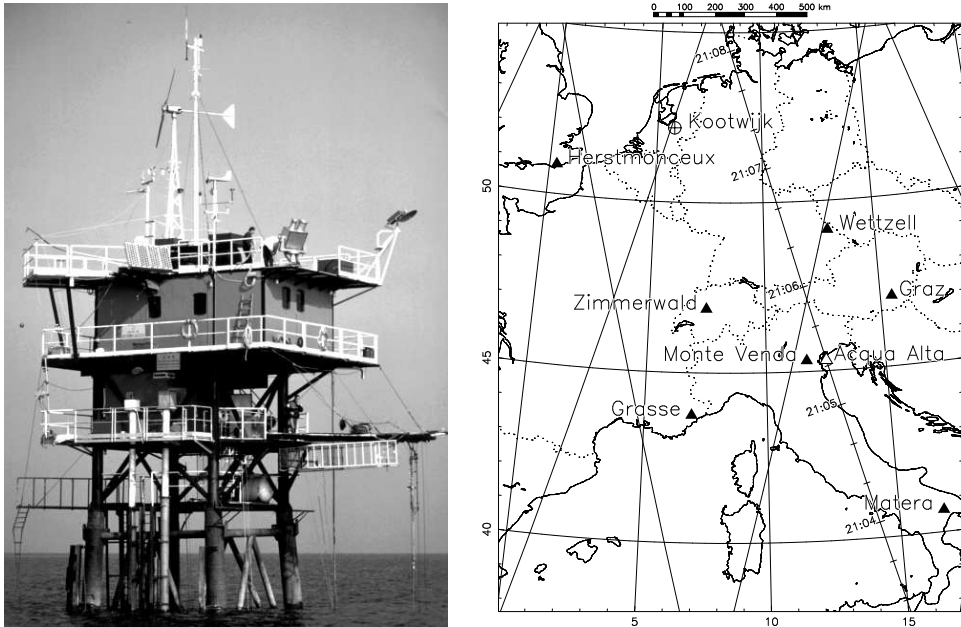


Figure 4.1 *Left:* The *Acqua Alta* tower during the calibration campaign. The microwave radiometer is visible on the upper platform. The wells of the analogue and digital tide gauges are mounted on either side of the access ladder. *Right:* The ECN laser sites (solid triangles) and the ERS-1 ground-tracks over Europe. The tick marks along the calibration pass over the *Acqua Alta* tower are drawn at 20-second intervals. The time of overflight is given in UTC.

caused the bias estimates to vary from time to time during the processing of the calibration data (see Table 4.13 at the end of this Chapter).

To meet all these requirements, the actual calibration was performed over an oceanographic research platform in the Adriatic Sea, about 15 km off the coast of Venice, standing fixed on the sea floor in 16 metres of water. This platform, called '*Acqua Alta*', is owned and operated by the Istituto per lo Studio della Dinamica delle Grandi Masse of the Consiglio Nazionale delle Ricerche (ISDGM/CNR). Figure 4.1 shows the platform during the campaign.

During the calibration period (28 July till 17 September 1991) the satellite overflew the platform every 3 days on a northward night-time pass, as illustrated in Figure 4.1, while it was tracked by several SLR systems, which have become known as the European Calibration Network (ECN). In addition to the fixed sites in Grasse (France), Graz (Austria), Herstmonceux (England), Matera (Italy) and Zimmerwald (Switzerland), a new laser site near the platform was required to obtain highly accurate vertical positioning of the satellite along its pass over the calibration area. This site was installed 60 km west of the platform at Monte Venda in

the hills near Padova, and was occupied throughout the campaign by the Modular Transportable Laser Ranging System (MTLRS-2) operated by DUT's Kootwijk Observatory for Satellite Geodesy. As will be discussed in more detail in Section 4.3, this constellation of tracking SLR systems proved to possess considerable redundancy.

The fact that the calibration passes of ERS-1 were all night-time passes, overflying the *Acqua Alta* platform at approximately 21:55 local solar time (23:05 local daylight saving time, 21:05 UTC), was particularly favourable for the SLR systems. In the first place the laser systems have a higher performance at night time, but also aiming of lasers was considerably facilitated because the satellite was visible as a bright object moving along the night sky during the summer. An additional advantage is the reduction of ionospheric delay of the radar pulse (and the associated uncertainty in its determination) as the ionospheric density is minimal at night.

#### 4.1.2 Details of the calibration procedure

The basic concept of the altimeter calibration was to provide an independent assessment of the range between the satellite and the sea surface and compare it to the range measured by the radar altimeter. This required accurate determination of the satellite's altitude—which can be obtained from a precise orbit determination based on SLR tracking data—and monitoring of the sea level by a tide gauge of which the position is accurately known.

The altimeter range bias, which is defined as the *excess* path length of the altimeter measurements, can, however, only be determined accurately if the independent (computed) range has a high precision. Therefore, a painstaking, dedicated calibration procedure was undertaken. Figure 4.2 presents a sketch of this calibration concept. From this Figure and Eq. (1.2) it may be concluded that, at the time of overflight of the tide gauge,

$$b = h_{alt} - (H_{orb} - H_{tide}) = H_{tide} - H_{alt} \quad , \quad (4.1)$$

where

$b$  = altimeter height bias;

$h_{alt}$  = measured altimeter height above the sea surface around the tide gauge, corrected for instrumental and propagation effects and centre-of-mass offset;

$H_{orb}$  = satellite altitude above a reference ellipsoid (WGS 84);

$H_{alt}$  = altimetric sea surface height with respect to the reference ellipsoid, at the position of the tide gauge;

$H_{tide}$  = sea surface height above the reference ellipsoid, as measured by the tide gauge.

The altimeters of GEOS 3 (1976) [Martin and Kolenkiewicz, 1981] and Seasat (1978) [Kolenkiewicz and Martin, 1982] have been calibrated in a similar way, using overflights of Bermuda supported by the Bermuda laser. Since these passes

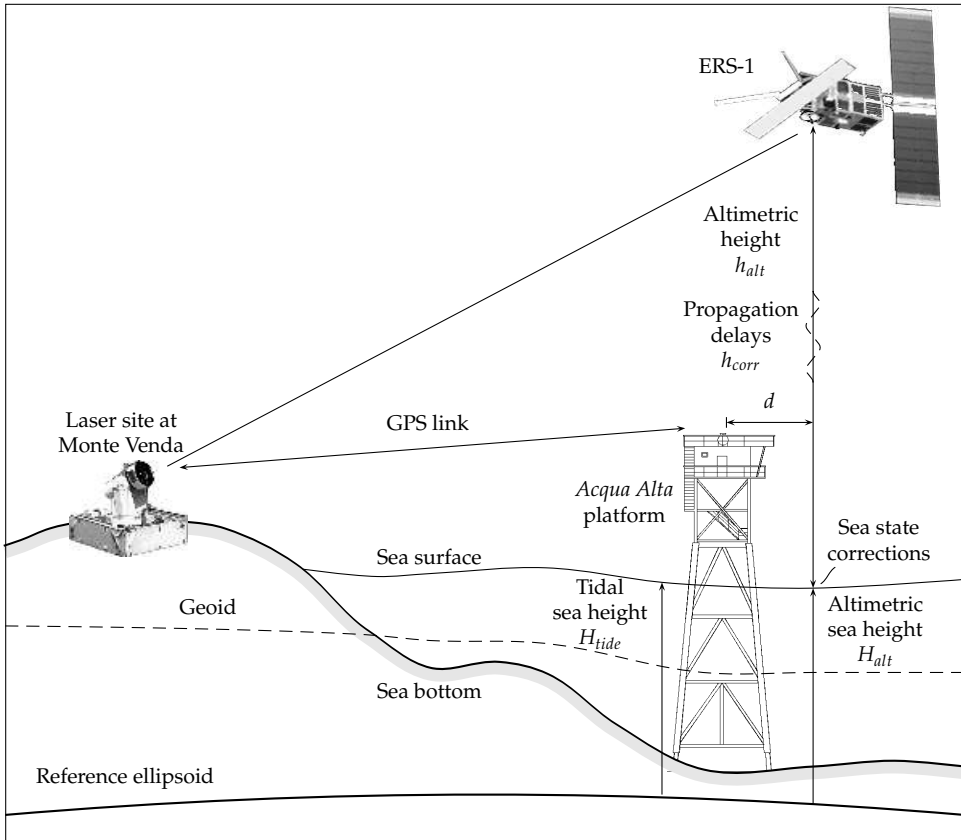


Figure 4.2 Schematic illustration of the ERS-1 calibration over the *Acqua Alta* platform.

were almost overhead, the laser ranging data from this single site could be used for a highly accurate determination of the orbital altitude. A drawback in this Bermuda scenario is that no altimeter data were available when the satellite was in the zenith of the laser, because of land in the altimeter footprint. This poses a problem since the resulting altimeter data gap just occurs at the moment that the satellite's computed radial position component has maximum accuracy. Moreover, the tide gauge was not located vertically beneath the satellite's pass, which may have introduced additional problems. Although the calibration procedure for ERS-1 is quite similar to this previous scenario, it differs in just these two points: (1) ERS-1 overflies the tide gauge directly (or at least within 600 m), (2) the tide gauge is located on an off-shore platform, thus avoiding corruption of the altimeter measurement by land masses in the footprint.

Figure 4.3 summarises the general data flow and processing steps involved in the ERS-1 radar altimeter calibration activity. Five separate categories can be identified:

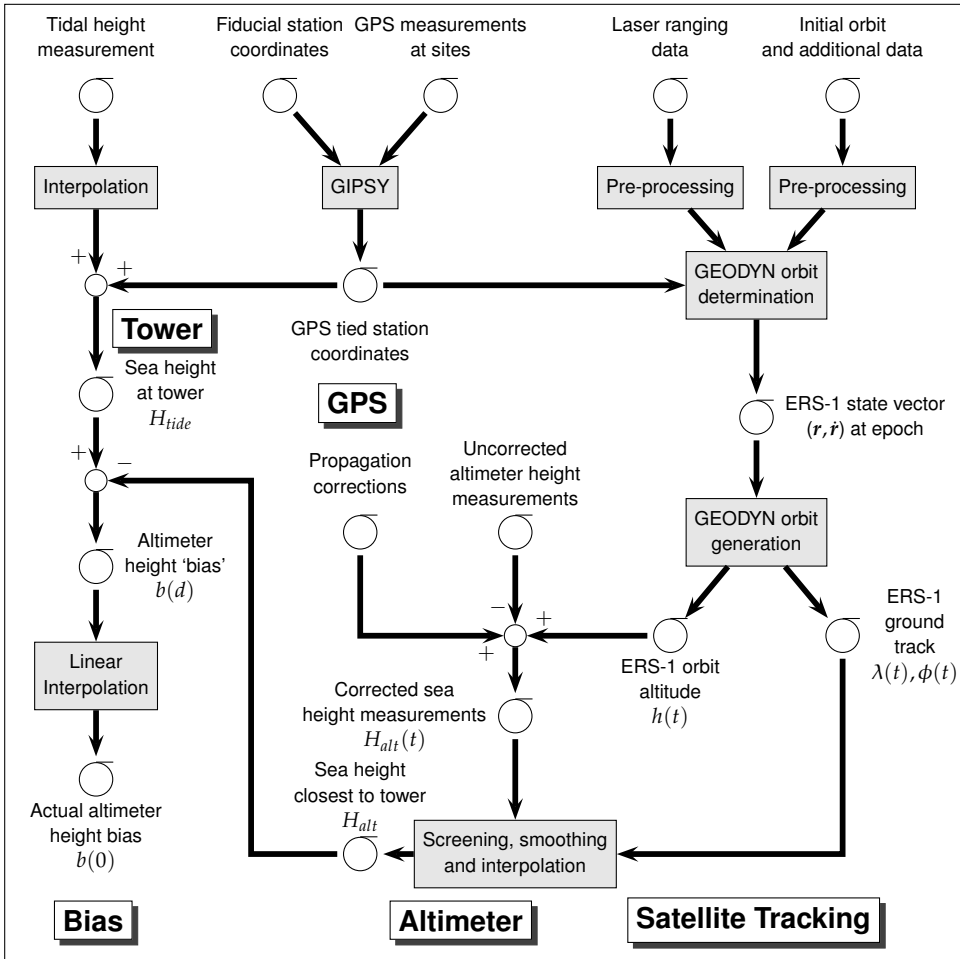


Figure 4.3 ERS-1 radar altimeter calibration processing diagram.

1. Tracking of ERS-1 by SLR systems provides the possibility to accurately determine the satellite's location and altitude. Unfortunately, PRARE failed soon after launch and was thus not able to contribute to the orbit determination. The details of the short-arc orbit determination are given in Section 4.3.
2. After they are corrected for internal and external delays, the altimeter range measurements are subtracted from the orbital altitude to form samples of the sea surface height along the satellite's track in the vicinity of the *Acqua Alta* tower. The corrections applied are instrumental (such as the internal delay of the radar pulse and the centre-of-mass offset), environmental (tropospheric and ionospheric delays, measured by equipment on board of the tower), or physical (Doppler effect and sea state bias). A smoothing and interpolation technique

(based on least-squares collocation, see Appendix A) was specially developed to determine the altimetric sea height closest to the tower. The processing of the altimeter measurements is further described in Section 4.4.

3. The tide gauge at the *Acqua Alta* tower produces an independent assessment of the sea surface height (see Section 4.5). Unfortunately, however, tide gauges usually measure a relative sea height, and not an absolute one. In case of the *Acqua Alta* tide gauge, the zero-level is just determined by the bottom of the paper chart on which the sea level is recorded, and was thus not well-defined, and certainly not linked to the 'outside world' prior to the calibration campaign. Consequently, the tide gauge reading could not have been compared directly with the altimetric sea height, and a link had to be established between the SLR station coordinates and the tide gauge.
4. GPS surveys has been used to tie the *Acqua Alta* tide gauge to the reference frame of the tracking systems. Additionally, local surveys have been conducted to refer the GPS markers to the origins of the laser ranging systems and the tide gauge. In that way both the sea height measured by the altimeter and by the tide gauge are brought into the same reference frame, and can be compared. For more details, see Section 4.2.
5. The difference between the tide gauge measurement and the altimetric sea level, corrected for the sea surface slope along the shortest line between the tower and the ERS-1 ground track, gives the altimeter measurement bias. As ERS-1 passed the *Acqua Alta* tower within 600 m, a correction can be computed from the local deflection of the vertical. In this approach it was assumed that the local sea surface slope equals the geoid slope, which is a realistic assumption since currents around the tower are small (around 3 cm/s) [e.g., *Malanotte-Rizzoli and Bergamasco*, 1983]. Alternatively, a linear fit through a number of bias estimates, determined along various tracks and at varying distances from the tower, provides an independent assessment of the local mean sea surface slope. In Section 4.6.2, both techniques will be tested.

A complete overview of the combination of all kinds of measurements into a single bias estimate is given in Section 4.6.

## 4.2 GPS campaigns and local surveys

One of the most critical elements in the ERS-1 Calibration Campaign was to locate the sea level measured at the *Acqua Alta* platform in the same frame of reference as the ECN laser systems. This required a link to be established between the tide gauge reading (being a relative measurement of which the datum is defined by the bottom of the paper chart on which it is recorded) and the actual tidal sea height,  $H_{tide}$ . Because this tie was foreseen to be the most important source of invariant errors in the bias estimation [*Francis and Duesmann*, 1988], considerable effort was devoted to the issue over several years. Especially the vertical position of the *Acqua*

*Alta* tower, which has a 1:1 relation with the ERS-1 altimeter bias estimate and is thus directly added (in root-sum-square sense) to the total error budget, requires a determination within a couple of centimetres.

The link between the tide gauge and the ECN sites was obtained in three steps, which will be discussed in detail in the next Sections:

1. Determine the exact position of the *Acqua Alta* platform in the laser frame of reference, in all three directions, by means of two independent GPS campaigns in 1990 and 1991;
2. Determine the relative positions of some reference markers on the ‘legs’ of the tower;
3. Record the tide gauge reading when the sea level is exactly at one of these markers.

Especially the last two steps proved to be formidable tasks.

#### 4.2.1 The October 1990 GPS campaign

In order to bring the *Acqua Alta* tower into the same reference frame as the SLR sites, a five-day GPS campaign was undertaken. From 14 to 19 October 1990, a number of GPS receivers of the calibration team were operated at the fixed SLR sites Grasse (2), Graz, Matera, Wettzell, and Zimmerwald, and at Monte Venda (2) and on the Venice Tower (2).

The GPS marker coordinates at the five fixed sites and at Monte Venda were tied to the markers of the laser systems by means of local surveying. The local ties include:

- A vector between the reference (SLR) monument (indicated by a four-digit number, *e.g.*, Monte Venda 7542) and the GPS monument over which the antenna is installed (*e.g.*, Monte Venda WM90);
- A vector between the GPS monument and a reference mark on the antenna;
- A vector between the reference mark and the antenna’s phase centre.

By the time the GPS observations were processed, however, it appeared that an additional local GPS survey was needed to tie the Monte Venda GPS marker WM90 to the SLR marker 7542 on the laser pad, which is located about 600 m away, too far to be surveyed by optical means. This major eccentricity was the result of the fact that the construction of the laser pad on Monte Venda, starting in November 1990, was cancelled after remains of an old monastery had been revealed during excavations. Therefore, the location of the laser site was moved to a close-by hill, named Baiamonte. Nevertheless, the current marker name ‘Monte Venda 7542’ was maintained. This short baseline was determined in April 1991 using two GPS receivers [Del Rosso, 1992].

Figure 4.4 presents a schematic illustration of the geodetic connection between the ECN laser network and the *Acqua Alta* platform. The SLR monuments of the



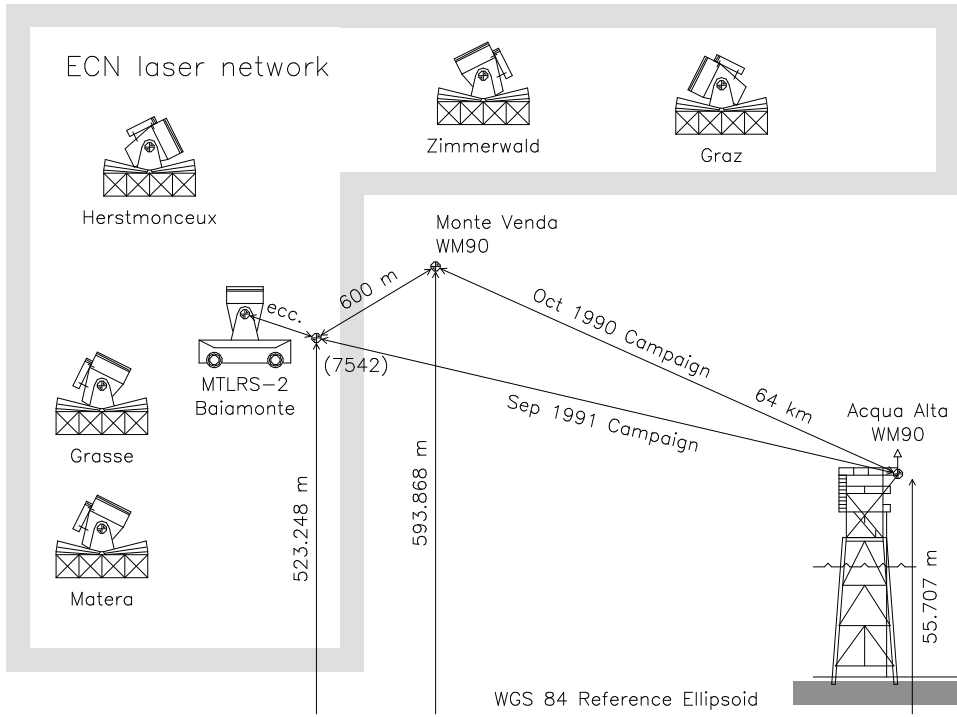


Figure 4.4 Schematic illustration of geodetic tie between the European Calibration Network (ECN) and the *Acqua Alta* platform. Heights of the relevant markers are given with respect to the WGS 84 reference ellipsoid, as derived from the average of the various GPS baseline solutions.

ECN laser systems themselves are connected through the DUT ERS90B coordinates solution, which is based on SLR tracking data to the LAGEOS satellite. This coordinate set is listed in Table 4.5 of Section 4.3, where it will be discussed in more detail.

Finally, all GPS measurements recorded by the various GPS receivers were used to solve for the coordinates of the GPS markers at Monte Venda and on the *Acqua Alta* tower; the coordinates of all other GPS markers were held fixed to the laser coordinates via the local ties. These data were processed independently at DUT and the Astrophysical Institute of the University of Berne (AIUB), using the GIPSY software developed at JPL and the Bernese GPS software, respectively.

### 4.2.2 The September 1991 GPS campaign

An additional GPS campaign was conducted by the Institute for Space Research in Graz from 2 to 4 September 1991. In contrast to the 'Large' 1990 Campaign, a GPS receiver was placed this time directly over the 7542 SLR marker.

These two sites and four fixed SLR sites were equipped with Ashtech dual-frequency receivers. In addition, data from the Rogue receiver at Kootwijk was included into the processing performed at AIUB.

### 4.2.3 GPS results

Table 4.1 summarises the GPS coordinate solutions for the Monte Venda 7542 and the *Acqua Alta* WM90 markers performed at DUT (for the 1990 Campaign) and AIUB (for both 1990 and 1991 Campaigns), as well as the SLR derived coordinates for the Monte Venda 7542 marker in the ERS90B system. The bottom part of this Table lists the three baseline components and height difference of the two markers for each individual solution and their weighted average.

Because the 7542 marker was not occupied during the 1990 Campaign, the local GPS-derived baseline between the WM90 was accounted for in order to transform the WM90 coordinates to the SLR marker. The eccentricity between the optical centre of the MTLRS-2 laser and the SLR marker, was dealt with accordingly. Both local vectors are presented in Table 4.2.

Year	Proc.	Marker	$x$ (m)	$y$ (m)	$z$ (m)	$H$ (m)
1990	AIUB	MV 7542	4 399 363.527	910 506.391	4 512 940.815	523.186
1990	DUT	MV 7542	4 399 363.582	910 506.368	4 512 940.800	523.210
1991	AIUB	MV 7542	4 399 363.564	910 506.408	4 512 940.772	523.183
1990	AIUB	AA WM90	4 386 229.603	973 073.288	4 512 012.437	55.634
1990	DUT	AA WM90	4 386 229.670	973 073.271	4 512 012.435	55.677
1991	AIUB	AA WM90	4 386 229.651	973 073.347	4 512 012.393	55.645
1990	AIUB	Baseline	13 133.924	-62 566.897	928.378	467.552
1990	DUT	Baseline	13 133.912	-62 566.903	928.365	467.533
1991	AIUB	Baseline	13 133.913	-62 566.939	928.379	467.538
Weighted average		Baseline	13 133.916	-62 566.913	928.374	467.541

Table 4.1 Solutions of Monte Venda 7542 and *Acqua Alta* WM90 marker, and their respective baseline, based on the 1990 and 1991 GPS Campaigns processed at AIUB and DUT. The solutions include local eccentricities between the monuments and antenna phase centre.

	North $x$	East $y$	Up $z$	Distance
MTLRS-2 optical centre	-2.649 2.759	0.091 0.664	1.355 -0.899	2.977
Monte Venda WM90	-659.263 530.485	-112.661 -5.258	70.584 -413.353	672.534

Table 4.2 Eccentricity of the MTLRS-2 optical centre and the Monte Venda WM90 marker ('A') from the main Monte Venda 7542 monument at Baiamonte (Marker 'O'). Values are in metres.

The baseline results compare favourably between the two groups at DUT and AIUB, and between the two campaigns. Especially the individual solutions for the most important component of the baseline, the height difference, range over less than 2 cm. The differences between the separate solutions for the absolute positions of the baseline endpoints are somewhat larger.

The average baseline solution, presented at the bottom of Table 4.1 will be used forthwith to tie the *Acqua Alta* tower to the ECN network, by adding this baseline to the SLR-derived Monte Venda 7542 coordinates. Comparisons between the 1990 and 1991 results, their formal errors and the repeatability of the daily solutions, suggest an accuracy of the vertical component of the baseline of about 2 cm. This figure easily meets the requirements set for the ERS-1 radar altimeter calibration.

#### 4.2.4 *Acqua Alta* tower survey

As discussed earlier, the analogue tide gauge of the ISDGM on the *Acqua Alta* tower does not record the absolute sea level (in the laser frame of reference), nor was it tied by any means to a physical position anywhere on the platform. However, this absolute reference, or at least a relative positioning of the sea level to any point on the tower (and finally to the GPS WM90 marker 'O'), is essential for the calibration. Subsequently the sea level is brought into the laser reference frame through the Monte Venda–*Acqua Alta* baseline.

Therefore, a local survey at the *Acqua Alta* tower was needed to refer the zero sea level height to the GPS marker on the platform. Thus the actual height of the water column in the tide gauge well (Section 4.5) had to be known when the tide gauge was reading a certain value. Figure 4.5 presents a sketch of the determination of the distance,  $s$ , between the GPS marker and the sea level (in the tide gauge well), which proved to be one of the most complicated links in the whole calibration chain.

It was realised that a direct measurement of this distance from the marker down to the sea level was not feasible, because the sea surface would never be sufficiently flat, and would not keep its position for an adequately long period to make redundant measurements. Therefore, at low tide, a small steel slightly sloping reference mark was welded on the structure of the tower close to the water level, such that it would be flooded when the tide would be rising (point T in Figure 4.5). When the sea level is exactly at the level of T, the distance  $s$  equals the distance  $c$  between the GPS marker O and the welded marker T. At that very moment the tide gauge is recording a relative sea level  $l_T$  on the scale of the paper chart, and is marked off, manually. Consequently, the distance  $s$  between the GPS marker and the actual sea level is given at any subsequent or previous moment by the distance  $c$  minus the sea level change  $d$ , which can be read from the tide record as  $l - l_T$ . At a convenient time, when marker T was above sea level, the vertical distance  $c$  was measured with a calibrated metre directly from the level of marker O downward, and, for redundancy, as a sum of two vertical stretches with respect to an intermediate mark M0 at the level of one of the platform terraces.

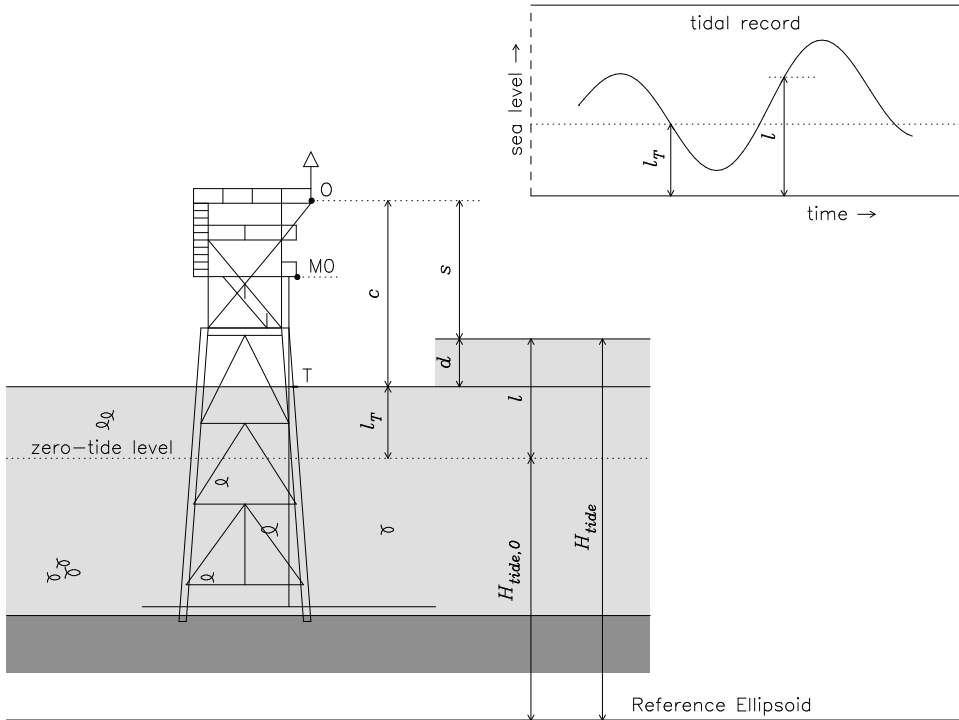


Figure 4.5 Schematic diagram of the determination of the absolute tidal sea level ( $H_{tide}$ ) from the tide gauge reading ( $l$ ) and local surveys on the *Acqua Alta* tower.

In fact, this process was performed twice, since two markers T (T1 and T2) were welded at different levels on the legs of the tower. A third marker was lost, after it was rammed by an unknown vessel, before the necessary measurements could be made. Finally, it was found that the distance between the WM90 marker and the sea level is given by the relation

$$s = 13.457 \text{ m} - l \quad , \quad (4.2)$$

where 13.457 m is the distance from the WM90 marker above the 'zero tide level', a fictitious position of the sea level corresponding to a reading of '0' on the tide gauge record.

This completes the link between the laser network and the sea level at the tower: the sea level is positioned relative to the GPS marker on the tower, and the location of the tower is determined relative to the Monte Venda monument, which, in turn, is embedded into the laser network by means of LAGEOS tracking data. This makes it convenient to write the absolute sea level height (in the laser frame of reference),  $H_{tide}$ , as the sum of the tide gauge reading,  $l$ , and the height of

the 'zero tide level',  $H_{tide,0}$

$$H_{tide} = H_{tide,0} + l \quad (4.3)$$

Consequently, the absolute height of the 'zero tide level' equates to

Absolute height of the Monte Venda 7542 marker	523.240	
Height of <i>Acqua Alta</i> WM90 wrt Monte Venda 7542	-467.541	
Height of 'zero tide level' wrt <i>Acqua Alta</i> WM90	-13.457	(4.4)
Absolute height of the 'zero tide level' ( $H_{tide,0}$ )	42.242	+

### 4.3 Orbit determination

On 26 July 1991, 9.7 days after launch, ERS-1 was manoeuvred into the 'Venice Orbit', a sun-synchronous near-polar orbit in which the ground-track retraced itself precisely after 3 days (43 orbital revolutions). This orbit, which was maintained until 13 December 1991, was phased such that the satellite crossed the Adriatic Sea every three days on an ascending (South-North) pass and overflowed the *Acqua Alta* oceanographic research platform within 1 km for calibration purposes.

The precise orbit for the calibration pass was computed in two steps. First, a long-arc solution was generated using quick-look normal points from a global network of satellite laser ranging systems. At the time these orbits had a radial orbit precision of around 1 metre (see Chapter 3).

Second, the long-arc orbit served as a priori information for the determination of a short-arc orbit (15 minutes in length) over the *Acqua Alta* tower and the ECN network. This procedure maximised the orbit accuracy over the *Acqua Alta* tower and minimised the possibility of obtaining an unrealistic or non-converging orbit solution. Once they had become available the short-arc orbits were based on high-quality full-rate SLR data.

To accurately track the satellite during its pass over the *Acqua Alta* tower, MTLRS-2 arrived on 17 April 1991 at Monte Venda in the Euganei Mountains near Padova (Italy). The distance between this laser site and the *Acqua Alta* tower is about 64 km. Between its arrival and the launch of ERS-1 the MTLRS-2 system had already tracked 48 passes of the geodetic satellite LAGEOS from this site. Until 18 September, when the system returned to The Netherlands, it tracked another 23 LAGEOS passes in between the first-priority ERS-1 passes. The locations of Monte Venda, the six other ECN laser sites and the ground tracks of ERS-1 in this area have been shown in Figure 4.1. The calibration pass is shown as a thick line.

For additional tracking, two PRARE ground stations were planned to be installed at Monte Venda and at the *Acqua Alta* tower. Before the ground stations were delivered, however, the PRARE equipment on board of ERS-1 had a serious malfunction, as mentioned earlier, and would not provide any useful tracking data. Therefore, the precise ERS-1 orbits had to be computed exclusively from the laser tracking data.

Configuration	A	B	C	D	E	F
Monte Venda	•		•		•	
3 fixed sites West of the track	•	•	•	•		
3 fixed sites East of the track	•	•			•	•
Error sources						
Dynamics	0	0	0	0	0	0
Coordinates	2	5	6	15	4	15
Measurements	3	3	7	11	5	11
Refraction	4	4	9	13	6	13
Root-sum-square error	5	7	13	24	9	24

Table 4.3 Contribution of errors in the measurements and dynamic models to the error in the ERS-1 computed altitude near Venice for different tracking system configurations. Values are listed in centimetres.

Although, in contrast to the Bermuda approach, none of the tracking systems is vertically beneath the calibration pass, the network of tracking systems is sufficient to ensure an accurate determination of the satellite's height. Many pre-launch simulation studies have been performed to investigate the radial orbit accuracy achievable with different tracking station configurations and applying realistic measurement and dynamic error models. Table 4.3 summarises part of the results for 6 possible laser tracking configurations. It shows that the tracking by the Monte Venda laser, which is closest to the pass over the *Acqua Alta* tower, is essential for achieving a high radial orbit accuracy, especially when some of the fixed laser systems are not able to track ERS-1. Since for this short-arc analysis no dynamic model errors propagate into the radial orbit error budget, it is clear that the dynamical determination of the orbit height is virtually equivalent to any geometrical solution. The results show that if sufficient laser tracking is available a radial orbit accuracy of better than 10 cm can be realised, which, at the time, was an extraordinary high precision.

To obtain the most accurate orbit determination, high-quality station coordinates were imperative. During the ERS-1 Radar Altimeter Calibration Campaign two alternative sets of coordinates were used.

- The ETRF-89 set (Table 4.4) is based on the 1989 set of SLR coordinates published by IERS. Since this set does not include the Monte Venda coordinates, these were obtained from the 1990 GPS Campaign.
- The ERS90B set (Table 4.5) is converted from the DUT ERS90 coordinates solution (Ron Noomen, priv. comm.). The SLR marker coordinates of Grasse, Graz, Herstmonceux, Matera and Wetzell are computed from LAGEOS full-rate normal points SLR data, covering the period September to December 1990. The SLR coordinates of Zimmerwald and Monte Venda are computed from quick-

Station	$x$ (m)	$y$ (m)	$z$ (m)	$H$ (m)
Monte Venda (7542) <sup>‡</sup>	4 399 363.596	910 506.474	4 512 940.862	523.280
Grasse (GRSL)	4 581 691.810	556 159.420	4 389 359.400	1322.887
Graz (GRZL)	4 194 426.720	1 162 693.899	4 647 246.558	539.442
Herstmonceux (HERL)	4 033 463.837	23 662.378	4 924 305.031	75.385
Matera (MATL)	4 641 965.093	1 393 069.975	4 133 262.234	535.866
Wetzell (WETL)	4 075 530.074	931 781.339	4 801 618.189	661.141
Zimmerwald (ZIML)	4 331 283.617	567 549.563	4 633 139.956	951.061
MTLRS-2 optical center*	4 399 366.355	910 507.138	4 512 939.963	524.635
<i>Acqua Alta</i> WM90 <sup>†</sup>	4 386 229.680	973 073.387	4 512 012.488	55.739

<sup>‡</sup> Based on the 1990 GPS Campaign; \* From the local eccentricity vector;

<sup>†</sup> From the *Acqua Alta* WM90 → Baiamonte GPS-baseline

Table 4.4 Coordinates of the SLR markers of the ECN lasers in the IERS ETRF-89 frame. The height  $H$  of the markers is with respect to the WGS84 ellipsoid.

Station	$x$ (m)	$y$ (m)	$z$ (m)	$H$ (m)
Monte Venda (7542)	4 399 363.5405	910 506.4189	4 512 940.8705	523.2395
Grasse (GRSL)	4 581 691.7390	556 159.3355	4 389 359.3075	1322.7647
Graz (GRZL)	4 194 426.6561	1 162 693.8029	4 647 246.5027	539.3422
Herstmonceux (HERL)	4 033 463.7612	23 662.2808	4 924 305.0003	75.3128
Matera (MATL)	4 641 964.9980	1 393 069.8736	4 133 262.2314	535.7728
Wetzell (WETL)	4 075 530.0019	931 781.2485	4 801 618.1924	661.0840
Zimmerwald (ZIML)	4 331 283.5505	567 549.5497	4 633 139.9254	950.9920
MTLRS-2 optical center*	4 399 366.2995	910 507.0829	4 512 939.9714	524.5944
<i>Acqua Alta</i> WM90 <sup>†</sup>	4 386 229.6245	973 073.3319	4 512 012.4965	55.6986

\* From the local eccentricity; <sup>†</sup> From the *Acqua Alta* WM90 → Baiamonte GPS-baseline

Table 4.5 Coordinates of the SLR markers of the ECN lasers in the DUT ERS90B frame (epoch: 1 September 1991). The height  $H$  of the markers is with respect to the WGS84 ellipsoid.

look LAGEOS SLR data, acquired until 25 June 1991. All solutions are converted to the epoch 1 September 1991.

The position of the *Acqua Alta* WM90 marker is merged into these reference frames by accounting for the baseline between this point and the Baiamonte SLR marker (7542). This baseline was determined from the 1990 and 1991 GPS Campaigns, discussed in Section 4.2. The *Acqua Alta* WM90 coordinates are obtained by subtracting the  $\{\Delta x, \Delta y, \Delta z\}$  components of the baseline (bottom of Table 4.1) from the Baiamonte coordinates.

For the computation of precise short-arc orbits over the *Acqua Alta* tower the tracking coverage of the ECN lasers during the ERS-1 zenith pass over the tower is, of course, extremely important. Table 4.6 lists the ECN laser systems which have acquired tracking data for the 15-minute arc, in which the satellite passes directly

Station	July		August									September						
	28	31	3	6	9	12	15	18	21	24	27	30	2	5	8	11	14	17
Monte Venda				•	•	•	•	•	•		•	•	•	•		•		•
Grasse		•					•	•	•								•	•
Graz					•						•		•	•		•		•
Herstmonceux	•	•				•	•	•	•	•	•	•		•				•
Matera		•				•												
Wetzell																		
Zimmerwald			•	•		•	•		•					•				•
Borowiec						•	•	•										
Potsdam	•	•		•		•	•		•	•	•	•	•	•		•	•	
Riga		•	•			•	•		•	•	•	•	•			•		
Altimeter		•	•			•	•	•	•	•	•	•	•	•		•	•	•
Analysed						•	•	•	•		•	•	•	•		•		•

Table 4.6 Tracking coverage by the ECN lasers and other European lasers during the ERS-1 passes over the *Acqua Alta* tower during the calibration campaign (28 July – 17 September 1991). The bottom lines also lists the availability of altimeter data over the Adriatic, and which passes have been analysed.

over the *Acqua Alta* tower. This Table illustrates the sparse tracking coverage at the time. The altimeter passes of 3 and 6 August were tracked by only one ECN laser, while in many cases only 2 or 3 out of the 7 lasers have acquired tracking data. The Monte Venda laser, which played a crucial role in the computation of the precise radial position of ERS-1 over the *Acqua Alta* tower, has tracked the satellite during all zenith passes after 3 August, except for the passes on 24 August, and 8 and 14 September. Since it is known that the orbit accuracy degrades rapidly as less stations track the satellite, it was decided to use only those passes, during which the satellite was tracked by the Monte Venda laser and at least three of the other ECN lasers.

From these arguments it may be concluded that the tracking coverage and the amount of tracking data from the ECN laser systems is certainly not optimal to compute precise short-arc orbits for all passes. Apart from that, on some of the passes the altimeter did not operate properly or did not provide any data. Consequently, eight of the eighteen passes have not been analysed, because either MTLRS-2 did not contribute to the tracking, or no altimeter data were available.

The short-arc orbit computations referred to in this Chapter are all based on the high-quality full-rate (FR) laser ranging data converted to normal points (NP). Like in the POD (Section 3.4.1), observations are corrected for any known internal or external delay of the laser pulse, and the geometrical offset from the satellite's centre-of-mass. The measurements are attached a system-dependent weight based on the root-sum-square of the system noise and an overall model error of 2 cm (Table 4.8). The geometric and dynamic modelling is described in Table 4.7. Note that the overall model error is significantly smaller than in the case of global long



<b>Measurement model</b>	
– Observations	Full-rate SLR data, converted to normal points.
– SLR corrections	Offset of LRR optical center wrt LRR geometrical center (6.1 cm), and the LRR geometrical center offset wrt nominal center of mass (see Table 3.1). Marini-Murray topospheric refraction.
– Data weighting	Station dependent (see Table 4.8).
– Speed of light	$c = 299\,792.458$ km/s.
– Editing	Cutoff elevation set at $20^\circ$ . Editing at 3.5 times $\sigma$ .
<b>Satellite model</b>	
– Mass	$m = 2377.13$ kg.
– Cross-section	From geometry table.
<b>Dynamic model</b>	
– Gravity Model	NASA/GSFC PGS-4591 model; $GM = 398\,600.4360$ km <sup>3</sup> /s <sup>2</sup> , $a_e = 6378.1370$ km, $1/f = 298.257$ .
– Solid Earth tides	Frequency-dependent <i>Wahr</i> [1981] model; permanent tide excluded according to IERS Standards [McCarthy, 1996].
– Ocean tides	NASA/GSFC PGS-4591 model.
– Third body attraction	Sun and Moon, JPL DE200 ephemeris.
– Atmospheric drag	Jacchia 1971 density model with daily values for $F_{10.7}$ and $A_p$ .
– Solar radiation	Pressure at 1 AU = $4.5783 \times 10^{-6}$ N/m <sup>2</sup> . Umbra, penumbra, and occultation by Moon modelled.
<b>Reference frame</b>	
– Station coordinates	DUT ERS90B SLR coordinates as described in Table 4.5.
– Earth rotation	Values from IERS Bulletin B.
– CIS	Mean equator and equinox of J2000.0.
– Precession	IAU 1976 (Lieske model).
– Nutation	IAU 1980 (Wahr model) plus Herring corrections.
– Plate motion	Not applied.
– Tidal uplift	Wahr model, including frequency dependent and permanent tides ( $h_2 = 0.609$ , $l_2 = 0.0852$ ).
– Ocean loading	Not applied.
<b>Estimated parameters</b>	
– State vector	Position and velocity at epoch.
– $C_D$ and $C_R$	Not adjusted (fixed to long-arc solution).

Table 4.7 Models and data used to compute the precise short-arc orbits of ERS-1 over the Adriatic and beyond.

arc, because gravity field model errors play virtually no role in the short-arc orbit determination.

Figure 4.6 portrays the SLR range residuals (*i.e.*, the observed minus the computed distance between satellite and tracking station) for six of the ten selected passes, and Table 4.9 lists the residual statistics. The RMS of the residuals, which indicates how well the computed orbit fits to the observations, ranges from 0.2–

Station	$\sigma_{system}$	$\sigma_{model}$	$\sigma$
Monte Venda	5.0	2.0	5.4
Grasse	2.0	2.0	2.8
Graz	1.0	2.0	2.2
Herstmonceux	4.0	2.0	4.5
Matera	12.0	2.0	12.2
Wetzell	1.0	2.0	2.2
Zimmerwald	6.0	2.0	6.3

Table 4.8 Weights attached to the normal points generated from the full-rate observations gathered by each of the ECN laser stations. The observation uncertainty ( $\sigma$ ) is the root-sum-square of the single-shot precision of the full-rate observations ( $\sigma_{system}$ ) and the overall model uncertainty ( $\sigma_{model}$ ). Uncertainties are in centimetres.

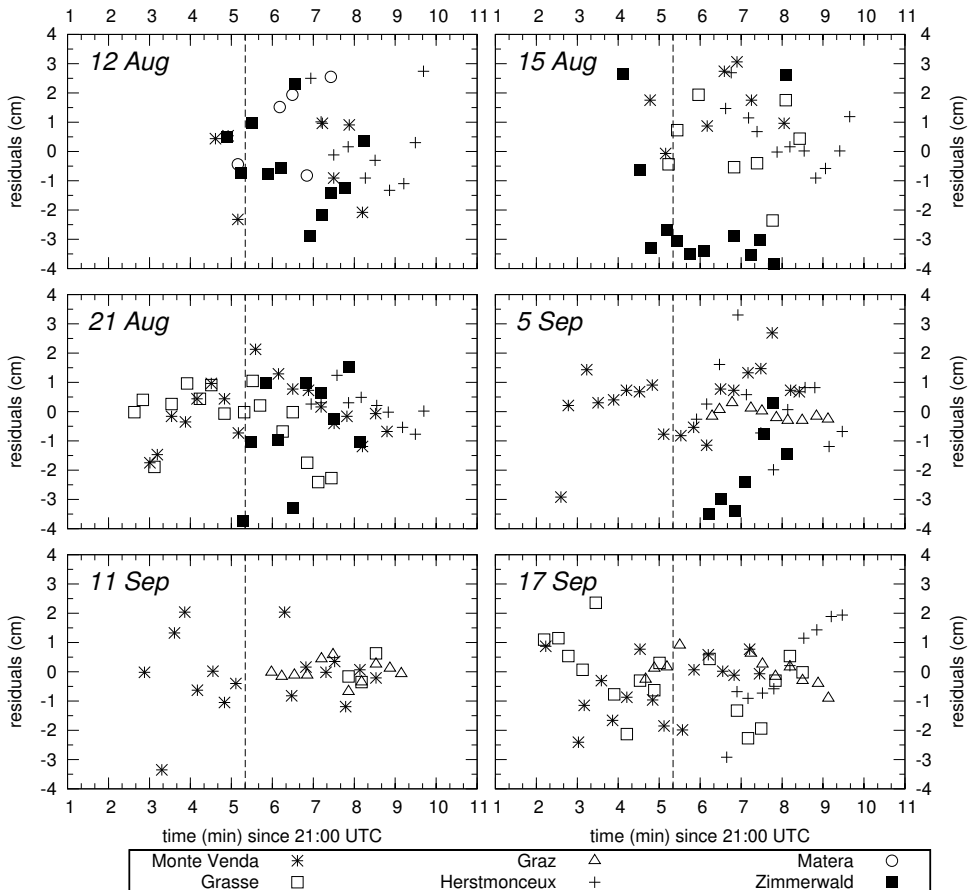


Figure 4.6 SLR normal point residuals for six processed passes in the ERS90B coordinate frame. The dashed vertical line indicates the time of the overflight of the *Acqua Alta* tower.

Date	Observation Period		Station	ERS90B Resid.				ETRF-89 Resid.			
	(UTC)	(sec)		FR	NP	mean	RMS	NP	mean	RMS	
12 Aug	21:04:27–21:08:21	233.9	Monte Venda	88	7	-0.4	1.3	7	-0.4	1.5	
	21:01:36–21:07:28	352.2	Matera	72	9	2.5	6.2	9	2.6	5.9	
	21:06:52–21:09:40	167.9	Herstmonceux	693	10	0.3	1.4	10	0.3	1.8	
	21:04:46–21:08:20	213.6	Zimmerwald	196	11	-0.5	1.5	11	-0.4	1.6	
	Total			1049	37	0.5	3.3	37	0.5	3.2	
15 Aug	21:04:42–21:08:23	221.0	Monte Venda	172	7	1.6	1.9	7	2.0	2.4	
	21:04:55–21:09:11	256.4	Grasse	87	8	0.1	1.3	8	0.5	1.5	
	21:05:47–21:09:42	234.8	Herstmonceux	551	11	0.5	1.1	11	0.6	2.4	
	21:03:53–21:08:18	264.6	Zimmerwald	469	13	-2.3	3.2	13	-3.3	4.4	
	Total			1279	39	-0.3	2.2	39	-0.5	3.1	
21 Aug	21:02:57–21:08:56	359.3	Monte Venda	1367	18	0.0	1.0	18	0.4	0.8	
	21:02:03–21:09:17	434.0	Grasse	315	17	0.0	1.6	18	0.1	2.4	
	21:06:45–21:09:42	177.5	Herstmonceux	926	10	0.2	0.5	10	0.1	1.9	
	21:05:11–21:08:19	188.1	Zimmerwald	320	10	-0.6	1.8	10	-1.9	3.1	
	Total			2928	55	-0.1	1.3	56	-0.2	2.1	
5 Sep	21:02:03–21:08:42	398.5	Monte Venda	700	20	0.7	1.8	21	0.4	2.3	
	21:06:17–21:09:13	176.0	Graz	226	10	-0.1	0.2	10	-0.1	0.3	
	21:05:52–21:09:40	228.2	Herstmonceux	757	12	0.2	1.3	12	0.1	1.3	
	21:06:09–21:08:14	125.5	Zimmerwald	437	7	-2.0	2.4	7	-0.7	2.0	
	Total			2120	49	0.0	1.6	50	0.1	1.8	
11 Sep	21:02:51–21:08:35	344.0	Monte Venda	270	16	0.0	1.1	16	-1.6	3.2	
	21:07:41–21:10:39	177.6	Grasse	231	3	0.0	0.4	3	1.1	1.3	
	21:05:57–21:09:12	194.8	Graz	255	11	0.0	0.3	11	0.2	0.4	
	Total			756	30	0.0	0.8	30	-0.7	2.4	
17 Sep	21:02:06–21:07:43	336.8	Monte Venda	557	18	-0.4	1.9	18	-4.6	5.3	
	21:01:30–21:10:17	527.4	Grasse	706	18	0.1	1.8	18	0.9	2.1	
	21:04:38–21:09:14	275.6	Graz	233	11	0.0	0.5	11	0.6	1.1	
	21:06:39–21:09:36	176.5	Herstmonceux	664	10	0.1	1.5	10	-0.3	0.6	
	21:08:03–21:08:17	13.1	Zimmerwald	18	1	-5.3	5.3	1	-8.6	8.6	
	Total			2178	58	-0.2	1.7	58	-1.2	3.4	
Total of all 10 overflights			Monte Venda	4071	118	0.2	1.7	118	-0.7	2.9	
			Grasse	2104	66	0.0	1.7	67	0.4	2.0	
			Graz	1572	64	-0.0	0.4	64	0.1	0.6	
			Herstmonceux	4526	80	0.2	1.1	80	0.1	1.4	
			Matera	72	9	2.5	6.2	9	2.6	5.9	
		Zimmerwald	1440	42	-1.4	2.5	42	-1.9	3.4		
Total			13785	379	0.0	1.8	380	-0.3	2.4		

Table 4.9 Statistics of the SLR normal point residuals (in centimetres) from tracking ECN laser systems, per pass and per station, and for six orbit solutions in both the ERS90B and ETRF-89 coordinate frames (FR = total number of full-rate measurements; NP = number of accepted full-rate normal points).

Date	TCA (UTC)	$H$ (m)	$\Delta H$ (m)
12 Aug	21:05:21.9102	784 271.281	0.048
15 Aug	21:05:22.8833	784 337.910	0.012
18 Aug	21:05:23.6533	784 297.794	0.027
21 Aug	21:05:22.9070	784 244.107	0.039
27 Aug	21:05:22.2835	784 332.726	0.058
30 Aug	21:05:22.8474	784 310.359	0.032
2 Sep	21:05:22.1490	784 293.966	0.045
5 Sep	21:05:20.5340	784 279.569	0.038
11 Sep	21:05:21.1293	784 329.485	0.022
17 Sep	21:05:20.8607	784 294.740	0.101
Total		Mean	0.042
		RMS about mean	0.026
Total (except 17 Sep)		Mean	0.036
		RMS about mean	0.013

Table 4.10 Altitude of the ERS-1 center of mass ( $H$ ) above the WGS84 reference ellipsoid (ERS90B solution) at the time of the closest approach (TCA) to the *Acqua Alta* tower and the altitude difference ( $\Delta H$ ) between the ETRF-89 and ERS90B solutions.

6.2 cm per pass with an average of 1.9 cm, and consists for a large part of remaining system noise in the normal points. The MTLRS-2 system at Monte Venda performs very well with an RMS of fit between 1.0 and 2.5 cm and an average of 1.9 cm. Another important parameter is the mean of the residuals. If stations have a high mean residual for one pass, this means either improper coordinates (*e.g.*, a vertical shift) or an incorrect orbit solution. If this offset is persistent, then the coordinates must be suspect. However, this does not seem the case for any of the stations, giving an indication that both the orbit and the coordinates are accurate.

In order to make a quantitative assessment of the radial orbit accuracy, the orbit determination is also run with the ETRF-89 coordinate set. As can be seen from Table 4.9, this solution gave slightly worse residual statistics than in the former solution, from which we can conclude that the ERS90B solution is a bit more consistent. The level of accuracy can be quantified by comparing the radial position of the satellite over the *Acqua Alta* tower (which is of the most importance) for all ten passes, listed in Table 4.10.

Surprisingly, the radial orbit difference on 17 September is significantly different from those on other passes. This is not so remarkable if we compare this to Table 4.9. Also here the residuals differ considerably between the two coordinate sets, which makes the ETRF-89 solution of 17 September rather suspect. For the remaining passes, the average difference between the satellite altitude solutions in either frame is 3.6 cm, which corresponds to a similar difference in the height solution of the *Acqua Alta* tower GPS marker (3.2 cm). Hence, this hardly affects the altimeter bias determination. However, the RMS of the radial orbit difference about this mean, being 1.3 cm, is a clear indication of the orbit uncertainty caused

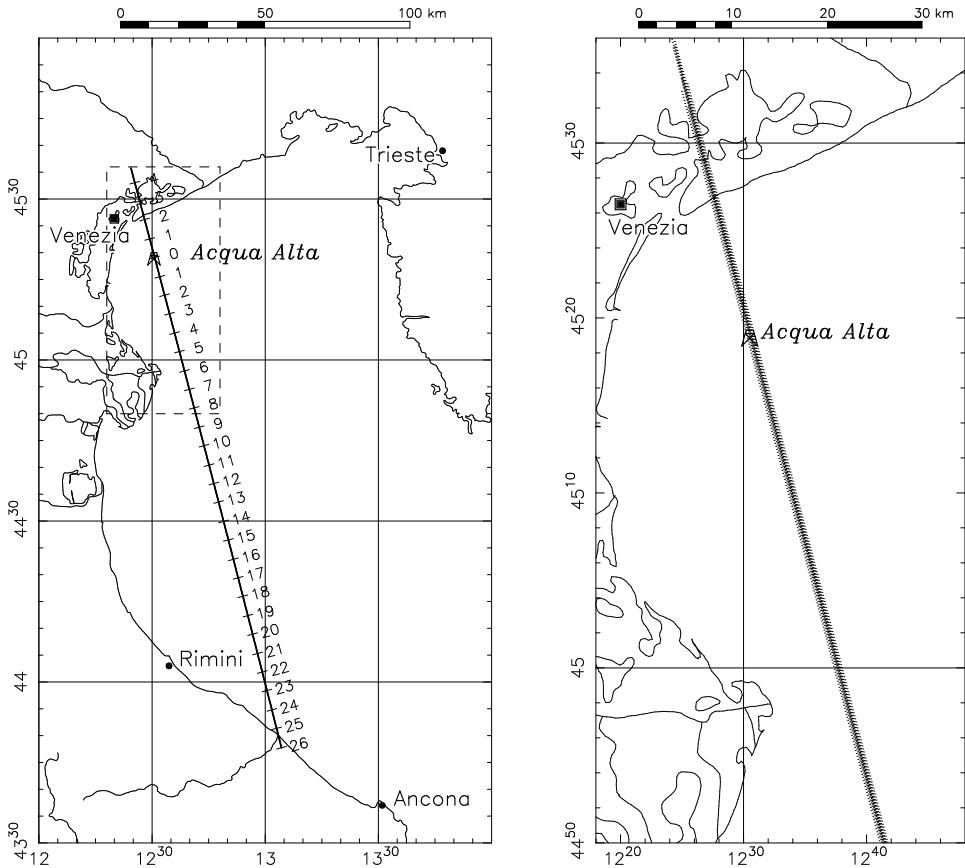


Figure 4.7 Ground track of the ERS-1 calibration pass over the Adriatic. The numbers along the ground track in the left plot indicate the number of seconds till the *Acqua Alta* overflight. The right plot shows the locations of all individual measurements along the ten calibration passes in the vicinity of Venice.

by uncertainties in the station coordinates. Since the ETRF-89 and ERS90B sets are independent, we may assume the uncertainty in either solution to be  $1/\sqrt{2}$  times this, or roughly 1.0 cm. ERS90B, being slightly more consistent than ETRF-89, produces less than 1 cm radial orbit error.

## 4.4 Altimeter measurements

The ground-track of the calibration pass over the northern Adriatic Sea and the *Acqua Alta* platform is shown in Figure 4.7. On this pass ERS-1 gathers about 25 seconds worth of altimeter data over the Adriatic Sea, extending over about

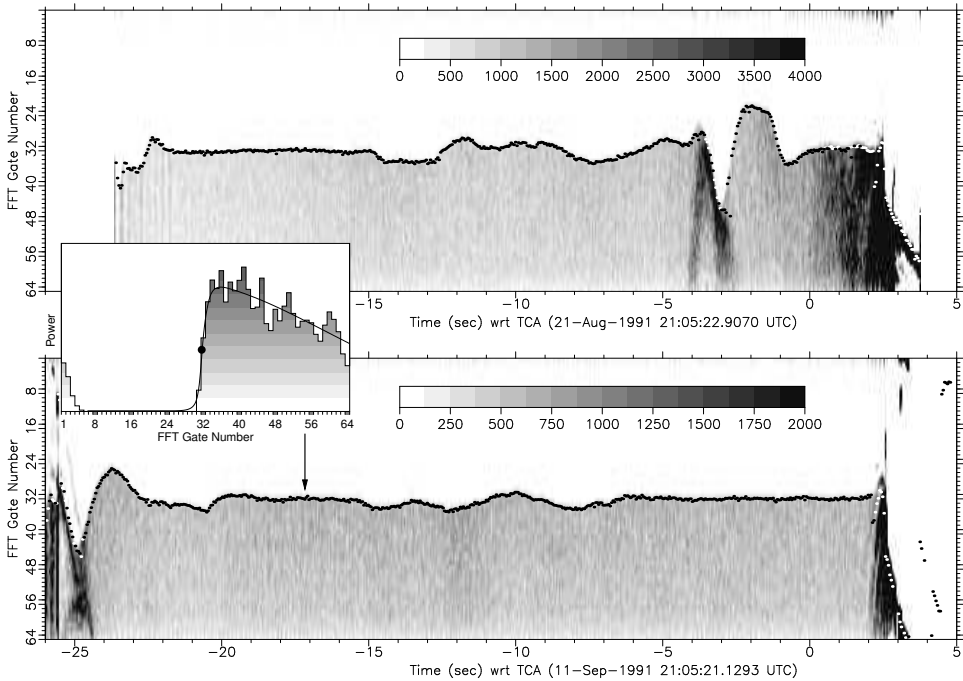


Figure 4.8 Radar altimeter waveforms over the Adriatic Sea along the calibration passes of 21 August (top) and 11 September 1991 (bottom). The waveforms are stacked from left to right according to the time relative to the tower overflight. Every vertical section pertains to one 20-Hz measurement. The power in each of the 64 spectral components is then indicated from top to bottom by a grey shade. The dots indicate the tracking points that determine the altimeter range. The corresponding position of the satellite is shown in Figure 4.7.

170 km South to 30 km North of the platform. The calibration analyses do not use the 1-per-second averaged altimeter readings, which are generally used by the ERS-1 data users community, but the full 20-per-second series of original height observations. To improve their accuracy, the individual radar echoes received by the satellite are carefully reprocessed at ESTEC. The tracking loop rapidly picks up the sea returns as the satellite passes the beaches between Rimini and Ancona, usually within one second, and maintains lock even beyond the *Laguna Veneta*. It is also apparent from this Figure 4.7 that the ground-track did not always pass directly over the platform; the overall cross-track spread is about one kilometre.

Figure 4.8 displays the waveforms of some of the 20-Hz measurements over the Adriatic Sea along the calibration passes of 21 August and 11 September 1991. The plots show the spectral power in each of the 64 spectral components (gates) of the signal received by the altimeter, averaged over 50 pulses (chirps), as a function

of the time,  $t$ , relative the platform overflight. The corresponding position of the satellite is shown in Figure 4.7.

Although the altimeter was operating in *Ocean Mode* during the entire pass, it also made some successful acquisitions over land. The first waveforms of the pass of 11 September ( $t < -25$  seconds in Figure 4.8) are typical land echos, acquired over the flat land near the shore North of the Apennines.

The next second of measurements are a mixture of land and sea echos, and can not be used as valid height measurements. The first perfect ocean waveforms are obtained around  $t = -24$  seconds. Note how the tracking loop pans the window to the right position, such that the leading edge of the waveform is around gate number 32. Some eighteen seconds later the ground track passes the delta of the river Po within about 8 km. Fortunately, the land is very flat and has a maximum elevation of only 2 m and remains unnoticed in the pass of 11 September. The pass of 21 August, however, located about 500 m more to the west is clearly affected right at this point (Figure 4.8). At  $-6.5$  seconds, the tracker locks onto a highly specular feature that entered the range window half a second earlier. On the other hand, there is no indication of any contamination of the waveforms by the *Acqua Alta* platform.

Finally, around  $t = 1.5$  seconds, the waveforms become distorted by echoes from land masses in the *Laguna Veneta*. So at least some thirty valid 20-Hz measurements are obtained after the overflight of the platform.

#### 4.4.1 Altimeter data processing per pass

With the altimeter data passes over the *Acqua Alta* tower some problems were encountered. During the first pass (28 July) no altimeter data were taken, due to a parameter setting error in one of the altimeter computers. The second pass (31 July) did produce altimeter data, but the output from the on-board tracker showed some disturbances due to specular echoes from the calm sea. The wave height and wind speed altimeter products indicated significant 'glassy' calm patches. A least-squares waveform fit of the data at ESTEC has largely eliminated these disturbances. The altimeter pass on 3 August, and some of the passes at later dates, again showed these disturbances, but the least-squares tracker applied at ESTEC to re-track the altimeter waveforms showed negligible degradation.

The altimeter data on the ten passes mentioned in Section 4.3, which had a reasonable ECN laser tracking geometry and good-quality altimeter measurements, have been processed to determine the ERS-1 altimeter bias. First, all altimeter height observations are corrected for:

- offset of the altimeter reference point (the centre of the antenna aperture plane) with respect to the nominal centre-of-mass of the satellite. This distance is 851.9 mm;
- instrument internal delay of the radar pulse. The measured value for this delay was subtracted from the two-way travel time of the echoes;

- Doppler shift due to the vertical velocity of the satellite with respect to the sea surface (see Section 4.4.2);
- Electro-Magnetic (EM) bias derived by taking 2% of the wave height measured in-situ. Because the sea-state in this area is usually very low, the altimeter was not able to reliably measure the wave heights;
- tropospheric and ionospheric propagation delay of the altimeter signal. Both the dry and the wet component of the tropospheric delay are measured by a zenith looking microwave radiometer and other meteorological instruments placed on the *Acqua Alta* tower. Although these corrections only apply to altimeter measurements taken vertically above the tower, the same corrections are applied to all measurements over the Adriatic sea. Furthermore, a local GPS receiver provides the ionospheric correction through the processing of dual-frequency GPS observations. Additionally, ionospheric delays were computed from the Faraday Rotation measured at Firenze (Italy), and TEC measurements provided by the DORIS system on SPOT 2.

Then, the sea surface height profile  $H_{alt}$  along the track over the Adriatic Sea is determined by subtracting all 20-per-second fully-corrected altimeter range measurements  $h_{alt}$  from the orbital height  $H_{orb}$ .

Since none of these ‘full-rate’ sea surface heights, which are separated by about 340 m along track, will actually be made over the tower, and their noise is about 8 cm instead of the 2 cm quoted for the 1-per-second averages, a smoothing and interpolation has to be performed. The smoothing and interpolation scheme is based on the technique of least-squares collocation, also known as objective analysis, which makes optimal use of *a priori* information of the expected ‘shape’ of the altimeter profile. The spatial covariance function was taken to be a homogeneous and isotropic one, based on the expected deviations of the sea level from the 360×360 Ohio State University geoid model OSU91A [Rapp *et al.*, 1991]. For longer wavelengths (above the spatial resolution of the geoid model) the covariance function was determined by the calibrated degree standard deviation of this model, and for short wavelengths (down to 20 km) by Kaula’s rule of thumb. The technique of collocation and its implementation is described in Appendix A.

The altimetric sea height profiles along two of the ten passes are shown in Figure 4.9. In order to remove the major slopes in the sea height profiles, they are all plotted with respect to the OSU91A geoid model. The markers in these plots represent the reprocessed samples. Circles indicate samples used to form the smoothed sea surface profile (curved full line). Triangles and crosses indicate erroneous measurements. The time is measured relative to the time of closest approach to the *Acqua Alta* tower. The shaded areas show when the satellite is over land. The bit of sea in between is the *Laguna Veneta*.

In order to obtain a reasonable interpolation of the sea height near the tower in case there are only little proper altimeter measurements in the vicinity (such as on 15 and 21 August), the ‘average’ of the other eight profiles was used as a reference. This reference profile was determined in three steps:



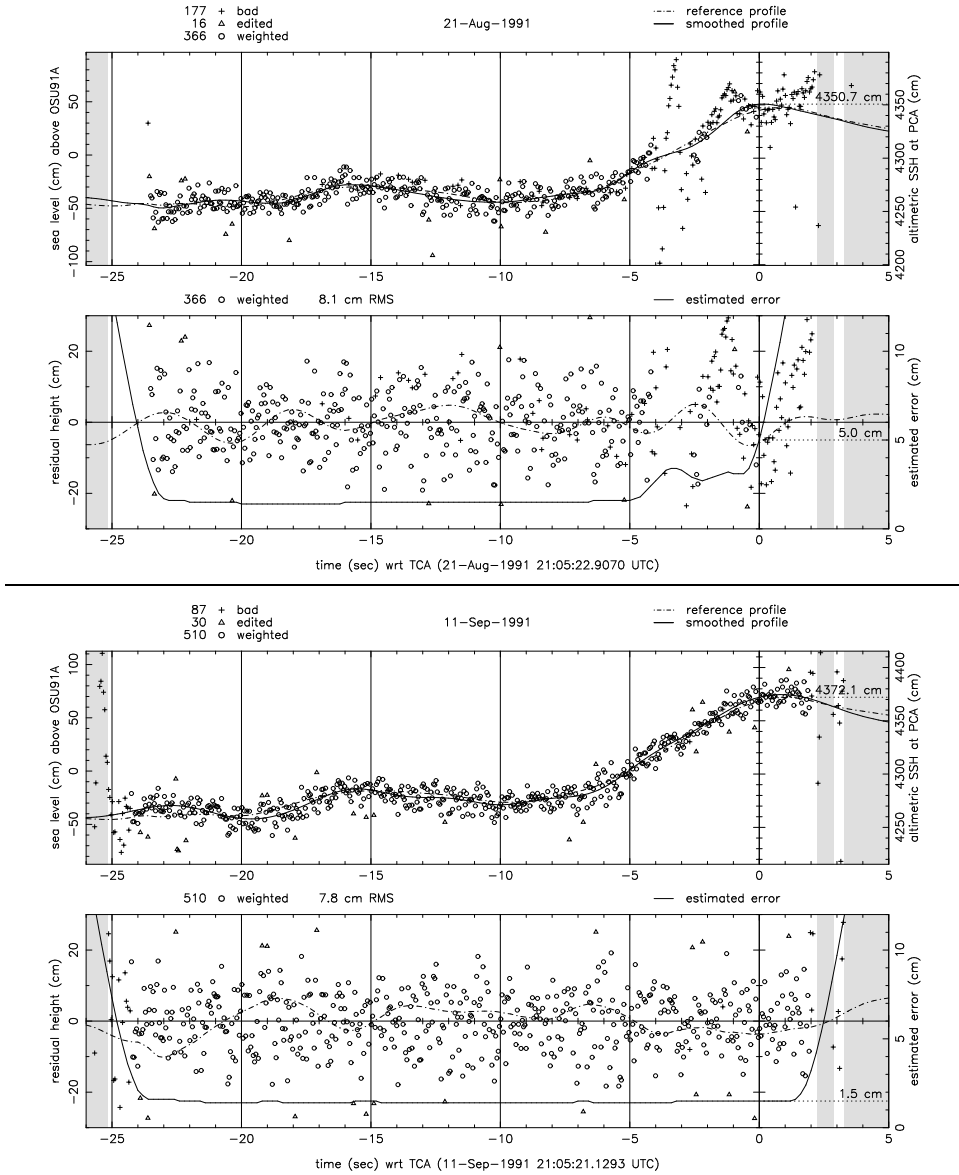


Figure 4.9 Smoothing and interpolation of the relative sea surface height derived from ERS-1 20-per-second altimeter samples during overflights of 21 August and 11 September 1991. The circles indicate samples used to form the smoothed sea surface profile (curved full line). Triangles and crosses indicate erroneous measurements. The time is measured relative to the time of closest approach to the *Acqua Alta* tower. The upper panel of each pair shows the smoothed altimetric sea surface height, and the lower panel the residuals and estimated interpolation error.

1. a tilt and bias was fitted through each profile and then subtracted;
2. the weighted mean of the eight profiles is computed (the weight along each track is determined by the estimated interpolation error);
3. the thus obtained profile is fitted through the weighted altimetric sea height samples along each track while adding a solved-for tilt and bias, thus obtaining ten reference profiles with equal shapes, but a different origin and slope.

Although the altimeter measurements have a noise of about 8 cm, the interpolation of the sea level can be performed up to an accuracy of about 2 cm. The interpolated value and the estimated error can be read from the right hand axes in Figure 4.9.

#### 4.4.2 Doppler correction

The vertical relative velocity of the satellite will cause a Doppler shift in the frequency of the returned chirp. Given the way the ERS-1 altimeter operates, registering received frequency as a function of time, a Doppler shift directly introduces an error in the altimeter range measurement [e.g., Chelton et al., 2001].

For a given vertical velocity  $\dot{h}$  and transmitted frequency  $f$  (13.8 GHz), the Doppler shift  $\Delta f$  on the two-way signal equals

$$\Delta f = -2\frac{\dot{h}}{c}f$$

The minus sign indicates that the frequency decreases for positive altitude rates. A negative change in received frequency with respect to the deramping chirp, having a decreasing frequency, will have the same effect as if the pulse was received earlier, i.e., decrease the intermediate frequency. An increase of the received frequency will, likewise, lead to a travel time delay (see Figure 1.3 in Chapter 1). The resulting two-way travel time delay thus equals

$$\Delta\tau = \Delta f \frac{T}{B}$$

where  $B$  is the chirp bandwidth (330 MHz), and  $T$  the chirp duration (20  $\mu$ s). This two-way time delay then corresponds to a one-way range error

$$\Delta h = \frac{c\Delta\tau}{2} = -\dot{h}f \frac{T}{B} \quad , \quad (4.5)$$

and should be removed from the measured range to correct for the Doppler effect.

Over the *Acqua Alta* tower the altitude rate of the satellite is approximately 12.5 m/s, which results in a Doppler shift of about -10.5 mm to be subtracted from the altimeter range measurements.

## 4.5 Tide gauge measurements

The sea level at the *Acqua Alta* tower is constantly monitored by a fast-response tide gauge [Cavaleri and Curiotto, 1979]. This analogous gauge has been operated by the ISDGM since 1977 and is very suitable for the calibration, since its attenuation properties are somewhat similar to the altimeter. As the altimeter averages the sea surface over a footprint with a diameter of approximately 8 km over calm water, the tide gauge filters more than 99% of the wind driven waves in another way. By connecting four narrow tubes with their openings spread out over a radius of 15 m to a wide tide gauge well, the tide gauge reading effectively becomes a spatio-temporal average. In addition, by placing the inlets at the sea bottom, it takes advantage of the wave attenuation with depth. Nevertheless, the gauge responses almost unitary to sea level changes with oscillation periods longer than 5 minutes. The overall RMS error is assessed at about 2 cm.

## 4.6 The results

As described in Section 4.1.2 the sea level profile for each of the altimeter passes is computed by subtracting the measured altimeter height from the orbital altitude. This orbital height is computed from SLR data in two steps: a global long-arc and local short-arc. The derived altimetric sea level is compared to the sea level recorded by the tide gauge to form an altimeter bias estimate for each pass. Finally, the ERS-1 bias is determined by means of a linear interpolation of the various bias estimates per pass toward the *Acqua Alta* tower.

### 4.6.1 Error budgets

Errors which may occur in the final radar altimeter bias estimate consist of two types. Systematic errors (also called *static* or *bias errors*) are always present and affect all passes to equal extent. They are, for instance, caused by measurement biases or errors in models, like (relative) station coordinate offsets. The other type of errors are the non-static (random or noise) errors, which differ from pass to pass and are uncorrelated. Increasing the number of calibration passes, and hence the number of bias estimates, reduces the effect of this type of errors. The total budget of the non-static errors can be derived from the scatter of the pass-by-pass bias estimates.

Table 4.11 lists the contribution of errors in the measurements and models leading to the single-pass bias estimates. These budgets are split up in: those affecting the orbit determination, those affecting the altimeter measurement, and those affecting the tidal sea surface height measurement.

As far as the orbit determination is concerned, the contribution of errors in the station coordinates was assessed in Section 4.3 at the 1 cm level. In this respect it is to be mentioned that any shift in the entire station coordinate frame has no effect on

Entity	Method	Static error	Random error
<b>Tide Gauge</b>			
Recorded sea level	Analogue tide gauge	0.0	2.0
Height of zero tide level wrt GPS marker WM90	Local survey	2.0	–
Height of GPS marker WM90	GPS	2.0	–
Local solid Earth tide	Wahr Model	1.0	1.0
<b>Orbit</b>			
Dynamics	(See Table 4.7)	0.0	0.0
Station coordinates	ERS90B coordinate set	1.0	1.0
Measurement noise and biases		0.0	2.0
Refraction corrections	Marini-Murray model	0.0	2.0
<b>Altimeter</b>			
Acquisition	Radar altimeter	0.0	2.0
Noise propagating through smoothing	Collocation	0.0	2.0
Ionospheric delay	GPS	0.0	3.0
Tropospheric delay	Radiometer	0.0	3.0
CoM correction	Geometry	0.1	–
Sea state bias	Radar altimeter	0.0	2.0
<b>Bias estimate per pass</b>	<i>Root-sum-square</i>	3.2	6.6

Table 4.11 Estimated errors of the various entities building up the bias estimates per pass. Both the static error and precision are given in centimetres.

the radar altimeter bias estimate, since we are dealing with relative distances and altitudes, and, in principle, not with the absolute altitude reference. Only ‘friction’ in the SLR coordinate set, caused by errors in some off the station coordinates, and in particular those of the Baiamonte (7542) site, may contribute to static errors in the altimeter bias estimates.

The measurement corrections on the altimeter range and SLR measurements are likely to be unbiased. The solid Earth tide model has a global validity and may have small local imperfections of less than 1 cm. But most important are errors in invariant entities like the GPS-tie between the SLR network and the *Acqua Alta* tower, the local tie between the ‘zero tide level’ and the GPS marker, and (to minor extent) the centre-of-mass offset of the radar altimeter reference point.

The overall uncertainty due to static errors is estimated to be  $\pm 3.2$  cm.

## 4.6.2 The final result

A compilation of all relevant values leading to the ten independent bias estimates which have been derived during the calibration campaign is listed in Table 4.12.

- The sea level recorded by the tide gauge on the *Acqua Alta* tower is added to the zero reference height of the gauge, which is a fictitious marker on the *Acqua Alta* tower that indicates where the sea level is when the gauge is indicating ‘0’.

Date	12 Aug	15 Aug	18 Aug	21 Aug	27 Aug	30 Aug	2 Sep	5 Sep	11 Sep	17 Sep
Time (sec. past 21:05 UTC)	21.9102	22.8833	23.6533	22.9070	22.2835	22.8474	22.1490	20.5340	21.1293	20.8607
Location wrt tower (m East)	302	32	-287	-118	175	15	122	508	350	199
<b>Tracking</b>										
Monte Venda	•	•	•	•	•	•	•	•	•	•
Grasse		•	•	•					•	•
Graz					•		•	•	•	•
Herstmonceux	•	•	•	•	•	•		•		•
Matera	•									
Zimmerwald	•	•		•				•		•
<b>Tide gauge</b>										
Recorded sea level	1.040	0.703	0.774	0.924	1.180	0.718	0.634	0.958	1.075	0.749
Height of zero tide level wrt GPS marker WM90					-13.457					
Height GPS marker WM90					55.699					
Local solid Earth tide	-0.091	-0.111	-0.099	-0.061	-0.043	-0.104	-0.121	-0.038	-0.038	-0.068
Tidal SSH at tower	43.191	42.833	42.917	43.104	43.378	42.855	42.754	43.162	43.279	42.922
<b>Altimeter</b>										
Nr. of alt. measurements	579	559	586	559	595	579	579	559	627	579
<i>idem</i> (weighted)	499	85	470	366	422	282	228	487	510	466
RMS of residuals	0.079	0.080	0.077	0.082	0.085	0.083	0.071	0.074	0.078	0.078
Orbital altitude (784 000+)	271.281	337.910	297.794	244.107	332.726	310.359	293.966	279.569	329.485	294.740
Altimeter range (784 000+)	229.364	296.534	256.263	202.242	290.653	268.766	252.469	237.616	287.490	253.107
Ionospheric delay	0.026	0.025	0.038	0.040	0.055	0.023	0.029	0.033	0.030	0.048
Dry+wet tropo delay	2.542	2.508	2.509	2.461	2.520	2.457	2.513	2.502	2.551	2.556
Doppler range error	-0.010	-0.010	-0.010	-0.010	-0.010	-0.010	-0.010	-0.010	-0.010	-0.010
CoM. correction					0.852					
EM bias	0.009	0.002	0.011	0.003	0.017	0.016	0.010	0.005	0.007	0.004
Altimetric SSH	43.632	43.049	43.227	43.507	43.803	43.227	43.187	43.631	43.721	43.379
<b>Error estimates (1<math>\sigma</math>)</b>										
Orbital altitude	0.020	0.020	0.030	0.015	0.030	0.030	0.030	0.020	0.025	0.020
Sea level	0.005	0.004	0.004	0.007	0.005	0.006	0.003	0.009	0.005	0.005
Iono/tropo	0.018	0.020	0.041	0.022	0.025	0.011	0.010	0.010	0.020	0.020
Interpolation	0.014	0.182	0.015	0.050	0.015	0.015	0.015	0.015	0.015	0.016
Total $\sigma$	0.031	0.184	0.053	0.057	0.042	0.036	0.035	0.029	0.036	0.033
<b>ERS-1 altimeter bias estimate</b>										
From single pass	-0.441	-0.216	-0.310	-0.403	-0.425	-0.372	-0.433	-0.469	-0.442	-0.457
Difference from fit	-0.020	0.201	0.102	0.011	-0.006	0.044	-0.015	-0.044	-0.020	-0.037
Fit: bias					-0.416					
Fit: tilt (m/km)					-0.016					
<b>Additional information</b>										
Defl. of vertical (SN, ")					-3.87					
Defl. of vertical (WE, ")					-2.48					
Ground speed (km/s)	6.724	6.724	6.724	6.724	6.724	6.724	6.724	6.724	6.724	6.724
Orb. altitude rate (m/s)	12.462	12.375	12.364	12.357	12.530	12.513	12.500	12.490	12.539	12.521
Azimuth of track ( $^{\circ}$ )	-14.816	-14.815	-14.815	-14.816	-14.814	-14.813	-14.813	-14.814	-14.811	-14.811
Geoid height wrt tower	0.005	0.001	-0.005	-0.002	0.003	0.000	0.002	0.008	0.006	0.003

Table 4.12 Parameters and measurements at the point of closest approach to the *Acqua Alta* tower, leading to the individual bias estimates per pass. Values are in metres, unless otherwise indicated.

This level was determined to be 13.457 m below the GPS marker WM90, which is at 55.699 m above the reference ellipsoid. Finally, since the sea level rides together with the tower and its tide gauge on the solid Earth tides, the tidal sea level is corrected for the solid Earth tidal elevation computed according to the *Wahr* [1981] model, including the permanent and frequency-dependent tides.

- The altimetric sea surface height comes from the smoothed and interpolated sea surface profiles presented in Section 4.4. The Table indicates which corrections have been applied and which was the orbital altitude at the time of closest approach, as well as the ‘raw’ (though smoothed and interpolated) altimeter measurement.
- The orbit altitude error, the altimeter correction errors and sea surface height interpolation error are root-sum-squared to form the total error of the single-pass bias estimate.
- A comparison of the altimetric sea surface height at the point of closest approach (PCA) to the tower and tidal sea surface height at the tower gives the single-pass bias estimate, as described by (4.1). The bias estimates per pass, so obtained, range from  $-46.9$  to  $-21.6$  cm. The latter value is for 15 August. On this date, the altimeter lost lock about ten kilometres before the tower overflight, leading to a large interpolation error. This result has therefore been given little weight in the final bias estimate.
- The last part of the table presents some additional information, such as the deflection of the vertical measured on the tower, the horizontal and vertical velocity of the satellite, the azimuth of the ground-track, and the geoid height at PCA with respect to that at the tower.

Figure 4.10 shows the estimated biases per pass (and their  $1\text{-}\sigma$  error bars) as a function of the distance of the PCA to the *Acqua Alta* tower, derived from Table 4.12. The values appear to decrease toward the east, suggesting a significant geoid slope. The weighted least-squares fit is shown by the dashed line. However, the slope of this line ( $-17.2$  cm/km) is unrealistically large. We have to assume that the slope is a coincidence. The slope of the solid line represents the actual cross-track geoid slope ( $-1.6$  cm/km) based on the deflections of the vertical measured at the tower; the errors of these measurements were estimated at  $\pm 0.5$  arcsec, or  $\pm 0.3$  cm/km in cross-track slope. The origin of the solid line is determined by the weighted average of the single-pass bias estimates and is shown by the black dot and error bars in Figure 4.10.

The combined bias estimate from this weighted fit is  $-41.5 \pm 2.0$  cm. The uncertainty in this fit must be interpreted as the combination of all non-static errors, which vary pass-by-pass. This must be combined with the estimated magnitude of the static errors, as derived in Section 4.6.1. This results in a final bias estimate and total uncertainty of  $-41.5 \pm 5.2$  cm.

The computed bias has varied constantly during the calibration process. Errors were discovered in the altimeter data product or in the post-processing. Atmospheric corrections became more accurate as more measurements became avail-

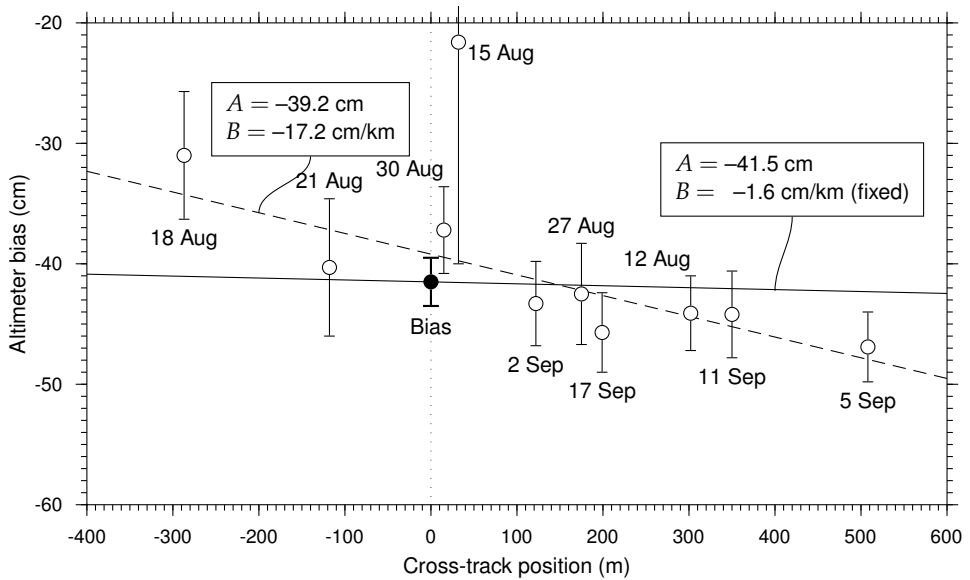


Figure 4.10 Individual bias estimates (white circles) as a function of the distance of the PCA to the *Acqua Alta* tower. The vertical bars indicate a  $1\text{-}\sigma$  uncertainty in each estimate. The sloped dashed and solid lines ( $\text{bias} = A + B \times \text{distance}$ ) represent the best fit with  $B$  estimated or fixed (equaling the measured cross-track geoid slope), respectively. Interpolated bias shown as black circle with error bars.

able. More passes were included. The full history of the bias estimate, starting at +4.50 m, hovering around 0 cm and ending up at  $-41.5$  cm is described in Table 4.13.

Date	Value	Comment
<b>1991</b>		
20 Sep	+4.50 m	First bias estimates based on altimeter passes of 12 and 18 August 1991.
23 Sep	+3.45 m	The speed of light used in the ERAC processor corrected to end on 448 in stead of 458 m/s. The tropospheric and ionospheric corrections changed from first guesses to more realistic values.
3 Oct	+3.50 m	Passes of 12, 18, 21, and 27 August processed. Height of the <i>Acqua Alta</i> GPS marker changed from 55.604 m to 55.595 m (based on DUT(LSC)91L01 station coordinate solution)
26 Nov	-46 cm	Correct altimeter open-loop calibration values applied. Error in referencing of the leading edge by 3.6 FFT gates (see Figure 1.4) accounted for. New station coordinates (DUT(SSC)ERS90 solution) resulted in a change of the GPS marker height to 55.638 m. Solid Earth tides applied (Wahr model). Ionospheric and tropospheric corrections from in-situ measurements, given in centimetres. Also passes of 5, 11, and 17 September included.
<b>1992</b>		
10 Feb	-45 cm	Included pass of 15 August 1991. Orbits based on laser normal points instead of full-rate measurements.
17 Feb	+8.4 cm	Tide gauge reference point changed from 13.430 m to 13.023 m below the GPS marker. Frequency-dependent components included in solid Earth tide values. Better ionospheric and wet tropospheric corrections from radiosondes and <i>in-situ</i> upward-looking microwave radiometer applied. Straight line fitted through the series of recovered biases per pass to correct for the sea surface slope.
6 Mar	-23.2 cm	Tide gauge reference point changed to 13.292 m. Altimeter time-tag corrections applied. A ninth pass of 2 September 1991 included. Bias value determined from the six best values, with sea surface slope according to deflection of the vertical.
12 Mar	-22.9 cm	Tighter constraints for altimeter interpolation profiles. Faraday rotation measurements included for ionospheric delay values.
31 Mar	-23.7 cm	Improved ionospheric and tropospheric corrections applied. Altimeter time-tag corrections revised. A tenth pass of 30 August 1991 included. Bias value still based on six best values, weighted by their sigma value.
9 Apr	-19.2 cm	Altimeter Doppler correction applied. DORIS ionosphere model used for the interpolation and verification of radiosonde measurements. Bias based on weighted straight line fit through all ten available individual solutions with slope determined by measured deflection of the vertical.
29 Sep	-25.1 cm	Better estimate of tropospheric corrections, lower correction sigma. Timing errors finalised and incorporated. EM-bias applied.
18 Nov	-41.6 cm	One of the reference marks on the legs of the platform was wrongly identified, leading to a 16.5 cm shift in the results. The tide gauge zero level thus changed to 13.457 m below the GPS marker. Slippage of the tide gauge mechanism over the intervening year between the original measurements and the determination of the tide gauge reference is ignored.
<b>1993</b>		
16 Apr	-40.9 cm	Transformation of orbital position to geographical coordinates adjusted to include polar motion. This had only a small effect on the vertical position.
10 Sep	-41.5 cm	Error in converting the MTLRS-2 eccentricity vector fixed. Final published value.

Table 4.13 History of the ERS-1 altimeter range bias estimate.



## Chapter 5

# The Time Tag Bias of ERS Altimeter Data

The time tags attached to the altimeter measurements featuring on the ERS-1 and ERS-2 OPRs are systematically early by over a millisecond. Apart from a mean offset, the timing error also exhibits an annual variation. Although this timing error was discovered already some years ago [Scharroo, 1995b], an explanation was never found. Object of this Chapter is to examine possible causes of the time stamping errors: the time determination mechanism of the ERS altimeters, processing errors, and the variation in the on-board clock frequency.

It is shown that the source of the static time errors in the ERS altimeters may lie in the low resolution of the on-board clock. The apparent annual variation of the time errors can be attributed only partially to the variation of the frequency of on-board clock and its value at the Kiruna overpass when the time-correlation to UTC is made. The timing error also appears to depend on the time of day.

## 5.1 Introduction

The time stamping of measurements of the satellites ERS-1 and -2 is performed by the on-board clock. This clock contains an oscillator with a fixed frequency that triggers a counter to be increased by one on every cycle of the oscillator. To correlate the clock count to UTC (Coordinated Universal Time) the clock count is compared to an accurate atomic clock at the Kiruna ground station in Sweden while the satellites are dumping their data. Errors in the time stamping may result from errors in this clock correlation or from unmonitored variations of the oscillator frequency around the orbit.

An error in the time tagging of altimeter data manifests itself as an error in the estimated sea level through the convolution with the orbital altitude rate. Since the altitude rate ranges up to 25 m/s, an error of 1 ms leads to an error of 25 mm in computed orbital altitude and likewise in the inferred sea level. This is best seen at

crossover locations where ascending and descending tracks cross and the altitude rates on the respective tracks have the opposite sign (Figure 5.1). The timing error can thus be estimated as a multiplication factor onto the altitude rate that best fits (in a least-squares sense) the crossover height differences (Figure 5.2) [Scharroo, 1995b; Scharroo and Visser, 1998]. This technique is analogous to the one used to estimate the (much larger) timing errors of the Seasat altimeter data [Schutz *et al.*, 1982].

The timing error is also referred to as *time tag bias*. A positive time tag bias means that the time stamping of the altimeters measurements is late; in other words, the value indicating the time that the altimeter pulse bounced off the ocean surface is too large.

All ERS OPR (version 3 and 6) altimeter products (until mid-2002) were enhanced as described in Chapter 2 and analysed for timing errors<sup>1</sup>. To trace down the source of the timing errors a few years worth of time correlation files (PATN) [Paganini and Louet, 1992; Saavedra de Miguel and Femenias, 2000] were analysed as well. Data from ERS-1 Phases A and B are only shown as reference but are not included in the analyses because the construction of the time correlation changed shortly after Phase C started [Paganini and Louet, 1992].

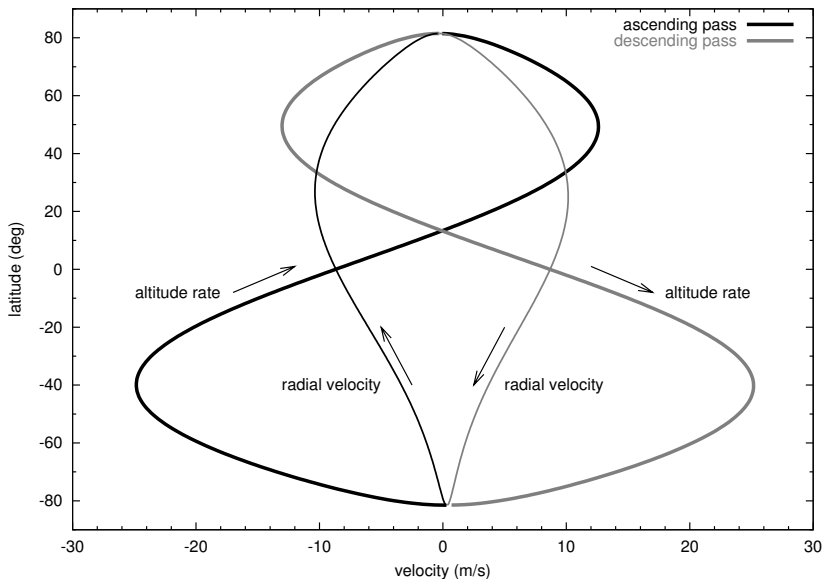


Figure 5.1 The altitude rate (or vertical velocity) of the ERS satellites as a function of latitude is shown by the thick lines. The thin lines relate to the radial velocity and are only shown for comparison.

<sup>1</sup>In fact, the time bias corrections of 1.5 and 1.3 ms were applied as well, but are removed again in the results presented in this Chapter as if the corrections were not applied.

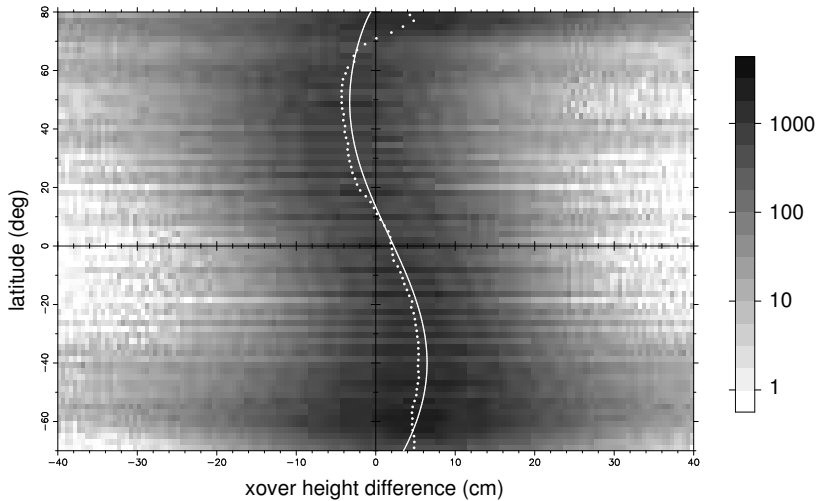


Figure 5.2 Distribution of ERS-2 crossover height differences (Cycles 0–74) as a function of latitude before applying any timing error corrections. The dotted line indicates the actual mean crossover height difference for each latitude. The curved solid line represents the theoretical effect of a timing error of  $-1.5$  ms.

## 5.2 The variation of the timing error with time

Figure 5.3 shows the variation of the estimated timing error of ERS-1 and ERS-2 throughout the missions, as deduced from crossover height differences. Monthly means are shown in order to suppress the noise in the original daily estimates. The timing errors of both satellites clearly exhibit some annual variation with an amplitude of about 0.15 ms on top of an average of about  $-1.5$  and  $-1.2$  ms for ERS-1 and ERS-2 respectively, where the minus sign means that the time tags are systematically early.

Previous results [Scharroo *et al.*, 2000d] showed a much larger annual variation for ERS-2 and a more consistent one for ERS-1. This suggests that recent enhancements to the altimeter corrections, like upgrading from the FES95.2.1 to the GOT00.2 tide ocean model, may have caused the timing bias estimations to change. If this is the case, we have to be careful while interpreting our results. Apparently, errors in the corrections can mimic themselves as errors in the time tagging.

A mean difference between the ERS-1 and ERS-2 timing error of 0.2 ms could be traced back to an error in the OPR production software [Stum *et al.*, 1998]. The remaining mean error, as well as the annual variation remains to be explained.

One must realise that the estimate of the timing error as presented in Figure 5.3 is highly sensitive to the situation around  $40^\circ$  South. This is because the altitude rate is here the highest (see Figure 5.1), the crossover height differences are there-

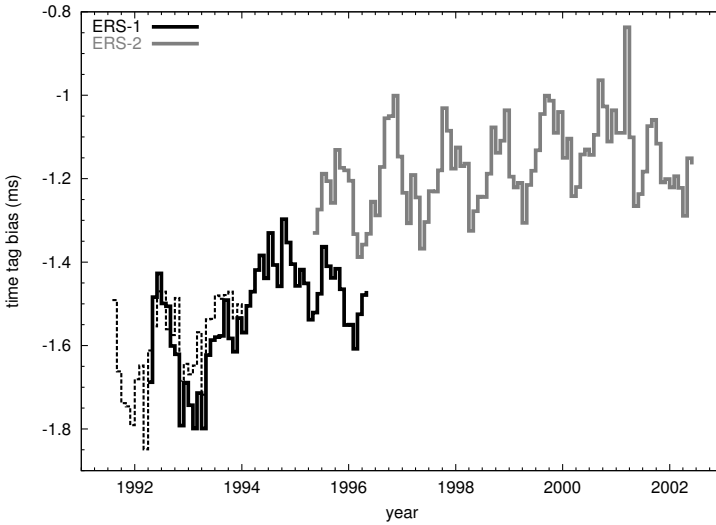


Figure 5.3 Estimates of the timing error of ERS-1 and -2 throughout their missions. The thick lines represent the monthly mean estimates based on crossover height differences. For reference, the dashed line shows the results for ERS-1 Phases A and B (up to April 1992) and OPR version 3 data for Phase C. Negative values of the timing error indicate that the time tags are systematically early.

Parameter	ERS-1 (Phase C–G)		ERS-2 (Cycle 0–74)	
	value	xover RMS	value	xover RMS
<b>A priori</b>		93.00 mm		87.83 mm
$a_0$	-1.527 ms	53.08 mm	-1.169 ms	40.37 mm
$a_1$	-0.056 ms		0.035 ms	
$b_1$	-0.036 ms		-0.083 ms	
$c_1$	0.066 ms	1.61 mm	0.090 ms	2.20 mm
$\phi_1$	-146.7°		-67.1°	
Maximum at	4.4 Aug		24.2 Oct	
<b>A posteriori</b>		76.32 mm		77.94 mm

$$\Delta t = a_0 + a_1 \cos \phi + b_1 \sin \phi = a_0 + c_1 \cos(\phi - \phi_1)$$

Table 5.1 Parameters of a least-squares fit of an annual varying timing error to the crossover height differences. The amount of RMS crossover height difference explained by the constant and harmonic terms, and the a priori and the a posteriori RMS are also indicated.

fore the largest, and the inferred timing errors are the most significant. Also, along this parallel most is ocean and crossovers are closely spaced, which results in an unevenly high number of measurements at these latitudes compared to others. Less than a quarter of the crossovers are located on the northern hemisphere.

An estimate of the average and annual variation of the timing error can be obtained by estimating 3 parameters (mean and in-phase and quadrature amplitudes) directly from the crossover height differences, similar to estimating just a single time tag bias parameter. The results are presented in Table 5.1.

Note that between 20 and 30% of the variance of the crossover height differences can be explained by an annual varying time tag bias. However, the variance explained by the constant term ( $a_0$ ) is much larger than that of the harmonic terms ( $a_1$  and  $b_1$ ). In fact, the later only explains a mere percent of the remaining variance. Noteworthy is also that after such a 3-parameter time tag bias correction is applied, the remaining variance is nearly the same for ERS-1 and ERS-2.

The purpose of this Chapter is:

- To attempt explain the cause of timing errors;
- To understand the reason for the annual variation and its phase;
- To link the amplitude of the signal to a physical phenomenon;
- To find the cause of the average bias on top of the variation;
- To explain the difference between ERS-1 and ERS-2;
- To model a suitable correction for the timing errors.

## 5.3 ERS altimeter datation mechanism

Before trying to explain the cause of the timing error and its variation, it is essential to review the ERS altimeter datation mechanism. The spacecraft hosts a number of clocks, implemented as binary counters. In our analysis we are interested in the platform clock, called *On-Board Clock (OBC)* and the clock of the altimeter, called *instrument clock* (Figure 5.4).

The OBC is a 32-bit counter, while the altimeter instrument clock is a 36-bit counter. The two counters are triggered by the same signal, and are synchronised after the instrument switch-on in such a way that the most significant 32 bits of the instrument clock have the same value as the OBC counter, and the least significant 4 bits are set to zero. This means that the altimeter clock reports the same time of the OBC, but with a resolution 16 times finer. The value of the OBC counter is called *Satellite Binary Time (SBT)*. The frequency of the OBC counter is approximately 256 Hz. In other words, SBT counter is increased by 256 in approximately 1 second.

The counter value of the altimeter instrument clock is reported to the ground in the altimeter telemetry, and is used to compute the measurement time tag. The counter value of the OBC is reported every second in real-time during each contact

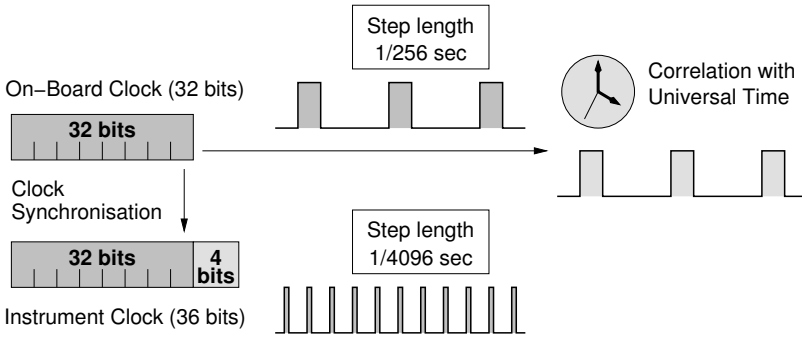


Figure 5.4 The timing system of the ERS altimeters.

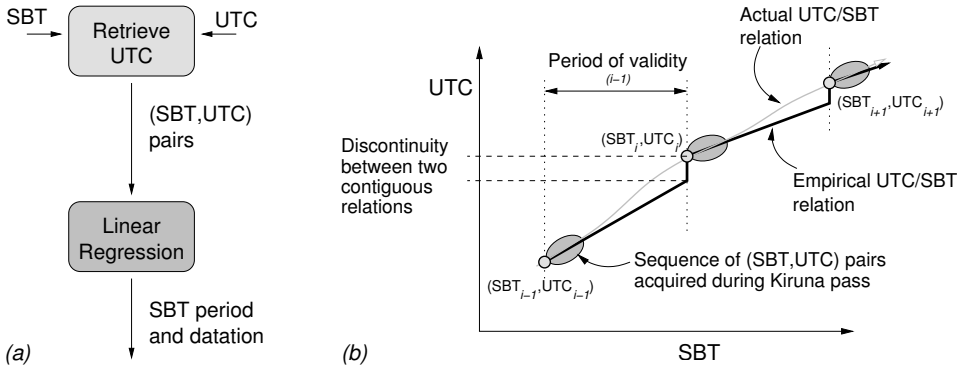


Figure 5.5 (a) Correlation of SBT and UTC pairs during the Kiruna overflight. (b) Building a piecewise linear relationship between SBT and UTC.

with the primary station of Kiruna and, among other things, is regularly correlated with the UTC. Thus, during each pass over Kiruna a significant number of SBT-UTC pairs are available. A linear regression of these pairs essentially provides three parameters: the UTC time and SBT counter value at the beginning of the Kiruna overflight and the clock period or step length of the on-board clock counter (Figure 5.5a). This linear fit can be used as an empirical model for the SBT→UTC relation during the Kiruna pass (Figure 5.5b).

There are approximately 10 Kiruna overflights per day, each of about 10 minutes duration. The next issue is how to extend the SBT→UTC relation *beyond* the Kiruna passes during the time that there is not direct comparison between SBT and UTC possible. A logical assumption is that the clock frequency is stable, so that the SBT→UTC relation remains the same throughout the orbit, at least until the next Kiruna overflight. This leads to a piecewise linear model to relate SBT (of the On-Board Clock and instrument clock) to UTC throughout the orbits:

$$UTC = f_i(SBT) = UTC_i + P_i \cdot (SBT - SBT_i) \quad , \quad (5.1)$$

where

- UTC<sub>*i*</sub> ≡ UTC time at time beginning of interval *i*;
- SBT<sub>*i*</sub> ≡ SBT counter value at the beginning of interval *i*;
- P<sub>i</sub>* ≡ clock period or step length of the counter at the beginning of interval *i*.

This function is illustrated in Figure 5.5*b*. The straight line segments  $f_i(\text{SBT})$  define the relationship SBT→UTC valid for successive periods of time, *i*. These periods are the intervals between two acquisitions at Kiruna, when several (SBT,UTC) pairs are collected to determine the step length *P<sub>i</sub>*.

The three time correlation parameters of each given segment (UTC<sub>*i*</sub>, SBT<sub>*i*</sub>, *P<sub>i</sub>*) are determined by fitting a straight line through a series of correlated pairs (SBT,UTC) acquired during a Kiruna overpass. These parameters are recorded in so-called *PATN files* and are used by the entire ERS ground segment to determine the UTC time tags of measurements out of SBT counter values.

It is worth adding that the UTC used on ground must be corrected to refer exactly to the spacecraft clock time, *e.g.*, telemetry propagation delays and delays of the receiving equipment must be compensated for in the ground processing. One can note that, by construction, the empirical SBT→UTC relation is not continuous; however, in normal circumstances, the discontinuities are supposed to be smaller than 0.1 ms. We will see later that they are not.

## 5.4 Constant time errors induced by the time-stamping quantisation

The above mechanism assumes that the errors of the SBT correlation have zero average, or better, that they are Gaussian. However, since the time-stamping of the Satellite Binary Time takes place asynchronously, the error can be as large as one satellite clock period (*P*), as shown in Figure 5.6. In other words, when a time correlation is made, and the satellite clock reports an integer SBT value *k*, the actual Satellite Time may refer to any point in the interval [*k*, *k*+1), with uniform probability.

In the end we see that the empirical time correlation function  $\text{UTC} = f(\text{SBT})$  will be based on several (SBT,UTC) pairs, in each of which the SBT value is low by a random number  $\epsilon$ , with uniform probability on the interval between 0 and 1. Given a sufficient amount of pairs, the SBT in this relation is low by an average of  $\frac{1}{2}$ . This means that the true relation between UTC and SBT is given by  $\text{UTC} = f(\text{SBT} - \frac{1}{2})$  rather than  $\text{UTC} = f(\text{SBT})$ .

When the empirical UTC/SBT time correlation function is used to infer the UTC time stamp from an accurate SBT, a time stamping error is introduced. If one calls the time stamping error the difference between the inferred UTC time stamp and the actual UTC referring to the SBT, it is possible to write the following relation:

$$\Delta\text{UTC} = f(\text{SBT}) - f(\text{SBT} - \frac{1}{2}) = \frac{1}{2}P \quad . \quad (5.2)$$

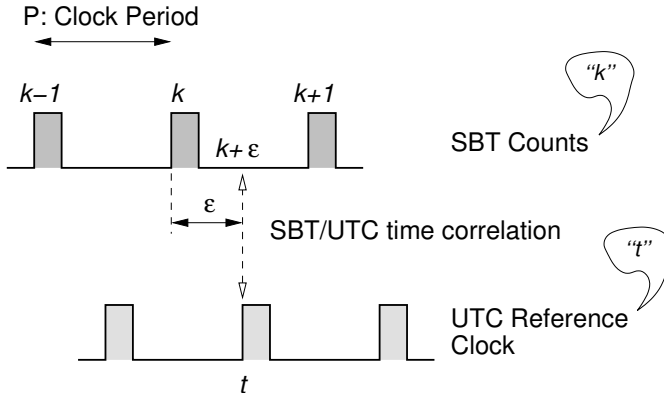


Figure 5.6 The time stamping error  $\epsilon$  is the difference between the true (*real*) value of the SBT and the integer number reported by the SBT.

From this we can conclude that the empirical SBT→UTC relation *overestimates* the inferred UTC time, and that the intrinsic bias equals  $\frac{1}{2}P$ .

For ERS,  $P$  is around 1/256 seconds or 3.9 ms, so the intrinsic time tag bias due to the quantisation is 1.95 ms. In other words, when the SBT value associated with a certain measurement is converted to UTC using the empirical SBT→UTC relation, then the UTC time stamp would be late by 1.95 ms. But this holds *only* when the input SBT value is the *real* value, and not the *integer* value. If the latter is the case, the quantisation error is, on average, cancelled.

On the other hand, it is the altimeter instrument clock counter that is used to determine the UTC time stamp of altimeter measurements. This clock has a 16 times higher frequency and therefore a smaller period and quantisation error, so that a significant part of the time tag bias remains. This makes the time tag bias on the altimeter data due to quantisation of the On-Board and instrument clocks  $\frac{1}{2}P(1 - \frac{1}{16})$ . In other words, the UTC time stamps are systematically *late* by  $\frac{15}{32}$  of the OBC period or 1.82 ms.

This value is in the opposite direction with respect to the figures provided by the crossover analyses. The implication is that the satellite itself presents a bias even higher, being the sum of the two, approximately 3 ms. It is extremely difficult at this point to identify the parts (satellite, instrument, or processing) responsible for such bias.

## 5.5 Temperature and clock frequency variations

The temperature of the satellite (both inside and out) varies around the orbit. During approximately one-third of the orbit (34 minutes) the satellite is eclipsed; it flies through the shadow of the Earth and all satellite elements, including the oscillator will cool down. The remaining 66 minutes the satellite is in full sunlight during



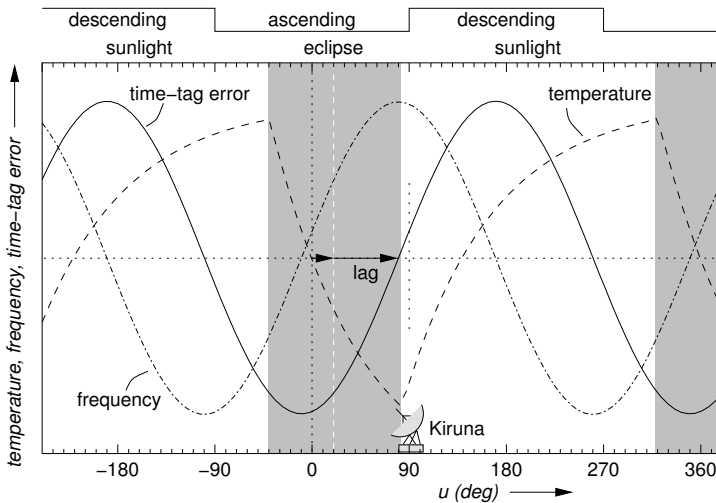


Figure 5.7 Impression of the variation of temperature, oscillator frequency and timing error around the orbit of the ERS satellites. This graph simulates the situation around the winter solstice.

which the elements heat up. The quartz crystal inside the oscillator will expand when heated, causing the frequency to lower and the clock to slow down. The expansion and the sensitivity of the oscillator frequency to temperature depends on the thermal coefficient of the crystal, which may differ from one specimen to the other. A justifiable hypothesis is that the oscillator frequency change is (negatively) proportional to the temperature change. In fact, a correlation between the OBC step length (and hence the oscillator frequency) and the temperature of the ERS-1 platform controller (located near the oscillator) has been demonstrated.

In Figure 5.7 the variation of temperature of a body in a changing sunlit and eclipsed environment is sketched. During heating the temperature increases asymptotically toward the equilibrium temperature in sunlight, during eclipse it cools down exponentially toward the equilibrium temperature in absence of direct sunlight. The warmest state is reached by the beginning of the eclipse period, the coldest at the end of the eclipse.

Support for this hypothesis of the impact of the temperature on the oscillator frequency (and hence its step length) comes from the UTC/SBT time correlation itself. Analysis has shown that the estimates of the step length ( $P$ ) of the ERS-2 OBC depend primarily on the season and secondly on the time of day of the Kiruna overpass.

An annual cycle is observed in Figure 5.8: the step length varies by about 1 ns around the nominal value of 3 906 250 ns (1/256 second) and the maximum falls around the winter solstice. Apart from a momentary excursion during 1997, the ERS-1 oscillator seems less sensitive to the season (and hence temperature) than ERS-2.

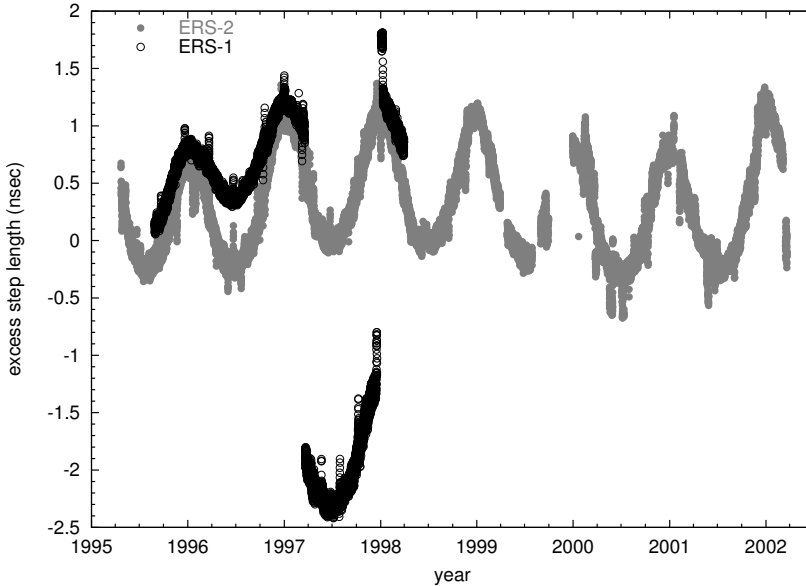


Figure 5.8 Step length of the ERS-1 (black circles) and ERS-2 (grey dots) on-board clock oscillators determined at the Kiruna overpasses. The value of the step length is in excess of 3 906 250 ns.

It also appears that the estimated step length at Kiruna generally falls short of the average step length throughout the orbit, especially in summer. This behaviour was found by comparing the step length recorded in the PATN files with an 'interpolated' step length. The interpolated step length is determined by division of the time between two consecutive Kiruna overpasses and the number of clock cycles that have occurred in the same period. The thus acquired delta step length becomes

$$\Delta P_i = P_i - \frac{UTC_{i+1} - UTC_i}{SBT_{i+1} - SBT_i} \quad (5.3)$$

and is shown in Figure 5.9 as a function of the UTC time of day at the Kiruna overflight. The fact that the delta step length is generally negative confirms our hypothesis displayed in Figure 5.7 that the OBC frequency is relatively high (step length is short) during the Kiruna overpass, because the oscillator temperature is relatively low at that moment as it just comes out of eclipse. However, at the same time the hypothesis is contradicted by the fact that the step length is shortest in summer when the oscillator temperature over Kiruna should actually have gone up and the step length increased with respect to a winter overpass.

Nonetheless, there is an obvious relationship between the oscillator temperature and the time lapse since the exit of the eclipse: the longer the satellite has been in the sun, the warmer the oscillator. Now it is important to realise that the Kiruna

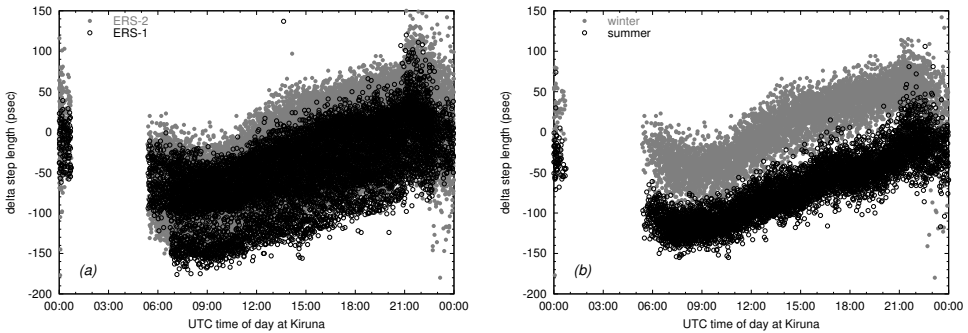


Figure 5.9 Delta step length = step length of the ERS-1 and ERS-2 on-board clock oscillators determined at the Kiruna overpasses *minus* the ‘interpolated’ step length, shown as a function of the UTC time of the Kiruna overpass. (a) ERS-1 (black circles) and ERS-2 (grey dots). (b) ERS-2 values for summer (Jun, Jul, Aug: black circles) and winter (Dec, Jan, Feb: grey dots).

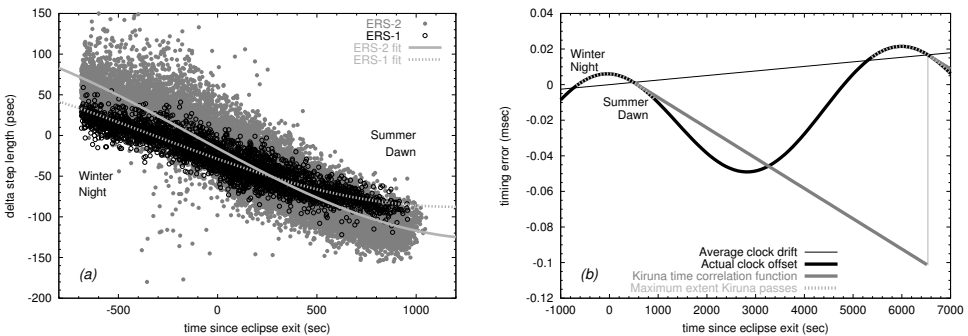


Figure 5.10 (a) Delta step length observed at Kiruna plotted as a function of the time since the exit of the last eclipse of the satellite. Values for ERS-1 are represented by black circles, ERS-2 by grey dots, with harmonic fits shown by grey dashed and solid lines, respectively. (b) Model timing error along the orbit (black curve) based on the observed delta step length. The empirical SBT→UTC relation is shown by the thick grey line.

overflight takes place at various local solar times, owing to the fact that Kiruna is located so far North and is able to contact the satellite on 10 out of 14 passes per day. Overflights take place at night time, when the satellite is still eclipsed up to early morning when the satellite is already in sunlight for quite some time. The time since the eclipse also depends on the season. In summer the Sun is toward the North, and the eclipse toward the South, hence the time since the eclipse will be larger in summer time than in winter time. Figure 5.10a shows the delta step length as a function of the time since the eclipse: the points on the far left refer to those Kiruna passes occurring during the winter nights, on the far left are those occurring during summer at dawn.

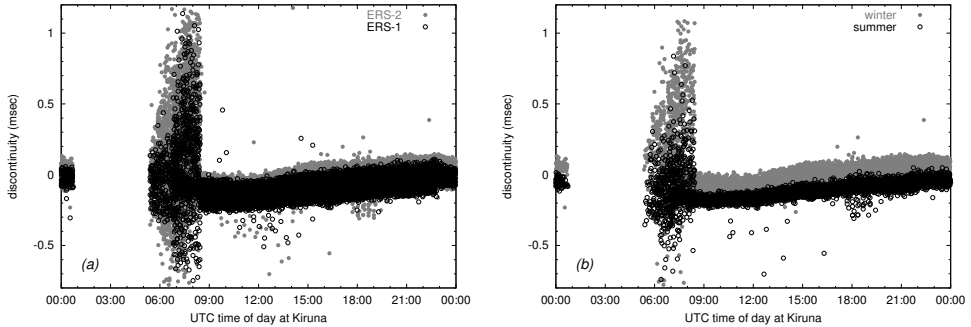


Figure 5.11 Discontinuities in the UTC/SBT relation due to propagation errors related to the OBC oscillator step length, shown as a function of the UTC time of the Kiruna overpass when the discontinuity occurs. (a) ERS-1 (black circles) and ERS-2 (grey dots). (b) ERS-2 values for summer (Jun, Jul, Aug: black circles) and winter (Dec, Jan, Feb: grey dots).

The distribution of these points is strikingly narrow and suggests a harmonic 1-cpr variation of the delta step length around the orbit. The solid lines in Figure 5.10a are the fits of a 1-cpr harmonic for ERS-1 and ERS-2. They have an amplitude of 88 and 129 psec, respectively. The actual time tag error will be the integral of this, shown by the black curve in Figure 5.10b. The amplitudes of this time tag error are marginal (only 22 and 32  $\mu\text{sec}$  for ERS-1 and ERS-2, respectively), so by no means is this variation able to explain the observed time tag bias. However, there is a second issue associated with this. Note how in Figure 5.10b the Kiruna pass only covers a small part of the orbit. The SBT $\rightarrow$ UTC relation will be based on this short period, leading to an anomalous linear trend as illustrated in Figure 5.10b. Especially during summer time the propagation of the empirical relation will undercut the actual clock variation. During winter the propagation errors will be smaller as the step length determined from the SBT/UTC correlation will be closer to its around-orbit average.

At the next Kiruna overpass there will be a discontinuity in the UTC/SBT time correlation from one period of validity of this relation to the next. In our definition this will be a negative discontinuity, meaning that the UTC value determined by the time correlation function jumps up, like it is shown in Figure 5.5b.

The propagation error or discontinuity can simply be determined by multiplying the delta step length with the length of the period over which the step length is valid. So the longer the validity period, the larger the discontinuity. Formally we write:

$$\text{discontinuity}_{i+1} = f_i(\text{SBT}_{i+1}) - \text{UTC}_{i+1} \quad (5.4)$$

Figure 5.11 shows that particularly in the early morning, after 4-5 hours without Kiruna contact, the discontinuity can be as much as 1 ms and far exceed the claimed 0.1 ms level, even though for the rest of the day the discontinuities are

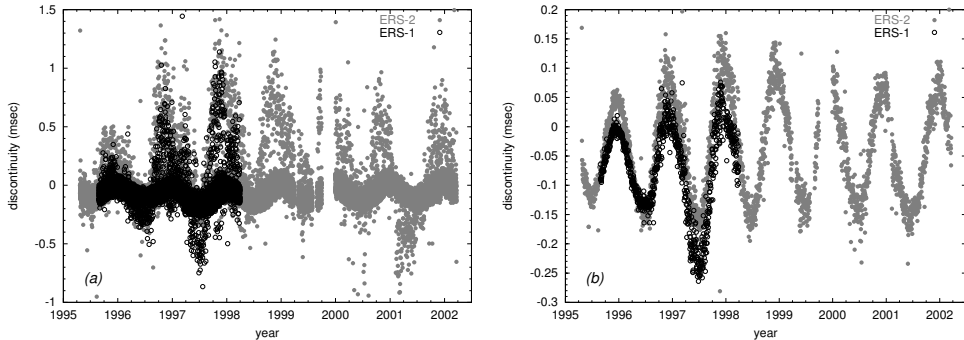


Figure 5.12 Discontinuities in the UTC/SBT relation due to propagation errors related to the OBC oscillator step length: ERS-1 (black circles) and ERS-2 (grey dots). (a) All values. (b) Daily averaged values.

at about the 0.1 ms level. Figure 5.11 also demonstrates that indeed, as expected from the illustration in Figure 5.10*b*, in the winter, apart from the excursions in the early morning, the discontinuities are small, while in summer the discontinuities are larger (more negative).

The discontinuities throughout the years 1995-2002 are displayed in Figure 5.12. On the left a gentle annual cycle is seen, criss-crossed by the larger excursions occurring in the early mornings. On the right daily averages of the discontinuities maintain the annual cycle with an amplitude of about 0.15 ms and a mean of about  $-0.06$  ms.

The fact that there is an error resulting from the propagation of the UTC/SBT correlation leads to think that it can have an impact in the time tagging of the radar altimeter data. Since the propagation errors are generally negative an early time stamping for the altimeter data is expected. Although we have to realise that the *mean* effect of the discontinuities on the timing error is *half* as big, it appears that this can still explain most of the observed the annual variation of the timing error, but only about 2% of its mean.

The temperature dependency of the oscillator also implies that the step length varies along the orbit. We have made an attempt at modelling this behaviour by allowing for a constant, 1- and 2-cpr time tag bias in a crossover analysis similar to the above. These five parameters were estimated by means of least-squares minimisation of the crossover height differences of ERS-1 (Phase C-G) and ERS-2 (Cycles 0-74). The resulting a posteriori crossover difference RMS, however, did not significantly differ from the one found with the 3-parameter model presented in Table 5.1.

Yet, the previous exercises have shown that there is at least a daily variation of the step length, of the oscillator frequency, and hence of the timing error. Again the crossover height differences come to help to estimate such a diurnal variation. In stead of estimating daily timing errors (as in Figure 5.3) we can also estimate one value for each, let's say, half hour of the day, as shown in Figure 5.13*a*. There is

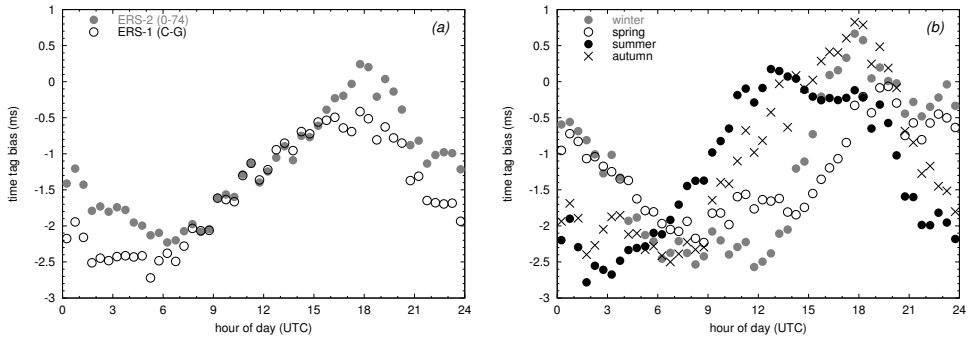


Figure 5.13 Estimates of a daily varying timing error of ERS-1 and ERS-2 recovered by least-square minimisation of crossover height differences, shown as a function of the UTC time of day. (a) ERS-1 (black circles) and ERS-2 (grey dots). (b) ERS-2 values for winter (Dec, Jan, Feb: grey dots), spring (Mar, Apr, May: black circles), summer (Jun, Jul, Aug: black dots) and autumn (Sep, Oct, Nov: black crosses).

a remarkable coherence between the timing errors and the delta step length (compare Figure 5.9): low (significantly negative) during the morning hours and higher (less negative) during the evening hours. The transition from one level to the other is rather sharp and the low noise suggests that this is a significant feature. The coherence with the delta steplength is the more remarkable since we would expect a strong coherence with the observed timing error and the *integral* of the delta step length, the discontinuity. However, comparison between Figure 5.13 and Figure 5.11 displays little to no coherence.

Now, in Figure 5.13a ERS-1 and ERS-2 show about the same picture, large negative timing errors in the morning and smaller ones in the evening. The question is whether this behaviour is not only similar between the two satellites, but also stable throughout the year or even mission. Thus Figure 5.13b was created to show virtually the same as Figure 5.13a, but now separated by season (ERS-2 only). Although there is some seasonal dependency, the marked diurnal variation remains.

## 5.6 Daily and annual variation of the timing error

It may well be that the final explanation of the timing bias and its daily and annual variation, or at least the proper modelling of this behaviour, may lie in Figure 5.13. We clearly have to model both an annual and daily variation of the timing error, and likely these variations are not harmonic. Thus it was chosen to make a 2-dimension parameter space, the time of day along the horizontal axis and the time in the mission along the vertical axis. Before computing an annual cycle, it is important to see whether there is such a cycle. Figure 5.14 shows the result, both for ERS-1 and ERS-2.

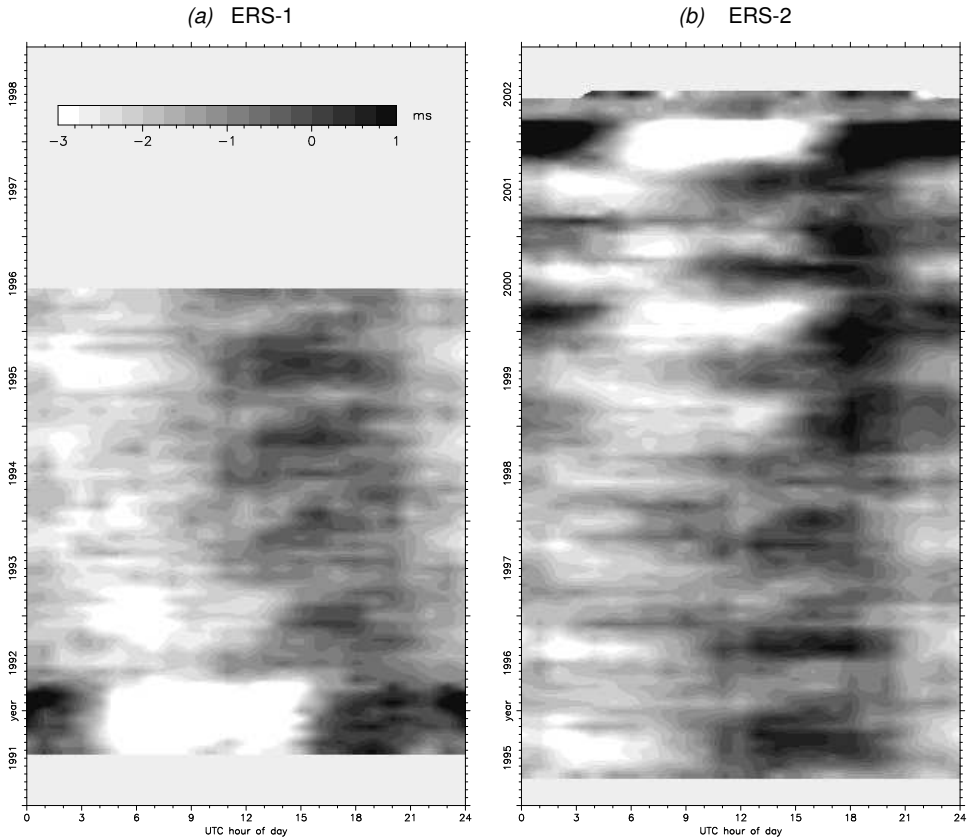


Figure 5.14 Estimates of the timing errors of ERS-1 (a) and ERS-2 (b) based on the minimisation of crossover height differences. The 2-dimensional parameter space contains the UTC hour of the day on the horizontal axis and years along the vertical axis.

It becomes immediately obvious that the annual cycle is not very strong. There is some annual variation, but it is not strongly repetitive and not always harmonic; in other words, there is also some inter-annual variation. Also, the diurnal variation slowly alters phase over the years. The most striking is the anomalous behaviour at the beginning of the ERS-1 mission, before Phase C. As indicated before, this was before the time stamping scheme was implemented as it is now.

Although each of the timing correction models discussed so far are easy to implement in the data processing, it is worth investigating what benefit it has to the altimeter data. Thus, Table 5.2 shows the crossover height difference RMS explained by the various models discussed in this Chapter and what remains. The conclusion to be drawn from this Table is that, unless a more fitting model can be found, a simple invariant timing bias correction is sufficient. This conclusion, however, does not invalidate the search for a better modelling of the time tag errors in

Time bias correction	ERS-1 (Phase C–G)		ERS-2 (Cycle 0–74)	
	explained RMS (mm)	a posteriori RMS (mm)	explained RMS (mm)	a posteriori RMS (mm)
No correction (0 ms)	—	93.00	—	87.83
Constant value (–1.527 ms, –1.169 ms)	53.08	76.34	40.37	77.97
Annual variation (Table 5.1)	53.10	76.32	40.43	77.94
Diurnal variation (Figure 5.13)	53.42	76.13	40.86	77.75
2-D parameter space (Figure 5.14)	54.01	75.70	42.04	77.12

Table 5.2 Reduction of the crossover height difference RMS after applying several models for the modelling of the time tag bias.

ERS altimeter data and certainly not a better implementation of a SBT→UTC relation by the ERS ground segment.

But how can it be that we observe such large diurnal variations in the timing bias, and to a lesser extend annual variations, while the impact of these variations on the crossover height differences is so small? To answer this question we should have a more detailed look at possible geophysical signals that could mimic a timing error.

## 5.7 Possible geophysical effects and other explanations

Since the ERS satellites fly in a sun-synchronous orbit, the local solar time at which the satellites overfly a particular location is fixed. At the equator the local solar time is 22:30 for ascending tracks and 10:30 for descending tracks. Any geophysical signal that has produced a time-invariant height difference between crossing tracks, or one that has a (harmonic) diurnal variation will show up as a constant crossover height difference and may be wrongly interpreted as a constant timing error.

### 5.7.1 Diurnal variation of the timing bias

One such signals is the geographically anti-correlated radial orbit error. It has the same magnitude, but opposite signs, on two crossing tracks and is constant from one repeat cycle to the next. (See Chapter 6 for a more detailed discussion of this type of orbit error.) Figure 5.15 shows the geographical distribution of ERS-2 crossover height differences averaged over 7 years, which mainly reflects the anti-correlated radial orbit error, but also gives a hint of ionosphere correction errors in the shape of two parallel lines along the geomagnetic equator.

Whatever the cause of the crossover differences, they may be conceived as resulting from timing errors in the timing bias estimation processes described in this Chapter. For the average –1.2 to –1.5 ms this is not likely to be the case. The



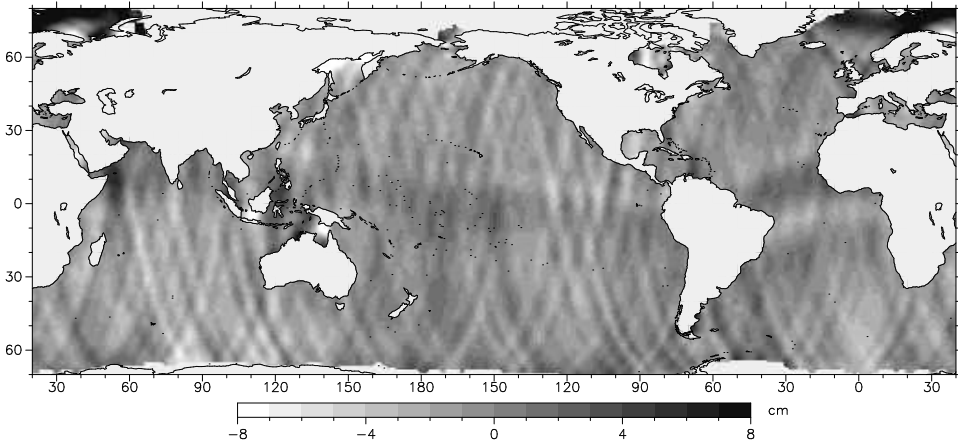


Figure 5.15 Mean ERS-2 crossover height difference, averaged over Cycles 0-74, May 1995 to June 2002. A 1.3 ms timing bias was corrected for in advance.

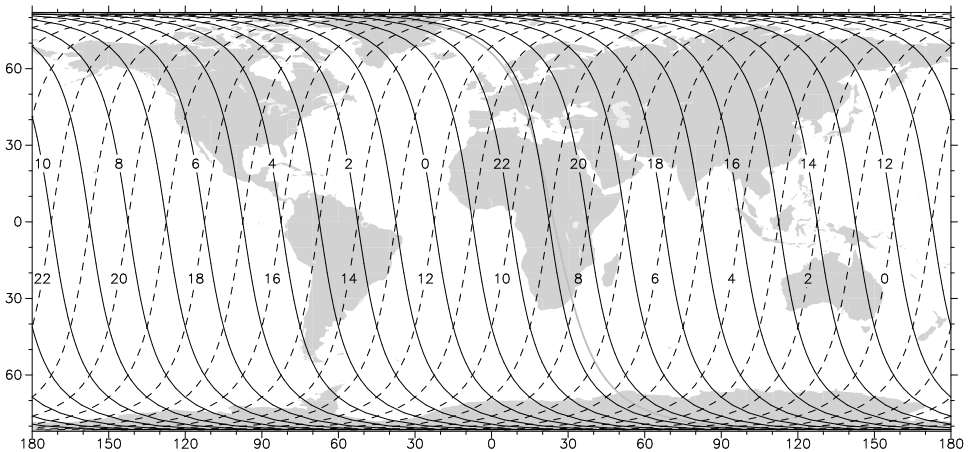


Figure 5.16 UTC time of day of the overflight of the ERS satellites. The solid black lines pertain to ascending passes, dashed lines to descending passes. The numbers indicate the UTC hour (0 is midnight, 12 is noon). The solid gray line shows the groundtrack of a single ascending pass.

zonal distribution of the crossover height differences (before timing bias correction) shown in Figure 5.2 is too convincingly close to the S-curve distribution that would result from a constant timing bias to be a hoax.

However, the diurnal variation is another matter. Consider the fact that the ERS satellites are sun-synchronous: then UTC time of day at which a measurement is taken varies with longitude, almost like time zones do, as shown in Figure 5.16. For example, all measurements taken around midnight UTC fall in the Atlantic

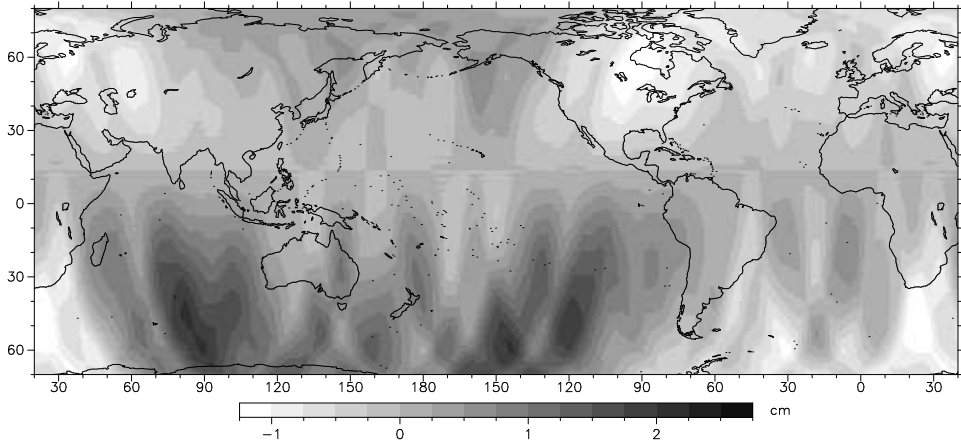


Figure 5.17 Impact of diurnal variation of the ERS-2 timing bias correction displayed in Figure 5.13 on ERS-2 crossover height differences.

Ocean on ascending passes and in the western Pacific Ocean on descending passes, and the reverse around noon UTC. Since the local solar time on ascending and descending passes are 12 hours apart on the equator, so is the UTC time of day. In fact, for a large part crossovers, all within  $40^\circ$  from the equator, the passes are between 11 and 12 hours apart in local solar time and UTC time of day. If we then consider the diurnal variation of the timing error about the mean (Figure 5.13), we will recognise that for the majority of the crossovers this variation is out of phase by about 12 hours and nearly identical in magnitude but with opposite sign. To get the impact on the sea surface height, we multiply with the orbital altitude rate which has the same property, leading to nearly equal height corrections, and thus nearly vanishing crossover height difference.

In other words, even the sizable diurnal variation of timing bias has little impact on the crossovers (shown in Figure 5.17), or, conversely, is difficult to estimate from crossovers. As Figure 5.17 shows, the least-square estimation process tries to compensate negative mean crossover differences in the Indian Ocean and positive ones in the South Atlantic Ocean, at the expense of creating unrealistically large, and likely fictitious, diurnal variations in the estimated parameter, the timing error.

## 5.7.2 Annual variation of the timing bias

To better interpret the annual variation in the timing error, Figure 5.18 shows the amplitude of the annual variation in 7 years' worth of ERS-2 crossover height differences. Noteworthy are the large 20 cm signal in the Hudson Bay, the extensive region of approximately 6 cm annual signal in the eastern Indian Ocean, and the obvious signal along the geomagnetic equator. These annual signals will show up

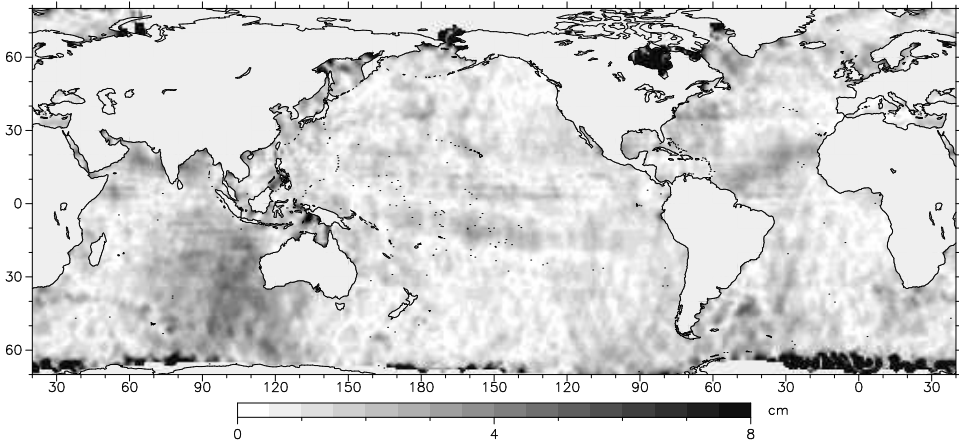


Figure 5.18 Annual variation of ERS-2 crossover height differences, determined over Cycles 0-74, May 1995 to June 2002. A 1.3 ms timing bias was corrected for in advance.

as an annual signal in the timing error estimates, and other signals with an even longer period can create the inter-annual variation suggested in Figure 5.14.

Note, however, that these are not annual signals as seen by a local observer. At a fixed location, these signals are diurnal with an annual modulation, such as the main luni-solar diurnal tide,  $K_1$ . Seen by the satellite though, these signals are *aliased* into annual signals [Smith, 1999]. The reduction of the annual variation of the timing error compared to previous results [Scharroo *et al.*, 2000d] can therefore be attributed to improvements in modelling of the  $K_1$  tide between the previously used FES95.2.1 model and the current GOT00.2 model (Section 2.5). If all of the annual variation should be attributed to tide model errors, however, is questionable, since, for example, the area in the Indian Ocean is not the region where major tide model improvements have recently occurred or are to be expected.

The signal along the geomagnetic equator, is easily attributable to the ionospheric correction (Section 2.4.4). Apart from the obvious diurnal (night/day) variation, the ionospheric correction exhibits also an annual variation, and not surprisingly, so does the error in the models.

### 5.7.3 Mean timing bias

For the mean value of the timing bias, however, most, if not all, suggested geophysical causes can be eliminated, because they would not explain the annual variation (like gravity induced orbit errors that vary by location but are otherwise time invariant), or because the distribution of crossover height differences (Figure 5.2) is too conspicuously close to the variation of altitude rate (Figure 5.1). Hence, we are forced to resort to explanations stemming from the instrument or

the processing to account for the approximately  $-1.5$  and  $-1.3$  ms timing bias of ERS-1 and -2, respectively.

- As mentioned before, an error in the ERS-1 OPR processing accounts for the fact that the ERS-1 time tags are 0.2 ms earlier than ERS-2 [Stum *et al.*, 1998].
- Clock asymmetry makes the time tags late by 1.82 ms, which means that a total of  $-3.1$  ms of timing error has to be explained.
- The timing of each waveform requires making a correction from the original transmit time, to the *ground strike time*, the time at which the pulse is reflected by the surface. Given the satellite altitude of roughly 800 km, this relates to a 2.67 ms delay to be added. If this correction was omitted, this would make the time tags early by that amount. If applied with the wrong sign, the time tags will be early by 5.34 ms. Upon verification (Bruno Greco, priv. comm.), the OPR processing does account of the delay, be it based on a constant altitude of 800 km, in stead of one varying between 785 and 815 km, leading to a 1-cpr timing error with an amplitude of about 0.05 ms.
- The Doppler correction (Section 4.4.2) is proportional to the altitude rate, so that omitting it will have the same effect on sea surface heights are making a timing error of 0.84 ms (see Eq. (4.5)), in the sense that time tags will seem early. If applied with the wrong sign, which happened in earlier ERS fast-delivery data [Scharroo, 1995a], time tags will appear early by 1.68 ms.

## 5.8 Conclusions

Crossover analyses demonstrate that the time stamps of the altimeter measurements of ERS-1 and ERS-2 are systematically early by an average of about 1.3 ms. The timing error estimates also exhibit an annual fluctuation with an amplitude of 0.1 to 0.2 ms. A larger mean bias, but smaller fluctuation is found for ERS-1. The analyses also suggest large diurnal variations in the timing error.

The annual and diurnal variations are for the most part attributable to geophysical phenomena and are not actual variations in the on-board clock. The annual variation that is caused by discontinuities in the UTC/SBT relation has an amplitude of about 0.08 ms.

The time tag bias due to the OBC quantisation is  $\frac{15}{32}$  of the OBC step length, making UTC time stamps late by 1.82 ms. Unfortunately, this sense is opposite to the values provided by the crossover analyses. Another 3 ms remains to be explained.

As a result of temperature variation along the orbit, the OBC frequency, and hence the step length of the clock counter changes. Since the step length is generally short at the Kiruna overpass, when SBT is correlated to UTC, the propagation of the UTC/SBT relation will result in early time tags. On average this accounts for about 0.04 ms. But it can also explain part of the annual variation in the time tag bias: during summer these propagation errors are larger than during winter.

---

The annual, diurnal and 1-cpr variations of the on-board clock, however, have such small impact on the sea surface heights that further detailed analysis is futile. At the same time, this also suggests that the variations can be ignored, and that a single constant time tag bias can be used for each of the satellites:  $-1.53$  ms for ERS-1,  $-1.17$  ms for ERS-2.



# Gravity Field Model Tailoring for the ERS Satellites

Between the start and the end of the ERS-1 mission significant advances have been made in gravity field modelling, culminating in general-purpose models like JGM-3 [Tapley *et al.*, 1996], TEG-3 [Tapley *et al.*, 1997] and EGM96 [Lemoine *et al.*, 1997]. However, even these models reveal significant defects when applied to orbit determination of some altimeter satellites, leading to large orbit errors, characterised by the geographically-correlated nature of the altimeter crossover height differences.

The perception that orbit errors can be reduced significantly by introducing more up-to-date general-purpose gravity field models, suggests that even more advancements can be made by creating a gravity model that is specifically tuned, or *tailored* to the orbit of the ERS satellites [Zandbergen *et al.*, 1986]. Obviously, such tailoring should not go at the expense of other satellite orbits; the aim is to create a gravity field model that performs better for ERS than general-purpose models, while at least performing as well as the general-purpose models for other satellites.

This Chapter describes how the ERS-tailored Delft Gravity Model DGM-E04 [Scharroo and Visser, 1998] was developed from JGM-3 by first isolating the gravity-induced part of the radial orbit error from crossover height differences and then attempting to eliminate them from the gravity field model. The quality of the tailored model is assessed and compared to other gravity field models, including the recent model GRIM5-C1 (GFZ, GRGS) [Gruber *et al.*, 2000]. Table 6.1 lists and describes the models discussed in the Chapter.

## 6.1 Linear perturbation theory

Gravity-induced orbit errors are, because of their origin, *geographically correlated*; that is, they are repetitive along the same ground track, repeat cycle after repeat cycle. This means that along two such collinear ground tracks gravity-induced

Year	Institute	Model	Description [Reference]
1992	NASA+CSR	JGM-1/2	First TOPEX-tuned models were a significant improvement over their precursors. [Nerem <i>et al.</i> , 1994]
1993	NASA+CSR	JGM-3	General-purpose solution, but 'tailored' to TOPEX. Large geographically correlated orbit errors, seen in average crossover height differences. [Tapley <i>et al.</i> , 1996]
1994	GFZ	PGM055	ERS-tailored version of GRIM4. Performs worse than JGM-3. [Gruber <i>et al.</i> , 1997]
1996	DUT/DEOS	DGM-E04	Based on JGM-3. Tailored to ERS by minimisation of average crossover height differences. Significant improvement over JGM-3. [Scharroo and Visser, 1998]
1996	NIMA+NASA	EGM96	General-purpose model based on satellite tracking and surface gravity. Complete to degree and order 360. Used only up to degree and order 70 in orbit determination. For ERS, not much better than JGM-3, worse than DGM-E04. [Lemoine <i>et al.</i> , 1997]
1996	UT/CSR	TEG-3	Multi-satellite solution with similar performance as EGM96. [Tapley <i>et al.</i> , 1997]
1998	UT/CSR	TEG-3P	Based on TEG-3. Tailored to ERS using PRARE tracking residuals. [Bordi, 1999]
1999	DUT/DEOS	DGM-E09	Based on EGM96. Tailored to ERS by minimisation of average crossover height differences, SLR and PRARE residuals. Improvement over DGM-E04: lower tracking residuals. [Scharroo <i>et al.</i> , 2000b]
2000	GFZ+GRGS	GRIM5-C1	General-purpose solution based on satellite tracking and surface gravity. Complete to degree and order 120. First model that performs better than DGM-E04. [Gruber <i>et al.</i> , 2000]

Table 6.1 Gravity field models of the ERS age, listed in chronological order of development.

orbit errors are identical and cancel when differencing the altimetric sea surface profiles along these tracks<sup>1</sup>. This is not the case for two crossing tracks; the different 'history' of gravity sensed along the ascending and descending passes causes the orbit error to be essentially different along each pass. Thus, we have to refine the term 'geographically correlated'.

Figure 6.1 shows how the gravity-induced radial orbit errors along ascending and descending tracks ( $\Delta r^{\text{asc}}$  and  $\Delta r^{\text{des}}$ , respectively) can alternatively be decomposed into a *geographically fully-correlated* and *geographically anti-correlated* component ( $\Delta r^c$  and  $\Delta r^s$ ). By definition, the first component is identical on both passes; the second is of equal magnitude on both passes but of opposite sign. In literature [e.g., Tapley and Rosborough, 1985; Rosborough, 1986] these components are often given the confusing indications 'mean error' and 'variability error'. It should be stressed that there is nothing 'variable' about the component  $\Delta r^s$ , which is just as time-invariant as the 'mean' component  $\Delta r^c$ , with the only difference that  $\Delta r^s$  has

<sup>1</sup>If this is not immediately evident, read Appendix B first.



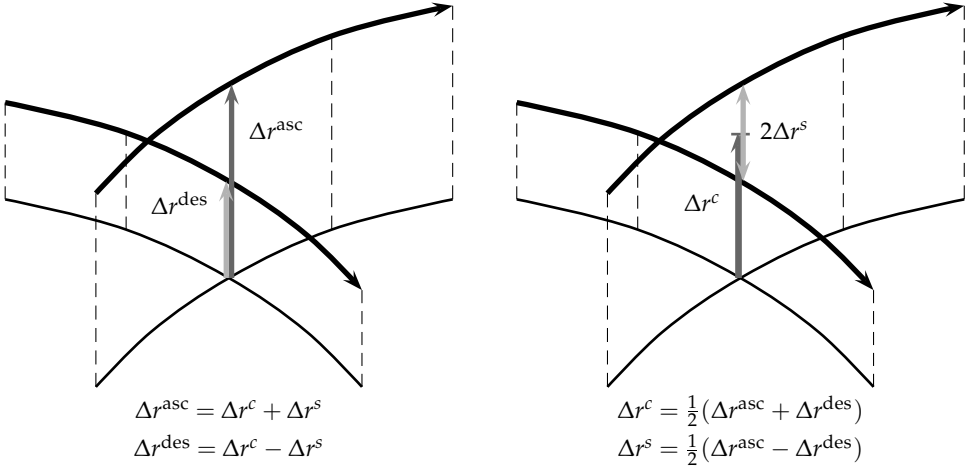


Figure 6.1 Geographically correlated orbit errors along two crossing passes.

an opposite sign on the two passes. Thus, we write for the gravity-induced radial orbit error in a crossover point

$$\Delta r = \Delta r^c \pm \Delta r^s \quad , \quad (6.1)$$

where the plus sign is used for the ascending pass and the minus sign for the descending pass.

Linear Perturbation Theory (LPT) (Appendix B) describes the three orthogonal components of the orbit error as a linear combination of terms due to (commission or omission) errors in the gravity model coefficients. Each coefficient produces errors at various frequencies, depending on their harmonic degree  $l$  and order  $m$ . It can be easily shown (Eq. (B.34) in Section B.8) that on the near-circular, Sun-synchronous, and ‘frozen’ ERS orbit, the dominant errors have frequencies

$$\psi_{lmp} = (l - 2p) \text{ cpr} - m \text{ cpd} \quad , \quad (6.2)$$

where  $p$  ranges from 0 to  $l$ , cpr is cycles per revolution and cpd is cycles per day. Some combinations of  $l - 2p$  and  $m$  cause  $\psi_{lmp}$  to be close to the resonance frequencies 0 and 1 cpr (Section B.8.3). For ERS’ 35-day repeat this happens for coefficients of order 43 because 43 cpd is very close to 3 cpr.

Appendix B explains how the temporal variation of the radial orbit error maps into a spatial distribution. A convenient formulation is:

$$\Delta r = \sum_{l=1}^{\infty} \sum_{m=0}^l \Delta r_{lm}^c \pm \Delta r_{lm}^s \quad , \quad (6.3)$$

with

$$\Delta r_{lm}^c = \overline{Q}_{lm}^c (\Delta \overline{C}_{lm} \cos m\bar{\lambda} + \Delta \overline{S}_{lm} \sin m\bar{\lambda}) \quad , \quad (6.4)$$

$$\Delta r_{lm}^s = \overline{Q}_{lm}^s (\Delta \overline{C}_{lm} \sin m\bar{\lambda} - \Delta \overline{S}_{lm} \cos m\bar{\lambda}) \quad , \quad (6.5)$$

where  $\overline{Q}_{lm}^c$  and  $\overline{Q}_{lm}^s$  are both functions of latitude and further depend on the orbit's mean semi-major axis, eccentricity, and inclination.

This yields the following:

1. When computing crossover differences,  $x$ , the fully-correlated part cancels, but the anti-correlated part of the orbit error is observed at double efficiency, since

$$\Delta x = \Delta r^{\text{asc}} - \Delta r^{\text{des}} = 2\Delta r^s \quad . \quad (6.6)$$

2. The zonal coefficients do not contribute to crossover differences since  $\sin m\bar{\lambda} = 0$  and  $\overline{S}_{lm} = 0$  for  $m = 0$ .
3. Non-zonal coefficients of the gravity field do contribute to crossover differences, each with a distinct global pattern.
4. *Vice versa*, when we can *isolate* and observe the effect of gravity model deficiencies in crossover differences, the non-zonal coefficients can be tuned to reduce the observed effect.
5. Because of singularities in  $\overline{Q}_{lm}^c$  and  $\overline{Q}_{lm}^s$ , resonant terms are not considered. However, as shown in Section B.8.4, this has little or no impact on our analysis of the geographically correlated orbit error.

The LPT has been used before to cancel gravity-induced radial orbit errors, but never in such a way that it actually provided a well-tuned gravity model. *Engelis* [1987, 1988] and *Visser* [1992] use LPT to simultaneously improve dynamic topography and geoid from Seasat and Geosat altimeter data. The link between geoid and orbit errors provide the means to partially separate geoid and dynamic topography. *Visser* [1995] extends the technique by including SLR and single- and dual-satellite crossover differences. Because the gravity-induced orbit error was not isolated from other orbit errors, each of the additional estimated parameters in orbit determination also had to be readjusted. Novel in the approach proposed here is the use of crossover height differences instead of altimetric sea heights (thus cancelling geoid and dynamic topography errors) and the use of the two-step approach: first isolating the gravity-induced signal and then adjusting the gravity field coefficients.

## 6.2 Isolating the gravity-induced orbit errors

The geographically anti-correlated orbit error is only one of the many contributions to crossover differences. The assumption we make is that all contributions, except the constant gravitational, are time variant and average out to zero over a

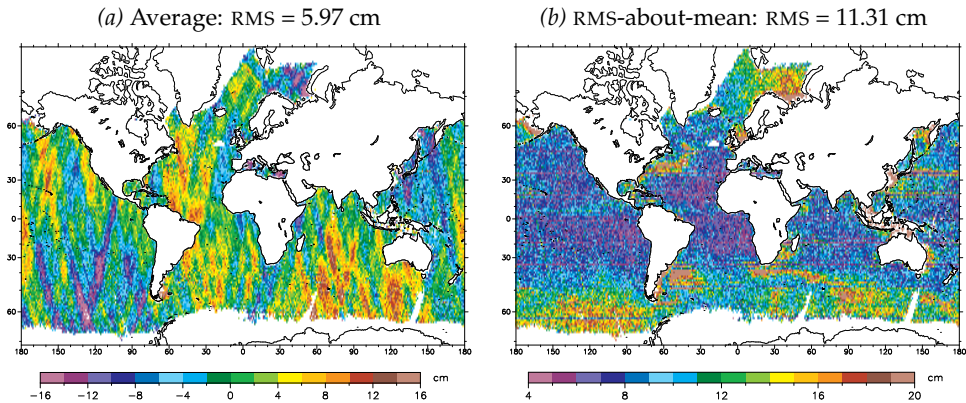


Figure 6.2 (a) Average and (b) RMS-about-mean of stacks of ERS-1 and ERS-2 single-mission altimeter crossover height difference residuals for the period of April 1992 till August 1995. Gravity model JGM-3. Apparent altimeter time tag bias is applied.

sufficiently long period, like a year or more, or are not observed at the maximum time interval of 17.5 days in our set of crossover differences.

The generation of local average crossover differences can easily be performed by gridding the data on a regular latitude-longitude grid. However, this will remove some signal at high latitudes where, because of the closure of crossover locations, the spatial scales are much shorter than around the equator.

A more sophisticated approach takes advantage of the fact that crossovers are already located on a more or less regular ‘grid’ which densifies toward the poles. Crossovers can be stacked together at the ‘grid points’. Following a  $3.5\text{-}\sigma$  editing in each stack, the average of the crossover differences in each grid point ( $\bar{x}$ ) represents twice the geographically anti-correlated orbit error ( $2\Delta r^2$ ), while the RMS-about-mean ( $\sigma_x$ ) resembles  $\sqrt{2}$  times the root-sum-square of the non-gravitational orbit error, sea surface variability, and altimeter correction errors. An additional  $3.5\text{-}\sigma$  editing is performed over all  $\sigma_x$  values to eliminate data in areas of extreme variability.

We ignore the fact that the crossover locations actually vary from repeat cycle to repeat cycle within a radius of about 1 km because of drifting of the ground track around the nominal position by the same amount. This is allowed since the signal we are isolating has much longer wavelengths than 1 km. Also, we are not hampered by cross-track geoid slopes since we have constructed the crossover differences at their true locations and not nominal locations, and if we had, this would have been tackled by taking a high-resolution mean sea surface model as reference.

This technique was applied to a total of about 1 000 000 ERS-1 and ERS-2 single-mission crossovers for the period of April 1992 until August 1995, created from the OPR altimeter products as described in Section 1.2.5. All crossover differences were first adjusted by replacing the GFZ orbits by DUT second-generation

JGM-3 orbits, simultaneously accounting for an estimated time tag bias of  $-1.3$  and  $-1.1$  ms for ERS-1 and ERS-2, respectively<sup>2</sup>. The average and the RMS-about-mean of the crossover differences at the 45 000 ‘grid points’ are sketched in Figure 6.2. The RMS-about-mean clearly resembles what we know of meso-scale sea surface variability (high in Western Boundary Currents, low in the Central Pacific) and areas with large ocean tide modelling errors (*e.g.*, East China Sea, Indonesian Archipelago). Clearly noticeable are a few latitude bands with remarkable low local variance, crossing clear through the high-variability regions; these bands pertain to crossovers with a time lag of about 12 hours, during which sea surface variability is minimal. Note also the significance of the averages compared to the RMS-about-mean: in areas with little or no variance (central Pacific) the average may be a couple of times larger than the RMS-about-mean. This indicates that the isolation of the gravity-induced contribution to crossover differences functions quite well and that the gravity-induced orbit error is sizable compared to non-gravitational errors.

The perception that much of the radial orbit error is caused by deficiencies of JGM-3, leads to the attempt to develop a model specifically tailored to ERS orbit determination. This is done by adjusting a well-chosen set of gravity field coefficients such that the gravity-induced orbit error observed in the crossover differences is minimised.

### 6.3 Tailoring the gravity field model

Tailoring a gravity field model involves the tuning of its coefficients such that residuals of observations from a single satellite are reduced. Usually, only a subset of coefficients is adjusted because others may not affect the residuals; like, in our case, we cannot observe errors in the zonal coefficients in the crossover differences. We limit ourselves to those combinations of degree and order  $(l, m)$  that, according to LPT, produce a global RMS crossover difference of 2 mm or more, assuming a  $1\text{-}\sigma$  error in either JGM-3 coefficient  $\bar{C}_{lm}$  or  $\bar{S}_{lm}$ . This leads to a set of 550 pairs of  $\bar{C}_{lm}$  and  $\bar{S}_{lm}$  coefficients to be adjusted while other gravity coefficient errors are deemed to be too poorly observed in the crossover differences for any adjustment to be realistic. This selection of coefficients captures nearly all of the predicted orbit error spectrum.

Solving the gravity coefficient adjustments  $\Delta\bar{C}_{lm}$  and  $\Delta\bar{S}_{lm}$  from (6.5) and (6.6) leads to a set of linear equations with 45 000 observations and 1100 unknowns. Because the number of observations far exceeds the number of unknowns, we solve the unknowns in a Bayesian linear least-squares fashion

$$(A^T W A + f N) c = A^T W x \quad , \quad (6.7)$$

<sup>2</sup>Late 1995, second-generation JGM-3 orbits, Bent ionospheric correction, FES95.2.1 ocean and load tides, and OSU MSS95 mean sea surface model were used instead of the models mentioned in Chapter 2. This explains why some crossover statistics presented in this Section may compare unfavourable to those listed in the later verifications based on the current state-of-the-art orbits and models.

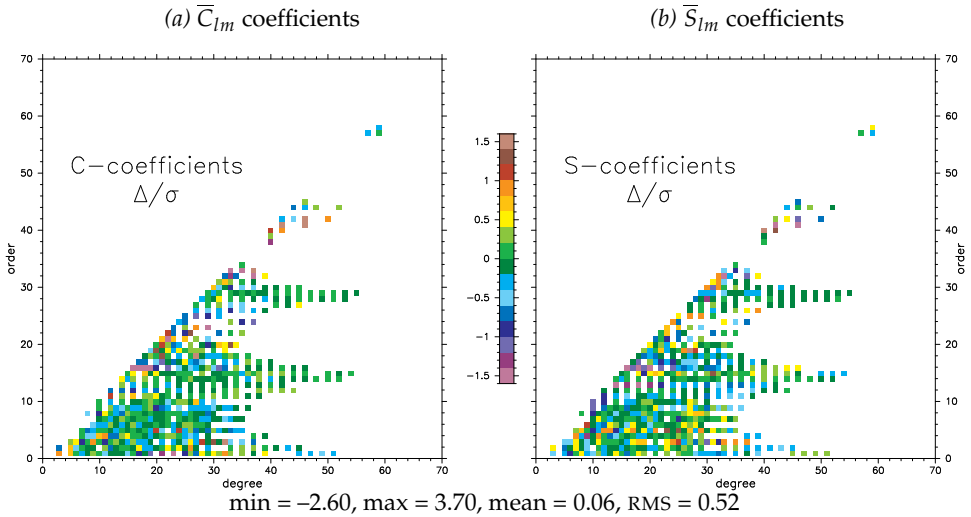


Figure 6.3 Estimated gravity coefficient adjustments to JGM-3 to obtain DGM-E04. All adjustments ( $\Delta$ ) are normalised through division by the formal error ( $\sigma$ ) of the original JGM-3 coefficients.

where

- $c$  = the vector of unknowns ( $\Delta\bar{C}_{lm}, \Delta\bar{S}_{lm}$ );
- $x$  = the vector of average crossover differences ( $\bar{x} \approx \Delta x$ );
- $A$  = the matrix of partials ( $2\bar{Q}_{lm}^s \sin m\bar{\lambda}, -2\bar{Q}_{lm}^s \cos m\bar{\lambda}$ );
- $W$  = a diagonal matrix of observation weights, given by  $n/(\sigma_x)^2$ , where  $n$  is the number and  $\sigma_x$  is the RMS-about-mean of crossover differences in each stack; and
- $fN$  = the JGM-3 normal matrix  $N$  (= inverse of the error variance-covariance matrix, kindly provided by John Ries, CSR) multiplied by a weighting factor  $f$ .

Because we only have observations over oceans and only up to a certain latitude, we need to constrain the solution elsewhere. This is done by adding the relevant part of the JGM-3 normal matrix to the normal equations. The factor  $f$  further determines how tight the solution is to be constrained. The optimal value for  $f$  (=10) was found experimentally, weighing between an almost total reduction of the geographically anti-correlated orbit error but unrealistically large gravity field adjustments (small  $f$ ) and small adjustments but insignificant reduction of the orbit error (large  $f$ ).

Figure 6.3 shows the adjustments to the 1100  $\bar{C}_{lm}$  and  $\bar{S}_{lm}$  coefficients of JGM-3 divided by their formal standard deviations ( $\Delta/\sigma$ ). The RMS of all values  $\Delta/\sigma$  is 0.52, which means that the new solution falls well within the error budget of JGM-3. Largest adjustments are to some coefficients around orders 16, 33, and 41

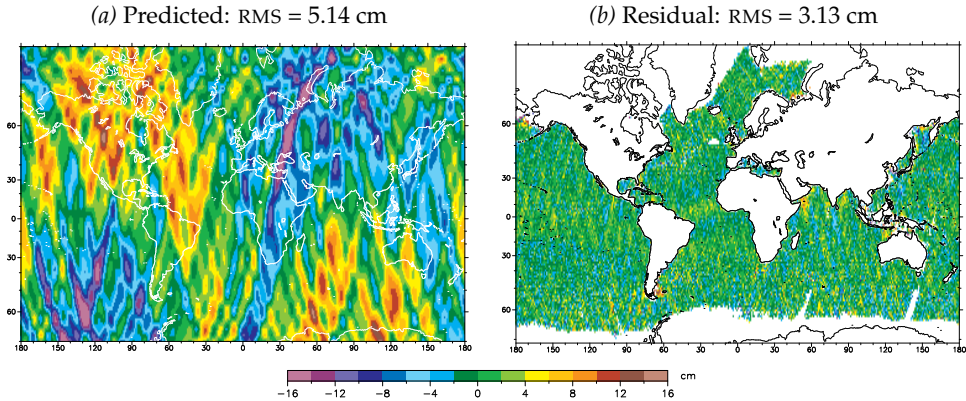


Figure 6.4 (a) Geographically anti-correlated orbit error implied by the differences between the JGM-3 and DGM-E04 gravity models. Values are multiplied by 2 to resemble the average crossover differences in Figure 6.2a. (b) Residual averaged crossover differences when subtracting Figure 6.4a from the average crossover differences in Figure 6.2a.

but are still within acceptable limits. Thus we have generated the ERS-tailored *Delft Gravity Model DGM-E04*.

With (6.5) and (6.6) it is quite easy to determine the global distribution of the geographically anti-correlated orbit error implied by the coefficient adjustments, as shown in Figure 6.4a. Note that the implied errors over the continents are not significantly different in size from ocean areas, which again indicates that the constraint was successfully applied. From this it is an easy step to project how the remaining average crossover differences would look when replacing JGM-3 for DGM-E04 in the POD (Figure 6.4b). It reduces the global RMS of the average crossover differences from 5.98 to 3.13 cm, which implies that the geographically anti-correlated orbit error reduces from about 3.0 to 1.6 cm.

## 6.4 Independent assessment of DGM-E04

Reducing one particular manifestation of errors in a gravity field model by changing a few of its coefficients is one thing, *improving* the model is another. First of all, the adjustment of the gravity coefficients implies a change in the geoid, as shown in Figure 6.5a. Clearly, the JGM-3 geoid was well constrained over the oceans, allowing little or no adjustments to occur there. The improvements, or at least the changes, come from areas where the JGM-3 geoid is most weakly determined: over the polar regions. To demonstrate that these geoid adjustments are not excessive, Figure 6.5b displays the geoid difference between JGM-3 and its direct successor, EGM96, truncated to degree and order 70. Again, adjustments are minor over oceans and significant over the polar regions and some continental areas. The

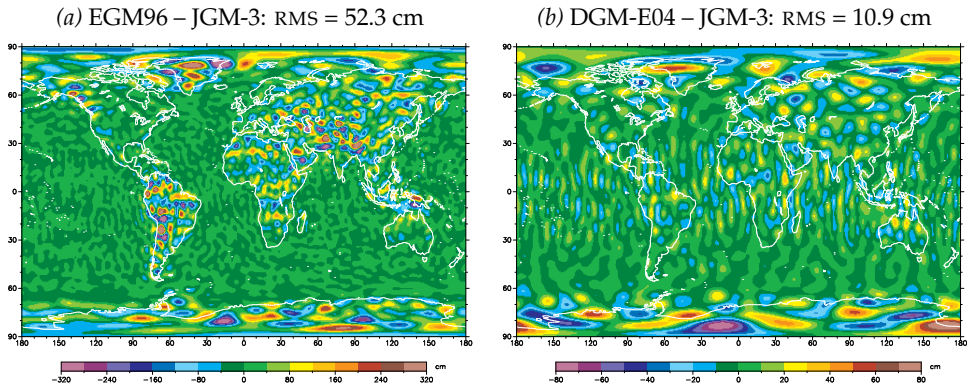


Figure 6.5 Geoid height differences between JGM-3 and newer gravity field models: (a) EGM96 (truncated at degree and order 70), and (b) DGM-E04. RMS values are weighted by area. Note the difference in colour scale.

RMS geoid difference between these models is even five times larger than between JGM-3 and DGM-E04, indicating that relatively small gravity field adjustments can introduce significant orbit improvements.

Richard Rapp (OSU, personal communication, 1997) verified the lower degree and order coefficients (up to 14) of DGM-E04 by applying it as a long-wavelength reference geoid for the extraction of a global ocean dynamic topography from TOPEX/Poseidon sea surface heights. The resulting topography differs from the numerical ocean model POCM-4B by 12.55 cm RMS. The same analysis with JGM-3 gives a similar RMS residual of 12.62 cm. This suggests that for this application, DGM-E04 indeed acts within the error margins of JGM-3.

Frank Lemoine (GSFC, personal communication, 1997) tested the suitability of DGM-E04 for TOPEX orbit determination. Having a completely different orbit from ERS, its sensibility to the gravity field is likewise dissimilar. This means that adjustments to some coefficients that had little effect on the ERS orbit might produce significant errors in the TOPEX orbit. Table 6.2 shows the results of computing a random set of four TOPEX orbits based on SLR and DORIS tracking data and each using three different gravity models: JGM-2, JGM-3, and DGM-E04. The data fits appear least sensitive to the choice of gravity model. Comparisons of the SLR/DORIS orbits with GPS reduced-dynamic orbits produced by JPL, however, show a clear preference for the DGM-E04 model. Since the GPS reduced-dynamic orbits are virtually unaffected by gravity model errors, this test would indicate that the one that comes closest has the least gravity-induced orbit error. In 11 out of the 12 cases it is the DGM-E04 orbit that fits the GPS orbit best in radial, cross-track, and along-track direction.

Gravity model	Data fits		RMS diff. with GPS arc (cm)		
	SLR (cm)	DORIS (mm/s)	Radial	Cross	Along
<b>Cycle 10</b>					
JGM-2	4.58	0.580	3.02	6.85	11.89
JGM-3	<b>4.60</b>	<b>0.577</b>	2.18	6.45	8.97
DGM-E04	4.63	<b>0.577</b>	<b>2.14</b>	<b>5.99</b>	<b>8.28</b>
<b>Cycle 19</b>					
JGM-2	4.42	0.551	3.71	5.17	10.51
JGM-3	<b>4.24</b>	<b>0.546</b>	3.00	3.52	7.66
DGM-E04	4.29	<b>0.546</b>	<b>2.98</b>	<b>3.43</b>	<b>7.45</b>
<b>Cycle 21</b>					
JGM-2	3.05	0.539	3.20	5.40	7.93
JGM-3	<b>2.86</b>	<b>0.537</b>	<b>2.46</b>	5.03	5.86
DGM-E04	2.89	<b>0.537</b>	2.48	<b>4.73</b>	<b>5.83</b>
<b>Cycle 46</b>					
JGM-2	3.00	0.565	2.48	6.76	7.80
JGM-3	<b>2.73</b>	<b>0.563</b>	<b>1.74</b>	4.53	5.11
DGM-E04	2.74	<b>0.563</b>	<b>1.74</b>	<b>3.63</b>	<b>4.76</b>

Table 6.2 Statistics of TOPEX orbit computations with the JGM-2, JGM-3, and DGM-E04 gravity models performed at GSFC (Frank Lemoine, personal communication, 1997). Parameterisation of the orbits is the same as in the second-generation TOPEX precise orbits, as documented by *Marshall et al.* [1995]. Listed are the SLR and DORIS tracking data residuals and orbit differences with the JPL reduced-dynamic orbits based on GPS tracking data. Lowest values for each cycle are printed in bold font.

## 6.5 Gravity-induced orbit errors

The third-generation orbits (Section 3.2.3) cover the entire ERS Tandem Mission, starting on 29 April 1995 with the switch-on of the ERS-2 altimeter and ending on 2 June 1996 with the switch-off of the ERS-1. We have chosen this period to compare the results obtained with the JGM-3, EGM96, DGM-E04, and GRIM5-C1 gravity models and to analyse the respective orbit accuracies. Because only 30% of the Tandem Mission overlaps with the data period of the DGM-E04 tailoring, the verification can be considered to be nearly independent. Naturally, we expect the gravity model tuning to have the same effect on the orbits for this particular period as on any other.

In this Section we will first show the impact of the gravity model selection on the tracking data residuals, followed by an assessment of the geographically correlated orbit errors based on ERS single- and ERS/TOPEX dual-satellite cross-overs, and finally look at the orbit differences. In Section 6.6.1, collinear altimeter profiles are analysed to determine the orbit errors due to non-conservative forces.



Data type	Number	Orbit solution			
		JGM-3	EGM96	DGM-E04	GRIM5-C1
<b>ERS-1</b>					
SLR residuals (RMS), cm	47 207	4.75	4.73	3.86	2.68
Crossover differences (RMS), cm	132 718	9.52	9.15	8.13	8.15
Altim. time tag bias (mean $\pm\sigma$ ), ms	104	-1.24 $\pm$ 0.16	-1.43 $\pm$ 0.16	-1.50 $\pm$ 0.13	-1.48 $\pm$ 0.12
<b>ERS-2</b>					
SLR residuals (RMS), cm	47 213	4.64	4.73	3.77	2.65
Crossover differences (RMS), cm	127 228	9.63	9.25	8.23	8.24
Altim. time tag bias (mean $\pm\sigma$ ), ms	104	-1.05 $\pm$ 0.14	-1.25 $\pm$ 0.15	-1.28 $\pm$ 0.14	-1.26 $\pm$ 0.13
<b>ERS-1 minus ERS-2</b>					
Altim. range bias (mean $\pm\sigma$ ), cm	104	4.14 $\pm$ 0.51	4.13 $\pm$ 0.53	4.15 $\pm$ 0.51	4.15 $\pm$ 0.49

Table 6.3 Results of the simultaneous ERS orbit determination for 104 orbital arcs of the Tandem Mission. Only tracking data in the middle 3.5 days of each arc are considered. The SLR residuals pertain to a set of 12 high-performance stations only (listed in Table 6.4). The crossover difference residuals pertain to each single component of a crossover, so each crossover is counted twice and no differentiation is made between single- and dual-satellite crossovers. The altimeter time tag biases and relative range bias are estimated independently for each orbital arc. Only arcs without significant orbital manoeuvres are considered.

### 6.5.1 Precise orbit determination results

The tracking data residuals (measured minus computed SLR ranges and crossover height differences) are a measure for the orbit accuracy. These residuals should be interpreted with care, since the data that have been used in the POD are likely to underestimate the actual orbit error. Moreover, the SLR range residuals are a measure of the orbit accuracy in all three directions, whereas the crossover differences depend on the radial orbit error only.

Table 6.3 presents the results for 104 arcs of 5.5 days, in which ERS-1 and ERS-2 orbits are determined simultaneously, alternatively computed with the JGM-3, EGM96, DGM-E04, and GRIM5-C1 gravity models. Listed are the statistics of the SLR range residuals of 12 high-performance stations, the statistics of the satellite-specific components of the crossover difference residuals (so each single and each dual crossover are counted twice), and the estimates of the apparent altimeter time tag bias and relative altimeter range bias.

Note that the crossover difference residuals are the smallest in the DGM-E04 solutions. This is to be expected since crossover differences have been used to tailor the gravity model, starting from JGM-3. More relevant is the fact that DGM-E04 even performs better than the more recent EGM96 model, not only in terms of the RMS crossover difference, but also judging from the SLR residuals, and this while SLR data have not been used to tune the model. The GRIM5-C1 model, however, clearly masters any of the other models as far as the SLR residuals are concerned.

The POD also provides estimates for deficiencies in the datation of the altimeter data. Although the estimated parameters could also absorb part of the 2-cpr errors in the restituted orbital altitude as well as constant along-track errors, the larger part will indeed be related to the altimeter datation. Table 6.3 clearly shows that the OPR altimeter time tags are systematically early by 1.3 to 1.5 ms for ERS-2 and ERS-1, respectively, which is in accordance with findings presented in Chapter 5.

## 6.5.2 High-elevation SLR passes

Despite the aforementioned limitations, the SLR residuals of high-elevation overflights of laser ranging stations can provide at least some indication of the orbit's vertical accuracy. Along near-vertical overflights the cross-track orbit error does not affect the residuals, and system noise and along-track orbit error can be separated from the radial by fitting a two-parameter curve through the SLR residuals. The two parameters, range bias and timing bias, relate closely to the radial and along-track orbit error. Table 6.4 lists the statistics of these apparent range biases for near-vertical overflights of ten high-performance SLR stations.

When we distinguish between ascending and descending passes, the average of the apparent range biases per station becomes a measure for the local geographically correlated radial orbit error along each pass, *i.e.*,  $-\Delta r^{\text{asc}}$  and  $-\Delta r^{\text{des}}$ , where

Site	Location	Number of passes		JGM-3			EGM96			DGM-E04			GRIM5-C1		
		asc	des	Mean	$\sigma$		Mean	$\sigma$		Mean	$\sigma$		Mean	$\sigma$	
AREL	Arequipa, Peru	59	31	-21	-24	16	-35	-11	22	-7	10	20	-21	-14	14
GRSL	Grasse, France	40	7	-9	-53	19	4	-21	22	0	-14	17	-3	-10	16
GRZL	Graz, Austria	61	18	-11	-33	18	-1	-24	22	0	-4	19	0	2	14
GOFL	Greenbelt, Maryland	23	13	1	-10	16	-15	-3	20	3	6	13	-2	-14	11
HERL	Herstmonceux, England	62	43	3	-10	18	4	0	20	0	0	17	6	1	12
MONL	Monument Peak, Calif.	74	41	14	24	20	8	33	30	17	0	25	10	9	16
ORRL	Orroral Valley, Victoria	10	9	2	28	24	-13	12	21	-29	24	27	-32	-6	16
POTL	Potsdam, Germany	89	5	-5	-24	22	0	2	20	5	4	21	5	8	15
7109	Quincy, California	34	15	9	39	22	6	47	21	12	11	16	2	1	13
YARL	Yarragadee, W-Australia	69	47	-16	3	18	-16	-2	15	-7	1	14	-2	-3	11
MDOL	Fort Davis, Texas	0	0												
WETL	Wetzell, Germany	0	0												
Total (RMS)		521	229	12	23	19	14	21	22	9	7	19	10	8	14
(des+asc)/2 (RMS)							17		15			5			9
(des-asc)/2 (RMS)							10		10			7			3

Table 6.4 Statistics of the apparent SLR range biases of near-vertical overflights. The apparent range bias is estimated simultaneously with a timing bias for each pass with at least eight measurements before and after the culmination point and a highest elevation of at least  $65^\circ$ . For all three orbit solutions the average range biases along ascending passes (asc) and along descending passes (des) and the RMS-about-mean ( $\sigma$ ) of the range biases around the respective means are shown. Values are in millimetres.

the minus signs come from the fact that the SLR range residuals are ‘observed minus computed’ and the orbit errors are ‘computed minus true’. The station-by-station averaging removes the time variant part of the orbit error associated with non-conservative forces (listed in Table 6.4 under ‘ $\sigma$ ’) and isolates the time-invariant geographically correlated part (under ‘Mean’).

The mean of a station’s ascending and descending averages would resemble the geographically fully-correlated orbit error ( $-\Delta r^c$ ), if it were not for constant system biases and station coordinate errors persisting in this value. Computing half the difference between the descending and ascending averages eliminates the constant errors and provides a better estimate for the geographically anti-correlated orbit error ( $-\Delta r^s$ ). The RMS of these linear combinations are listed at the bottom of Table 6.4 and are indicative of the improvement of DGM-E04 over JGM-3 and even over EGM96, but should not be regarded as an accurate representation of the actual geographically correlated orbit error.

The fact that the estimates for the geographically correlated orbit errors in DGM-E04 and GRIM5-C1 are similar demonstrates how well the DGM-E04 model performs in that respect. However, the lower RMS-about-mean of the apparent range biases in the GRIM5-C1 case indicates that DGM-E04 has improved SLR residuals to some extent, but not enough. The lingering along- and cross-track orbit errors cause the DGM-E04 orbits to be less consistent.

### 6.5.3 Geographically anti-correlated orbit error

To demonstrate that the reduction of the geographically anti-correlated orbit error is also apparent in the actual computed orbits for the Tandem Mission, we have generated local averages and RMS-about-mean of crossover differences like in Section 6.2 and alternatively took the GFZ PGM055 orbit from the OPR data or substituted our third-generation orbits<sup>3</sup>. In each case the  $\sim 870\,000$  crossovers covering the Tandem Mission are reduced to some 50 000 locations.

The statistics and graphs in Figure 6.6a-e indeed show that the average crossover differences are the smallest with DGM-E04. Both PGM055 and, to a lesser extent, JGM-3 display large geographically correlated orbit errors in distinctive narrow patterns,  $10^\circ$  to  $20^\circ$  wide. These patterns can be associated with errors in the near-resonant terms of the gravity field. These terms appear slightly better conditioned in the EGM96 model, in which broader features, however, still persist. In the DGM-E04 solution all of these features are absent, like in the GRIM5-C1 solution. What remains is a chaotic pattern of small spatial scales of which the origin is not clear.

The RMS of the geographically anti-correlated radial orbit error equals half the RMS of the average crossover differences displayed in Figure 6.6. Note that the result for DGM-E04 is virtually the same as was predicted in Figure 6.4b, and compares favourably to GRIM5-C1.

<sup>3</sup>All other corrections are as described in Chapter 2.

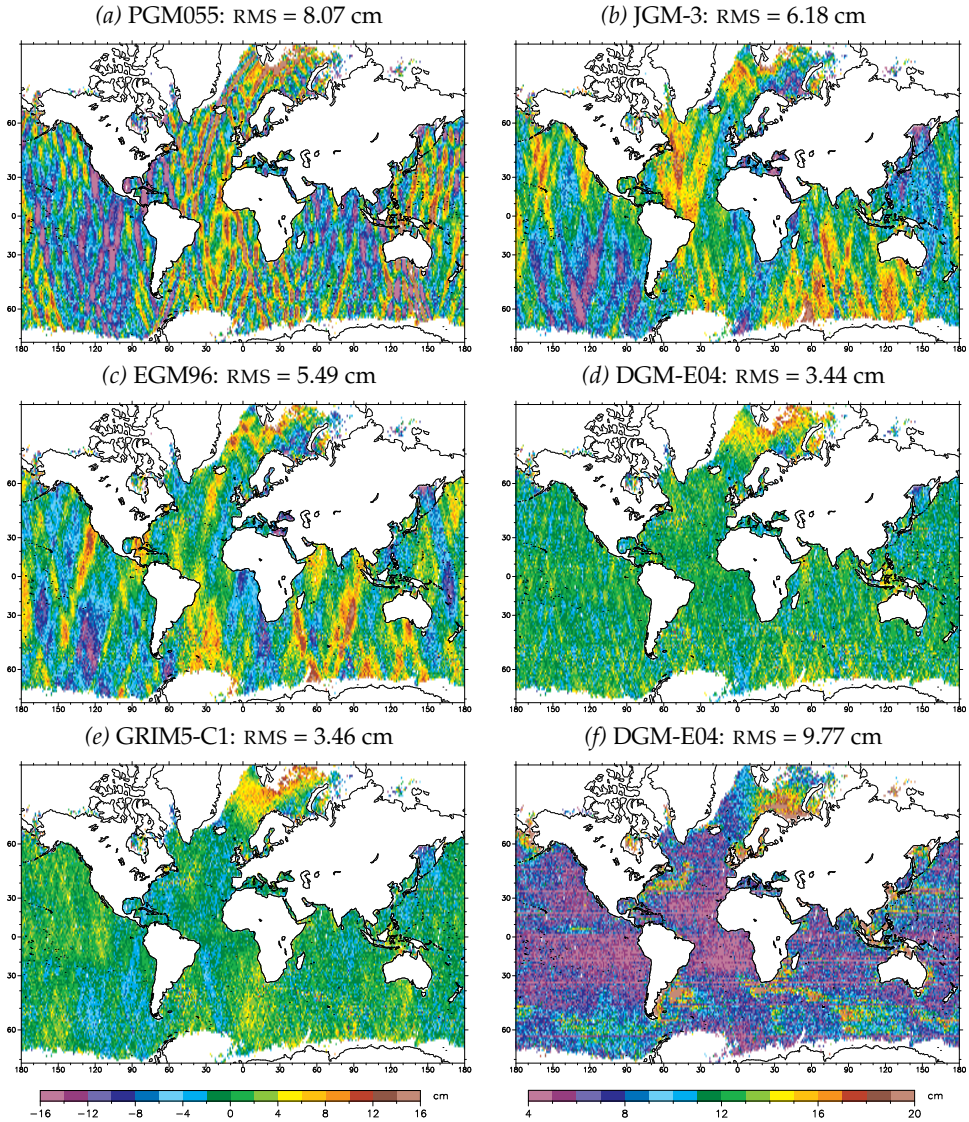


Figure 6.6 (a-e) Averages of stacks of ERS-1 and ERS-2 single-mission crossover height difference residuals (Tandem Mission). The various graphs pertain to five different ERS orbit solutions: (a) GFZ PGM055 and (b) DUT JGM-3, (c) EGM96, (d) DGM-E04, and (e) GRIM5-C1. (f) Local RMS-about-mean of stacks of ERS-1 and ERS-2 single-mission crossover height difference residuals based on DGM-E04 orbits (Tandem Mission).

The RMS-about-mean of the crossover differences displayed in Figure 6.6*f* is for DGM-E04, but is quite indifferent between the various orbit solutions. The larger part of the variance can be attributed to sea level variability.

#### 6.5.4 Geographically fully-correlated orbit error

Until now we have mainly considered the geographically *anti*-correlated orbit error, which is observed in single-satellite crossover differences and is used to tune the gravity model. The *fully*-correlated orbit error ( $\Delta r^c$ ), which is invisible in crossover differences, has, by rule of thumb, about the same variance [Rosborough, 1986]. To verify whether the tuning also reduced the geographically fully-correlated orbit error, or at least did not increase it, we have computed ERS/TOPEX dual-altimeter crossovers for the same period during the Tandem Mission, as before. The TOPEX data are extracted from the latest release of merged geophysical data records (cycles 98–136) [AVISO, 1996], applying the appropriate corrections, as discussed in Chapter 2.

A justifiable assumption is that TOPEX orbit errors are small compared to those of ERS [Le Traon *et al.*, 1995*b*; Marshall *et al.*, 1995], such that ERS/TOPEX dual satellite crossover differences display ERS' orbit errors rather than TOPEX's. Again, local averaging of crossover differences can be used to eliminate time variant errors. Because ascending and descending passes of ERS do not meet in the same crossover with TOPEX passes, it is actually more practical to average on an equi-rectangular grid. The acquired average ERS/TOPEX crossover difference is representative of the geographically fully-correlated orbit error for ERS.

Figure 6.7 shows averages of ERS-1/TOPEX and ERS-2/TOPEX crossover differences for five different ERS orbit solutions: PGM055, JGM-3, EGM96, DGM-E04, and GRIM5-C1. Appropriate time tag biases and range biases for ERS-1 and ERS-2 are applied to give a good match with TOPEX. PGM055 is again the one to show the most evident track-like pattern associated with near-resonant terms. Striking is the broad structure that seems to persist throughout JGM-3, EGM96, and DGM-E04 orbit solutions. It even appears to be the only significant structure remaining in the DGM-E04 solution. The reduction of the RMS-about-mean from 4.73 (JGM-3) to 2.87 cm (DGM-E04) remains a remarkable achievement, since the fully-correlated orbit error was not involved in the gravity field tailoring process. It demonstrates that the fully-correlated orbit error is correlated with the anti-correlated orbit error; evidently, the tailored model indeed constitutes an overall improvement, not merely a reduction of one observable.

It is not certain that the remaining pattern for DGM-E04 (Figure 6.7*d*) is a true reflection of the actual geographically correlated orbit error of ERS. The ERS/TOPEX crossover differences will be partly corrupted by TOPEX orbit errors and any time-invariant or geographically correlated difference between ERS and TOPEX altimetry. Even though we have attempted to harmonise the altimeter biases, sea state bias, and the ocean tide corrections, persistent differences in the modelling of propagation corrections may cause part of the effect. The distribution

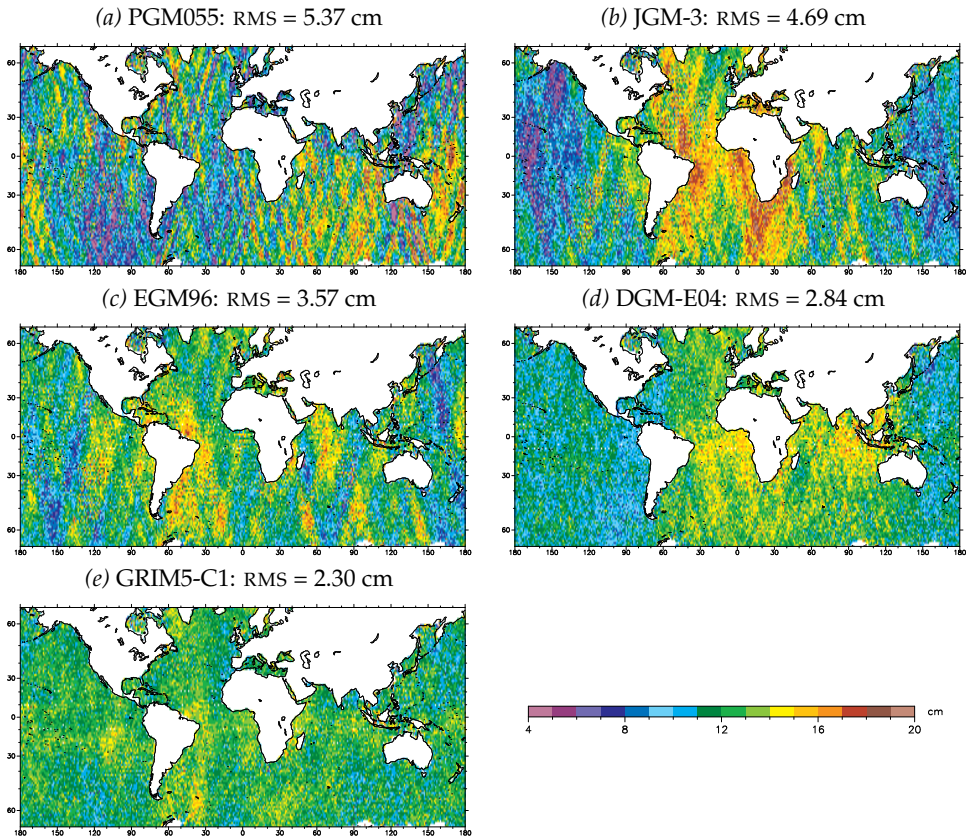


Figure 6.7 Locally averaged ERS–TOPEX dual-satellite crossover height difference residuals for the ERS Tandem Mission. The graphs pertain to five different orbit solutions for ERS: (a) GFZ PGM055 and (b) DUT JGM-3, (c) EGM96, (d) DGM-E04, and (e) GRIM5-C1. Sea surface heights of ERS-1 and ERS-2 have been reduced by 2.7 and 6.7 cm, respectively.

of the ERS/TOPEX crossover differences based on the DGM-E04 orbits suggests, at first glance, a geocentre offset between the station coordinates used to compute the ERS orbits on one hand and the TOPEX orbits on the other. Such geocentre offsets are estimated and listed in Table 6.5. A significant reduction of RMS-about-mean of the crossover differences can be obtained by removing the geocentre offsets, particularly in the case of the JGM-3 and DGM-E04 orbit solutions.

Although the same stations coordinates were used in the computation of all DUT orbits, the estimated geocentre offset of the GRIM5-C1 orbits is much smaller than the others. Hence, it becomes more likely that what we observe is caused by errors in a few (zonal) gravity coefficients. DGM-E04 evidently ‘inherited’ some of these defects from the JGM-3 model.

ERS orbit solution	Geocentre Offset			Residuals	
	$\Delta X$	$\Delta Y$	$\Delta Z$	a priori	a posteriori
GFZ PGM055	-0.36	2.68	-0.29	5.37	5.20
DUT JGM-3	5.58	0.33	0.04	4.69	3.70
DUT EGM96	1.67	-0.41	0.13	3.57	3.46
DUT DGM-E04	2.33	1.87	0.22	2.84	2.42
DUT GRIM5-C1	0.59	-0.20	-0.02	2.30	2.28

Table 6.5 Estimated geocentre offsets ( $\Delta X$ ,  $\Delta Y$ ,  $\Delta Z$ ) between ERS and TOPEX orbits suggested by the averaged crossover height differences depicted in Figure 6.7. The reduction of the RMS-about-mean of the averaged crossover height difference is listed in the rightmost two columns. Values are in centimetres.

Finally, we would like to emphasise that for many applications of altimetry, such as the monitoring of ocean currents and computation of marine gravity, the slope error is more important than the absolute error. This makes the DGM-E04 orbits even more favourable because slopes in the orbit error are almost an order of magnitude smaller than in the PGM055 orbits (order 0.2 versus 1  $\mu\text{rad}$ , respectively).

### 6.5.5 Orbit differences

Figure 6.8 depicts the predicted and observed spectra of the radial orbit differences between four DUT orbit solutions. The predicted spectra are according to LPT and the differences in the gravity field coefficients ( $\Delta C_{lm}$ ,  $\Delta S_{lm}$ ). The observed spectra are periodograms of the actual differences between the orbit solutions.

The JGM-3/DGM-E04 difference has a major peak at 0.93014 cpr (= 1 cpr – 1 cpd), and corresponds to  $l - 2p = 1$  and  $m = 1$  in (6.2), *i.e.*, gravity coefficients of odd degree and order 1. This 1-cpr signal with a daily modulation is precisely the near-resonant signal we held responsible for the track-like patterns in the average crossover differences with JGM-3 (Section 6.5.3). This peak is indeed markedly smaller in the EGM96/DGM-E04 difference, explaining the reduced track pattern in the average crossover differences with EGM96. Note that the spectral difference between DGM-E04 and GRIM5-C1 consists of only two peaks at the 1 cm level, and another few that exceed 2 mm. Clearly, gravity field models start to converge.

Because we have not excluded the near-resonant terms in the predicted spectra, they have large peaks close to 0 and 1 cpr caused by the harmonics of order 43. Having periods or a modulation longer than the length of the orbital arc, they are effectively absorbed by the state vector or the daily empirical along-track accelerations, as a result of which they do not show up in the observed spectra. The JGM-3/DGM-E04 spectra show an almost one-to-one match between predicted and observed. Near-resonant terms are absent here because they are simply copied from JGM-3 into DGM-E04. Orbit differences caused by non-conservative forces, with a nearly continuous distribution of power around 1 cpr, are minute.

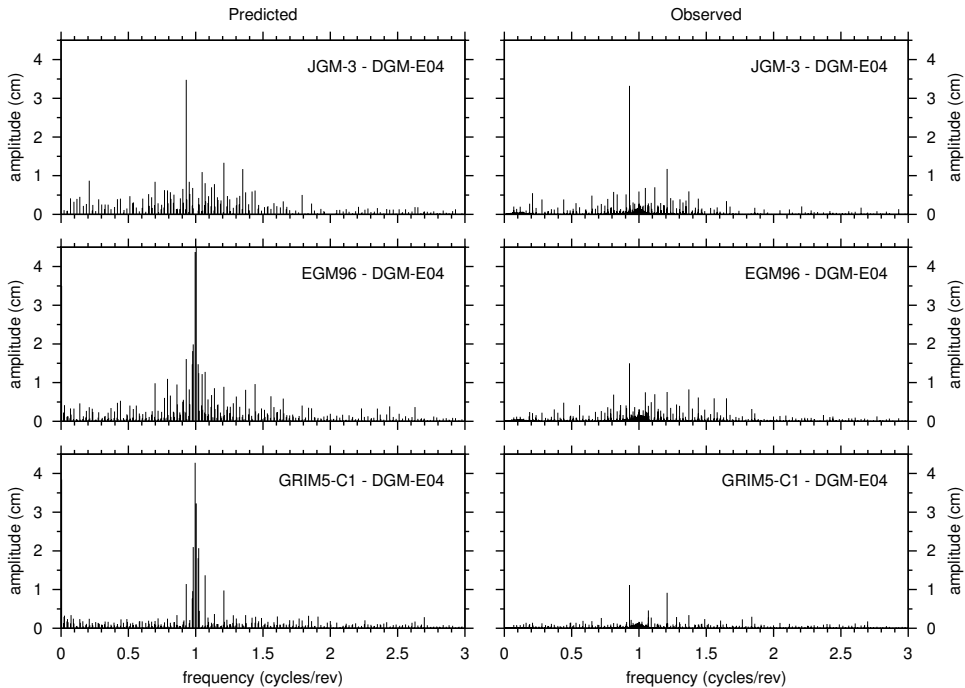


Figure 6.8 Predicted and observed spectra of the radial differences between ERS orbits computed with the JGM-3, EGM96, GRIM5-C1, and DGM-E04 gravity models.

Orbit solutions	ERS-1 orbit difference RMS				ERS-2 orbit difference RMS			
	Radial	Cross	Along	Total	Radial	Cross	Along	Total
JGM-3 – EGM96	3.94	14.12	15.18	21.11	4.00	13.83	14.91	20.73
JGM-3 – DGM-E04	4.23	11.70	17.52	21.49	4.34	10.63	17.38	20.83
EGM96 – DGM-E04	3.76	15.86	14.66	21.92	3.87	15.55	14.20	21.41
GRIM5-C1 – DGM-E04	2.36	12.31	8.96	15.41	2.45	12.48	8.98	15.57
PGM055 – JGM-3	7.58	18.81	27.23	33.96	7.73	16.98	27.97	33.62
PGM055 – DGM-E04	6.27	19.09	22.73	30.33	6.38	17.07	22.72	29.13

Table 6.6 Differences between GFZ (PGM055) and DUT orbit solutions. A  $3.5\text{-}\sigma$  editing is imposed on the total orbit difference to remove bad orbits. Values are in centimetres.

Table 6.6 shows that the orbit solutions based on the four gravity models are quite close. Irrespective of which combination of DUT orbit solutions is compared, the RMS orbit difference is around 4 cm in radial and around 15 cm in cross- and along-track direction. The favourable exception is the difference between DGM-E04 and GRIM5-C1, with only about 2.5, 12.5 and 9.0 cm RMS differences in the three orthogonal orbit components.

Because they are fully independent, the GFZ PGM055 and DUT DGM-E04 orbit



solutions differ quite a bit more. Yet the radial orbit difference of only 7 cm is a very encouraging figure, likely to indicate that either orbit solution is at least as accurate as that. Encouraging is also that, coming from JGM-3, the EGM96 and DGM-E04 solutions appear to converge.

## 6.6 Non-gravitational orbit errors

As indicated before, gravity-induced orbit errors are the same along two collinear passes and cancel when differencing the two altimetric sea surface profiles. The remaining non-conservative forces cause orbit errors around 1 and 2 cpr and are easily separated from the short-scale sea height differences associated with measurement and correction errors and sea level variability. Orbit differences on overlapping orbital arc are another indicator of non-gravitational orbit errors.

### 6.6.1 Collinear tracks

Figure 6.9 gives an example of a pair of collinear tracks of ERS-1 and ERS-2 with a time interval of only 1 day. Figure 6.9*a* shows the locations of the measurements. Figure 6.9*b* gives the relative sea surface height profile with respect to the GSFC00.1 mean sea surface model. A 0.5-degree Gaussian filter is applied to remove the altimeter noise. Figure 6.9*c* gives the significant wave height for both collinear tracks derived by the two altimeters. Again, a Gaussian smoother has been applied. Figure 6.9*d* shows the residual difference between the smoothed sea surface profiles. A five-parameter orbit error model (displayed as the thin solid line) is fitted through the residuals and absorb constant, 1-cpr and 2-cpr signals. The constant can be attributed largely to the difference in the range bias of ERS-1 and ERS-2; the harmonic signals capture differences in orbit errors, which, in this case, amount to 1.1 cm RMS. The deviations from the fit are a result of sea level variability and errors in the geophysical corrections to the altimeter data and amount (in this case) to 4.7 cm RMS.

The top part of Table 6.7 gives the statistics of about 10 000 collinear pairs of ERS-1 and ERS-2 with a 1-day time interval. Obviously, because of the clear separation between orbit error and short-wavelength errors the RMS value of the residual sea height differences (5.59 cm) is independent of the gravity model used in the orbit computation. The RMS value of the five-parameter fits is significantly higher for the GFZ/PGM055 orbits than for the DUT (JGM-3, EGM96, DGM-E04, and GRIM5-C1) orbits, which suggests that the modelling of the non-conservative forces at GFZ is less optimal. Yet, unexpectedly, also the choice of the gravity model appears to affect the long-wavelength fits slightly (2.42 cm for GRIM5-C1 and a few millimetres more for others). This indicates that a small part of the gravity-induced orbit error is aliased into the non-conservative force parameters (drag coefficients and empirical forces). When the aliasing would be purely geographically correlated or otherwise invariant from repeat cycle to repeat cycle, we

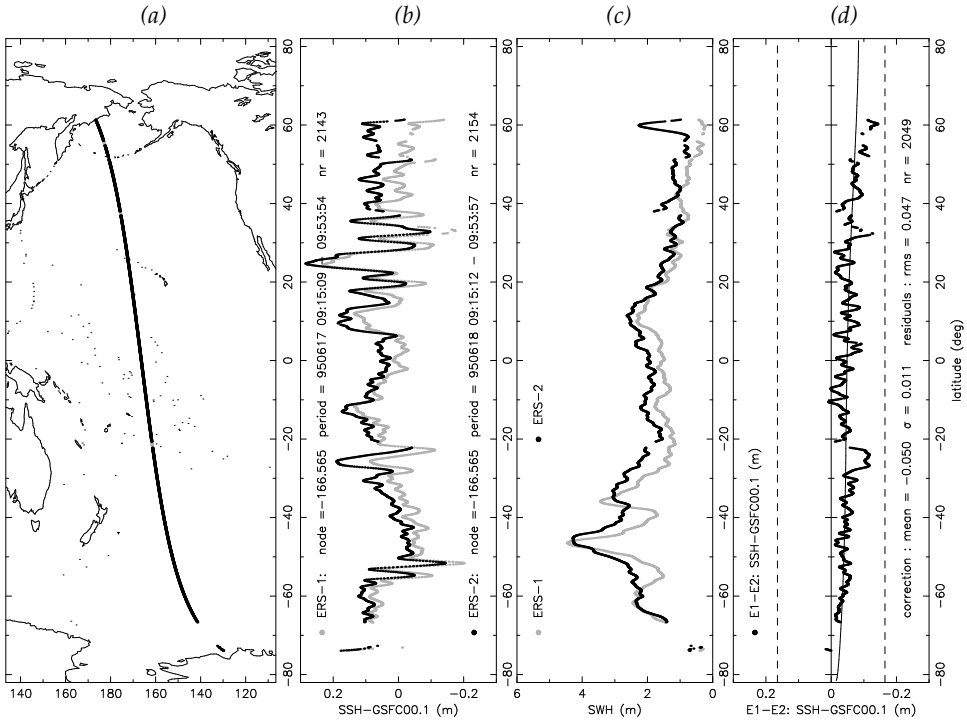


Figure 6.9 A collinear pair of sea surface height profiles of ERS-1 (grey) and ERS-2 (black) with a time interval of 1 day. Ascending pass 480, May 13-14, 1995. (a) Location, (b) sea surface height with respect to GSFC00.1, (c) SWH, and (d) height difference, including five-parameter fit.

would still not detect it in the collinear track differences. Elimination of a larger part of the gravity induced orbit error thus appears to reduce the aliasing and makes the absorption of non-conservative forces more efficient. Again, Table 6.7 demonstrates the superiority of DGM-E04, in this respect, over its contemporaries. Only the very recent GRIM5-C1 outperforms DGM-E04.

When going from the short time interval of 1 day of dual-satellite collinears to a sizable interval of 35 days of single-satellite collinears, the short-wavelength height differences are significantly larger (around 10.5 cm RMS) because of the decorrelation of correction errors (mainly wet tropospheric correction) and increasing sea level variability.

In addition, the orbit errors tend to be highly correlated over a 1-day time lag because ERS-2 then still senses about the same atmospheric conditions as ERS-1 1 day before. This could be used to an advantage by coupling the non-conservative force parameters between the two satellites during the orbit determination. For 35-day time intervals the RMS value of the five-parameter fit thus increases to about

Orbit solution	Number of collinear pairs	Number of data points	Orbit error RMS (cm)	Height residual RMS (cm)
<b>ERS-1 minus ERS-2 (1-day interval)</b>				
PGM055	9 972	14 988 880	3.48	5.59
JGM-3	10 058	15 114 505	2.74	5.59
EGM96	10 068	15 131 645	2.69	5.59
DGM-E04	10 086	15 156 951	2.52	5.59
GRIM5-C1	10 087	15 155 813	2.42	5.59
<b>ERS-1 minus ERS-1 (35-day interval)</b>				
PGM055	9 584	14 297 653	5.13	10.06
JGM-3	9 536	14 213 137	4.75	10.06
EGM96	9 546	14 232 966	4.76	10.06
DGM-E04	9 566	14 257 593	4.60	10.06
GRIM5-C1	9 569	14 259 244	4.53	10.06
<b>ERS-2 minus ERS-2 (35-day interval)</b>				
PGM055	8 630	12 608 554	5.61	10.16
JGM-3	8 798	12 837 089	4.79	10.16
EGM96	8 794	12 834 860	4.81	10.17
DGM-E04	8 805	12 845 546	4.62	10.16
GRIM5-C1	8 812	12 843 532	4.58	10.16

Table 6.7 Orbit error differences and sea height residuals between collinear pairs of ERS-1 and ERS-2. The radial orbit error differences are based on a five-parameter fit of the sea surface height differences; height residuals are indicative of measurement and correction errors and sea surface variability. Pairs are edited out when the orbit difference exceeds 3.5 times the nominal RMS.

5.0 cm (for DGM-E04, Table 6.7). Assuming full decorrelation, this indicates that the radial orbit error due to non-conservative forces is  $\sqrt{2}$  times smaller, 3.5 cm.

### 6.6.2 Orbital overlaps

Differences between the orbit solutions of two overlapping arcs are a measure for the *consistency* of the orbit solutions. Inconsistencies are caused by errors in tracking data as well as errors in the POD models, which, to the POD process, are inseparable. Since the errors in the tracking data are the same for the four different sets of orbits and all else being kept the same, the overlap statistics, listed in Table 6.8, are indicative of the overall performance of the different gravity models. From these numbers we can conclude that DGM-E04 excels over JGM-3 (and EGM96) in the modelling of the radial orbit component (as expected) as well as the along-track, but remains weak in the cross-track. It is this component that gains the most from the transition to GRIM5-C1, and to a lesser extend the along-track and radial components.

Gravity model	ERS-1 overlap RMS				ERS-2 overlap RMS			
	Radial	Cross	Along	Total	Radial	Cross	Along	Total
JGM-3	1.85	12.76	10.41	16.57	1.89	10.49	10.14	14.71
EGM96	1.64	13.07	10.06	16.58	1.57	11.73	9.73	15.33
DGM-E04	1.36	11.27	8.32	14.08	1.38	11.24	8.36	14.08
GRIM5-C1	1.10	9.18	7.54	11.93	1.14	8.80	6.93	11.26

Table 6.8 Orbit differences at overlaps between consecutive orbital arcs based on four different gravity field models. Arcs with large orbit manoeuvres are excluded from the statistics. Values are in centimetres.

Source	Height budget (Crossover budget)					
	PGM055	JGM-3	EGM96	DGM-E04	GRIM5-C1	TOPEX
	<b>Radial orbit errors</b>					
Geograph. anti-correl.*	40 (81–81)	31 (62–62)	27 (55–55)	17 (34–34)	17 (35–35)	10 (20–20)
Geograph. fully-correl.†	54 ( 0– 0)	47 ( 0– 0)	36 ( 0– 0)	28 ( 0– 0)	23 ( 0– 0)	10 ( 0– 0)
Non-gravitational‡	38 (35–51)	33 (27–48)	33 (27–48)	31 (25–46)	30 (24–46)	20 (15–28)
Total	77 (88–96)	65 (68–78)	55 (61–73)	46 (42–57)	41 (42–57)	24 (25–34)
	<b>Corrections and sea surface variability (common to all)</b>					
Dry tropo correction			3 ( 3– 4)			
Wet tropo correction			29 (10–21)			
Ionospheric correction			19 (15–18)			
Ocean tides			78 (26–26)			
Solid Earth tides			2 ( 3– 3)			
Sea state bias			20 (20–20)			
Instrument noise			25 (35–35)			
Sea surface variability			40 (20–56)			
Total			101 (55–79)			
	<b>Total error budget</b>					
Total	127 (103–124)	120 (87–111)	115 (82–107)	111 (69–97)	109 (69–97)	103 (60–86)

\*On the basis of Figure 6.6. †On the basis of Figure 6.7. ‡On the basis of Table 6.7.

Table 6.9 Contribution of orbit errors, altimeter corrections, and sea surface variability to the error budget of altimetric sea surface heights and crossovers. The ranges within brackets relate to crossovers with a short time interval (1 day) to a long time interval (weeks). Values (in millimetres) are given for various ERS orbit solutions; TOPEX results with JGM-3 orbits are given for reference. Values for TOPEX are from *Marshall et al.* [1995].

## 6.7 Error budget

Table 6.9 summarises the results obtained in the previous Sections and lists the three components of the radial orbit error (geographically anti-correlated, fully-correlated, and non-conservative) for each of the orbit solutions discussed in this Chapter. Table 6.9 also gives the contributions of the orbit error to crossover differences with a short time interval (typically up to 1 day) and a long time interval (typically 2 weeks or more). Note that the fully-correlated part does not contrib-

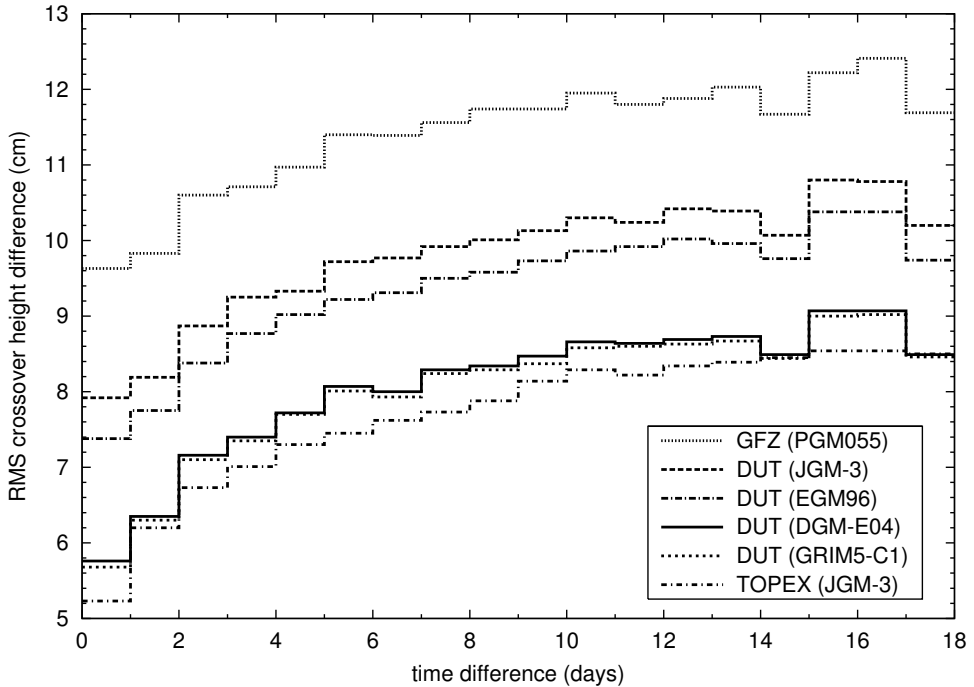


Figure 6.10 The RMS crossover difference (ascending–descending) as a function of time interval, based on several ERS orbit solutions. Results for TOPEX are shown for reference. Data beyond  $66^\circ$  latitude and in high-variability areas are excluded. A  $3.5\text{-}\sigma$  editing is applied.

ute to the crossover differences, that the anti-correlated part adds to the crossover differences at double efficiency, and that the non-conservative part has a certain decorrelation time.

After adding contributions for errors in the various altimeter geophysical corrections and sea level variability we obtain an overall budget for the RMS crossover differences, ranging from the short to long time intervals. Figure 6.10 confirms these results and shows a dramatic reduction of the crossover differences from the PGM055 orbits to GRIM5-C1 orbits. The latter coincides with the level of DGM-E04 and nears that of TOPEX, which is shown for reference and indicates that at this point the altimeter correction errors and sea surface variability have a significantly larger contribution to the RMS crossover differences than the orbits. In conclusion, for the ERS Tandem Mission the radial RMS accuracy of the GFZ PGM055 orbits is 7.7 cm; the DUT third-generation precise orbits have a radial RMS accuracy of 6.5 cm (JGM-3), 5.5 cm (EGM96), 4.6 cm (DGM-E04), and 4.1 cm (GRIM5-C1).

## 6.8 Conclusions and outreach

We have demonstrated the limitations of currently available gravity models for the computation of ERS orbits. Focusing on the local average (time-invariant part) of crossover differences reveals structures that can be linked to errors in various gravity field coefficients, especially those that can be associated with orbit errors of frequencies close to 1 cpr. The PGM055 gravity model appears to have been an unfortunate choice for the generation of the orbits on the OPRs. This model causes geographically anti-correlated orbit errors much larger even than the older JGM-3 model.

The time-invariant part of the crossover differences forms the basis for the development of an ERS-tailored gravity model DGM-E04 within the error margins of JGM-3. This technique has demonstrated its strength: crossover differences reduce exactly as predicted by the adjustments in the gravity coefficients. Also, the acquired gravity model performs significantly better in terms of SLR tracking residuals, and is competitive with JGM-3 for TOPEX orbit determination. Crossing ERS and TOPEX altimetry demonstrates a reduction of the geographically fully-correlated radial orbit error on top of the forced reduction of the anti-correlated part. Remarkably, the non-conservative force modelling errors also appear to have diminished in the DGM-E04 orbits compared to their JGM-3 counterpart. The step-wise improvement of the orbit determination for ERS seems now to have culminated in a radial RMS accuracy of 5.0 cm for the DGM-E04 orbits.

### 6.8.1 Room for improvement

When studying ERS/TOPEX dual-satellite crossover differences, the geographically fully-correlated orbit error appears to be larger than the anti-correlated. It is not yet certain that the observed differences are fully accountable to gravity model errors. When this is clarified, this data type can easily be included in the gravity model tailoring process. Likewise, we can add SLR, and finally PRARE data, as well and use an averaging process similar to what is shown in Section 6.5.2 to isolate the gravity-induced part of the residuals. This paves the way to include also the zonal gravity coefficients in the tuning process.

Such a tailoring process was conducted 3.5 years after the development of DGM-E04. Crossovers, SLR and PRARE data were used to adjust all coefficients of EGM96 up to degree and order 70 [Scharroo *et al.*, 2000b]. The resulting model, DGM-E09, constitutes a less than marginal improvement of the radial orbit error over DGM-E04; its main strength is in the two other components. However, both models are now superseded by GRIM5-C1.

By far the largest contributor to the orbit error, however, is the time variant part. This suggests that there is margin for improvement of the surface forces (drag and solar radiation). The time variant part, however, also comprises the gravitational effect of solid Earth and ocean tides, which so far have not been considered.

Yet this does not affect our results, since all time variant orbit errors are simply mingled into the one that we labelled ‘non-conservative’ or ‘non-gravitational’.

### 6.8.2 Remaining considerations

A widely distributed legend argues that when orbit computations use the same gravity field for all altimeter satellites, there is no mismatch between the gravity-induced orbit errors and hence they cancel when differencing the different data sets. This is, however, not true. Because of their distinct inclination, repeat cycle, altitude, and choice for orbital arc length, gravity model errors impact differently on the computed orbital altitude. The best choice of gravity model is the one that introduces the least errors for each particular mission. Tailored models which are tuned to a particular satellite mission are therefore the best candidates for adoption in the POD, as long as these act within the error margins of a state-of-the-art general-purpose model.

This is irrevocably demonstrated when differencing ERS and TOPEX altimetry in Figure 6.7 of Section 6.5.4. Nearly the worst of all performance is given by using the same gravity model, JGM-3, for both satellites. The best match is obtained using DGM-E04 for ERS and JGM-3 for TOPEX. In fact, JGM-3 is very much optimised for TOPEX (if not actually *tailored* to TOPEX), which is also reflected in the error variance-covariance matrix of JGM-3. The tailoring to ERS thus mainly concerns the weakly determined (lumped) coefficients that are best observed in ERS crossover differences. Consequently, for TOPEX orbit determination, DGM-E04 and JGM-3 are very similar, as was also demonstrated in Section 6.4.

Only when a tailored model is superseded by another general-purpose model and it is established that produces a ‘better’ orbit—where ‘better’ is a stretchable term and has to be seen in the light of various analyses, like those discussed in this Chapter—, it is wise to make the transition. These analyses have shown that the technique of gravity model tailoring using averaged crossover height differences is as elegant as it is effective. For years, DGM-E04 was the *de facto* gravity model for ERS, performing better than the later general-purpose model EGM96, until four years later GRIM5-C1 was released.

This means that, with the onset of CryoSat, with its inclination of  $92^\circ$ , different from any previous altimeter satellite, the same opportunity arises.





## Chapter 7

# Conclusions and Recommendations

The ERS-1 and ERS-2 altimeter missions have long been regarded as ‘inferior’ to missions like TOPEX/Poseidon. This notion was and is mainly based on the quality of its official OPR products provided by ESA, which content is frozen in the status of 1995, never to evolve. Half of the ERS-1 data never even unleashed itself from 1991 models and algorithms. However, it should be indisputable, after reading this thesis, that ERS-1 and ERS-2 have made valuable contributions to operational oceanography, to geophysics, to climate research, and to the development of new orbit determination techniques and gravity field models. The gap between the two points of view is bridged by the efforts of many in the altimetric community, including some of my own in the fields of calibration and validation, and orbit determination.

The quality of the orbit determination has benefited strongly from the application of novel techniques, like the inclusion of altimeter height and crossover measurements as tracking data, during a period that no other tracking data were available than those from a sparse network of SLR stations. It is demonstrated that these additional data stabilise the computed orbit without the suspected negative effect of aliasing oceanographic signals into the orbit. Although not shown in this thesis, these orbits are compatible in quality to those based on SLR and PRARE tracking data. However, with the ongoing degradation of the PRARE network, the use of altimeter tracking data has become a necessity again. Besides, the significant delay in the release of the PRARE data made the use of this technique imperative for operational near-realtime orbit determination, to benefit operational monitoring of meso-scale ocean currents.

A second prime contributor to the reduction of the satellite orbit error, and hence the improvement of the ERS-derived sea surface heights, has been the creation of a gravity field model tailored to the orbit of ERS. Whereas gravity field improvement using crossovers has failed before, the novelty in the technique pro-

posed in this thesis is to first isolate the gravity field induced signal by local averaging of the crossover height differences. That signal is then converted into adjustments to a general-purpose gravity field model, leading to the tailored model DGM-E04. Although tailored to the orbit determination of the ERS satellites, the model passes tests with orbit determination for other satellites, like TOPEX/Poseidon, with flying colours. We can therefore conclude that the new model is not unrealistic. Besides, as far as ERS orbit determination is concerned, it still outperformed a general-purpose model released about a year later, and it remained doing so until GRIM5-C1 became available, only recently.

The mechanism of gravity field tailoring can also be applied to other satellites in a repeat mission, like GFO and the future CryoSat. It is definitely a quick, and not so dirty, way to improve upon existing models. Additionally, the technique of isolating the gravity field induced signal is valuable for the validation of any gravity field model to be released in the future, as is shown in the case of the validation of the GRIM5-C1 model in this thesis.

The upgrading of the ERS altimeter data is imperative. A long list of enhancements have to be made to the measurements and corrections. Important is also the harmonisation between the earlier and later versions of the OPR products. Once the upgrades are made to the measurements of altimeter range and significant wave height, as well as basically all altimeter range corrections, the results obtained in climate-related studies like the monitoring annual and secular variations of global sea level, ERS performs nearly as well as TOPEX/Poseidon. Moreover, ERS data provides an essential quality check for the TOPEX/Poseidon data, which, in the past, have been showing drifts which may have gone unnoticed for a much longer time without the ERS reference. In this respect it was demonstrated that the ionospheric correction plays an important role in the monitoring of sea level rise. In the absence of a dual-frequency altimeter, the choice of the ionosphere model can make or break the case for moderation in the emission of greenhouse gases.

The calibration of the range of the ERS-1 radar altimeter over the oceanographic tower *Acqua Alta* off the coast of Venice, was a major undertaking, joining the expertise of several European institutes. Particularly, the interpolation of the altimeter data, the computation of short-arc orbits, and the compilation of the final bias result from the myriad of measurement, described in this thesis, were essential steps in this project. The final number,  $-41.5 \pm 5.2$  cm, can now be compared to a combination of laboratory calibrations of ERS-2 and the cross-calibration of ERS-1 and ERS-2. However, none of the later results appear to invalidate the Venice Calibration result.

The errors in the time tagging of the ERS altimeter data has long been a mystery and concern. With the unravelling of the problem, more questions seemed to be raised, and more variations in the time tagging uncovered, than there were solved. Although the actual cause of the timing error may be buried deep in the lines of code and lookup tables of the ERS ground segment, it is shown that the errors are basically constant and have values of  $-1.53$  ms for ERS-1 and  $-1.17$  ms for ERS-2.

The mission for ERS-2 still continues, and Envisat is being commissioned. Cur-

---

rently, new gravity field models from the CHAMP and GRACE missions are being made available. ERS-2 still forms an important test case for these models because of its unique orbit for a satellite altimeter, that it now shares with Envisat. These new models will render DGM-E04 obsolete, but not its technique with which it was designed. It will serve as a validation tool for future gravity fields and altimeter missions.

The RADS database system, has demonstrated to be a indispensable tool for the validation work done for this thesis. The ease at which altimeter data can be augmented with new corrections and compared with other satellite missions is striking. Such a database plus its software tools, available on-line and/or distributed over various mirroring sites, may be the future approach to the release of high-quality state-of-the-art altimeter products.



## Appendix A

# Least-Squares Collocation

The spatial distribution of ERS altimeter measurements is far from regular: they have a characteristic along-track spacing of about 6.6 km, and a completely incompatible cross-track spacing of about 50 km at mid-latitudes (in the 35-day repeat). The standard inverse-distance weighted averaging technique [e.g., Wisse *et al.*, 1995] is quite capable of interpolating (and smoothing) the data along the tracks, even at high spatial resolutions. However, mapping of the sea surface also requires interpolation between the tracks, at a most optimal resolution, taking into account all surrounding measurements and their characteristics. For this purpose the inverse-distance weighted averaging only performs well for mapping the longer wavelengths (wavelengths considerably longer than the cross-track spacing). At higher resolutions this technique tends to concentrate all detail along the tracks and produces unsatisfactory results.

In order to map at these high resolutions onto a regular 2-dimensional grid, additional *a priori* information on the expected shape of the surface should be incorporated. Rather than defining a functional relation between each observation and the grid points, the objective mapping technique (also known as Gauss-Markov interpolation, optimal analysis, inverse technique, and least-squares collocation) makes optimal use of the known (or approximated) correlation between measurements and grid values, and takes into account the correlation among the measurements and grid values themselves [Moritz, 1973, 1980]. Thus, local fluctuations in the mapped sea surface are restricted, based on the measurements and their correlation, and not merely on any functional relation.

In general, this technique allows the mapping of any type of observation taken on various positions (or epochs) onto any related entity on other positions (or epochs), provided the correlation between the observations and the related entity is known. In our case, both the observed quantity and mapped signal are sea height residuals. This technique can be used for 2-dimensional mapping but also for 1-dimensional interpolation and smoothing of the altimeter data along a single track, like in the *Venice Arc Calibration* (Chapter 4). There we are sometimes

faced with a sizable data gap near the *Acqua Alta* platform, exactly at the point that we want to have an accurate measure for the sea surface height. This Appendix explains, in detail, the method of objective mapping for the smoothing and interpolation of altimetric sea surface heights. The method is applicable to both 1-dimensional and 2-dimensional mapping.

## A.1 Theory of least-squares collocation

Assume a set of  $q$  measured quantities  $\{x_1, x_2, \dots, x_q\}$ , forming the measurement vector  $x$ ,

$$x = [x_1 \ x_2 \ \dots \ x_q]^T \quad , \quad (\text{A.1})$$

and a set of  $m$  signals  $\{s_1, s_2, \dots, s_m\}$ , forming the signal vector  $s$ ,

$$s = [s_1 \ s_2 \ \dots \ s_m]^T \quad , \quad (\text{A.2})$$

which both have an expected value equal to zero. Thus, the measurements are assumed to be unbiased, but may include random or correlated noise. Consequently, the measurement vector can be divided into a *signal part*,  $t$ , and a *noise part*,  $n$ , such that

$$x = t + n \quad . \quad (\text{A.3})$$

The measurement vector  $x$  is known, the signal vector  $s$  is unknown. Least-squares collocation provides a linear estimate of  $s$  based on the correlations between measurements  $x$ , the correlations between the signals  $s$ , and their cross-correlation. In this, least-square collocation differs from least-squares estimation and other smoothers where there is always some functional relationship between  $x$  and  $s$ .

A linear estimate for  $s$  has the form

$$\hat{s} = Ax \quad , \quad (\text{A.4})$$

where  $A$  is some  $m \times q$  matrix, so each element of the signal vector  $s$  is approximated by a linear combination of the data  $x$ . As in every statistical estimation, least-squares collocation seeks the best linear estimate  $\hat{s}$  of  $s$  by minimising the variance of the error vector  $\epsilon = \hat{s} - s$ . This requirement leads to the *fundamental formula for least-squares collocation* [Moritz, 1980]:

$$\hat{s} = C_{st} \bar{C}^{-1} x \quad \text{with} \quad \bar{C} = C_{tt} + C_{nn} \quad , \quad (\text{A.5})$$

where

$C_{tt}$  = the  $q \times q$  *auto-covariance* matrix of the signal part of the measurement vector;

$C_{nn}$  = the  $q \times q$  auto-covariance matrix of the measurement noise;

$C_{st}$  = the  $m \times q$  matrix of the *cross-covariance* between the measured signal,  $t$ , and the estimated signal,  $s$ .

The elements of the matrices are given by

$$\begin{aligned} c_{kj}^{st} &= \text{cov}(s_k, t_j) & k = 1, \dots, m & , \\ c_{ij}^{tt} &= \text{cov}(t_i, t_j) & \forall i = 1, \dots, q & , \\ c_{ij}^{nn} &= \text{cov}(n_i, n_j) & j = 1, \dots, q & . \end{aligned} \quad (\text{A.6})$$

In most practical cases,  $n$  will be random noise, so  $\text{cov}(n_i, n_j)$  is zero for each  $i \neq j$ , making  $C_{nn}$  a diagonal matrix. However, this is not essential.

Given the covariance matrices and the measurements, the formula (A.5) relates any observed quantity,  $x$ , be it sea height residuals or any other geodetic measurement, to any related unbiased quantity,  $s$ . In our case, however, both  $x$  and  $s$  are vectors of sea height residuals:  $x$  measured at the measurement locations and  $s$  to be estimated at the grid points<sup>1</sup>.

Least-squares collocation also provides a full error variance/covariance matrix for the computed signal vector  $s$  [Moritz, 1980]:

$$\epsilon_{ss} = C_{ss} - C_{st} \bar{C}^{-1} C_{ts} \quad , \quad (\text{A.7})$$

where  $C_{ts}$  is simply the transpose of  $C_{st}$ .

## A.2 Covariance functions

In order to determine the auto-covariance matrix,  $C_{tt}$ , and the cross-covariance matrix,  $C_{st}$ , a functional description of the covariance between the sea height residuals at two points  $P$  and  $Q$  on (or close to) the reference ellipsoid should be available. Since the sea height residuals are in nature (wave length and power) similar to unmodelled geoid undulations with respect to the geoid model, an *undulation covariance function* can be used to approximate the covariances between the sea height residuals in  $P$  and  $Q$ .

The geoid undulation,  $N$ , is given by the Bruns' formula [Kaula, 1966; Heiskanen and Moritz, 1967]

$$N = \frac{V}{\gamma} \quad , \quad (\text{A.8})$$

where  $V$  is the geopotential, usually expressed as a spherical harmonic expansion

$$V = \frac{\mu}{r} \sum_{l=0}^{\infty} \left( \frac{a_e}{r} \right)^l \sum_{m=0}^l \bar{P}_{lm}(\sin \phi) [\bar{C}_{lm} \cos m\lambda + \bar{S}_{lm} \sin m\lambda] \quad , \quad (\text{A.9})$$

<sup>1</sup>The term 'grid points' is used here for the 2-dimensional case. For the 1-dimensional case these will be points along the ground track in which the sea heights have to be interpolated.

and  $\gamma = \mu/r^2$  is the normal gravity. For the other expressions in (A.9) see under Eq. (B.2) in Appendix B.

If  $P$  and  $Q$  are assumed to be located on a sphere with radius  $a_e$ , these relations lead to the spatial covariance function for  $N$ , written as

$$C(P, Q) = \sum_{l=0}^{\infty} c_l P_l(\cos \psi) \quad , \quad (\text{A.10})$$

where  $P_l$  is the Legendre function of degree  $l$ ,  $\psi$  is the spherical distance between  $P$  and  $Q$ , and  $c_l$  is the undulation degree variance, expressed by

$$c_l = a_e^2 \sum_{m=0}^l (\bar{C}_{lm}^2 + \bar{S}_{lm}^2) \quad . \quad (\text{A.11})$$

Note that the covariance function is merely a function of  $\psi$ , under the assumption of homogeneity and isotropy of the gravity field.

As far as the longer wave length nature of the geoid undulations (up to degree and order 360) is concerned, the undulation degree variance can be computed from the gravitational potential coefficients  $\bar{C}_{lm}$  and  $\bar{S}_{lm}$  approximated by the geoid model. However, since the geoid model was subtracted from all sea height measurements in the first place, the remaining covariance only concerns the commission errors (errors in the coefficients up to degree and order 360) and omission errors (the part that is not modelled, above degree and order 360). Consequently, (A.11) is rewritten to

$$c_l = a_e^2 (2l + 1) \sum_{m=0}^l \sigma_l^2(\bar{C}_{lm}, \bar{S}_{lm}) \quad . \quad (\text{A.12})$$

For lower degrees, the degree standard deviation  $\sigma_l(\bar{C}_{lm}, \bar{S}_{lm})$  of the coefficients  $\bar{C}_{lm}$  and  $\bar{S}_{lm}$  is given by the RMS of the standard deviations (errors) of all  $2l + 1$  coefficients  $\bar{C}_{lm}$  and  $\bar{S}_{lm}$  of degree  $l$ . For higher degrees, we need to model the magnitude of the geopotential coefficients that are not included in the geoid model. Estimates of the variation of the coefficients are provided by a large variety of degree variance models [Jekeli, 1978; Rapp, 1979]. One of them is the well-known Kaula's rule of thumb [Kaula, 1966],

$$\sigma_l(\bar{C}_{lm}, \bar{S}_{lm}) \approx \frac{10^{-5}}{l^2} \quad . \quad (\text{A.13})$$

The undulation degree variance  $c_l$ , as defined above, is shown in Figure A.1 as a function of  $l$ . Clearly, the estimated error of the higher degree coefficients of the OSU91A geoid model already tend to reach the magnitude of the coefficients hypothesised by Kaula's rule. Consequently, the transition from commission to omission errors is quite smooth. The cumulative degree variance reaches its maximum at about degree 2000; further extension of the model is hardly necessary,



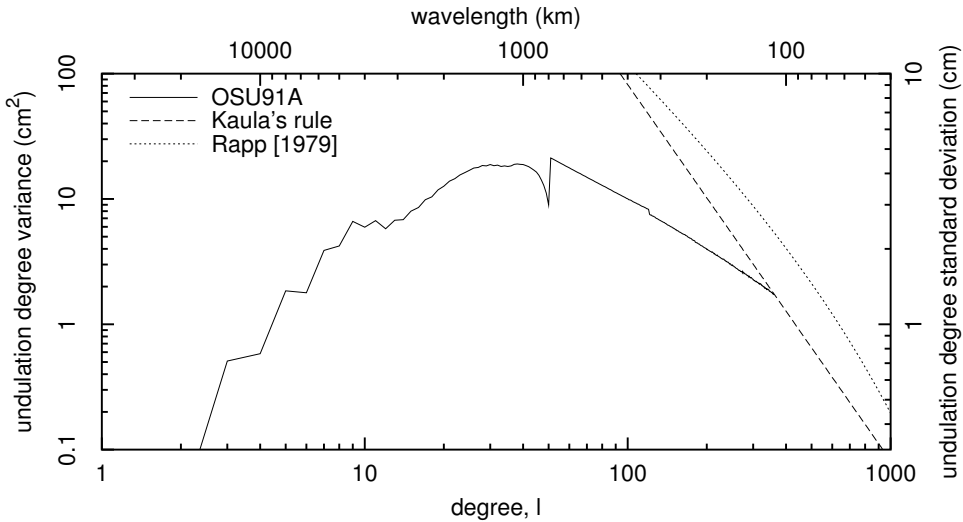


Figure A.1 Undulation degree variance based on the standard deviations of the coefficients in the OSU91A model [Rapp *et al.*, 1991] (full line), Kaula's rule of thumb (dashed line), and the empirical function of Rapp [1979] (dotted line).

besides Kaula's rule does not actually converge. Finally, Figure A.2 shows that the undulation covariance  $C(P, Q)$  can be neglected for distances  $\psi$  larger than  $2.0^\circ$ . Kaula's rule was chosen since it allows less variance at the shorter wavelength than the Rapp [1979] model and thus leads to a smoother mapping.

### A.3 Implementation

In a least-squares estimation process the size of the matrix to be inverted, the normal matrix, is based on the number of parameters to be estimated. In contrast, in least-squares collocation, the size of the matrix to be inverted,  $\bar{C}$ , is based on the number of measurements in the vector  $x$ . Obviously, in least-squares estimation, the number of measurements is always larger than the number of parameters. Thus, least-squares collocation requires more intensive computation than least-squares estimation. With the number of measurements running in the thousands, actual inversion of the matrix  $\bar{C}$  becomes a computational burden. However, the actual inversion of  $\bar{C}$  can be avoided, as illustrated below.

A simple recipe for the smoothing and interpolation of  $m$  sea height residuals onto  $q$  grid points is as follows:

- Store the sea height residuals in vector  $x$ .
- Determine the undulation covariance as a function of distance  $\psi$  up to a certain

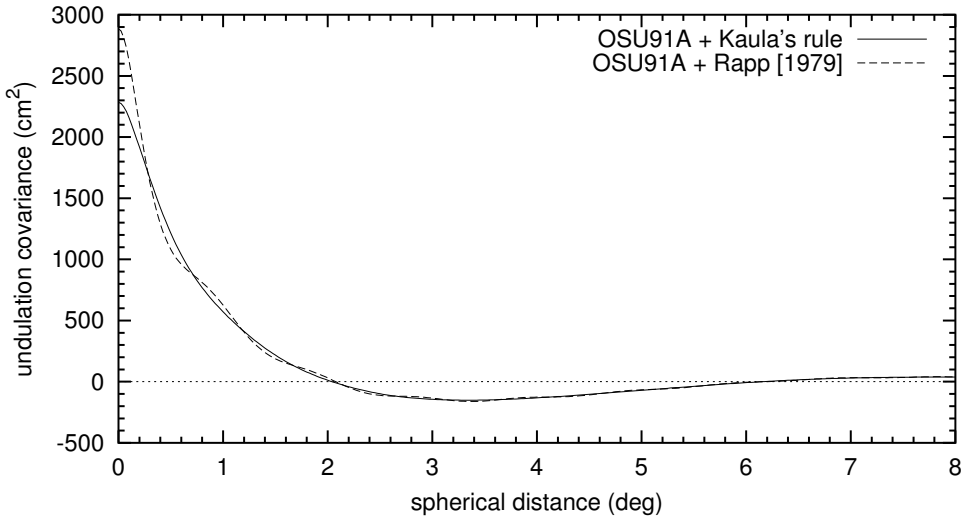


Figure A.2 Undulation covariance function based on the OSU91A degree variances (degree 36 to 360) extended by Kaula's rule of thumb or the empirical function by *Rapp* [1979] (degree 361 to 2000).

cutoff after which the covariance can be neglected. Tabulate the covariance for a large number of values  $\psi$  between 0 and the cutoff.

- Determine the distance between all measurement points  $P$ . Interpolate the undulation covariance from the table. Store the result in the appropriate elements of  $C_{tt}$ .
- Determine the distance between all measurement points  $P$  and grid points  $Q$ . Interpolate the undulation covariance from the table. Store the result in the appropriate elements of  $C_{st}$ .
- Assuming all measurement errors are uncorrelated, add a diagonal noise covariance matrix  $C_{nn}$  to  $C_{tt}$  and obtain  $\bar{C}$ .
- Avoid inversion of the  $\bar{C}$  matrix by splitting up the collocation formula (A.5) into two steps:

$$\text{Solve } \mathbf{y} \text{ from: } \mathbf{x} = \bar{\mathbf{C}} \mathbf{y} \quad (\text{A.14})$$

$$\text{Multiply: } \hat{\mathbf{s}} = \mathbf{C}_{st} \mathbf{y} \quad (\text{A.15})$$

The vector  $\hat{\mathbf{s}}$  now contains the smoothed/interpolated sea height residuals at the grid points.

- In a similar way, compute the error variance/covariance matrix  $\epsilon_{ss}$ . Again

avoiding inversion of  $\bar{\mathbf{C}}$ , (A.7) is split up into two steps:

$$\text{Solve } \mathbf{z} \text{ from: } \mathbf{C}_{st}^T = \bar{\mathbf{C}} \mathbf{z} \quad (\text{A.16})$$

$$\text{Multiply and subtract: } \boldsymbol{\epsilon}_{ss} = \bar{\mathbf{C}} - \mathbf{C}_{st} \mathbf{z} \quad . \quad (\text{A.17})$$

Note that in least-squares estimation, the number of parameters always has to be smaller than the number of measurements. In least-squares collocation there is no limit on the number of measurements  $m$  with respect to the number of grid points  $q$ . Generally  $m$  will be larger than  $q$ , but this is not essential.



## Appendix *B*

# The Gravity Induced Radial Orbit Error

One of the main contributors to radial orbit errors in precise orbit determination has been the lack of precise knowledge of the gravity field of the Earth. These radial orbit errors hamper the use of satellite altimetry for geodetic and oceanographic purposes since they enter directly into the observed sea surface height. On the other hand, this makes it also possible to observe the radial orbit errors in altimeter height residuals and crossover height differences. In this Appendix we will make a distinction between the geographically correlated orbit error, its mean and variance, gravity field induced errors, and orbit errors introduced by other forces.

## B.1 Introduction

In the early days of satellite orbit determination all deviations from a perfect Keplerian orbit were considered *perturbations*. Many studies have been concentrated on finding analytical formulations for the orbit perturbations due to atmospheric drag, solar radiation, and the non-central part of the gravity field. A basic tool for this were the *Lagrange Planetary Equations*, that express the rates of change of the Keplerian elements as a function of forces acting on the satellite. Nowadays, the Lagrange Planetary Equations are usually used to determine the effect of a *mismodelling* of the force field, rather than the complete one. Hence, the terms *orbit perturbations* (deviations from a Keplerian orbit) and *orbit errors* (mismodelling of the orbit) are intertwined and will be exchanged frequently throughout this Appendix.

A major breakthrough was the work by *Kaula* [1966], who found expressions for the perturbations in all six Keplerian elements caused by the full geopotential force field. Since the radial position of the satellite is a function of only three of

these elements (semi-major axis, eccentricity, and mean anomaly), an expression for the radial orbit perturbations is found in a rather straightforward way.

Still, it took till the 1980s, when altimetry became more 'popular', that research started to be focused on the radial part of the orbit error. In this context, the report by *Rosborough* [1986] can be considered to be the most extensive contribution to the representation of the gravity field induced orbit behaviour and its behaviour in time and space. The specific application to altimetry, using similar formulations, is discussed by many others [*Wagner*, 1985; *Tapley and Rosborough*, 1985; *Schrama*, 1989].

This Appendix is intended to produce some insight into the matter. For a full description of the theory and arithmetic involved, one is referred to the aforementioned works.

## B.2 The problem

As pointed out in Section 1.2.5 the crossover height differences are indicative of the radial orbit error. Although a small part of it should be contributed to actual sea level change, altimeter noise and correction errors, the global RMS of the crossover height differences ( $\sigma_x$ ) is largely determined by the RMS radial orbit error difference at crossover points. If the orbit errors at the crossing points of each ascending and descending pass were completely uncorrelated,  $\sigma_x$  could be equally divided over both passes, leading to a radial orbit error estimate of  $\frac{1}{2}\sqrt{2}\sigma_x$  for all passes. However, part of the radial orbit error is merely a function of the geographical position of the sub-satellite point and will not show up in crossover height differences.

Gravity field model errors may induce regional vertical offsets of the orbit, that are common to both the ascending and the descending pass. Because the gravity field is 'scanned' the same way during each repeat cycle, a considerable part of the gravity-induced radial orbit errors is purely geographically correlated and can not be observed from crossover height differences. But also other statistical analyses (orbital differences, altimeter height residuals, collinear track analyses) do not provide any information on this part of the radial orbit error. This phenomenon is known as the non-observability of the geographically-correlated radial orbit error. Nevertheless, the geographically-correlated component of the radial orbit error is believed to be quite small; at worst the *total* radial orbit error is in the order of  $\sigma_x$  [*Shum et al.*, 1990].

The term *geographically-correlated radial orbit error* is, however, not equivalent to the *gravity field induced radial orbit error*. In the first place, gravity field errors also introduce orbit errors that are purely uncorrelated on ascending and descending tracks, as will be discussed in Section B.2. Second, there are also orbit errors that are not related to the gravity field, but still have a geographically-correlated nature. In particular, radial orbit errors with a frequency of 1-cpr (or any integer multiple of this frequency) are also poorly resolved from crossover height differences. Every such  $k$ -cpr orbit error can be represented by a zonal component (with extremes

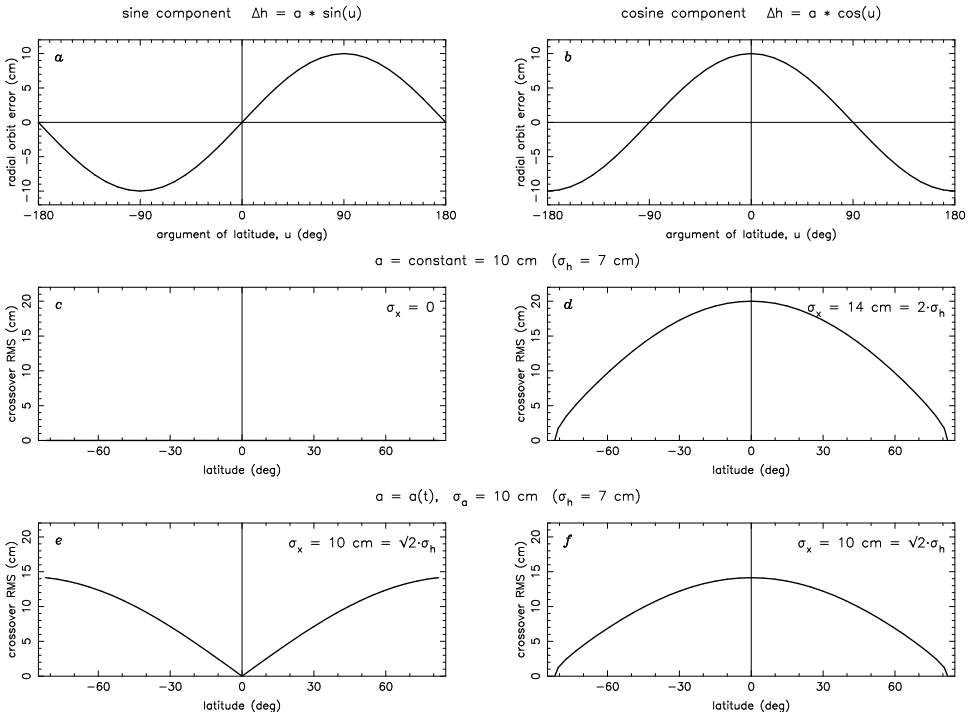


Figure B.1 The effect of a 1-cpr orbit error on the global crossover RMS. A 1-cpr signal consists of a sine (a) and cosine (b) constituent. If the amplitude is constant (c and d) only the cosine component shows up in the crossover with twice the power of the original signal. Of a modulated 1-cpr signal, both the sine (e) and cosine (f) component are observed in the crossover RMS at equal efficiency ( $\sqrt{2}$  times the power of the modulated signal).

over the poles:  $u = \pm 90^\circ$ ) and a non-zonal component that is orthogonal to the zonal one. The effect on the crossover height differences of the 1-cpr compound, is shown in Figure B.1.

If the amplitude of the 1-cpr error is constant, the sine-component ( $\Delta h = a \sin u$ , Figure B.1a) has a global distribution which is zonal and purely latitude-dependent. In each crossover the error is thus identical on both the ascending and descending pass. Consequently, none of the zonal component is observed in the crossover height differences (Figure B.1c). At the same time, in each crossover, the cosine component of the 1-cpr error ( $\Delta h = a \cos u$ , Figure B.1b) has an equal magnitude on both the ascending and descending passes, but with an opposite sign. The resulting crossover height differences will be maximum around the equator and will have a global RMS value which is *twice* the power of the cosine component (Figure B.1d).

The 1-cpr error, which is the most notorious of the  $k$ -cpr errors, is mainly caused

by state vector defects and drag mismodelling. Because the state vector and drag parameters are estimated independently for each separate arc, both the zonal and non-zonal components tend to have varying amplitudes from arc to arc. At time scales of a few days to a week, the correlation between the zonal 1-cpr errors on the ascending and descending passes will decrease. As a consequence, crossover differences computed from measurements with a significant time lapse will include zonal 1-cpr errors (Figure B.1e). Likewise, the anti-correlation of the non-zonal component will disappear, which results in a less pronounced equatorial maximum of the crossover differences (Figure B.1f). Therefore, over time spans of a month (spanning a considerable amount of orbital arcs), both the zonal and non-zonal components of the  $k$ -cpr error will contribute equally to the crossover RMS with a value equal to  $\sqrt{2}$  times the RMS of the orbit error, like any other radial orbit error component. Thus  $\frac{1}{2}\sqrt{2}\sigma_x$  remains a good estimate for the radial orbit error when we ignore any other contributions.

### B.3 The geopotential

A common way of representing the Earth's geopotential (outside the Earth),  $U$ , is the spherical harmonic expansion, obtained by solving the Laplace's equation

$$\nabla^2 U = 0 \quad . \quad (\text{B.1})$$

while imposing the boundary condition that the geopotential tends to zero at an infinite distance from the Earth. This solution can be written as a sum of geopotential terms  $U_{lm}$ , each scaled by a pair of geopotential coefficients  $\{\bar{C}_{lm}, \bar{S}_{lm}\}$ ,

$$U = \sum_{l=0}^{\infty} \sum_{m=0}^l U_{lm} \quad \text{with} \quad (\text{B.2})$$

$$U_{lm} = \frac{\mu}{r} \left( \frac{a_e}{r} \right)^l \bar{P}_{lm}(\sin \phi) [\bar{C}_{lm} \cos m\lambda + \bar{S}_{lm} \sin m\lambda] \quad ,$$

where

- $\mu \equiv$  the Earth's gravitational parameter, the product of the universal gravitational constant,  $G$ , and the mass of the Earth,  $M$ ;
- $a_e \equiv$  scaling factor close to the mean equatorial radius of the Earth;
- $r, \phi, \lambda \equiv$  geocentric distance, latitude, and longitude of any position on or near Earth;
- $\bar{C}_{lm}, \bar{S}_{lm} \equiv$  normalised geopotential harmonic coefficients of degree  $l$  and order  $m$ ;
- $\bar{P}_{lm} \equiv$  the normalised associated Legendre functions.

Due to this definition, the geopotential terms and the respective coefficients can be divided into three separate classes, as illustrated in Figure B.2,



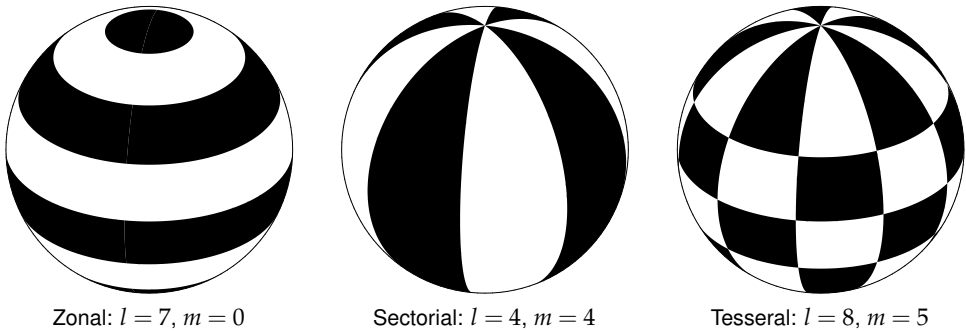


Figure B.2 Examples of the distribution of positive (black) and negative (white) geopotential for zonal, sectorial and tesseral harmonics.

**Zonals.** For  $m = 0$ , the geopotential term  $U_{lm}$  is no longer a function of longitude,  $\lambda$ , and thus varies only with latitude. Note that the coefficients  $\bar{S}_{l0}$  have no relevance, and are thus taken to be zero.

**Sectorials.** For  $m = l$ , the associated Legendre function is non-negative, zero at the poles and maximum at the equator. The variation with longitude results in  $2m$  longitudinal sections of alternating positive and negative geopotential.

**Tesserals.** For all other orders  $0 < m < l$ , the geopotential varies in both longitudinal and latitudinal direction. In total there are  $2m$  meridians and  $l - m$  parallels along which the geopotential term  $U_{lm}$  is zero, dividing the Earth in a checker board pattern of positive and negative potential.

In many cases the central body term,  $U_{00} = \mu/r$ , is separated from the expansion, leaving only the terms that cause perturbations on a Keplerian ellipse. Also, when the origin of the Earth fixed reference frame is at the Earth centre of mass, the degree-one terms disappear, leaving a *disturbing potential*

$$R = U - \frac{\mu}{r} = \sum_{l=2}^{\infty} \sum_{m=0}^l U_{lm} \quad . \quad (\text{B.3})$$

Theoretically, the degree  $l$  ranges from 0 to infinity, but in most practical cases it is restricted to a finite level. Until the 1990's, most gravity field models included only some 1000 geopotential coefficients up to degree  $l = 36$ . In recent gravity field models, like JGM-3, all terms are considered up to degree and order  $l = 70$ , thus comprising more than 5000 coefficients.

If the gravity field contained only the central term, and there were no other forces present, the satellite would revolve in a perfect Keplerian orbit: an ellipse with a fixed orientation in space. The size, shape, and orientation of the ellipse as well as the position of the satellite along the orbit can uniquely be defined by the six *Keplerian elements*:

$a \equiv$  semi-major axis = half the length of the long axis of the ellipse;

- $e \equiv$  eccentricity = the amount of non-circularity;  
 $i \equiv$  inclination = the angle of the orbital plane with respect to the equator;  
 $\Omega \equiv$  right ascension of the ascending node = the angle between the Vernal equinox and the ascending node of the orbit;  
 $\omega \equiv$  argument of the perigee = the position of the point along the orbit that is closest to the geocentre, as measured along the orbit from the ascending node;  
 $M \equiv$  mean anomaly = a pseudo-angle, representing time.

Using this set of coordinates has the advantage that in a central force field all of them are constant, except for the mean anomaly,  $M$ , which will increase linearly with time. In a non-central force field, however, all elements will tend to diverge from this ideal case. Most of the variations in the orbital elements are short-periodic and average out over one orbital revolution of the satellite. The remaining long-periodic behaviour is expressed by the *mean orbital elements*, denoted with an overbar, e.g.,  $\bar{a}$ .

In the following we will study the effect of the non-central terms of the gravity field on the orbit of the satellite, especially in the radial direction. This requires the formulation of expressions for the changes in the orbital elements  $a$ ,  $e$ , and  $M$ , as a function of the geopotential field and the position of the satellite along the orbit. Therefore, the general formulation of the geopotential in terms of the geocentric position of the satellite was converted to Keplerian elements by *Kaula* [1966]. A full description of the rather tedious arithmetic involved to come to these general formulations falls outside the scope of this thesis. Here we will present the commonly used form after *Kaula* [1966, eq. (3.70)] and briefly clarify the various terms.

The geopotential terms can be written in the form

$$U_{lm} = \frac{\mu}{a} \left( \frac{ae}{a} \right)^l \sum_{p=0}^l \bar{F}_{lmp}(i) \sum_{q=-\infty}^{\infty} G_{lpq}(e) S_{lmpq}(\omega, M, \Omega, \theta) \quad , \quad (\text{B.4})$$

where  $\{a, e, i, \Omega, \omega, M\}$  are the instantaneous or *osculating Keplerian orbital elements* and  $\theta$  is the Greenwich Sidereal Time.

The functions  $\bar{F}_{lmp}(i)$  are the so-called *normalised inclination functions* that account for the fact that the orbit is inclined to the equator. These functions can be constructed from their unnormalised counterparts, given by *Kaula* [1966, eq. (3.62)], by applying the same normalisation factor as for the associated Legendre polynomials. An important characteristic of  $\bar{F}_{lmp}$  are the relations for zonal terms ( $m = 0$ ):

$$\bar{F}_{l,0,p} = \begin{cases} \bar{F}_{l,0,l-p} & \text{if } l \text{ is even,} \\ -\bar{F}_{l,0,l-p} & \text{if } l \text{ is odd.} \end{cases} \quad (\text{B.5})$$

The terms  $G_{lpq}(e)$  are known as *eccentricity or Hansen functions* and are the only terms that relate to the non-circularity of the orbit. A full mathematical description

of these terms can also be found in *Kaula* [1966, eq. (3.67)]. In general, the functions  $G_{lpq}(e)$  are of the order  $\mathcal{O}(e^{|q|})$ , so it is sufficient to consider only  $q = 0$  and  $q = \pm 1$  for nearly circular orbits ( $e < 0.002$ ). The first terms of the Taylor series expansion of these terms can be written as [Wagner, 1985]

$$\begin{aligned} G_{l,p,0}(e) &= 1 + \mathcal{O}(e^2) \quad , \\ G_{l,p,+1}(e) &= \frac{e}{2}(3l - 4p + 1) + \mathcal{O}(e^3) \quad , \\ G_{l,p,-1}(e) &= \frac{e}{2}(-l + 4p + 1) + \mathcal{O}(e^3) \quad . \end{aligned} \tag{B.6}$$

Finally, the phase function  $S_{lmpq}$  is defined as

$$S_{lmpq} = \tilde{C}_{lm} \cos \psi_{lmpq} + \tilde{S}_{lm} \sin \psi_{lmpq} \quad , \tag{B.7}$$

where

$$\tilde{C}_{lm} = \begin{cases} \bar{C}_{lm} \\ -\bar{S}_{lm} \end{cases} \quad \text{and} \quad \tilde{S}_{lm} = \begin{cases} \bar{S}_{lm} & \text{if } l - m \text{ is even,} \\ \bar{C}_{lm} & \text{if } l - m \text{ is odd,} \end{cases} \tag{B.8}$$

and the phase argument  $\psi_{lmpq}$  is given by

$$\psi_{lmpq} = (l - 2p)\omega + (l - 2p + q)M + m(\Omega - \theta) \quad . \tag{B.9}$$

Note that  $S_{lmpq}$  is merely a function of the in-orbit position of the satellite (through  $M$  and  $\omega$ ) and the position of the ascending node relative to the Greenwich meridian ( $\Omega - \theta$ ); the eccentricity,  $e$ , and inclination,  $i$ , only enter in (B.4) through the eccentricity function and inclination function, respectively. As we will see later,  $a$ ,  $e$ , and  $i$  are, to first order, constant and  $M$ ,  $\Omega$ ,  $\omega$  and  $\theta$  linear functions of time. This puts all the temporal variation of  $U_{lm}$  in  $S_{lmpq}$ .

## B.4 The Lagrange planetary equations

The motion of a satellite in an inertial Cartesian frame can be expressed by a set of three second-order differential equations,

$$\ddot{\mathbf{r}} = \nabla U \quad , \tag{B.10}$$

where  $U$  represents the potential of the entire gravity field. These three second-order equations can be rewritten to six first-order equations in terms of the rectangular coordinates of satellite's position,  $\mathbf{r} = \{x, y, z\}$ , and velocity,  $\dot{\mathbf{r}} = \{\dot{x}, \dot{y}, \dot{z}\}$ , in the same geocentric inertial frame. Alternatively, the position and velocity can be converted to the six osculating Keplerian elements  $\{a, e, i, \Omega, \omega, M\}$ . The six resulting equations that describe the variations of the oscillating orbital elements are

generally known as the Lagrange planetary equations and written in terms of the disturbing potential,  $R = U - \mu/r$ , as follows [Kaula, 1966]:

$$\begin{aligned}
 \frac{da}{dt} &= \frac{2}{na} \frac{\partial R}{\partial M} \quad , \\
 \frac{de}{dt} &= \frac{1-e^2}{na^2e} \frac{\partial R}{\partial M} - \frac{\sqrt{1-e^2}}{na^2e} \frac{\partial R}{\partial \omega} \quad , \\
 \frac{di}{dt} &= \frac{\cos i}{na^2\sqrt{1-e^2}\sin i} \frac{\partial R}{\partial \omega} - \frac{1}{na^2\sqrt{1-e^2}\sin i} \frac{\partial R}{\partial \Omega} \quad , \\
 \frac{d\Omega}{dt} &= \frac{1}{na^2\sqrt{1-e^2}\sin i} \frac{\partial R}{\partial \omega} \quad , \\
 \frac{d\omega}{dt} &= -\frac{\cos i}{na^2\sqrt{1-e^2}\sin i} \frac{\partial R}{\partial i} + \frac{\sqrt{1-e^2}}{na^2e} \frac{\partial R}{\partial e} \quad , \\
 \frac{dM}{dt} &= n - \frac{1-e^2}{na^2e} \frac{\partial R}{\partial e} - \frac{2}{na} \frac{\partial R}{\partial a} \quad ,
 \end{aligned} \tag{B.11}$$

with

$$n = \sqrt{\frac{\mu}{a^3}} \quad . \tag{B.12}$$

## B.5 Secular perturbations

The disturbing potential is dominated by the  $U_{20}$ -term, since the  $\bar{C}_{20}$  coefficient is at least two orders of magnitude larger than any of the other  $\bar{C}_{lm}$  and all  $\bar{S}_{lm}$  coefficients. This term, known as the *dynamical flattening* of the Earth, is directly correlated with the *geometrical flattening*,  $f$ , which expresses the difference of about 21 km between the Earth's polar and equatorial radius. Due to this flattening (and some other zonal terms) the satellite's orbital plane precesses about the Earth's spin axis, and the periapsis moves along the orbit, with secular rates depending on the orbital inclination, altitude, and eccentricity. This secular or mean motion is described by the mean orbital elements  $\{\bar{a}, \bar{e}, \bar{i}, \bar{\Omega}, \bar{\omega}, \bar{M}\}$ . All remaining terms of the geopotential cause small perturbations on this secularly precessing ellipse. This leads to a formulation in the form,

$$\begin{aligned}
 a &= \bar{a} + \Delta a \quad , \\
 e &= \bar{e} + \Delta e \quad , \\
 i &= \bar{i} + \Delta i \\
 \Omega &= \bar{\Omega} + \Delta\Omega = \bar{\Omega}_0 + \dot{\bar{\Omega}}t + \Delta\Omega \quad , \\
 \omega &= \bar{\omega} + \Delta\omega = \bar{\omega}_0 + \dot{\bar{\omega}}t + \Delta\omega \quad , \\
 M &= \bar{M} + \Delta M = \bar{M}_0 + \dot{\bar{M}}t + \Delta M \quad .
 \end{aligned} \tag{B.13}$$

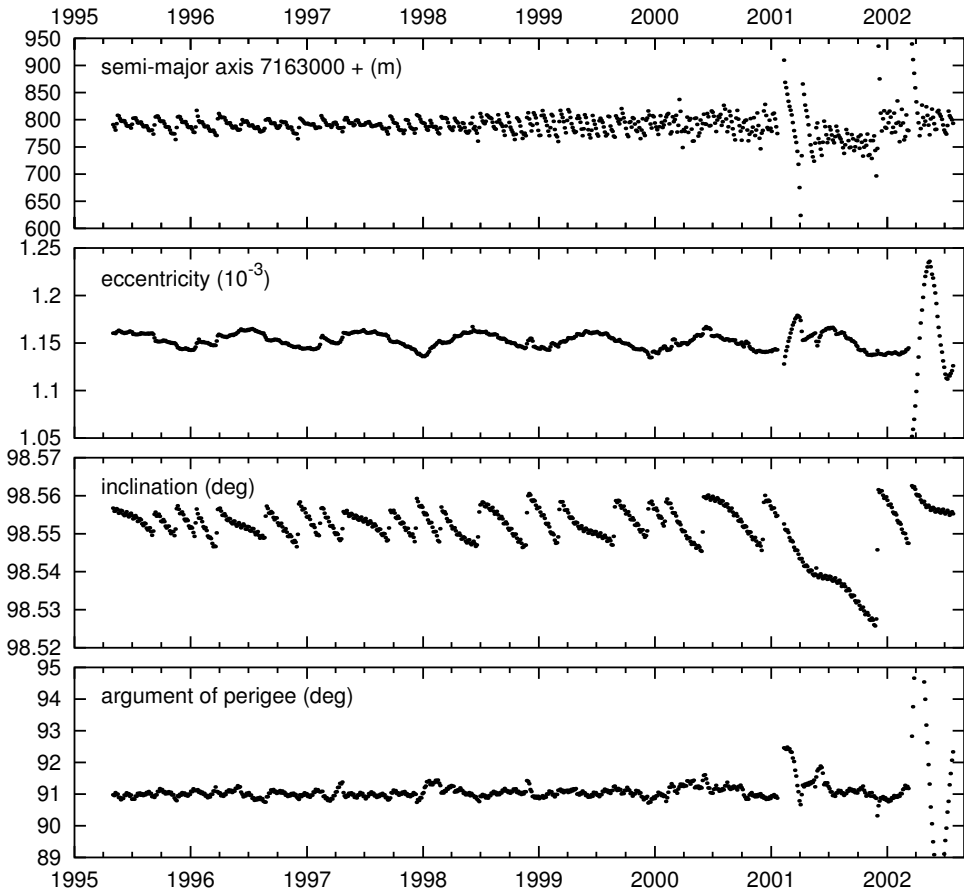


Figure B.3 Evolution of the mean orbital elements (semi-major axis, eccentricity, inclination, and argument of perigee) of ERS-2 (1995-2002).

For the recent and current altimeter missions of Geosat, ERS, TOPEX/Poseidon, GFO, Jason-1 and Envisat the mean elements  $\bar{a}$ ,  $\bar{e}$ ,  $\bar{i}$ , and  $\bar{\omega}$  are chosen such that the secular precession of the orbit are well tuned to perform some practical and important purposes: the ground track repeats itself after a well-chosen period, the perigee is fixed over the North Pole, and, in case of ERS and Envisat, the orbit is sun-synchronous.

Figure B.3 shows the variation of the most important mean orbital elements of ERS-2: semi-major axis, eccentricity, inclination, and argument of perigee. The discontinuities are due to orbital manoeuvres correcting the secular decay of orbital altitude and drift of the inclination. Since inclination manoeuvres were not possible while the satellite was flying in zero-gyro mode during 2001, the excursion of inclination was significant.

Satellite	Mission	Period (days)	Nodal Days $N_D$	Revolutions $N_R$
Geosat, GFO	Exact Repeat Mission	17.05	17	244
ERS-1	Commissioning Phase	3.00	3	43
	Ice Phase	3.00	3	43
	Multi-disciplinary Phase	35.00	35	501
	Geodetic Phase	176.00	176	2523
	Tandem Mission	35.00	35	501
ERS-2, Envisat	Multi-disciplinary Phase	35.00	35	501
TOPEX/Poseidon, Jason-1	Exact Repeat Mission	9.92	10	127

Table B.1 Repeat periods of recent and current altimeter satellites.

### B.5.1 Ground track repetition

To monitor variations in the sea level with altimetry, it is essential that the measurements are made repeatedly at the same location. The period between successive measurements may range from a week to a month, depending on the type of features to be sampled. To accomplish repetition of measurements, the satellite is manoeuvred into a repeat orbit. During each repeat cycle, the satellite's ground track describes a regular pattern of ascending and descending tracks and then starts to retrace itself within a certain dead-band of about one kilometre. This is only obtained when the Earth has revolved an exact integer number of times ( $N_D$ ) with respect to the secularly precessing orbit, during which time the satellite has completed a full integer number of revolutions ( $N_R$ ). This yields,

$$N_D \frac{2\pi}{\dot{\theta} - \dot{\Omega}} = N_R \frac{2\pi}{\dot{\omega} + \dot{M}} \quad (\text{B.14})$$

or

$$\frac{\dot{M} + \dot{\omega}}{\dot{\theta} - \dot{\Omega}} = \frac{N_R}{N_D} \quad (\text{B.15})$$

The period  $2\pi/(\dot{\theta} - \dot{\Omega})$  is called a *nodal day* and is approximately equal to one (sidereal) day. Table B.1 lists the lengths of the various repeat cycles of recent and current altimeter satellites.

### B.5.2 Frozen orbit

The ERS radar altimeter has two tracking modes: a course *Ice Mode* and an accurate *Ocean Mode*. At the cost of having a lower resolution, the Ice tracking mode is able to follow steeply sloping ice sheets without losing acquisition. Increasing the resolution means shortening the range window of the altimeter. Since the position

of the range window is determined from previous measurements, rapid changes of altitude will cause the return pulse to fall outside the preset range window. In Ocean Mode, the altimeter loses track over rough terrain, but keeps lock on and provides highly precise measurements over oceans, seas and major lakes, and even tracks occasionally over shallow land areas.

Such restrictions on the altitude rate has also implications on the orbit geometry. The vertical velocity of the satellite above a flattened Earth is minimal when the orbit is slightly eccentric and the mean perigee is over one of the poles ( $\bar{\omega} = \pm 90^\circ$ ). In first approximation, this is also the state in which the mean perigee does not drift along the orbit (in other words,  $\dot{\bar{\omega}} = 0$ ). Hence, this state is called a *frozen orbit*.

### B.5.3 Sun-synchronous orbit

The orbits of the ERS and Envisat satellites have the additional property that the nodal day equals exactly one solar day, so the sun maintains roughly the same inclination to the orbit. This is called a *sun-synchronous orbit*. This makes it possible to make observations of the same location always at the same local solar time (LST), which is a major advantage for comparison of SAR images made on different repeat cycles. For moderate latitudes, the northbound ERS overflight takes place at about 22:30 local solar time; on southbound passes at about 10:30 LST. A sun-synchronous orbit is obtained when the orbital plane precesses exactly  $360^\circ$  to the East during one (solar) year, *i.e.*,  $\dot{\bar{\Omega}} = 360^\circ/\text{year}$ .

There is one important downside to a sun-synchronous orbit, and that is precisely the fact that the satellite is observing the same place always at the same local solar time. This means that the altimeter always measures the same phase of the solar tide. Therefore, a constant elevation of sea level is indistinguishable from the tidal elevation so that the determination or the improvement of the solar tide with ERS data is not possible. It is for this reason that the orbits of TOPEX/Poseidon Jason-1 are *not* sun-synchronous, but are optimised to allow the best separation of all tidal signals [*e.g.*, Smith, 1999].

But, the sun-synchronous orbit has other advantages. The solar panel can receive a nearly constant and optimal amount of power (outside of the eclipse) with a solar panel spinning around a single axis pointing in a direction perpendicular to the orbital plane. When the orbit is not sun-synchronous, a second axis of rotation is required, or the satellite has to steer around itself, which is the case with TOPEX/Poseidon, but is not possible with ERS because of the pointing requirements of the other instruments.

## B.6 Linear orbit perturbations

The gravitational orbit perturbations are determined by substituting Kaula's expression for the geopotential (B.4) in the Lagrange planetary equations (B.11) and

then integrating the various rates of change of the orbital elements over the phase argument  $\psi_{lmpq}$ . The contributions of each individual  $lmpq$  combination to the perturbations in the Keplerian elements can then be written as

$$\begin{aligned}
 \Delta a_{lmpq} &= 2\bar{a} \left(\frac{a_e}{\bar{a}}\right)^l \bar{F}_{lmp} G_{lpq} (l-2p+q) \frac{\bar{n}}{\dot{\psi}_{lmpq}} S_{lmpq} \quad , \\
 \Delta e_{lmpq} &= \frac{\sqrt{1-\bar{e}^2}}{\bar{e}} \left(\frac{a_e}{\bar{a}}\right)^l \bar{F}_{lmp} G_{lpq} \left[ \sqrt{1-\bar{e}^2} (l-2p+q) - (l-2p) \right] \\
 &\quad \times \frac{\bar{n}}{\dot{\psi}_{lmpq}} S_{lmpq} \quad , \\
 \Delta i_{lmpq} &= \frac{1}{\sin \bar{i} \sqrt{1-\bar{e}^2}} \left(\frac{a_e}{\bar{a}}\right)^l \bar{F}_{lmp} G_{lpq} [(l-2p) \cos \bar{i} - m] \frac{\bar{n}}{\dot{\psi}_{lmpq}} S_{lmpq} \quad , \\
 \Delta \Omega_{lmpq} &= \frac{1}{\sin \bar{i} \sqrt{1-\bar{e}^2}} \left(\frac{a_e}{\bar{a}}\right)^l \bar{F}'_{lmp} G_{lpq} \frac{\bar{n}}{\dot{\psi}_{lmpq}} S_{lmpq}^* \quad , \\
 \Delta \omega_{lmpq} &= \left(\frac{a_e}{\bar{a}}\right)^l \left[ \frac{\sqrt{1-\bar{e}^2}}{\bar{e}} \bar{F}_{lmp} G'_{lpq} - \frac{\cos \bar{i}}{\sin \bar{i} \sqrt{1-\bar{e}^2}} \bar{F}'_{lmp} G_{lpq} \right] \frac{\bar{n}}{\dot{\psi}_{lmpq}} S_{lmpq}^* \quad , \\
 \Delta M_{lmpq} &= \left(\frac{a_e}{\bar{a}}\right)^l \bar{F}_{lmp} \left[ 2(l+1)G_{lpq} - \frac{\sqrt{1-\bar{e}^2}}{\bar{e}} G'_{lpq} - 3G_{lpq} (l-2p+q) \frac{\bar{n}}{\dot{\psi}_{lmpq}} \right] \\
 &\quad \times \frac{\bar{n}}{\dot{\psi}_{lmpq}} S_{lmpq}^* \quad ,
 \end{aligned} \tag{B.16}$$

where the partial derivatives of  $\bar{F}_{lmp}$  and  $G_{lpq}$  are indicated as

$$\begin{aligned}
 \bar{F}'_{lmp} &= \frac{\partial \bar{F}_{lmp}}{\partial i} \quad , \\
 G'_{lpq} &= \frac{\partial G_{lpq}}{\partial e} \quad ,
 \end{aligned} \tag{B.17}$$

and  $S_{lmpq}^*$  is the integral of  $S_{lmpq}$  over  $\psi_{lmpq}$ , or

$$S_{lmpq}^* = \int_0^{2\pi} S_{lmpq}(\psi_{lmpq}) d\psi_{lmpq} = \tilde{C}_{lm} \sin \psi_{lmpq} - \tilde{S}_{lm} \cos \psi_{lmpq} \quad . \tag{B.18}$$

Note that  $S_{lmpq}^*$  differs from  $S_{lmpq}$  only by a lag of  $90^\circ$  in the phase argument, *i.e.*,

$$S_{lmpq}^*(\psi_{lmpq}) = S_{lmpq}(\psi_{lmpq} - 90^\circ) \quad . \tag{B.19}$$

In order to perform the integration of the Lagrange planetary equations we have tacitly made some simplifying assumptions:



- The coordinate frame in which the orbital elements are defined is assumed to be inertial. Thus, precession and nutation of the Earth's spin axis in the inertial space are neglected during the period of integration. In reality, the precessing spin axis describes a full cone with half a top angle of  $23.5^\circ$  in about 18600 years.
- The gravity field coefficients are treated as constants. This means that variations due to polar motion, post glacial rebound, and tides are ignored.
- Most important is the assumption that we have small linear perturbations. This means that each coefficient causes small orbit perturbations that are superimposed on the mean orbital elements. Also, the mean orbital elements  $\{\bar{a}, \bar{e}, \bar{i}\}$  are assumed to be constant and  $\{\bar{\Omega}, \bar{\omega}, \bar{M}\}$  to change secularly. These assumptions are the foundation under the *Linear Perturbation Theory (LPT)*.

## B.7 Radial orbit perturbations on a nearly circular orbit

So far, the first-order effect of the geopotential on the six Keplerian orbit elements is fully described. However, for altimeter missions it is more suitable to study the perturbations in position with respect to a mean (unperturbed) orbit. In particular, the radial position component requires special attention, because it directly influences the measurement of sea surface height. Just as the radial position of the satellite is a function of the Keplerian orbit elements, the perturbations in this component can be expressed in terms of the perturbations in the orbit elements. Especially for the nearly circular orbits ( $e < 0.002$ ) that are considered here, this transformation is quite straightforward.

The radial position of the satellite is given by

$$r = a(1 - e \cos E) \quad , \quad (\text{B.20})$$

where  $E$  is the *eccentric anomaly*. The functional relationship between this angle and the mean anomaly,  $M$ , is given by

$$M = E - e \sin E \quad , \quad (\text{B.21})$$

so we can write

$$r = a[1 - e \cos M + \mathcal{O}(e^2)] \quad . \quad (\text{B.22})$$

Because the orbits in question are nearly circular, the  $\mathcal{O}(e^2)$ -term can be neglected. Linearisation of the remaining terms yields [e.g., Colombo, 1984]

$$\Delta r \approx \Delta a (1 - \bar{e} \cos \bar{M}) - \bar{a} \Delta e \cos \bar{M} - \bar{a} \bar{e} \Delta M \sin \bar{M} \quad . \quad (\text{B.23})$$

Next step is to substitute the expressions for  $\Delta a$ ,  $\Delta e$ , and  $\Delta M$ , as defined by (B.16) into (B.23). Again, all terms of order  $\mathcal{O}(e)$  (and higher) can be neglected with

respect to unity. Taking also into account the expansions of  $G_{lpq}$  for  $q = -1, 0, 1$  (eq. (B.6)), only a few significant contributions remain:

$$\begin{aligned}
 \Delta a_{lmp0} &= 2\bar{a} \left(\frac{a_e}{\bar{a}}\right)^l \bar{F}_{lmp}(l-2p) \frac{\bar{n}}{\dot{\psi}_{lmp0}} S_{lmp0} \quad , \\
 -\bar{a} \Delta e_{lmp-1} &= \frac{\bar{a}}{2} \left(\frac{a_e}{\bar{a}}\right)^l \bar{F}_{lmp}(4p-l+1) \frac{\bar{n}}{\dot{\psi}_{lmp-1}} S_{lmp-1} \quad , \\
 -\bar{a} \Delta e_{lmp+1} &= \frac{\bar{a}}{2} \left(\frac{a_e}{\bar{a}}\right)^l \bar{F}_{lmp}(4p-3l-1) \frac{\bar{n}}{\dot{\psi}_{lmp+1}} S_{lmp+1} \quad , \\
 -\bar{a} \bar{e} \Delta M_{lmp-1} &= \frac{\bar{a}}{2} \left(\frac{a_e}{\bar{a}}\right)^l \bar{F}_{lmp}(4p-l+1) \frac{\bar{n}}{\dot{\psi}_{lmp-1}} S_{lmp-1}^* \quad , \\
 -\bar{a} \bar{e} \Delta M_{lmp+1} &= -\frac{\bar{a}}{2} \left(\frac{a_e}{\bar{a}}\right)^l \bar{F}_{lmp}(4p-3l-1) \frac{\bar{n}}{\dot{\psi}_{lmp+1}} S_{lmp+1}^* \quad .
 \end{aligned} \tag{B.24}$$

Note that since

$$S_{lmp-1} \cos \bar{M} + S_{lmp-1}^* \sin \bar{M} = S_{lmp+1} \cos \bar{M} - S_{lmp+1}^* \sin \bar{M} = S_{lmp0} \quad , \tag{B.25}$$

all terms  $S_{lmp\pm 1}$  and  $S_{lmp\pm 1}^*$  disappear when they are substituted in (B.23). Consequently, the zeroth order radial orbit perturbation for each  $lmp$  combination can be written as

$$\Delta r_{lmp} = \bar{a} \bar{n} \left(\frac{a_e}{\bar{a}}\right)^l \bar{F}_{lmp} \left[ \frac{2(l-2p)}{\dot{\psi}_{lmp0}} + \frac{4p-3l-1}{2\dot{\psi}_{lmp+1}} + \frac{4p-l+1}{2\dot{\psi}_{lmp-1}} \right] S_{lmp0} \quad . \tag{B.26}$$

The three fractional terms between square brackets in (B.26) are best transformed to a single fraction with a common denominator:

$$\dot{\psi}_{lmp0} \dot{\psi}_{lmp-1} \dot{\psi}_{lmp+1} = \dot{\psi}_{lmp0} (\dot{\psi}_{lmp0}^2 - \bar{M}^2) \quad .$$

Subsequent summation over all  $lmp$  combinations then yields

$$\Delta r \approx \sum_{l=1}^{\infty} \sum_{m=0}^l \sum_{p=0}^l D_{lmp} S_{lmp0} \quad , \tag{B.27}$$

where

$$D_{lmp} = \bar{a} \bar{n} \left(\frac{a_e}{\bar{a}}\right)^l \bar{F}_{lmp}(\bar{i}) \frac{\beta(l+1) - 2k}{\beta(\beta^2 - 1)} \quad , \tag{B.28}$$

$$S_{lmp0} = \tilde{C}_{lm} \cos \bar{\psi}_{lmp0} + \tilde{S}_{lm} \sin \bar{\psi}_{lmp0} \quad , \tag{B.29}$$

with

$$k = l - 2p \quad , \quad (B.30)$$

$$\beta = \dot{\bar{\psi}}_{lmp0} / \dot{\bar{M}} \quad , \quad (B.31)$$

$$\bar{\psi}_{lmp0} = k(\bar{\omega} + \bar{M}) + m(\bar{\Omega} - \bar{\theta}) \quad , \quad (B.32)$$

and

$$\tilde{C}_{lm} = \begin{cases} \bar{C}_{lm} \\ -\bar{S}_{lm} \end{cases} \quad \text{and} \quad \tilde{S}_{lm} = \begin{cases} \bar{S}_{lm} & \text{if } l - m \text{ is even,} \\ \bar{C}_{lm} & \text{if } l - m \text{ is odd.} \end{cases} \quad (B.33)$$

These equations are an analytical description of the radial orbit perturbations on a secularly precessing ellipse due to the full non-central gravity field of the Earth (modelled by the  $\bar{C}_{lm}$  and  $\bar{S}_{lm}$  coefficients). Since these equations are purely linear, they can also be applied to compute the radial orbit errors due to *imperfections* in the gravity field modelling. This requires merely the substitution of the gravity field model errors ( $\Delta\bar{C}_{lm}$  and  $\Delta\bar{S}_{lm}$ ) for the respective gravity field coefficients ( $\bar{C}_{lm}$  and  $\bar{S}_{lm}$ ). Therefore, all what is said in this Appendix about orbit perturbations due to the geopotential also holds for errors in the computed orbit due to errors in the geopotential coefficients; the two are completely analogue.

## B.8 Frequency spectrum of the radial orbit error

In the phase angle  $\bar{\psi}_{lmp0}$  (B.32) we recognise two base frequencies,

- a one per revolution component,  $(\bar{\omega} + \dot{\bar{M}})$ , responsible for short-periodic  $k$ -cpr perturbations in the orbit;
- a ‘daily’ component  $(\dot{\bar{\Omega}} - \dot{\bar{\theta}})$ , producing long-periodic perturbations: the  $m$ -dailies.

In a sun-synchronous orbit  $(\dot{\bar{\Omega}} - \dot{\bar{\theta}})$  stands for a frequency of exactly one cycle per day (cpd). Therefore the frequencies in the orbit perturbations can be written as:

$$\dot{\bar{\psi}}_{lmp0} = k \text{ cpr} - m \text{ cpd} \quad . \quad (B.34)$$

Combinations of the  $k$ -cpr and  $m$ -daily frequencies can lead to perturbations with very long periods, up to the length of the repeat cycle.

### B.8.1 Lumped coefficients

Equations (B.30) through (B.32) clearly demonstrate that the frequency of the perturbations on a given orbit are merely a function of  $k = l - 2p$  and  $m$ . Thus, for any  $m$  there are many combinations of  $l$  and  $p$  that will produce orbit perturbations

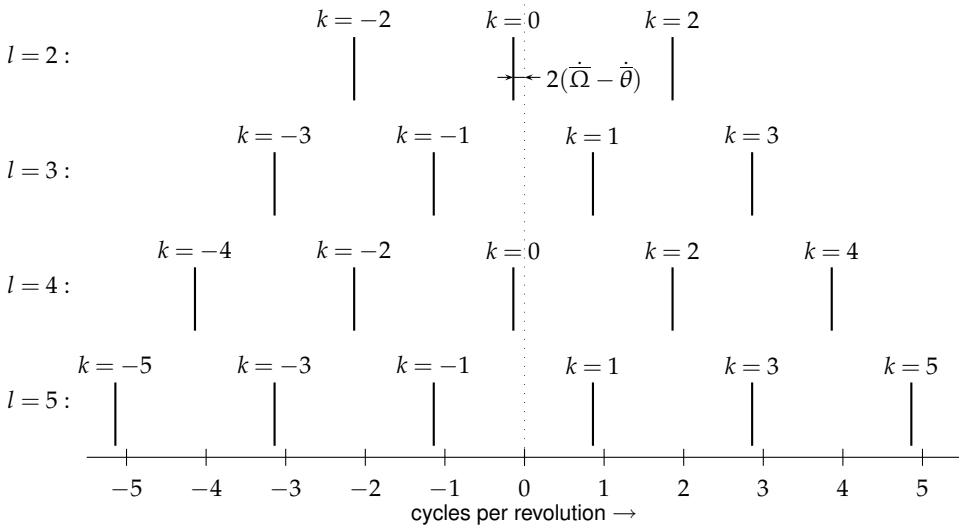


Figure B.4 Distribution of the spectral lines produced by gravity field coefficients of order  $m = 2$  and degree  $l = 2, 3, 4, 5$ . Note that all odd degrees have overlapping frequencies, as well as the even degrees. This diagram becomes more complicated when the negative frequencies are properly mapped to positive ones. (See Figure B.5.)

with the same frequency  $\dot{\psi}$ . For example:  $l, m, p = 3, 2, 1$  and  $l, m, p = 11, 2, 5$  both yield  $\dot{\psi} = (\dot{\omega} + \dot{M}) + 2(\dot{\Omega} - \dot{\theta})$ . This means that the gravity field coefficients  $\bar{C}_{3,2}$  and  $\bar{C}_{11,2}$  create orbit perturbations that partly overlap in frequency. In general, there is a complete family of combinations  $lmp$  that produce the same frequency. The gravity field coefficients that fall under this family are called *lumped coefficients*.

When we observe a certain perturbation frequency in a satellite orbit it is not always possible to pinpoint which gravity field coefficient is responsible for a certain orbit perturbation frequency, since several coefficients can produce the same frequency. But it is generally quite easy to figure out which set of lumped coefficients is the culprit.

Figure B.4 illustrates the spectrum of frequencies created by gravity field coefficients of order  $m = 2$  and various degrees  $l$ .

- Starting with  $l = 2$ , there are three lines in the frequency spectrum: one at the base frequency  $2(\dot{\Omega} - \dot{\theta})$  for ( $k = 0$ ) and one at each side of this, located at 2-cpr down and up the spectrum ( $k = \pm 2$ ). Note that negative frequencies should be wrapped to positive frequencies, as depicted in Figure B.5.
- For odd degree  $l = 3$ , there are four spectral lines: two at each side of the base frequency, 1-cpr and 3-cpr down and up the spectrum ( $k = \pm 1, \pm 3$ ).
- For the next even degree  $l = 4$ , the spectrum contains five lines, three of which are at the same frequency as for  $l = 2$ .

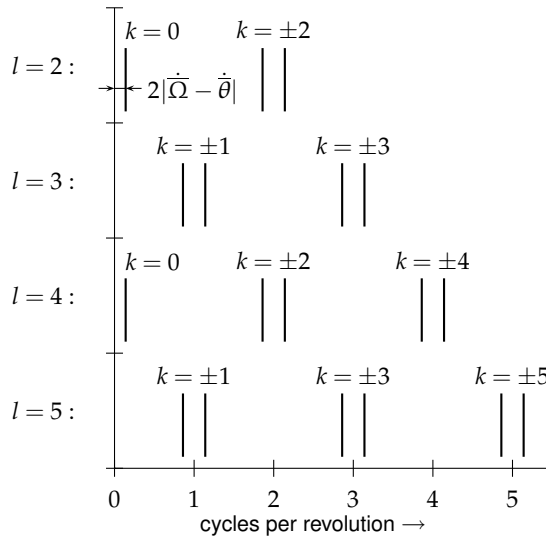


Figure B.5 Distribution of the spectral lines produced by gravity field coefficients of order  $m = 2$  and degree  $l = 2, 3, 4, 5$ . Negative frequencies are mapped to positive ones.

- Similarly, for  $l = 5$ , the spectrum contains two extra lines at each side of the four produced by  $l = 3$ , located 1-cpr down and up the frequency domain.

In general, for a given order  $m$ , each higher degree  $l$  introduces two extra lines to the spectrum, in addition to the  $l - 1$  lines it has in common with degree  $l - 2$ . So, odd degrees have only lines in common with odd degrees, and even with even degrees. Coefficients of different order  $m$  generally have no frequencies in common.

Only when the satellite performs an exact repeat mission, overlapping of perturbation frequencies will also occur for coefficients of different order  $m$ . This is can be illustrated by evaluating  $\dot{\psi}_{lmp0}$  for the condition of repetition imposed by (B.15), yielding

$$\begin{aligned}
 \dot{\psi}_{lmp0} &= \left[ k - m \frac{N_D}{N_R} \right] (\dot{\omega} + \dot{M}) \\
 &= k - m \frac{N_D}{N_R} \text{ cycles per revolution} \\
 &= kN_R - mN_D \text{ cycles per repeat period} \quad .
 \end{aligned}
 \tag{B.35}$$

For example, during the ERS-1 Commissioning Phase and during both Ice Phases the satellite performed 43 revolutions in 3 days. Consequently,  $k, m = 3, 0$ , and  $k, m = 0, 43$  will both produce a 3-cpr orbit perturbation. Still, lumping of coefficients of different order only occurs when  $m$  is a multiple of  $N_R$ . These coefficients are not only sparse, they also have little influence on the orbit, because of their

high order; in a longer repeat cycle, like the Multi-Disciplinary Phase of ERS (501 revolutions in 35 days), this first occurs at  $m = 501$ !

Equation (B.35) also shows that in a repeat mission all perturbation frequencies are integer multiples of 1 cycle per repeat period. This means that the period of the perturbations can be no longer than the repeat period and that the pattern of perturbations repeats after one repeat cycle. This conclusion is not so striking when we realise that after one repeat period the satellite follows the same ground track and hence encounters the same perturbation forces as the period before and therefore also exhibits the same orbit perturbations. In that respect gravity induced orbit perturbations are *geographically correlated*: they are repetitive at the same location along the ground track.

### B.8.2 Zonal coefficients

When we examine (B.27–B.33) for  $m = 0$ , it becomes clear that zonal coefficients,  $\overline{C}_{10}$ , only produce radial orbit perturbations that are symmetric with respect to the point of maximum latitude ( $\overline{\omega} + \overline{M} = 90^\circ$ ). In other words, the resulting perturbations also have a zonal distribution over the globe and are identical on ascending and descending satellite tracks. When we form crossover height differences their respective contributions to the measurement of sea surface height cancel. So, according to LPT, errors in the zonal gravity field coefficients have no impact on crossovers height differences. This means, *vice versa*, that errors in the zonal coefficients can not be resolved from crossover data only.

### B.8.3 Resonance

Looking back at (B.26), it is obvious that the first fractional term between square brackets is due to the changes in the semi-major axis, causing a singularity for  $\dot{\overline{\psi}}_{1mp0} = 0$  (or  $\beta = 0$  (B.31)). This is inherited from the fact that the linear perturbation theory does not cover constant or secular perturbations. The second and third fractional terms are the combined effect of perturbations in the eccentricity and mean anomaly, and are singular for  $\dot{\overline{\psi}}_{1mp0} = \pm \dot{\overline{M}}$  (or  $\beta = \pm 1$ ). This means that the constant and 1-cpr radial perturbations, that would result from constant offsets in the semi-major axis, the eccentricity or mean anomaly, are not represented by the linear perturbation theory.

We usually distinguish between three types of resonance (see also Figure B.6):

**Pure resonance** occurs precisely at the singularities of the analytical formulation of the radial orbit error, *i.e.*, at 0 and 1 cycle per revolution ( $\beta = -1, 0, +1$ )

**Shallow resonance** occurs close to the 0 frequency. When the period of the radial orbit error component is very large—it can be as long as the repeat period—, then the perturbation has ample time to grow. Even though the rate might be quite small, the amplitude can be considerable.

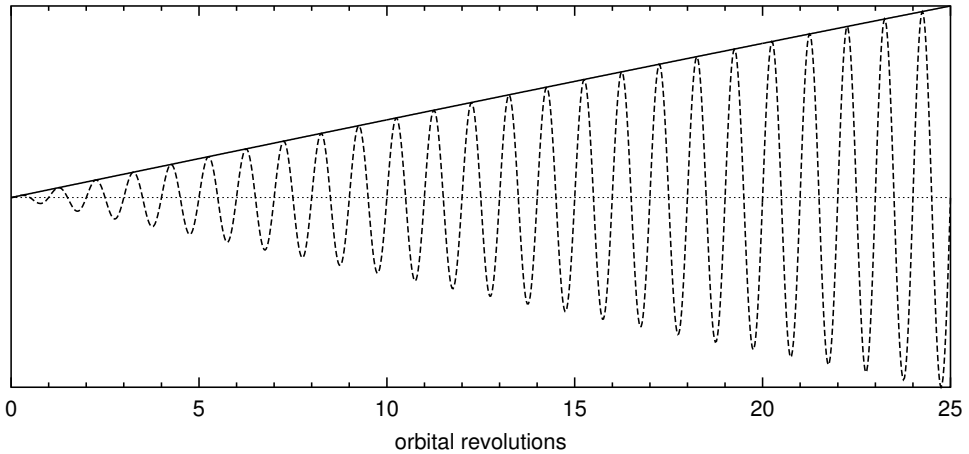


Figure B.6 *Shallow resonance* (solid line) occurs when the frequency is very low, resulting in a nearly secular signal. The dashed line results from a modulation with a 1-cpr signal, known as *deep resonance*.

**Deep resonance** occurs when the radial orbit perturbation is close to 1 cycle per revolution. These components are always due to nearly secular changes in the orbital eccentricity or the along-track position, and appear as a 1-cpr radial orbit variation with a long periodic modulation of its amplitude. Again, this nearly secular modulation introduces amplitudes of considerable magnitude.

#### B.8.4 Limitations due to arc length

When  $\beta(\beta^2 - 1)$  in the denominator of (B.29) becomes small (for values of  $\beta$  close to 0 or  $\pm 1$ , the amplitude of the radial orbit perturbation can be rather large. The question is whether these cases of shallow or deep resonance will introduce perturbations that exceed the linearisation requirements and whether corruption of the solution by resonance can be avoided. We will see that, in fact, the argument is purely theoretical and becomes in practise a non-issue.

As mentioned in the previous Section, pure resonance at 0 and 1 cpr results from constant offsets in semi-major axis, eccentricity, or along-track position. These are precisely elements of the state vector that are estimated on arc-by-arc basis. Those elements will absorb any purely resonant term. In other words, when the orbit is fitted to the tracking data during the precise orbit determination, all 0- and 1-cpr orbit errors end up in adjustments of the state vector and will no longer be visible in the actual computed radial orbit position.

For the large part, this argument also holds for deep and shallow resonance. Theoretically, the period of the perturbation or of the modulation of the 1-cpr perturbation can be as long as the repeat period. In practise, the state vector is estimated every 3.5 days (roughly every 50 revolutions), thus picking up much of

the long-periodic signals. As a rule of thumb, all frequencies below 0.02 cpr and between 0.98 and 1.02 cpr are absorbed by the state vector and will *not* occur in the orbit error spectrum. In other words, it is no problem that resonant terms are not represented in the LPT (they will not occur in reality either) as long as we limit the LPT to only reflect frequencies that are sufficiently different from 0 and 1 cpr.

By the way, this does not mean that orbit errors at or close to 0 or 1 cpr do not exist. Of course, errors in the state vector (*e.g.*, as a result of errors in the tracking data) still occur and produce orbit perturbations at these frequencies. What is important to realise is that state vectors are very efficient in counteracting force model errors that would result in resonant or near-resonant orbit errors. This also means that these force model errors are very hard to recover from tracking data residuals, unless the arc length is extended to the length of the repeat period.

## B.9 Spatial distribution of the radial orbit error

In Section B.8.1 it was shown that the gravity induced orbit perturbations and the associated orbit errors are in some way geographically correlated. We are therefore interested in how the altitude varies spatially, in an Earth-fixed reference frame, as a function of latitude  $\phi$  and longitude  $\lambda$ . The spatial manifestation of the orbit perturbation is particularly useful in altimetric studies, like the determination of mean sea surfaces and mean ocean currents, where geographically correlated radial orbit errors may corrupt the results. The representation of the radial orbit perturbations as a function of geographical location instead of time will allow a direct analysis of this problem.

So far, we have demonstrated how the orbital altitude varies in time as a function of the angles  $(\bar{\omega} + \bar{M})$  and  $(\bar{\Omega} - \bar{\theta})$ . To do the conversion from the temporal to the spatial domain we first have to determine the relationship between these angles and the geographical location of the satellite and then convert the sine and cosine of the argument  $\bar{\psi}_{lmp0}$  to (series of) harmonics of  $\bar{\phi}$  and  $\bar{\lambda}$ .

### B.9.1 From orbital elements to geographic location

Figure B.7 can be used to derive some important relations between the satellite orbital elements and its Earth-fixed position. First of all

$$\bar{\Omega} - \bar{\theta} = \bar{\phi} - (\bar{\alpha} - \bar{\Omega}) \quad , \quad (\text{B.36})$$

where  $\bar{\phi}$  and  $\bar{\alpha}$  are the satellite's longitude and right ascension, respectively. Substituting this expression into  $\cos \bar{\psi}_{lmp0}$  and  $\sin \bar{\psi}_{lmp0}$  and using trigonometric relations to separate the terms  $\bar{\phi}$ ,  $(\bar{\omega} + \bar{M})$  and  $(\bar{\alpha} - \bar{\Omega})$  yields

$$\begin{aligned} \cos \bar{\psi}_{lmp0} &= \cos m\bar{\lambda} [\cos k(\bar{\omega} + \bar{M}) \cos m(\bar{\alpha} - \bar{\Omega}) + \sin k(\bar{\omega} + \bar{M}) \sin m(\bar{\alpha} - \bar{\Omega})] \\ &\quad - \sin m\bar{\lambda} [\sin k(\bar{\omega} + \bar{M}) \cos m(\bar{\alpha} - \bar{\Omega}) - \cos k(\bar{\omega} + \bar{M}) \sin m(\bar{\alpha} - \bar{\Omega})] \end{aligned} \quad (\text{B.37})$$



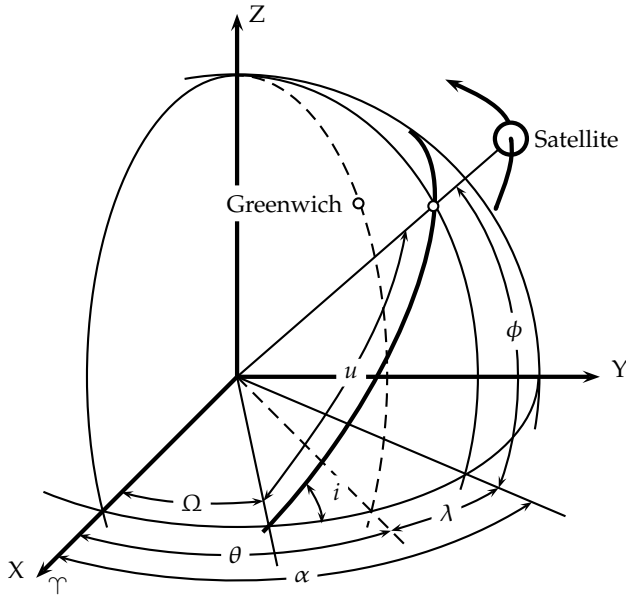


Figure B.7 Satellite orbit geometry with respect to the inertial and Earth-fixed coordinate systems.

and

$$\begin{aligned} \sin \bar{\psi}_{lmp0} = & \cos m\bar{\lambda} [\cos k(\bar{\omega} + \bar{M}) \cos m(\bar{\alpha} - \bar{\Omega}) + \sin k(\bar{\omega} + \bar{M}) \sin m(\bar{\alpha} - \bar{\Omega})] \\ & + \sin m\bar{\lambda} [\sin k(\bar{\omega} + \bar{M}) \cos m(\bar{\alpha} - \bar{\Omega}) - \cos k(\bar{\omega} + \bar{M}) \sin m(\bar{\alpha} - \bar{\Omega})] . \end{aligned} \tag{B.38}$$

The next step is to get rid of the cosine and sine of multiple angles using the formulae

$$\begin{aligned} \cos(n\alpha) &= \sum_{j=0}^{\frac{n}{2}} \binom{n}{2j} (-1)^j \cos^{n-2j} \alpha \sin^{2j} \alpha , \\ \sin(n\alpha) &= \sum_{j=0}^{\frac{n-1}{2}} \binom{n}{2j+1} (-1)^j \cos^{n-2j-1} \alpha \sin^{2j+1} \alpha . \end{aligned} \tag{B.39}$$

Note that  $n$  has to be positive. In case  $n$  is negative (and it *can* be, because  $k = l - 2p$  can be negative), we replace  $n\alpha$  by  $(-n)(-\alpha)$ .

The last ingredient needed is the conversion of the cosine and sine of the angles  $(\bar{\omega} + \bar{M})$  and  $(\bar{\Omega} - \bar{\theta})$  in terms of harmonics of  $\bar{\phi}$  and  $\bar{\lambda}$ . It is important to realise here that in circular orbits, and to zeroth order also in eccentric orbits, the angle  $(\bar{\omega} + \bar{M})$  is equal to the argument of latitude of the satellite  $\bar{u}$ . This approximation neglects terms of the order  $\mathcal{O}(e)$ .

Then Figure B.7 is used again to find the spherical trigonometric relations

$$\begin{aligned}\cos(\bar{\alpha} - \bar{\Omega}) &= \frac{\cos(\bar{\omega} + \bar{M})}{\cos \bar{\phi}} \quad , \\ \sin(\bar{\alpha} - \bar{\Omega}) &= \frac{\sin(\bar{\omega} + \bar{M}) \sin \bar{i}}{\cos \bar{\phi}} \quad ,\end{aligned}\tag{B.40}$$

where  $\bar{u}$  is already replaced by  $(\bar{\omega} + \bar{M})$ . Similarly, we find to zeroth order eccentricity

$$\begin{aligned}\sin(\bar{\omega} + \bar{M}) &= \frac{\sin \bar{\phi}}{\sin \bar{i}} \quad , \\ \cos(\bar{\omega} + \bar{M}) &= \pm \sqrt{1 - \sin^2(\bar{\omega} + \bar{M})} = \pm \frac{\sqrt{\sin^2 \bar{i} - \sin^2 \bar{\phi}}}{\sin \bar{i}} \quad ,\end{aligned}\tag{B.41}$$

where the positive sign holds ascending tracks and the negative sign for descending tracks.

Finally all the ingredients are available to make the conversion from the temporal to the spatial domain. The spatial representation for the orbit perturbations is obtained by substituting eqs. (B.37) through (B.41) into eqs. (B.27) through (B.33). This cumbersome chore is worked out in more detail in *Rosborough* [1986].

## B.9.2 Radial orbit error at a geographical location

In the end, the most convenient formulation for the spatial distribution of the radial orbit perturbation is written as the overall sum of contributions of each  $lm$  pair,

$$\Delta r = \sum_{l=1}^{\infty} \sum_{m=0}^l \Delta r_{lm}^c \pm \Delta r_{lm}^s \quad ,\tag{B.42}$$

where the choice of the sign is positive for ascending tracks and negative for descending tracks, and partial radial orbit perturbations are

$$\begin{aligned}\Delta r_{lm}^c &= \bar{Q}_{lm}^c (\bar{C}_{lm} \cos m\bar{\lambda} + \bar{S}_{lm} \sin m\bar{\lambda}) \quad , \\ \Delta r_{lm}^s &= \bar{Q}_{lm}^s (\bar{C}_{lm} \sin m\bar{\lambda} - \bar{S}_{lm} \cos m\bar{\lambda}) \quad .\end{aligned}\tag{B.43}$$

The two orthogonal latitude dependent functions  $\bar{Q}_{lm}^s$  and  $\bar{Q}_{lm}^c$  are given by

$$\begin{aligned}\bar{Q}_{lm}^c &= \sum_{p=0}^l D_{lmp} \tilde{\Phi}_{lmp}^c \quad , \\ \bar{Q}_{lm}^s &= \sum_{p=0}^l D_{lmp} \tilde{\Phi}_{lmp}^s \quad ,\end{aligned}\tag{B.44}$$

where

$$\tilde{\Phi}_{lmp}^c = \begin{cases} \overline{\Phi}_{lmp}^c \\ \overline{\Phi}_{lmp}^s \end{cases} \quad \text{and} \quad \tilde{\Phi}_{lmp}^s = \begin{cases} -\overline{\Phi}_{lmp}^s & \text{if } l - m \text{ is even,} \\ \overline{\Phi}_{lmp}^c & \text{if } l - m \text{ is odd.} \end{cases} \quad (\text{B.45})$$

and  $D_{lmp}$  is given by (B.28). The expressions for the latitude functions  $\overline{\Phi}_{lmp}^c$  and  $\overline{\Phi}_{lmp}^s$  are greatly simplified by the introduction of  $\kappa$ , a shorthand for the absolute value of  $(l - 2p)$ ,

$$\kappa = |l - 2p| \quad , \quad (\text{B.46})$$

making  $(l - 2p)/\kappa$  a convenient way of writing ‘the sign of  $(l - 2p)$ ’. This yields,

$$\begin{aligned} \overline{\Phi}_{lmp}^c &= \frac{1}{\cos^m \bar{\phi} \sin^{m+\kappa} \bar{i}} \left[ Y_\kappa^c \Psi_m^c + \frac{l-2p}{\kappa} Y_\kappa^s \Psi_m^s \right] \quad , \\ \overline{\Phi}_{lmp}^s &= \frac{1}{\cos^m \bar{\phi} \sin^{m+\kappa} \bar{i}} \left[ \frac{l-2p}{\kappa} Y_\kappa^s \Psi_m^c - Y_\kappa^c \Psi_m^s \right] \quad , \end{aligned} \quad (\text{B.47})$$

where

$$\begin{aligned} Y_\kappa^c &= \sum_{k=0}^{\frac{\kappa}{2}} \binom{\kappa}{2k} (-1)^k \left( \sin^2 \bar{i} - \sin^2 \bar{\phi} \right)^{\frac{\kappa-2k}{2}} \sin^{2k} \bar{\phi} \quad , \\ Y_\kappa^s &= \sum_{k=0}^{\frac{\kappa-1}{2}} \binom{\kappa}{2k+1} (-1)^k \left( \sin^2 \bar{i} - \sin^2 \bar{\phi} \right)^{\frac{\kappa-2k-1}{2}} \sin^{2k+1} \bar{\phi} \quad , \end{aligned} \quad (\text{B.48})$$

and

$$\begin{aligned} \Psi_m^c &= \sum_{k=0}^{\frac{m}{2}} \binom{m}{2k} (-1)^k \left( \sin^2 \bar{i} - \sin^2 \bar{\phi} \right)^{\frac{m-2k}{2}} \cos^{2k} \bar{i} \sin^{2k} \bar{\phi} \quad , \\ \Psi_m^s &= \sum_{k=0}^{\frac{m-1}{2}} \binom{m}{2k+1} (-1)^k \left( \sin^2 \bar{i} - \sin^2 \bar{\phi} \right)^{\frac{m-2k-1}{2}} \cos^{2k+1} \bar{i} \sin^{2k+1} \bar{\phi} \quad . \end{aligned} \quad (\text{B.49})$$

All functions  $\overline{Q}_{lm}^{c,s}$ ,  $D_{lmp}$ ,  $\overline{\Phi}_{lmp}^{c,s}$ ,  $Y_\kappa^{c,s}$  and  $\Psi_m^{c,s}$  have to be evaluated for each point on which the radial orbit perturbation is to be computed. Many of those evaluations require a significant amount of summations and computations of sines, cosines and binomial coefficients. This effort then has to be repeated, for example globally for each  $1^\circ \times 1^\circ$  cell, or for all crossover points, easily running into the hundreds of thousands reiterations of the process. It is evident that an efficient way has to be found to make all those computations within a respectable time on an average computer. This method is further described in Appendix C.

The expressions in this Section describe orbit perturbations or orbit errors based on known gravitational coefficients or known errors in these coefficients.

Similar expression can be derived for the orbit perturbations in the along-track and cross-track direction [Rosborough, 1987], but they are not considered in this thesis.

If a new gravity field model is developed, we can simulate the effect on the orbit from the differences with a previous gravity field solution. But this tells more about the previous than the new solution. The solution, however, generally comes with error estimates for the coefficients and their mutual correlations, in the form of a covariance matrix. It is relatively simple to transform the expressions above in expressions for an orbit error estimate in terms of coefficient covariances,  $P_{lmjk}$ , rather than coefficients,  $\bar{C}_{lm}$ , or their errors,  $\Delta\bar{C}_{lm}$  [Rosborough, 1986, 1988]. The variances of the two partial radial orbit errors described in (B.43) are given by

$$\begin{aligned}\sigma^2(\Delta r_{lm}^c) &= \sum_{j=1}^{\infty} \sum_{k=0}^j \bar{Q}_{lm}^c \bar{Q}_{jk}^c (P_{lmjk}^{cc} \cos m\bar{\lambda} \cos k\bar{\lambda} \\ &\quad - 2P_{lmjk}^{cs} \cos m\bar{\lambda} \sin k\bar{\lambda} + P_{lmjk}^{ss} \sin m\bar{\lambda} \sin k\bar{\lambda}) \quad , \\ \sigma^2(\Delta r_{lm}^s) &= \sum_{j=1}^{\infty} \sum_{k=0}^j \bar{Q}_{lm}^s \bar{Q}_{jk}^s (P_{lmjk}^{cc} \sin m\bar{\lambda} \sin k\bar{\lambda} \\ &\quad - 2P_{lmjk}^{cs} \sin m\bar{\lambda} \cos k\bar{\lambda} + P_{lmjk}^{ss} \cos m\bar{\lambda} \cos k\bar{\lambda}) \quad ,\end{aligned}\tag{B.50}$$

where  $P_{lmjk}^{cc,cs,ss}$  represent the covariances between the geopotential coefficient errors:

$$\begin{aligned}P_{lmjk}^{cc} &= E \left[ \Delta\bar{C}_{lm} \Delta\bar{C}_{jk} \right] \quad , \\ P_{lmjk}^{cs} &= E \left[ \Delta\bar{C}_{lm} \Delta\bar{S}_{jk} \right] \quad , \\ P_{lmjk}^{ss} &= E \left[ \Delta\bar{S}_{lm} \Delta\bar{S}_{jk} \right] \quad .\end{aligned}\tag{B.51}$$

## Appendix C

# An Efficient Way to Compute the Gravity-induced Radial Orbit Error

Appendix B described, based on the linear perturbation theory, how the radial orbit errors can be computed, based on the geopotential coefficients or their errors. The theory provides a way to determine the temporal and spatial characteristics of the perturbations.

The formulations for the radial perturbations as a function of time (B.27–B.33) are relatively straightforward, except for the matrix  $D_{lmp}$  which is based on the inclination functions  $\bar{F}_{lmp}(i)$ . When those formulae are transferred from the temporal to the spatial domain things get more complicated: the latitude functions  $\bar{Q}_{lm}^{c,s}$  (B.44) are introduced, which, in turn, require the functions  $\tilde{\Phi}_{lmp}^{c,s}$ ,  $Y_k^{c,s}$ , and  $\Psi_m^{c,s}$  (B.47–B.49). Each of these functions contain a number of summations, binomial coefficients, and/or trigonometric functions and are thus computationally intensive. When these functions are to be evaluated at hundreds of thousands of globally distributed crossover or grid points this can lead to excessive computational time.

Hence a set of subroutines is developed to efficiently process the complex functions at a large number of locations. A program based on these subroutines, determining the radial orbit errors on a regular grid, is illustrated in Section C.1; the performance of the program is evaluated in Section C.2.

### C.1 An example of the computation of geographically correlated radial orbit errors

Assume you want to compute the gravity-induced radial orbit errors of ERS-2 based on the difference between the coefficients of the JGM-2 and JGM-3 grav-

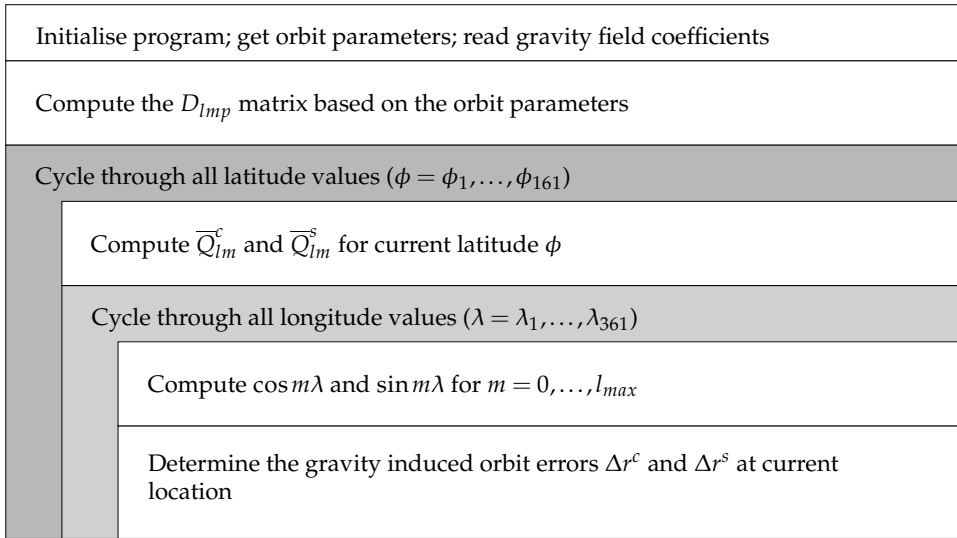


Figure C.1 Schematic overview of a program to compute gravity induced orbit errors on a regular grid.

ity field models. Assume you want to map these errors onto a regular grid with cells of  $1^\circ \times 1^\circ$ . Limiting the latitudes to the range of  $-80^\circ$  to  $+80^\circ$ , leads to a total of  $161 \times 361$  or 58 212 grid-points. To make this computation run within a reasonable time, let's say 10 minutes, the computational effort for each grid point should be less than 10 milliseconds. Simply evaluating all functions mentioned above leads to a processing time per grid point of 1 second or more on a standard workstation. A more efficient solution is illustrated in Figure C.1. The program consists of the following steps:

1. When the program is started, set the relevant parameters of the orbit ( $\overline{a}$ ,  $\overline{i}$ ,  $(\overline{\omega} + \overline{M})$ , and  $(\overline{\Omega} - \overline{\theta})$ ) and read all the gravity field coefficients ( $\overline{C}_{lm}$  and  $\overline{S}_{lm}$ ) or their errors ( $\Delta \overline{C}_{lm}$  or  $\Delta \overline{S}_{lm}$ ) from a file.
2. For the given mean inclination,  $\overline{i}$ , store inclination-dependent functions like  $\cos^m \overline{i}$  in a lookup table, compute and store matrix  $D_{lmp}$ , and create lookup tables for the binomial coefficients up to the maximum order of the gravity field. This procedure does not have to be repeated, unless the mean inclination is changed significantly. The computation of  $D_{lmp}$  (B.28–B.33) also requires the evaluation inclination functions  $\overline{F}_{lmp}(\overline{i})$ , which in turn rely on the Legendre polynomials  $\overline{P}_{lm}$ .
3. Now process parallel by parallel. This ensures that for each latitude  $\phi$  the functions  $\overline{Q}_{lm}^{c,s}$  have to be evaluated only once for each horizontal grid line.
4. Create lookup tables for a number of latitude dependent functions like

$(-1)^k \sin^{2k} \phi$ , then calculate  $Y_k^{c,s}$  and  $\Psi_m^{c,s}$ , and finally determine  $\overline{Q}_{lm}^{c,s}$  for this latitude and for all degrees and orders up to the maximum order of the gravity field model (B.44–B.49).

5. Cycle through all the meridians along the current parallel.
6. Create lookup tables for  $\cos m\lambda$  and  $\sin m\lambda$  for each degree  $m$  between 0 and the maximum order of the gravity field model  $l_{max}$ . This can be done fast using a recursive relation based on the trigonometric addition identities.
7. The orbit errors are a simple summation of functions  $\overline{Q}_{lm}^{c,s}$  multiplied by the appropriate gravity field coefficients and  $\cos m\lambda$  and  $\sin m\lambda$  (B.42–B.43).

The process for computing radial orbit errors in crossover locations runs similarly, since crossovers are located also on a more-or-less regular grid of distinct latitudes and longitudes (see Figure 1.6). In that case it is wise to order the crossovers by latitude, limiting the number of evaluations of  $\overline{Q}_{lm}^{c,s}$  to a minimum.

## C.2 Software performance

The software described in this Chapter was coded in FORTRAN and compiled and tested on a typical medium-performance workstation (a 366-MHz Pentium II laptop computer running the Linux operating system). Because of the reuse of arrays and lookup tables, the memory space requirements for the test program are very moderate; only 1.5 MBytes of memory is needed to run the program described in Section C.1.

Of larger concern is the processing time: does the program run fast enough to provide a grid of  $161 \times 361$  estimates of the radial orbit error within a reasonable amount of time? To assess this question, the time spent in the various subroutines was determined, not counting any writing of the results to file.

The performances for each routine and the overall test program are shown in Table C.1. Note that the most time consuming recurrent component is the computation of the  $\overline{Q}_{lm}^{c,s}$  matrices. It is therefore important to call this routine only when

Program step	Time (msec)	Number of iterations	Total time (sec)
Initialisation of the program	130	1	0.13
Computation of $D_{Imp}$	250	1	0.25
Computation of matrices $\overline{Q}_{lm}^c$ and $\overline{Q}_{lm}^s$ for each latitude	12.5	161	2.0
Computation of the radial orbit error for each location	0.5	$161 \times 361$	29.1
Total CPU time for the program			31.5

Table C.1 Processing time needed for the computation of the gravity induced radial orbit error on a grid of  $161 \times 361$  points. The CPU time per program step is indicated.

needed, when a computation for a new latitude is requested. The further computations needed for each new longitude appear marginal. The test program ultimately requires just over 30 seconds of processing time, which is far within practical limits on processing time.

Note that due to the assumption of linear perturbations this program can be used to compute the orbit errors introduced by the entire gravity field model or for errors in the coefficients of this model, as in the example, or for a subset of these coefficients. In a similar way entire covariance matrices can be propagated.



# Bibliography

- Aksnes, K., P. H. Andersen, S. Hauge, and H. Erlandsen (1994), ERS-1 orbit calculation with the Geosat software, in *Proceedings of the Second ERS-1 Symposium, Hamburg, Germany, 11–14 October 1993*, Eur. Space Agency Spec. Publ., ESA SP-361, vol. 2, edited by B. Kaldeich, pp. 741–745, January 1994.
- Andersen, O. B., and P. Knudsen (1998), Global marine gravity field from the ERS-1 and Geosat geodetic mission altimetry, *J. Geophys. Res.*, 130(C4), 8129–8137.
- Anzenhofer, M., and T. Gruber (1998), Fully reprocessed ERS-1 altimeter data from 1992 to 1995: Feasibility of detection of long term sea level change, *J. Geophys. Res.*, 103(C4), 8089–8112.
- Anzenhofer, M., T. Gruber, and M. Rentsch (1994), D-PAF sea surface models generated from different data sources, in *Proceedings of the Second ERS-1 Symposium, Hamburg, Germany, 11–14 October 1993*, Eur. Space Agency Spec. Publ., ESA SP-361, vol. 2, edited by B. Kaldeich, pp. 783–787, January 1994.
- Archiving, Validation, and Interpretation of Satellite Oceanographic data (1996), *AVISO user handbook: Merged TOPEX/Poseidon products*, Rep. AVI-NT-02-101-CN, Edition 3.0, Cent. Natl. d'Etudes Spatiales, Toulouse, France, July 1996.
- Attema, E., and C. R. Francis (1991), ERS-1 calibration and validation, *ESA Bulletin*, 65, 80–86.
- Bamber, J. L. (1994), A digital elevation model of the Antarctic Ice Sheet derived from ERS-1 altimeter data and comparison with terrestrial measurements, *Ann. Glaciol.*, 20, 48–54.
- Bamber, J. L., S. Ekholm, and W. Krabill (1998), The accuracy of satellite radar altimeter data over the Greenland Ice Sheet determined from airborne laser data, *Geophys. Res. Lett.*, 25(16), 3177–3180.
- Bedrich, S., F. Flechtner, Ch. Förste, Ch. Reigber, and A. Teubel (1997), PRARE System Performance, in *Proceedings of the Third ERS Symposium, Florence, Italy, 17–21 March 1997*, Eur. Space Agency Spec. Publ., ESA SP-414, vol. 3, edited by T.-D. Guyenne and D. Danesy, pp. 1637–1642.
- Bilitza, D. (1997), International Reference Ionosphere: Status 1995/96, *Adv. Space Res.*, 20(9), 1751–1754.
- Bilitza, D. (2002), International Reference Ionosphere, <http://nssdc.gsfc.nasa.gov/space/model/ionos/iri.html>.
- Bordi, J. J. (1999), Analysis of the Precise Range and Range-rate Equipment (PRARE) and application to precise orbit determination, *Tech. Rep. CSR-99-01*, Cent. for Space Res., Univ. of Texas at Austin, May 1999.
- Born, G. H., B. D. Tapley, and M. L. Santee (1986), Orbit determination using dual crossing arc altimetry, *Acta Astronaut.*, 13(4), 157–163.
- Brenner, A. C., C. J. Koblinsky, and B. D. Beckley (1990), A preliminary estimate of geoid induced variations in repeat orbit satellite altimeter observations, *J. Geophys. Res.*, 95(C3), 3033–3040.
- Brown, G. S. (1977), The average impulse response of a rough surface and its applications, *IEEE Trans. Antennas Propagat.*, AP-24, 67–74.
- Bruzzi, S. (1991), The processing and exploitation of ERS-1 payload data, *ESA Bulletin*, 65, 63–72.
- Calvez, M.-H. (1996), Validation of ERS-2 OPR cycle 000 (and later), *Reports CLS.OC.NT/96.001*, Collect., Localisation, Satell., Ramonville St. Agne, France.
- Cardon, K., P. Goryl, R. Scharroo, and J. Benveniste (1998), 1997/98 El Niño observed by

- ERS, *ESA Earth Observation Quarterly*, 59, 27–33, June 1998.
- Cartwright, D. E., and A. C. Edden (1973), Corrected tables of tidal harmonics, *Geophys. J. Roy. Astron. Soc.*, 33, 253–264.
- Cartwright, D. E., and R. J. Taylor (1971), New computations of the tide-generating potential, *Geophys. J. Roy. Astron. Soc.*, 23, 45–74.
- Cavaleri, L., and S. Curiotto (1979), A fast-response shallow-water tide gauge, *Il Nuovo Cimento, Serie 1*, 2C(3), 273–287.
- Cazenave, A., and J. Y. Royer (2001), Applications to marine geophysics, in *Satellite Altimetry and Earth Sciences: A Handbook of Techniques and Applications*, edited by L.-L. Fu and A. Cazenave, pp. 407–439, Academic Press, San Diego, California, ISBN 0122695423.
- Cazenave, A., P. Schaeffer, M. Bergé, C. Brossier, K. Dominh, and M. C. Gennero (1996), High-resolution mean sea surface computed with altimeter data of ERS-1 (Geodetic Mission) and TOPEX/Poseidon, *Geophys. J. Int.*, 125, 696–704.
- Cazenave, A., K. Dominh, M. C. Gennero, and B. Ferret (1998), Global mean sea level changes observed by TOPEX/Poseidon and ERS-1, *Phys. Chem. Earth*, 23(9–10), 1069–1075.
- Centre ERS d'Archivage et de Traitement (1994), *Altimeter products, User manual*, C1-EX-MUT-A21-01-CN, issue 2.6, Plouzané, France, February 1994.
- Centre ERS d'Archivage et de Traitement (1996), *Altimeter and microwave radiometer ERS products, User manual*, C2-MUT-A-01-IF, version 2.2, Plouzané, France, October 1996.
- Challenor, P., and D. Cotton (1998), Trends in TOPEX significant wave height measurement, *Tech. rep.*, James Rennell Division for Ocean Circulation, Southampton Oceanography Centre, England.
- Chelton, D. B., E. J. Walsh, and J. L. MacArthur (1989), Pulse compression and sea level tracking in satellite altimetry, *J. Atmos. Oceanic Technol.*, 6(3), 407–438.
- Chelton, D. B., J. C. Ries, B. J. Haines, L.-L. Fu, and P. S. Callahan (2001), Satellite altimetry, in *Satellite Altimetry and Earth Sciences: A Handbook of Techniques and Applications*, edited by L.-L. Fu and A. Cazenave, pp. 1–131, Academic Press, San Diego, California, ISBN 0122695423.
- Cheney, R. E., and L. Miller (1988), Mapping the 1986–87 El Niño with Geosat altimeter data, *Eos Trans. AGU*, 69, 754–755.
- Cheney, R. E., J. G. Marsh, and B. D. Beckley (1983), Global mesoscale variability from colinear tracks of Seasat altimeter data, *J. Geophys. Res.*, 88(C7), 4343–4354.
- Colombo, O. L. (1984), *Altimetry, orbits and tides*, NASA Tech. Memo. 86180, 173 pp., EG&G Washington Analytical Services Inc.
- Dorandeu, J. (1999), Side-B TOPEX altimeter evaluation, *Tech. note CLS/DOS/NT/99.175*, Collect., Localisation, Satell., Ramonville St. Agne, France, June 1999.
- Dorandeu, J., and P. Y. Le Traon (1999), Effects of global mean atmospheric pressure variations on mean sea level changes from TOPEX/Poseidon, *J. Atmos. Oceanic Technol.*, 16(9), 1279–1283.
- Dorandeu, J., F. Mertz, and J. Stum (2000), Note on ERS-2 Sigma0 variations since January 2000, *Tech. note CLS/DOS/NT/00.286*, Collect., Localisation, Satell., Ramonville St. Agne, France, August 2000.
- Douglas, B. C. (1991), Global sea level rise, *J. Geophys. Res.*, 96(C4), 6981–6992.
- Duchossois, G. (1991), The ERS-1 mission objectives, *ESA Bulletin*, 65, 16–25.
- Ekholm, S. (1996), A full coverage, high-resolution, topographic model of Greenland computed from a variety of digital elevation data, *J. Geophys. Res.*, 101(B10), 21,961–21,972.
- Engelis, T. (1987), Radial orbit error reduction and sea surface topography determination using satellite altimetry, *Rep. 377*, Dep. of Geod. Sci. and Surv., Ohio State Univ., Columbus.
- Engelis, T. (1988), On the simultaneous improvement of a satellite orbit and determination of sea surface topography using altimeter data, *Manuscr. Geod.*, 13, 180–190.
- Eymard, L., and S. A. Boukabara (1996), MWR2 anomaly: Proposal for correction, CETP, Paris, France, November 1996.
- Eymard, L., and S. A. Boukabara (1997), Calibration-validation of the ERS-2 microwave radiometer, Final report, *ESA Contract 11031/94/NL/CN*, CETP, Paris, France.
- Fenoglio-Marc, L. (2002), Long-term sea level change in the mediterranean sea from multi-satellite altimetry and tide gauges, *Phys. Chem. Earth*, p. 13 pp., in press.

- Fortescue, P. W., and J. P. W. Stark (eds.) (1995), *Spacecraft Systems Engineering*, John Wiley & Sons.
- Francis, C. R. (1991), RA data chains, *ESA Doc. ER-IS-ESA-GS-0001 issue 2B*, ESA/ESTEC, Noordwijk, The Netherlands, July 1991.
- Francis, C. R., and B. Duesmann (1988), ERS-1 altimeter calibration, *ESA Doc. ER-TN-ESA-RA-0003 issue 3*, 128 pp., ESA/ESTEC, Noordwijk, The Netherlands, July 1988.
- Francis, C. R., G. Graf, P. G. Edwards, M. McCaig, C. McCarthy, P. Dubock, A. Lefebvre, B. Pieper, P. Y. Pouvreau, R. Wall, F. Wechsler, J. Louet, and R. Zobl (1991), The ERS-1 spacecraft and its payload, *ESA Bulletin*, 65, 26–48.
- Francis, C. R., A. Caporali, L. Cavaleri, A. Cenci, P. Ciotto, L. Ciraolo, W. Gurtner, F. H. Massmann, D. del Rosso, R. Scharroo, P. Spalla, and E. Vermaat (1993), The Calibration of the ERS-1 Radar Altimeter – The Venice Calibration Campaign, *ESA Report ER-RP-ESA-RA-0257 issue 2.0*, ESA/ESTEC, Noordwijk, The Netherlands, March 1993.
- Fu, L.-L., and A. Cazenave (eds.) (2001), *Satellite Altimetry and Earth Sciences: A Handbook of Techniques and Applications*, 624 pp., Academic Press, San Diego, California, ISBN 0122695423.
- Fu, L.-L., and D. B. Chelton (2001), Large-scale ocean circulation, in *Satellite Altimetry and Earth Sciences: A Handbook of Techniques and Applications*, edited by L.-L. Fu and A. Cazenave, pp. 133–169, Academic Press, San Diego, California, ISBN 0122695423.
- Gaspar, P., and J.-P. Florens (1998), Estimation of the sea state bias in radar altimeter measurements of sea level: Results from a new non-parametric method, *J. Geophys. Res.*, 103(C8), 15,803–15,814.
- Gaspar, P., and F. Ogor (1996), Estimation and analysis of the sea state bias of the new ERS-1 and ERS-2 altimeter data (OPR version 6), *Report of task 2, IFREMER contract 96/2.246 002/C*, Collect., Localisation, Satell., Ramonville St. Agne, France.
- Gaspar, P., and R. Ponte (1997), Relation between sea level and barometric pressure determined from altimeter data and model simulations, *J. Geophys. Res.*, 102(C1), 961–971.
- Gaspar, P., and R. Ponte (1998), Correction to “relation between sea level and barometric pressure determined from altimeter data and model simulations”, *J. Geophys. Res.*, 103, 18,809.
- Gruber, T., A. Bode, C. Reigber, and P. Schwintzer (1997), D-PAF global earth gravity models based on ERS, in *Proceedings of the Third ERS Symposium, Florence, Italy, 17–21 March 1997*, *Eur. Space Agency Spec. Publ., ESA SP-414*, vol. 3, edited by T.-D. Guyenne and D. Danesy, pp. 1661–1668.
- Gruber, T., A. Bode, C. Reigber, P. Schwintzer, G. Balmino, R. Biancale, and J. M. Lemoine (2000), GRIM5-C1: Combination solution of the global gravity field to degree and order 120, *Geophys. Res. Lett.*, 27(24), 4005–4008.
- Haines, B. J., S. Desai, B. Iijima, S. Keihm, G. Kruizinga, G. Born, D. Kubitschek, and S. Gill (1999), The Harvest Experiment: Towards joint verification of TOPEX/Poseidon and Jason-1, Poster presented at the 1999 TOPEX Science Working Team Meeting.
- Haines, B. J., D. Kubitschek, G. Born, and S. Gill (2002), Dual calibration of Jason-1 and TOPEX/Poseidon at the Harvest Platform: Initial results from the tandem mission, Poster presented at the 2002 TOPEX Science Working Team Meeting.
- Hancock III, D. W., G. S. Hayne, R. L. Brooks, D. W. Lockwood, and J. E. Lee (1999), TOPEX radar altimeter engineering assessment report: Update: From launch to turn-off of Side A on February 10, 1999, *NASA/WFF TOPEX Report*, NASA Goddard Space Flight Center, Wallops Flight Facility, Wallops Island, Virginia, August 1999, <http://topex.wff.nasa.gov/docs>.
- Hanssen, R., B. Vermeersen, R. Scharroo, B. Kampes, S. Usai, R. Gens, and R. Klees (2000), Deformatiepatroon van de aardbeving van 17 augustus 1999 in turkije gemeten met satelliet radar interferometrie, *Remote Sensing Nieuwsbrief*, 90, 42–44, February 2000.
- Hedin, A. E. (1987), MSIS-86 thermospheric model, *J. Geophys. Res.*, 92(A5), 4649–4662.
- Heiskanen, W. A., and H. Moritz (1967), *Physical Geodesy*, W. H. Freeman, San Francisco, California.
- Iijima, B. A., I. L. Harris, C. M. Ho, U. J. Lindqwister, A. J. Mannucci, X. Pi, M. J. Reyes, L. C. Sparks, and B. D. Wilson (1999), Automated daily process for global ionospheric total electron content maps and satellite ocean altimeter ionospheric calibration

- based on Global Positioning System data, *J. Atmos. and Solar-Terrestrial Phys.*, 61, 1205–1218.
- Imel, D. A. (1994), Evaluation of the TOPEX/Poseidon dual-frequency ionosphere correction, *J. Geophys. Res.*, 99(C12), 24,895–24,906.
- Janssen, P. A. E. M. (2000), ECMWF wave modeling and satellite altimeter wave data, in *Satellites, Oceanography and Society*, vol. 63 of *Elsevier Oceanography Series*, edited by D. Halpern, pp. 35–56, Elsevier, Amsterdam The Netherlands, ISBN 0-444-50501-6.
- Jekeli, C. (1978), An investigation of two models for the degree variances of global covariance functions, *Report No. 275*, Dep. of Geod. Sci. and Surv., Ohio State Univ., Columbus, September 1978.
- Jensen, J. R. (1999), Radar altimeter gate tracking: Theory and extension, *IEEE Trans. Geosci. Rem. Sens.*, 37(2), 651–658.
- Kaula, W. M. (1966), *Theory of Satellite Geodesy*, Blaisdell Press, Waltham, Mass.
- Klokočník, J., J. Kostelecký, and D. Karasová (1994), *Satellite Altimetry and Its Use in Geoscience*, Research Institute of Geodesy, Topography and Cartography, Zdíby, Czechia.
- Knudsen, P., and O. B. Andersen (1996), Ocean bottom topography from ERS-1 altimeter data, *ESA Earth Observation Quarterly*, 51, 16–18.
- Kolenkiewicz, R., and C. F. Martin (1982), Seasat altimeter height calibration, *J. Geophys. Res.*, 87(C5), 3189–3197.
- Kozel, B. J. (1995), Dual-satellite altimeter crossover measurements for precise orbit determination, *Report No. CSR-95-4*, Cent. for Space Res., Univ. of Texas at Austin.
- Kuijper, D. C. (1991), Modelling of the aerodynamic forces for the earth remote sensing satellite ERS-1, Faculty of Aerospace Engineering, Delft University of Technology, Delft, The Netherlands, March 1991.
- Le Provost, C. (2001), Ocean tides, in *Satellite Altimetry and Earth Sciences: A Handbook of Techniques and Applications*, edited by L.-L. Fu and A. Cazenave, pp. 267–303, Academic Press, San Diego, California, ISBN 0122695423.
- Le Provost, C., F. Lyard, J. M. Molines, M. L. Genco, and F. Rabilloud (1998), A hydrodynamic ocean tide model improved by assimilating a satellite altimeter-derived data set, *J. Geophys. Res.*, 103(C3), 5513–5529.
- Le Traon, P. Y., and R. Morrow (2001), Ocean currents and eddies, in *Satellite Altimetry and Earth Sciences: A Handbook of Techniques and Applications*, edited by L.-L. Fu and A. Cazenave, pp. 171–215, Academic Press, San Diego, California, ISBN 0122695423.
- Le Traon, P. Y., and F. Ogor (1998), ERS-1/2 orbit improvement using TOPEX/Poseidon: The 2 cm challenge, *J. Geophys. Res.*, 103(C4), 8045–8058.
- Le Traon, P. Y., P. Gaspar, F. Bouyssel, and H. Makhmara (1994), Reducing ERS-1 orbit error using TOPEX/Poseidon data, in *Proceedings of the Second ERS-1 Symposium, Hamburg, Germany, 11–14 October 1993*, Eur. Space Agency Spec. Publ., ESA SP-361, vol. 2, edited by B. Kaldeich, pp. 759–763, January 1994.
- Le Traon, P. Y., P. Gaspar, F. Ogor, and J. Dorandeu (1995a), Satellites work in tandem to improve accuracy of data, *Eos Trans. AGU*, 76(39), 385&389.
- Le Traon, P. Y., P. Gaspar, F. Bouyssel, and H. Makhmara (1995b), Using TOPEX/Poseidon data to enhance ERS-1 data, *J. Atmos. Oceanic Technol.*, 12(1), 161–170.
- Lemoine, F.G., D. E. Smith, L. Kunz, R. Smith, E. C. Pavlis, N. K. Pavlis, S. M. Klosko, D. S. Chinn, M. H. Torrence, R. G. Williamson, C. M. Cox, K. E. Rachlin, Y. M. Wang, S. C. Kenyon, R. Salman, R. Trimmer, R. H. Rapp, and R. S. Nerem (1997), The development of the NASA GSFC and NIMA Joint Geopotential Model, in *International Association of Geodesy Symposia, Gravity, Geoid and Marine Geodesy*, vol. 117, edited by J. Segawa *et al.*, pp. 461–469, Springer-Verlag, Berlin.
- Llewellyn, S. K., and R. B. Bent (1973), Documentation and description of the Bent ionospheric model, *Rep. AFCRL-TR-73-0657*, Air Force Geophysics Laboratory, Hanscom Air Force Base, Massachusetts.
- Louet, J. (1991), ERS-1 Laser Retro-Reflector (LRR) characterisation data, *ESA Doc. ER-TN-ESA-LRR-0001*, ESA/ESTEC, Noordwijk, The Netherlands, February 1991.
- Lutjeharms, J. R. E. (1981), Features of the Southern Agulhas Current circulation from satellite remote sensing, *S. Afr. J. Sci.*, 77, 231–236.
- Malanotte-Rizzoli, P., and A. Bergamasco (1983), The dynamics of the coastal region of the Northern Adriatic Sea, *J. Phys. Oceanogr.*, 13(7), 1105–1130.

- Marini, J. W., and C. W. Murray (1973), Correction of laser range tracking data for atmospheric refraction at elevations above 10 degrees, *Tech. Memo NASA-TM-X-70555*, Goddard Space Flight Center, Greenbelt, Maryland.
- Marsh, J. G., F. J. Lerch, B. H. Putney, T. L. Felsenreger, B. V. Sanchez, S. M. Klosko, G. B. Patel, J. W. Robbins, R. G. Williamson, T. L. Engelis, W. F. Eddy, N. L. Chandler, D. S. Chinn, S. Kapoor, K. E. Rachlin, L. E. Braatz, and E. C. Pavlis (1989), The GEM-T2 gravitational model, *NASA Tech. Memo. 100746*, 91 pp., Goddard Space Flight Center, Greenbelt, Maryland, October 1989.
- Marsh, J. G., F. J. Lerch, B. H. Putney, T. L. Felsenreger, B. V. Sanchez, S. M. Klosko, G. B. Patel, J. W. Robbins, R. G. Williamson, T. L. Engelis, W. F. Eddy, N. L. Chandler, D. S. Chinn, S. Kapoor, K. E. Rachlin, L. E. Braatz, and E. C. Pavlis (1990), The GEM-T2 gravitational model, *J. Geophys. Res.*, 95(B13), 22,043–22,071.
- Marshall, J. A., N. P. Zelensky, S. M. Klosko, D. S. Chinn, S. B. Luthcke, K. E. Rachlin, and R. G. Williamson (1995), The temporal and spatial characteristics of TOPEX/Poseidon radial orbit error, *J. Geophys. Res.*, 100(C12), 25,331–25,352.
- Martin, C. F., and R. Kolenkiewicz (1981), Calibration validation for the GEOS 3 altimeter, *J. Geophys. Res.*, 86(C9), 6369–6381.
- Martini, A., and P. Féménias (2000), The ERS SPTR2000 altimetric range correction: Results and validation, *Technical Note ERE-TN-ADQ-GSO-6001*, ESA/ESRIN, Frascati, Italy, November 2000.
- Massmann, F.-H., C. Reigber, R. König, J. C. Raimondo, and C. Rajasenan (1994), ERS-1 orbit information provided by D-PAF, in *Proceedings of the Second ERS-1 Symposium, Hamburg, Germany, 11–14 October 1993*, *Eur. Space Agency Spec. Publ.*, ESA SP-361, vol. 2, edited by B. Kaldeich, pp. 765–770, January 1994.
- Massmann, F.-H., J. C. Raimundo, C. Reigber, C. Falck, F. Flechtner, and A. Scherbatschenko (2000), The PRARE system onboard ERS-2: Status and results, in *Proceedings of the ERS-ENVISAT Symposium, Gothenburg, Sweden, 16–20 October 2000*, *Eur. Space Agency Spec. Publ.*, ESA SP-461.
- McCarthy, D. D. (ed.) (1996), IERS Standards (1996), *IERS Technical Note 21*, Central Bureau of IERS, Observatoire de Paris, France.
- Miguel, L. Saavedra de, and P. Femenias (2000), PATN propagation errors and step length, *ESA document*, ESA/ESRIN, Frascati, Italy.
- Mitchum, G. T. (1994), Comparison of TOPEX sea surface heights and tide gauge sea levels, *J. Geophys. Res.*, 99(C12), 24,541–24,553.
- Mitchum, G. T. (1998), Monitoring the stability of satellite altimeters with tide gauges, *J. Atmos. Oceanic Technol.*, 15(3), 721–730.
- Montenbruck, O., and E. Gill (2000), *Satellite Orbits: Models, methods, applications*, Springer-Verlag, Berlin, ISBN 3-540-67820-X.
- Moore, P. (1990), Global non-dynamic improvement of radial positioning for altimeter satellites, paper presented at XXVIII COSPAR, The Hague, The Netherlands.
- Moore, P., S. Ehlers, and S. Carnochan (1998), Accuracy assessment and refinement of the JGM-2 and JGM-3 gravity fields for radial positioning of ERS-1, *J. Geod.*, 72(7/8), 373–384.
- Moritz, H. (1973), *Least-Squares Collocation*, Verlag der Bayerischen Akademie der Wissenschaften, München.
- Moritz, H. (1980), *Advanced Physical Geodesy*, Herbert Wichmann Verlag, Karlsruhe, ISBN 3-87907-106-3.
- Naeije, M. C., E. Wisse, R. Scharroo, and K. F. Wakker (1994), Ocean dynamics from the ERS-1 35-day repeat mission, in *Proceedings of the Second ERS-1 Symposium, Hamburg, Germany, 11–14 October 1993*, *Eur. Space Agency Spec. Publ.*, ESA SP-361, vol. 1, edited by B. Kaldeich, pp. 501–506, January 1994.
- Nerem, R. S. (1995), Global mean sea level variations from TOPEX/Poseidon altimeter data, *Science*, 268, 708–710.
- Nerem, R. S. (1997), Global mean sea level change: Correction, *Science*, 275, 1053.
- Nerem, R. S., and T. Mitchum (2001), Sea level change, in *Satellite Altimetry and Earth Sciences: A Handbook of Techniques and Applications*, edited by L.-L. Fu and A. Cazenave, pp. 329–349, Academic Press, San Diego, California, ISBN 0122695423.
- Nerem, R. S., F. J. Lerch, J. A. Marshall, E. C. Pavlis, B. H. Putney, B. D. Tapley, R. J. Eanes, J. C. Ries, B. E. Schutz, C. K. Shum, M. M. Watkins, S. M. Klosko, J. C. Chan, S. B. Luthcke, G. B. Patel, N. K. Pavlis, R. G. Williamson, R. H. Rapp, R. Biancale, and F. Nouel (1994), Gravity model development for TOPEX/Poseidon: Joint Gravity Models 1 and 2, *J. Geophys. Res.*, 99(C12), 24,421–24,448.

- Nerem, R. S., B. J. Haines, J. Hendricks, J. F. Minster, G. T. Mitchum, and W. B. White (1997), Improved determination of global mean sea level variations using TOPEX/Poseidon altimeter data, *Geophys. Res. Lett.*, 24(11), 1331–1334.
- Nerem, R. S., D. P. Chambers, E. W. Leuliette, G. T. Mitchum, and B. S. Giese (1999), Variations in global mean sea level associated with the 1997–1998 ENSO event: Implications for measuring long term sea level changes, *Geophys. Res. Lett.*, 26(19), 3005–3008.
- Noomen, R., B. A. C. Ambrosius, H. Leenman, and K. F. Wakker (1988), Precise orbit computation of LAGEOS, in *Proceedings of the AIAA/AAS Astrodynamics Conference, Minneapolis, Minnesota, 15–17 August 1988*, pp. 17–25, American Institute of Aeronautics and Astronautics, Washington, D.C.
- Nouël, F., J. Bardina, C. Jayles, Y. Labrunne, and B. Troung (1988), DORIS: A precise satellite positioning doppler system, in *Adv. Astronaut. Sci.*, vol. 65, edited by J. K. Soldner *et al.*, pp. 311–320, Univelt Inc., San Diego, Calif.
- Paganini, M., and J. Louet (1992), Accurate Delta Times - PATN file format, *ESA doc ER-TN-ESA-GS-0259*, ESA/ESTEC, Noordwijk, The Netherlands.
- Phillippart, M. E., A. W. Gebraad, R. Scharroo, M. R. T. Roest, E. A. H. Vollebregt, A. Jacobs, H. F. P. van den Boogaard, and H. C. Peters (1998), Datum 2: Data assimilation with altimetry techniques used in a tidal model, 2nd program, *NRSP-2 Report 98-19*, 117, Netherlands Remote Sensing Board (BCRS), Delft, The Netherlands, October 1998, ISBN 90-5411-251-4.
- Pi, X. (2002), JPL-GPS networks and ionospheric systems development, <http://iono.jpl.nasa.gov>.
- Ponte, R. M., and P. Gaspar (1999), Regional analysis of the inverted barometer effect over the global ocean forced by barometric pressure, *J. Geophys. Res.*, 104(C7), 15,587–15,602.
- Ponte, R. M., D. A. Salstein, and R. D. Rosen (1991), Sea level response to pressure forcing in a barotropic numerical model, *J. Phys. Oceanogr.*, 21, 1043–1057.
- Rapp, R. H. (1979), Potential coefficient and anomaly degree variance modelling revisited, *Report No. 293*, Dep. of Geod. Sci. and Surv., Ohio State Univ., Columbus, September 1979.
- Rapp, R. H. (1993), Use of altimeter data in estimating global gravity models, in *Satellite Altimetry in Geodesy and Oceanography*, vol. 50 of *Lecture Notes in Earth Sciences*, edited by R. Rummel and F. Sansò, pp. 374–417, Springer-Verlag, Berlin.
- Rapp, R. H., Y. M. Wang, and N. K. Pavlis (1991), The Ohio State 1991 geopotential and sea surface topography harmonic coefficient models, *Report No. 410*, Dep. of Geod. Sci. and Surv., Ohio State Univ., Columbus, August 1991.
- Ray, R. (1999), A global ocean tide model from TOPEX/Poseidon altimetry: GOT99.2, *NASA Tech. Memo. 209478*, 58 pp., Goddard Space Flight Center, Greenbelt, Maryland, September 1999.
- Remy, F., and J. F. Minster (1997), Antarctica ice sheet curvature and its relation to ice flow, *Geophys. Res. Lett.*, 24(9), 1039–1042.
- Rosborough, G. W. (1986), Satellite orbit perturbations due to the geopotential, *Report No. CSR-86-1*, 154 pp., Cent. for Space Res., Univ. of Texas at Austin.
- Rosborough, G. W. (1987), Radial, transverse, and normal satellite position perturbations due to the geopotential, *Celest. Mech.*, 40, 409–421.
- Rosborough, G. W. (1988), Orbit error due to gravity model error, in *Adv. Astronaut. Sci.*, vol. 65, edited by J. K. Soldner *et al.*, pp. 1417–1425, Univelt Inc., San Diego, Calif.
- Rosso, D. del (1992), Local survey of the Monte Venda site and Venice Tower site, *Telespazio S.p.A.*, February 1992.
- Rummel, R., and F. Sansò (eds.) (1993), *Satellite Altimetry in Geodesy and Oceanography*, vol. 50 of *Lecture Notes in Earth Sciences*, 491 pp., Springer-Verlag, Berlin.
- Saastamoinen, J. (1972), Atmospheric corrections for the troposphere and stratosphere in radio ranging of satellites, in *The Use of Artificial Satellites for Geodesy*, vol. 15 of *Geophys. Monogr. Ser.*, edited by S. W. Hendriksen *et al.*, pp. 247–251, American Geophysical Union, Washington, D.C.
- Sandwell, D. T., and W. H. F. Smith (1997), Marine gravity from Geosat and ERS-1 altimetry, *J. Geophys. Res.*, 102(B5), 10,039–10,054.
- Sandwell, D. T., and W. H. F. Smith (2001), Bathymetric estimation, in *Satellite Altimetry and Earth Sciences: A Handbook of Techniques and Applications*, edited by L.-L. Fu and A. Cazenave, pp. 441–457, Academic Press, San Diego, California, ISBN 0122695423.

- Schäfer, W., and W. Schuman (1995), PRARE-2, building on the lessons learnt from ERS-1, *ESA bulletin*, 83, 38–40, August 1995.
- Scharroo, R. (1995a), ERS-1 and ERS-2 radar altimeter time tags and biases, *ERS-2 RA & MWR-2 Commissioning Working Group – DUT/NOAA Progress Report 5*, Delft University of Technology, Section Space Research and Technology, Delft, The Netherlands, 10 November 1995.
- Scharroo, R. (1995b), ERS-1 and ERS-2 radar altimeter time tags and bias issues, *ERS-2 RA & MWR-2 Commissioning Working Group – DUT/NOAA Progress Report 6*, Delft University of Technology, Section Space Research and Technology, Delft, The Netherlands, 11 December 1995.
- Scharroo, R. (1996), High-resolution mean sea surface from satellite radar altimeter data, presented at European Geophysical Society XXI General Assembly, The Hague, The Netherlands, 6–10 May 1996.
- Scharroo, R. (1997), ERS precise orbit determination, <http://www.deos.tudelft.nl/ers/precorbs>.
- Scharroo, R., and P. N. A. M. Visser (1998), Precise orbit determination and gravity field improvement for the ERS satellites, *J. Geophys. Res.*, 103(C4), 8113–8127.
- Scharroo, R., K. F. Wakker, B. A. C. Ambrosius, and R. Noomen (1991), On the along-track acceleration of the LAGEOS satellite, *J. Geophys. Res.*, 96(B1), 729–740.
- Scharroo, R., K. F. Wakker, B. A. C. Ambrosius, R. Noomen, W. J. van Gaalen, and G. J. Mets (1993a), ERS-1 precise orbit determination, in *Proceedings of the First ERS-1 Symposium, Cannes, France, 4–6 November 1992*, *Eur. Space Agency Spec. Publ.*, ESA SP-359, vol. 1, edited by B. Kaldeich, pp. 477–482, March 1993.
- Scharroo, R., K. F. Wakker, B. A. C. Ambrosius, R. Noomen, W. J. van Gaalen, and G. J. Mets (1993b), ERS-1 precise orbit determination, in *Adv. Astronaut. Sci.*, vol. 84, edited by J. Teles and M. V. Samii, pp. 293–307, Univelt Inc., San Diego, Calif., AAS paper 93-270.
- Scharroo, R., K. F. Wakker, and G. J. Mets (1994), The orbit determination accuracy of the ERS-1 mission, in *Proceedings of the Second ERS-1 Symposium, Hamburg, Germany, 11–14 October 1993*, *Eur. Space Agency Spec. Publ.*, ESA SP-361, vol. 2, edited by B. Kaldeich, pp. 735–740, January 1994.
- Scharroo, R., J. L. Lillibridge, and G. J. Mets (1995), First results of the ERS radar altimeter cross-calibration, *ERS-2 RA & MWR-2 Commissioning Working Group – DUT/NOAA Progress Report 1*, Delft University of Technology, Section Space Research and Technology, Delft, The Netherlands; National Oceanic and Atmospheric Administration, Satellite and Ocean Dynamics Branch, Silver Spring, Maryland, 15 May 1995.
- Scharroo, R., G. J. Mets, and P. N. A. M. Visser (1996a), TOPEX-class orbits for the ERS satellites, *Ann. Geofis.*, 14, suppl. 1, C 262.
- Scharroo, R., P. N. A. M. Visser, G. J. Mets, and B. A. C. Ambrosius (1996b), TOPEX-class orbits for the ERS satellites, *Eos Trans. AGU*, 77(17), Spring Meet. Suppl., S76.
- Scharroo, R., E. J. O. Schrama, and R. H. N. Haagsmans (2000a), Combination of space techniques into one integrated processing model, in *Towards an Integrated Global Geodetic Observing System (IGGOS)*, edited by R. Rummel *et al.*, pp. 13–18, Springer-Verlag, Berlin, ISBN 3-540-6707903.
- Scharroo, R., P. Visser, and N. Peacock (2000b), ERS orbit determination and gravity field model tailoring: Recent developments, in *Proceedings of the ERS-ENVISAT Symposium, Gothenburg, Sweden, 16–20 October 2000*, *Eur. Space Agency Spec. Publ.*, ESA SP-461, p. 11 pp.
- Scharroo, R., E. Schrama, M. Naeije, and J. Benveniste (2000c), A recipe for upgrading ERS altimeter data, in *Proceedings of the ERS-ENVISAT Symposium, Gothenburg, Sweden, 16–20 October 2000*, *Eur. Space Agency Spec. Publ.*, ESA SP-461, p. 10 pp.
- Scharroo, R., B. Greco, P. Femenias, J. Benveniste, and R. Francis (2000d), The time tag bias of ERS altimeter data, in *Proceedings of the ERS-ENVISAT Symposium, Gothenburg, Sweden, 16–20 October 2000*, *Eur. Space Agency Spec. Publ.*, ESA SP-461, p. 12 pp.
- Schrama, E. J. O. (1989), *The Role of Orbit Errors in Processing of Satellite Altimeter Data*, Ph.D. dissertation, Dep. of Geod., Delft Univ. of Technol., Delft, The Netherlands, May 1989.
- Schrama, E. J. O., and R. D. Ray (1994), A preliminary tidal analysis of TOPEX/Poseidon altimetry, *J. Geophys. Res.*, 99(C12), 24,799–24,808.
- Schutz, B. E., B. D. Tapley, and C. Shum (1982), Evaluation of the Seasat altimeter time tag bias, *J. Geophys. Res.*, 87(C5), 3239–3245.

- Shaer, S. (1999), *Mapping and Predicting the Earth's Ionosphere Using the Global Positioning System*, Ph.D. dissertation, Astronomical Institute of the University of Berne, Switzerland, March 1999.
- Shum, C. K., D. N. Yuan, J. C. Ries, J. C. Smith, B. E. Schutz, and B. D. Tapley (1990), Precision orbit determination for the Geosat Exact Repeat Mission, *J. Geophys. Res.*, 95(C3), 2887–2898.
- Shum, C. K., B. D. Tapley, B. J. Kozel, P. Visser, J. C. Ries, and J. Seago (1994), Precise orbit analysis and global verification results from ERS-1 altimetry, in *Proceedings of the Second ERS-1 Symposium, Hamburg, Germany, 11–14 October 1993*, *Eur. Space Agency Spec. Publ.*, ESA SP-361, vol. 2, edited by B. Kaldeich, pp. 747–752, January 1994.
- Smith, A. J. E. (1999), *Application of Satellite Altimetry for Global Ocean Tide Modeling*, Ph.D. dissertation, Delft University of Technology, The Netherlands, ISBN 90-407-1933-0.
- Smith, A. J. E., and P. N. A. M. Visser (1995), Dynamic and non-dynamic ERS-1 radial orbit improvement from ERS-1/TOPEX dual-satellite altimetry, *Adv. Space Res.*, 16(12), 123–130.
- Smith, A. J. E., B. A. C. Ambrosius, and K. F. Wakker (2000), Ocean tides from T/P, ERS-1, and GEOSAT altimetry, *J. Geod.*, 74(5), 399–413.
- Smith, W. H. F., and D. T. Sandwell (1994), Bathymetric prediction from dense satellite altimetry and sparse shipboard bathymetry, *J. Geophys. Res.*, 99(B11), 21,803–21,824.
- Smith, W. H. F., and D. T. Sandwell (1997), Global seafloor topography from satellite altimetry and ship depth soundings, *Science*, 277(5334), 1956–1962.
- Stum, J., F. Ogor, P. Y. Le Traon, J. Dorandeu, P. Gaspar, and J-P. Dumont (1998), An intercalibration study of TOPEX/Poseidon, ERS-1 and ERS-2 altimetric missions: Final report of IFREMER contract No. 97/2 426 086/C, *CLS/DOS/NT/98.070*, Collect., Localisation, Satell., Ramonville St. Agne, France, April 1998.
- Tai, C.-K. (1991), How to observe the gyre to global-scale variability in satellite altimetry: Signal attenuation by orbit error removal, *J. Atmos. Oceanic Technol.*, 8(2), 271–288.
- Tai, C.-K., and L.-L. Fu (1986), On crossover adjustment in satellite altimetry and its oceanographic implications, *J. Geophys. Res.*, 91(C2), 2549–2554.
- Tapley, B. D. (1989), Fundamentals of orbit determination, in *Theory of Satellite Geodesy and Gravity Field Determination*, vol. 25 of *Lecture Notes in Earth Sciences*, edited by F. Sansò and R. Rummel, pp. 235–260, Springer-Verlag, Berlin.
- Tapley, B. D. (1992), TOPEX/Poseidon precision orbit determination standards, memorandum, Bur. of Eng. Res., Univ. of Tex. at Austin, 20 May 1992.
- Tapley, B. D., and G. W. Rosborough (1985), Geographically correlated orbit error and its effect on satellite altimetry missions, *J. Geophys. Res.*, 90(C6), 11,817–11,831.
- Tapley, B. D., M. M. Watkins, J. C. Ries, G. W. Davis, R. J. Eanes, S. R. Poole, H. J. Rim, B. E. Schutz, C. K. Shum, R. S. Nerem, F. J. Lerch, J. A. Marshall, S. M. Klosko, N. K. Pavlis, and R. G. Williamson (1996), The Joint Gravity Model 3, *J. Geophys. Res.*, 101(B12), 28,029–28,050.
- Tapley, B. D., C. K. Shum, J. C. Ries, S. R. Poole, P. A. M. Abusali, S. V. Bettadpur, R. J. Eanes, M. C. Kim, H. J. Rim, and B. E. Schutz (1997), The TEG-3 Geopotential Model, in *International Association of Geodesy Symposia, Gravity, Geoid and Marine Geodesy*, vol. 117, edited by J. Segawa et al., pp. 453–460, Springer-Verlag, Berlin.
- Visser, P. N. A. M. (1992), *The Use of Satellites in Gravity Field Determination and Model Adjustment*, Ph.D. dissertation, Delft Univ. of Technol., Delft, The Netherlands, September 1992.
- Visser, P. N. A. M. (1993), ERS-1 precise orbit determination using TOPEX/ERS-1 dual satellite crossover differences, *Tech. Memo CSR-TM-93-07*, Cent. for Space Res., Univ. of Texas at Austin, October 1993.
- Visser, P. N. A. M. (1995), Gravity field model adjustment from ERS-1 and TOPEX altimetry and SLR tracking using an analytical orbit perturbation theory, *Adv. Space Res.*, 16(12), 143–147.
- Wagner, C. A. (1985), Radial variations of a satellite orbit due to gravitational errors: Implications for satellite altimetry, *J. Geophys. Res.*, 90(B4), 3027–3036.
- Wahr, J. W. (1981), Body tides on an elliptical, rotating, elastic, and oceanless Earth, *Geophys. J. Roy. Astron. Soc.*, 64, 677–703.



- Wahr, J. W. (1985), Deformation of the Earth induced by polar motion, *J. Geophys. Res.*, 90(B11), 9363–9368.
- Wakker, K. F., B. A. C. Ambrosius, and L. Aardoom (1983), Precise orbit determination for ERS-1, *ESOC contract report 5227/82/D/IM(SC)*, Faculty of Aerospace Engineering, Delft University of Technology, Delft, The Netherlands.
- Wakker, K. F., B. A. C. Ambrosius, R. C. A. Zandbergen, and G. H. M. van Geldorp (1987), Precise orbit computation, gravity model adjustment and altimeter data processing for the ERS-1 altimetry mission, *ESA contract report 6140/84/D/IM*, Faculty of Aerospace Engineering, Delft University of Technology, Delft, The Netherlands.
- Wakker, K. F., R. C. A. Zandbergen, M. C. Naeije, and B. A. C. Ambrosius (1990), Geosat altimeter data analysis for the oceans around South Africa, *J. Geophys. Res.*, 95(C3), 2991–3006&3421.
- Wingham, D. J., A. J. Ridout, R. Scharroo, R. J. Arthern, and C. K. Shum (1998), Antarctic elevation change from 1992 to 1996, *Science*, 282(5388), 456–458.
- Wisse, E., R. Scharroo, M. C. Naeije, and K. F. Wakker (1994), Mean sea surface computation from ERS-1 data, in *Proceedings of the Second ERS-1 Symposium, Hamburg, Germany, 11–14 October 1993*, *Eur. Space Agency Spec. Publ.*, ESA SP-361, vol. 2, edited by B. Kaldeich, pp. 1053–1058, January 1994.
- Wisse, E., M. C. Naeije, R. Scharroo, A. J. E. Smith, F. C. Vossepoel, and K. F. Wakker (1995), Processing of ERS-1 and TOPEX/Poseidon altimeter measurements; Final report, *BCRS study 1.2/OP-01, BCRS report 95–02*, Netherlands Remote Sensing Board (BCRS), Delft, The Netherlands, April 1995, ISBN 90-5411-149-6.
- Witter, D. L., and D. B. Chelton (1991), A Geosat altimeter wind speed algorithm and a method for altimeter wind speed algorithm development, *J. Geophys. Res.*, 96(C5), 8853–8860.
- Yi, Y. (1995), Determination of gridded mean sea surface from TOPEX, ERS-1 and Geosat altimeter data, *DGSS Rep. 434*, Dep. of Geod. Sci. and Surv., Ohio State Univ., Columbus, December 1995.
- Zandbergen, R. C. A. (1991), *Satellite Altimeter Data Processing: From Theory To Practice*, Ph.D. dissertation, Faculty of Aerospace Engineering, Delft University of Technology, Delft, The Netherlands, January 1991.
- Zandbergen, R. C. A., K. F. Wakker, and B. A. C. Ambrosius (1986), Analysis of radial orbit errors of ERS-1 and the development of super-tailored gravity models, *Adv. Space Res.*, 6(9), 183–194.
- Zlotnicki, V. (1993), Quantifying time-varying oceanographic signals with altimetry, in *Satellite Altimetry in Geodesy and Oceanography*, vol. 50 of *Lecture Notes in Earth Sciences*, edited by R. Rummel and F. Sansò, pp. 144–188, Springer-Verlag, Berlin.
- Zwally, H. J., and A. C. Brenner (2001), Ice sheet dynamics and mass balance, in *Satellite Altimetry and Earth Sciences: A Handbook of Techniques and Applications*, edited by L.-L. Fu and A. Cazenave, pp. 351–369, Academic Press, San Diego, California, ISBN 0122695423.



# Curriculum Vitae

I was born on 5 July 1966 in Den Haag (The Hague), The Netherlands. From 1978 to 1984 I visited Gymnasium at the Huygens Lyceum in Voorburg with mathematics, physics, chemistry, and Latin as main courses. In 1983 I reached the top ten in the national Mathematics Olympiad.

After secondary school my interests in aircraft design impelled me to study at the Faculty of Aerospace Engineering of the Delft University of Technology. However, after a period of two years spent on general topics of aeronautical engineering, astronautics caught my attention, leading to a final study period dedicated to satellite mission design and orbit determination. Valuable to this study were my experiences obtained during a three months training period at the Kootwijk Observatory for Satellite Geodesy.

In 1989, I graduated *cum laude* on the subject of LAGEOS orbit perturbations due to radiation pressure, and received the honour of best graduating student at the Faculty that year. After being employed as PhD student for several years, I accepted a position as Research Associate at the same Faculty in 1993 and became responsible for the coding of much of the altimeter data processing software used at the Section Orbital Mechanics, that would later become the Delft Institute for Earth-Oriented Space Research. In 1990, I got involved in the preparations for the orbit determination and absolute calibration of the ERS-1 altimeter, and joined the ERS cross-calibration team in 1995. Results on altimeter calibration, validation, and satellite orbit determination were presented at numerous international meetings and conferences and were published in refereed journals. Expertise in these fields is shared as a member of international geophysical societies, research groups, and the science advisory groups for the Envisat and CryoSat altimeter missions.

In 1997, I became Assistant Professor Satellite Systems and Instrumentation at the Faculty, lecturing to both first and fourth year students and advising numerous graduate students. Currently, I am on sabbatical leave at the Laboratory for Satellite Altimetry of the National Oceanic and Atmospheric Administration in Silver Spring, Maryland.

I am married and have two stepdaughters.